Determination of Volumetric Soil Water Content Using Ground Penetrating Radar

Bestimmung des volumetrischen Bodenwassergehaltes mit dem Bodenradar

DISSERTATION

Zur Erlangung des akademischen Grades eines

DOKTORS DER NATURWISSENSCHAFTEN

genehmigt von der Fakultät für Physik der
Universität Karlsruhe (TH)
vorgelegt von

Dipl.-Geophys. Kwasi Preko

aus

Abetifi in Ghana

Tag der mündlichen Prüfung:	07. Dezember 2007
Referent:	Prof. Dr. Friedemann Wenzel
Korreferent:	Prof. Dr. Helmut Wilhelm

To Alice, Kwaku, Adwoa and Afua

Before God we are equally wise - and equally foolish.

Albert Einstein

Abstract

I performed controlled flooding experiments on a loamy sand dike model at the Theodor-Rehbock laboratory of the Institute for Water and River Basin Management, University of Karlsruhe, Karlsruhe, Germany with the guided wave sounding (GWS) method, an invasive application of the ground penetrating radar (GPR) using 500 MHz and 900 MHz momotatic antennas. Guided wave reflections from the lower end of a metal rod lowered at 2.5 cm intervals through an access tube sunk through the dike's crest gave information about the dielectric properties of the dike and thus its soil water content distribution. Measured soil water infiltration at different flooding levels between 0 and 125 cm revealed that the cohesion of soil particles at the contact zone between soil layers at a depth of about 0.6 m was loose. This occurrence created a preferential infiltration path along the border zone of the two soil layers resulting in an anomalously high soil water content of 0.32 m^3m^{-3}. A breach of this nature in a dike could cause instability and eventual collapse of the dike structure if it is not early detected and checked. I performed a second experiment on a full-scale sand dike model at the Federal Waterways and Research Institute, Karlsruhe, under controlled precipitation conditions using water sprinklers. The experiment revealed that the dike body comprised of a 0.3 m thick organic overburden which had a relatively higher water storage capacity than the sand layers below. Comparing GWS with co-located reference measurements using the time domain reflectometry with intelligible microelements (TRIME TDR) on the two dike models showed comparable soil water distribution patterns, however, GWS had the advantage of a much higher depth resolution.

I performed a third experiment in the neighbourhood of the Bontioli Faunal Reserve ($11^\circ 10'$ N, $03^\circ 05'$ W) near Dano, Burkina Faso (from August 1-19, 2006) using the combined application of the wide angle reflection and refraction (WARR) and the common offset (CO) methods of GPR with 300 MHz bistatic antennas. Soil water information in the near $\sim$ 0.1 m at distance intervals of 10 cm was acquired along a 1 km long transect. As reference measurements, the time domain reflectometry (TDR) and frequency domain reflectometry (FDR) probes were buried at 200 m intervals along the transect to sample soil water content data at 10 cm and 20 cm depths respectively. These 3 ground experiments, i.e. the GPR, TDR and FDR, were designed to map the spatial heterogeneity of soil water content along the 1 km long transect and to serve as reference experiments for a satellite system with a horizontal spatial resolution of 25 km.

The GPR method, revealed strong heterogeneities in both spatial and temporal soil water content distribution, an information not covered by the discrete point measurements offered by TDR and FDR. Geostatistical analyses of the spatial soil water content distribution showed a correlation length between 50−102 m. This meant that TDR- and FDR-derived soil water content information which were acquired at distance intervals of 200 m were uncorrelated. Soil water content in Dano, Burkina Faso, West Africa during the raining season show strong spatial heterogeneity and spatial variability. It shows strong correlation with precipitation and no correlation with evaporation. Considering the strong heterogeneity in the spatial soil water content distribution pattern in Dano (which point measurements fail to explain), the larger volume of GPR data (> 9000 as compared to 6 from discrete point measurements) and the additional errors introduced by the invasive character of point measurements, I see GPR-derived soil water content as the more appropriate ground truth for comparison with satellite measurements than that from discrete point measurements. GPR has further advantages over discrete point measurements for being quasi-continuous, non-invasive and fast.

Contents

Zusammenfassung

Das Hauptthema dieser Arbeit ist die Charakterisierung der Bodenfeuchte in der ungesättigten (vadosen) Zone mit Hilfe des Bodenradars (ground penetrating radar, GPR). Es wurden kontrollierte GPR Experimente an Deichmodellen sowie Feldexperimente in der halb-trockenen Burkina Faso Region in Westafrika durchgeführt. Mit GPR misst man die Ausbreitungsgeschwindigkeit von elektromagnetischen Wellen durch den Boden und bestimmt daraus den dielektrischen Koeffizienten des Bodens. Mit Hilfe einer Kalibrationsgleichung kann dann der Feuchtegehalt des Bodens bestimmt werden. Die allgemein anerkannte Kalibrationsgleichung von Topp et al. (1980) wurde angewandt, um den Bodenwassergehalt durch dielektrische Koeffizientenmessungen zu bestimmen. Alle Daten wurden mit der Reflexw Software prozessiert.

Der erste Teil der Arbeit befasst sich mit Infiltrationsexperimenten an einem Deichmodell ($8,0\,\mathrm{m} \times 2,2\,\mathrm{m} \times 1,4\,\mathrm{m}$). Hierzu wurde die Guided Wave Sounding (GWS) Methode angewandt, eine invasive Anwendung der GPR Technik mit einer 500 MHz Antenne. Zum Vergleich mit GPR-hergeleiteten Bodenwassermessungen wurden an der gleichen Stelle des Deichmodells Messungen mit der Time Domain Reflectometry mit Intelligible Microelements (TRIME-TDR) Methode durchgeführt. Diese Experimente fanden am Kamm des Deichs statt. Während des Experiments wurde das Deichmodell bis zu verschiedenen Wasserständen zwischen 0 und 1,25 m geflutet. Bei jedem Wasserstand wurde die Wasserverteilung im Deich auf Grund von Infiltration untersucht. Der Zeitabstand zwischen den Messungen betrug 24 Stunden, um zu gewährleisten dass der Deich einen quasi-stationären Zustand erreicht hatte. Die Resultate aus den Infiltrationsexperimenten an den Deichmodellen zeigten, da die Randzone zwischen 2 Bodenschichten in einer Tiefe von ca. 0,6 m den größten Wassergehalt mit 0,32 $\mathrm{m^3m^{-3}}$ anzeigte. Diese Anomalie ist höchstwahrscheinlich auf mangelnde Kohäsion der Bodenpartikel in dieser Zone zurückzuführen, wobei ein bevorzugter Wasserinfiltrationspfad in dieser Zone erzeugt wurde. Parallele Experimente auf dem 2 m langen Deichkamm wurden mit der Common Midpoint (CMP) Methode mit einer 900 MHz Sende- bzw. einer 500 MHz Empfängerantenne durchgeführt. Die CMP Methode zeigte eine geringere Auflösung als die GWS Methode und der Vergleich der Feuchtedaten beider Methoden ergab einen mittleren Abweichung von 0,06 $\mathrm{m^3m^{-3}}$. Die Datenerfassung und -verarbeitung der CMP Methode sind sehr arbeits- und zeitintensiv. Dies macht die Methode besonders für Feldexperimente uninteressant.

Weitere Experimente dieser Arbeit wurden an einem realitätsgetreuen Deichmodell durchgeführt. Dieses Modell wurde mit Wassersprengern kontrolliert beregnet. Für die Experimente wurde die GWS Methode angewandt und auf der nassen Oberfläche des Deichmodells durchge-

führt. Es wurden 2 Bodenwasserverteilungsphasen untersucht direkt vor und nach 72-stündiger Beregnung. Die Resultate der Experimente ergeben, dass die oberste Schicht von 0,3 m den höchsten Wassergehalt aufweist. Innerhalb dieser Schicht nimmt der Bodenwassergehalt mit der Tiefe ab. Unterhalb der obersten Schicht bis zu einer Endtiefe von etwa 1,6 m nimmt der Wassergehalt hingegen wieder zu. Die Bodenschicht zwischen Oberfläche und etwa einer Tiefe von 0,3 m repräsentiert eine inhomogene organische Auflage (Boden). Dieser Boden zeichnet sich im Gegensatz zum unterliegenden Sand durch eine besonders hohe Wasserspeicherkapazität aus. Die Zunahme der Bodenfeuchte in den Sandschichten darunter ist auf die Einsickerung von Wasser aus den oberen Schichten und eine Stauung des Wassers an der Basis des Deiches zurückzuführen.

Zusätzlich zur GWS Methode wurde ein Experiment mit einer hängenden Metallstange (ca. 25 cm Länge und 4,5 cm Durchmesser) durchgeführt. Diese Stange wurde durch ein Zugangsrohr in Abständen von 5 cm herabgelassen, wobei das GPR im *Common Offset* (CO) Modus betrieben wird. Das Experiment lieferte nicht die erwarteten Ergebnisse, da bei bestimmten Tiefenlagen der Metallstange keine Reflexionen aufgezeichnet wurden. Diese Anomalie wurde möglicherweise durch destruktive Interferenz der einfallenden und der reflektierten Welle am oberen Ende der Metallstange hervorgerufen.

Die Infiltrationsexperimente mit GWS und TRIME-TDR an den beiden Deichmodellen lassen folgende Schlüsse zu:

- Mit GWS und TRIME-TDR bestimmte Bodenfeuchteverteilungen zeigen vergleichbare Trends mit einer mittleren Abweichung von 0,11 m^3m^{-3}. Dies geringe Abweichung beider Methoden zeigt, da neben den herkömmlichen Methoden zur Bodenfeuchtemessung wie TRIME-TDR die GWS Methode eine geeignete Alternative zur Erfassung der Bodenfeuchte darstellt. Die GWS Methode hat darüberhinaus den Vorteil einer viel größeren Tiefenauflösung. Des weiteren kann der Anwender durch die modale Analyse modellierter geführter Wellen die Dämpfung der elektromagnetischen Wellenausbreitung durch den untersuchten Boden sinnvoll bestimmen.
- Die GWS Methode kann begleitend zu etablierten Methoden wie lokalen Temperaturmessungen, Piezometrik, konventionellem TDR und die Tomographie des spezifischen elektrischen Widerstands (ERT) zur Überwachung von Leckagen in Dämmen verwendet werden, um deren Sicherheit zu gewährleisten.

Der letzte Teil der Arbeit befasst sich mit Feldmessungen zur Bestimmung der Bodenfeuchte. Diese wurden in West Afrika in der Nähe des Bontionli Faunal Reserve bei Dano in Burkina Faso durchgeführt. Dabei wurde die scheinbare Bodenwellen Methode (bei welcher GPR zuerst im *Wide Angle Reflection and Refraction* (WARR) Modus und später im common offset (CO) Modus angewandt wird) entlang eines 1 km langen Profils mit 2 monostatischen Antennen mit einer mittleren Frequenz von 300 MHz benutzt. Referenzmessungen wurden mit der konventionellen time domain reflectometry (TDR) durchgeführt. Zusätzlich wurde eine *Simple Soil Moisture Probe* (SISOMOP) entlang des Messprofils in 200 m Abständen positioniert.

Die experimentellen Ergebnisse und geostatistischen Eigenschaften von Bodenfeuchtemustern können wie folgt zusammengefasst werden:

- Die scheinbare Bodenenwelle wird im nassen Boden stärker abgestrahlt als im trockenen Boden. Dies kann darauf zurückzuführen sein, da die kapazitive Kopplung zwischen den Antennen und dem Boden bei feuchter Oberfläche besser ist als bei trockener Oberfläche.
- Der Bodenfeuchtegehalt zeigt starke zeitliche wie auch räumliche Heterogenitäten. Die zeitliche Abweichung wurde durch Niederschlags- und Evapotranspirationsraten bestimmt. Die untersuchte Region war im Mittel flach, also spielte die Topographie keine wesentliche Rolle bei den zeitlichen und räumlichen Verteilungen.
- Modellversuche der scheinbaren Bodenwellen-Frequenzabhängigkeit zeigten eine bessere Abstrahlung und bessere Registrierung bei Hochfrequenzantennen als bei Niedrigfrequenzantennen. Für geschichtete Medien im schwach niedrigen Frequenzbereich ist die scheinbare Bodenwellenregistrierung des Empfängers normalerweise zusammengesetzt aus mehreren scheinbaren Bodenwellenphasen, die sich entlang der Trennflächen von geschichteten Medium ausbreiten.
- Es konnte keine Korrelation zwischen dem mittleren Bodenfeuchtegehalt und dem Variationskoeffizienten (CV, Verhältnis der Standardabweichung zur mittleren Bodenfeuchte) emittelt werden. Die Anpassung der linearen Regression beider Daten ergab *R-quadrat* $R^2 = 0,306$. Der *F-test* lieferte für $N = 8$ und $k = 2$; $F_{1,6} = 2.64$. Dieser Wert ist geringer als der kritische Wert von 5,99 für 95 % Signifikanz. Die Untersuchung zeigt, dass eine eindeutige Aussage über die Beziehung zwischen dem mittleren Bodenfeuchtegehalt und dem Abweichungskoeffizienten nicht möglich ist. Untersuchungen von anderen Autoren konnten hierzu bislang auch keine eindeutigen Ergebnisse liefern.
- Geostatistische Modellierungen von Bodenfeuchtedaten zeigen sich in der Form der Modelle konsistent. Die Ergebnisse zeigen eine Art Periodizität (hole effect). Diese Periodizität wird höchstwahrscheinlich durch Heterogenitäten im Boden, welche die Entwicklung von präferenziellen Wasserinfiltrationspfaden beeinflussen, hervorgerufen. Hierbei wird ein schwingungsartiges Verhalten über dem Sill erzeugt.
- Messfehler und kleinere Veränderungen der Bodenfeuchteverteilung, die durch den Nugget-Effekt angezeigt werden, weissen eine steigende Tendenz bei größerer Feuchte (R^2= 0,88; $F_{1,6} = 44 > 5,99$ bei 95 % Signifikanz) auf.
- Der mittlere Feuchtegehalt war für die Korrelationslänge (R^2 = 0,07; $F_{1,6} = 0.46 < 5.99$ bei 95 % Signifikanz) nur wenig ausschlaggebend. Diese Eigenschaft wird wahrscheinlich von unterschiedlichen Prozessen kontrolliert. Die Korrelationslängen lagen zwischen 54 m und 102 m. Die Ergebnisse dieser Analyse (für eine Bodenfeuchte im oberflächennahen Bereich für Tiefen bis 0,1 m) zeigten, da die Bodenfeuchtedaten, die durch die Referenzmethoden TDR und SISOMOP im Abstand von 200 m entlang einer 1 km langen Linie gemessen wurden, unkorreliert sind. Die optimalen Positionen für TDR und

SISOMOP Messpunkte wären ungefähr alle 50 m. Dies konnte jedoch erst nach einer Erkundungskampagne mit GPR festgestellt werden.

- Ein Vergleich von GPR-abgeleiteten dielektrischen Koeffizienten mit denen aus TDR und SISOMOP zeigten mittlere Abweichungen von 0,86 bzw. 2,10. Die relativ größ Abweichung zwischen dem GPR und SISOMOP Werten könnte auf die größere Tiefe zurückzuführen sein, bei welcher die letztere Methode die Bodenfeuchteinformation misst. Die Erkundungstiefe bei GPR und TDR war ~10 cm im Vergleich zu ~20 cm bei SISOMOP. Schwankungen bei beregnungs- und verdampfungskontrollierten Bodenfeuchten waren also am stärksten in der oberen Schicht (~ 0,1 m) des Bodens gegenüber den tieferen Schichten. Es sollte auch erwähnt werden, dass der Unterschied im dem Bodenfeuchtegehalt zum einen bestimmt durch GPR und TDR, und zum anderen bestimmt durch GPR und SISOMOP teilweise von den verschiedenen Frequenzbereichen dieser Ausrüstungen abhängt. Der Dielektrizitätskoeffizient des Bodens ist frequenzabhängig, also registrieren die Instrumente verschiedene Dielektrizitätskoeffizienten. Aus diesem Grund sind die verschiedenen Methoden nur bedingt vergleichbar. Die mit GPR bestimmten Bodenfeuchtegehalte zeigen eine starke räumliche Variabilität in Dano. Die Datenmenge betrug mehr als 9000 pro Profil. Im Gegensatz dazu können die Punktmessungen (Anzahl = 6) von TDR und frequency domain reflectometry (FDR) diese räumliche Variabilität nicht erfassen, so dass ein Alias Effekt entstehen kann. Der invasive Charakter von TDR und SISOMOP und die relative kleine erhaltene Datenmenge (im Vergleich zu GPR) könnte eine zusätzliche Fehlerquelle darstellen. So bleibt abschliessend festzustellen, dass die Bestimmung der Bodenfeuchte mit GPR sinnvolle Eingangsdaten für die groß räumige satellitengestützte Bodenfeuchtebestimmung von Dano liefern kann.

Schwierigkeiten und offene Fragen

Die GPR Technik basiert auf Messungen des Dielektrizitätskoeffizienten. Das Problem bei Bodenfeuchtenbestimmungen, die auf dielektrische Messungen basieren, ist, dass das Verhältnis der Bodenfeuchte zur Bodenbeschaffenheit und Struktur sehr komplex und noch nicht komplett verstanden ist. Es wurden über die Zeit bereits mehrere Mischungsmodelle vorgeschlagen, die das dielektrische Verhalten des Bodens und dessen Interaktion mit Wasser beschreiben, aber bisher konnte das komplexe Bodenwassersystem nicht vollständig befriedigend dargestellt werden.

Die Kalibration ist ein weiteres Problem bei dielektrischen Messmethoden. Der ideale volumetrische Wassergehalt sollte besonders von der untersuchten Bodenart abhängen. Als einzige universelle Kalibrationsgleichung wird i.a. die nach Topp et al. (1980) (die unabhängig von der Bodenbeschaffenheit, der Bodenstruktur, Salinität und Temperatur ist) bei wissenschaftlichen Bodenuntersuchungen akzeptiert. Jedoch zeigen sich Abweichungen von dieser Kalibrationsgleichung , z.B. bei organischen Böden (z.B. Roth et al, 1992) und vulkanischen und mineralischen Böden mit niedriger Dichte (z.B. Miyamoto et al. 2001, Regalado et al., 2003). Die Frage ist, ob es eine in-situ GPR Methode gibt, durch welche Informationen über den Bodenfeuchtegehalt nur durch eine einzige Messung erhalten werden kann. Und ergeben sich durch eine solche Methode zusätzliche Informationen über die Bodenleitfähigkeit, Porosität, Salinität und Struktur?.

Bislang gibt es keine allgemeine akzeptierte Formel, die eine exakte Berechnung der Untersuchungstiefe beim GWS Verfahren liefert. Die Berechnung von Sperl (1999) aus Modellversuchen, die in dieser Arbeit angewandt wurde, gibt nur einen Näherungswert für diese Tiefe. Abschätzungen zur Eindringtiefe elektromagnetischer Wellen werden üblicherweise in Relation zur Wellenlänge der abgestrahlten Welle gebracht. Die Bestimmung der Eindringtiefe hängt allerdings vom Bodenfeuchtegehalt ab. So nimmt mit ansteigendem Bodenfeuchtegehalt die Eindringtiefe elektromagnetischer Wellen ab. Es bleibt allerdings ungeklärt, inwieweit zusätzliche Faktoren wie Oberflächenrauhigkeiten, die Vegetationsdecke oder die Polarisierung von Wellen die Bestimmung der Eindringtiefe beeinflussen. Möglicherweise könnten numerische Modellierungen Antworten auf diese Fragen liefern.

Ein Vergleich des mittleren Bodenfeuchtegehalts und des Variationskoeffizienten (CV) zeigte, dass mit dem Bodenfeuchtegehalt (R^2=0,306; $F_{1,6} = 2,64 < 5,99$ bei 95 % Signifikanz) auch die Variation anstieg. In der Fachliteratur gibt es verschiedene Erkenntnisse. Während Autoren wie Hubbard et al. (2002) einen Anstieg der Variation bei hoher Bodenfeuchte berichten, erwähnen Miyamoto et al (2003) aber eine Verringerung der Variation mit der Bodenfeuchte. Dagegen berichten andere Autoren wie Western et al. (2004) sowohl über einen Anstieg als auch über eine Verringerung der Variation bei ansteigender Bodenfeuchte. Es bleibt daher offen, welche Faktoren die Variation des Bodenfeuchtegehalts kontrollieren.

Chapter 1

Introduction

1.1 Project Objectives

The main objective of this research is to estimate soil water content in the vadose zone with the GPR technique under controlled and field conditions. The research is, however, conducted with the following additional objectives in mind:

- To validate the GPR technique as efficient and appropriate for soil water content estimation by comparison with co-located measurements from available conventional tools like time domain reflectometry with intelligible micro-elements (TRIME-TDR), the time domain reflectometry (TDR), gravimetric soil sample method and the simple soil water probe (SISOMOP).
- To investigate the spatial variability of soil water content with the help of geostatistical modelling.
- To study through infiltration experiments on dike models the feasibility of the GPR technique in detecting leakages in levee structures.
- To study the influence of soil water content on cloud formation.
- To upgrade the theoretical knowledge of GPR as a vital tool for soil water content estimation.

1.2 Thesis Layout

Chapter 1 introduces the reader to a short history of the GPR technique to give him an insight of its origin. This is followed by a literature review on the research topic. *Chapter 2* discusses various techniques used in assessing soil water content information. This discussion comes under two main groups: techniques based on dielectric permittivity measurements (e.g. ground penetrating radar, time domain reflectometry, frequency domain reflectometry) and techniques which are based on a different property (e.g. gravimetric soil sampling method, electrical resistivity method, neutron moderation method, neutron magnetic resonance method). The advantages and limitations of the methods are discussed. Precautional measures to be taken for field work with GPR, radiation characteristics of the antennas and their resolution as well as survey methods and procedures (such as the common offset (CO), common midpoint (CMP) and wide angle reflection and refraction (WARR) methods) commonly used in GPR and which were applied in this work are highlighted in *Chapter 3*. Fundamental equations which describe the theoretical background of GPR and properties controlling the propagation of electromagnetic wave propagation in the soil are discussed next in *Chapter 4*. *Chapter 5* treats the dielectric properties of the soil. Two to four-component dielectric mixing models of the soil, the frequency dependence of the dielectric coefficient and dielectric polarization of material are discussed. *Chapter 6* discusses the GPR ground wave and the influence of the frequency on the apparent ground wave velocity through modelling. The application of the guided wave sounding method in investigating water infiltration in flood controlled dike models is discussed in *Chapter 7*. Here, infiltration experiments on two dike models are performed under controlled flooding and precipitation conditions. Discussion includes reference and co-located measurements with the time domain reflectometry with intelligible microelements (TRIME-TDR). *Chapter 8* discusses the spatial and temporal variation of soil water content with the ground wave method on a field scale in a semi-arid region of Burkina Faso, West Africa. Soil water content distribution is analysed using classical statistics and geostatistics. Spatial soil water data acquired by GPR along a 1 km long transect are compared with reference measurements from conventional time domain reflectometry (TDR) and frequency domain reflectometry (FDR). The ground measurements with GPR, TDR and FDR, which were to measure the spatial soil water variability, served as reference for a remote sensing satellite system, Advanced Microwave Scanning Radiometer-Earth Observing System (AMSR-E), with a horizontal spatial resolution of 25 km. The final chapter, *Chapter 9*, gives a summary of the work. *Appendix 1* describes results of GWS and TRIME-TDR experiments on dike model A with the 900 MHz antenna. *Appendix 2* discusses the modal analysis of guided wave propagation along a metal conductor in the soil. *Appendix 3* highlights remaining plots of the comparison between GPR and point measurements in Dano, the frequency distribution of soil water content and geostatistical modelling of soil water distribution. The general description of the Subsurface Interface Radar (SIR©) System-3 equipment used, and an overview of the dike models on which my controlled experiments were performed are given in *Appendix 4*.

1.3 Previous Work with Ground Penetrating Radar

This section focuses on previous work with GPR in the area of soil water content estimation. However, as prefatory to this I introduce the reader to a short history of the GPR technique.

1.3.1 GPR History and Trends

Ra-d-a-r is an acronym which means Radio Detection and Ranging. Radar is a technique based on electromagnetic theory (fathered by Heinrich Hertz in 1864) and Maxwell's equations which were formulated by James Clerk Maxwell in 1886. The very first application of electromagnetic waves in locating remote metallic objects is attributed to a german physicist Hülsmeyer, who developed the Telemobiloskop, a prototype of the modern radar equipment in 1904. Six years later the exact description of this technique for locating buried metallic objects was given by Leimbach and Löwy (Löwy and Leimbach, 1910). Löwy developed this technique further in 1911 and could indicate the depth of buried interfaces by studying the interference between the reflected wave from the subsurface and the ground wave. Edward Victor Appleton continued the history by applying the basic principles of electromagnetic wave reflection to estimate the height of the ionosphere above the ground surface in 1924. Hülsmeyer (1904) succeeded in determining the structure of subsurface features using pulsed techniques from the knowledge that dielectric contrasts in subsurface materials produced reflection of waves propagating through them. However, the first application of the GPR is accredited the german geophysicist W. Stern who first sounded the depth of glacier correctly in 1929 in Austria (Robin (1930)). The radar technique became apparently dormant until about 1950 when research interests in the technique was reawaken by the discovery that snow and ice were transparent to high frequency radio signals. Radar altimeters on board aeroplanes read the distance above the ice surface wrongly resulting in numerous accidents of aeroplanes crashing into the Greenland ice (e.g. Evans (1963); Thompson et al. (1979), Clarke (1987)). Research interests in radar glaciology grew after this and subsequent researches were geared towards this area. Endangered soviet pilots recognised the importance of radar altimetry and soviet physicists including Bogorodsky and Rudakov, developed the theory of electromagnetic wave propagation through glaciers in 1955 (Bogorodsky et al. (1985)). The ability to detect subsurface tunnels and buried objects was of major concern during the world war II and short range radar technique gradually gained much attention for this purpose. Researchers like Lerner, Enticknap, Guillette, Nackoney and Chick continued this investigation after the war at the Lincoln laboratories (Lerner et al. (1967)).

In 1957, Armory Waite, a US army signals researcher, successfully employed seismic techniques and satellite radar interferometry to obtain data on ice depth in the course of expeditions made in the Artic and Antarctic (e.g. Waite and Schmidt (1962); Waite (1966);Rinker et al. (1966)). In 1960, John C. Cook first proposed the use of airborne VHF radar for the detection of subsurface reflections for ice and snow measurements (Cook (1960)) and supported by others he successfully used the application to detect reflections from buried objects (Moffatt and Puskar, 1976). Robin and Evans came out with the first VHF radar-echo sounding system in 1963 (Evans (1963); Bailey et al. (1964)). This whipped up the interest of other researchers to develop time domain short pulse radar systems which were used to map thick sheets of ice and glaciers in the in the Artic and Antarctica at operational frequencies ranging from 30 - 600 MHz (e.g. Evans (1963); Bryan (1974); Behrendt et al. (1979); Walford (1985), Evans et al. (1988); Gogineni et al. (1998)). During the Apollo 17 Lunar Sounder Experiment (ALSE), in 1970, an orbital imaging radar system operating at 3 radar wavelengths of 60 m, 20 m, and 2 m (5, 15, and 150 MHz) was used to detect and locate subsurface geologic structures and to generate a continuous lunar profile and surface images of the moon (e.g. Brown Jr (1972); Simmons et al. (1972); Leonard et al. (1974)). By the mid 1970s the pulse type GPR had found diverse applications for various non-invasive research interests. For example, the technique was employed in subsurface measurements of the water table (Caldecott et al. (1972); Morey (1974)), field scale mapping of potential pipeline routes in the Canadian Arctic in 1975 (Hagrey and Müller (2002)), for permafrost measurements (Annan and Davis (1976)) and for the location of salt deposits (e.g.Thierbach (1974); Unterberger (1978)).

The first digital GPR system was introduced by Sensors and Software of Mississauga, Ontario in the mid 1980s and this enhanced the use of the technique which had been restricted by logistic problems of the earlier commercial analogues. By the beginning of 1990 GPR had become one of the standard tools for environmental, engineering, archaeological, geological, geotechnical, meteorological and many other practical investigations into the subsurface.

1.3.2 Literature Review of GPR Soil Water Investigations

The GPR technique measures the volumetric water content of the soil from its apparent dielectric permittivity measurements through the use of calibration equations that relate the soil water content to the dielectric permittivity. Topp et al. (1980) carried out petrophysical experiments at frequencies between 1 MHz and 1 GHz on a wide range of soil specimens placed in a coaxial transmission line in the laboratory and out of this estimated the volumetric water content θ_v using empirical relations derived from measurement of the relative dielectric permittivity ε_r. Their corresponding calibration equation (see section 5.18, p. 52) which is a third order polynomial in ε_r is widely used by many authors to estimate the volumetric water content from the direct measurement of the relative dielectric permittivity. It is also used in this work to estimate θ_v from ε_r.

GPR has been non-invasively applied by many investigators to explore soil water. The speed with which GPR data can be acquired, the sampling depths and data resolution depend on the mode of operation, the type of medium and operational frequency. Over the past two decades reflection (common or multi-offset methods), apparent ground wave, air-launched surface reflection coefficient, amplitude spectra as well as structure transillumination methods of the GPR have been employed by different authors to investigate soil water content.

Reflection methods are of two kinds−the single or common offset reflection method where the antennas are maintained at a constant separation and moved as a unit along the survey line and the multi-offset reflection methods e.g. common-midpoint (CMP) and wide angle reflection and refraction (WARR) methods, where the antenna separation is stepwisely varied. These methods involve the use of the two-way travel times of the reflected GPR signal to deduce the radar wave propagating velocities as well as the electrical properties of the soil and with these calibrate the soil water content. The use of the reflection data permits not only the determination of soil water content estimates at comparable horizontal resolution with other methods discussed shortly, but also enables greater investigation depths to be reached.

Ulriksen, 1982 investigated the common offset GPR reflection time data and estimated volumetric water content (VWC) at various shallow depths under controlled conditions making use of artificial reflectors at known depths. Shih et al. (1986) and Asmussen et al. (1986) were able to identify the water table in a coarse textured soils with the help of the single offset reflection data. They observed that the difference between the water table depths from observation wells and radar profile was within 10 cm. Under the assumption of a homogeneous soil water content distribution Vellidis et al. (1990) determined the wetting front movement in the vadose zone of sandy soils by studying GPR reflection data from a buried metallic pipe. Fischer et al. (1992) showed using common offset GPR method with 100 MHz antennas in both fluvial and non-fluvial environments that a focused image can be produced by reverse time migration or through the use of any of the migration algorithms previously developed for seismic data. Reflections from buried metal reflectors were used by Grote et al. (2002) to determine the average VWC with a precision of ±0.01 m^3m^{-3} as compared to co-located gravimetric-derived water content estimates. Stoffregen et al. (2002) used the reflection travel-time of a 1000 MHz GPR antenna from the bottom of a lysimeter to estimate the VWC to a standard deviation of 0.01 m^3m^{-3}. Gish et al. (2002) used the reflected signal from metal plates buried laterally in trench side walls of varying depths between 0.5 m and 1.5 m to identify subsurface convergent flow paths resulting from funnel flow which are critical for determining field-scale water and chemical fluxes. Clement and Ward (2003) monitored the effectiveness of surface barriers by measuring the water content in the barrier using GPR ground wave reflection data. Grote et al. (2004) injected water into layered pavements over a period of several months and studied the vertical and horizontal variation of the layer water content with time using reflection data from ground coupled GPR common offset travel time data to quantitatively estimate the sub-asphalt water content under engineered conditions. GPR-derived water content estimates showed a difference of ±0.02 cm^3cm^{-3} as compared with estimates from gravimetric techniques. Lunt et al. (2005) have successfully investigated GPR reflections associated with a low permittivity clay layer located $0.8 - 1.3$ m below the ground surface in a winery and estimated the soil water content (above the reflector) with the aid of 100 MHz antennas. The clay layer which was identified with field infiltration tests and neutron log probes was coincident with the GPR-derived VWC values. The GPR incident wave is not totally reflected at an interface but part is refracted and scattered and the intensity of the reflected wave depends on the boundary reflectivity and the type of material traversed. With this information Parsiani et al. (2004) observed that reflected wave is attenuated, convolved, and compressed differently, as it travels through distinct materials and by defining and calculating a material characteristic in Fourier domain (MCFD) at every reflection, he determined the characteristics of the media by distinguishing between the wavelet properties of the electromagnetic signal before and after reflection from the media.

Besides the often used single offset reflection method of acquiring subsurface hydrological information the GPR has also been operated in a in invasive mode similar to the operation of the time domain reflectometry (TDR) to successfully assess soil water content variability to about 1 m depth on dike models. The guided wave sounding (GWS) method, discussed in chapter 7, makes use of the two way guided wave reflection time data from the lower end of a metallic rod lowered by constant increments through an access tube into the soil to determine its water content (e.g.

Igel et al. (2001); Schmalholz et al. (2004) Preko and Wilhelm (2006); Preko and Rings (2007)).

A number of investigators have also used the multi-offset GPR reflection data to measure soil water content variability. For example, Fisher et al. (1992) recorded a 40 channel wide aperture GPR data set using a multi-channel format akin to that of seismic surveys. Results showed a marked improvement over single-channel recordings in noise reduction and depth penetration, spatial positioning and reduction of diffraction artefacts. Tillard and Dubois (1994) used the CMP ground wave reflection data to measure soil water content and to detect millimetre-wide discontinuities such as fissures in the subsurface geological formations. Greaves et al. (1996) as well as van Overmeeren et al. (1997) investigated soil water content variation from multi-offset reflection data. The latter correlated water content estimates with the physical properties taken by soil cores and piezometry of the water table surface over a period of 13 months. Soil water content so determined was comparable to that taken with the capacitance probe measurements. Weiler et al. (1998) investigated the possibility of using the GPR as an in situ soil water detector. They made use of multiple reflection data from variably located reflectors to estimate water content under natural conditions and found this comparable with independent water measurements from both augur holes and the conventional TDR. Al Hagrey and Müller, 2000 studied reflections from 3 buried sand bodies saturated with water to various salinities to estimate the pore water content and salinity of sand. They observed that the reflection coefficient increased with the salinity of the soil water. Their results provide auxiliary assistance to addressing environmental issues especially in the areas of monitoring contamination and aquifer salinity. By operating the GPR at a central frequency of 100 MHz in the normal move-out and common midpoint survey modes, Nakashima et al. (2001) analysed data from multiple reflectors placed at discrete levels to successfully locate the water table at a depth of ~ 8 m. This was accomplished through the use of filtering and stacking techniques which suppressed noise and enhanced the signal-to-noise ratio of the radar image.

Generally, the CMP survey is laborious and requires relatively more time investment and hence, it is not very suitable for investigating large areas. Tillard and Dubois (1994); Greaves et al. (1996) observed an error in the order of 10 % with CMP velocity determinations.

The apparent ground wave (see section 6.4) which propagates in the air side of the air-soil boundary between the transmitter and receiver has also been greatly used to acquire soil water content information in the upper ~ 50 cm. In this case the GPR is often first operated in the WARR mode to define an optimal transmitter-receiver separation followed by the CO method which utilises the predefined antenna separation. Du and Rummel (1996) used the common and variable offset modes to identify the apparent ground wave and air wave. They observed that the CO showed lower water content values in the coarse-grained soils than in the clayey. Du (1996) and Sperl (1999) suggested formulae for defining the depth of influence of the apparent ground wave. The former suggested that this depth was linearly dependent on the wavelength λ of the propagating GPR wave and put it approximately in the range $0.5\lambda - \lambda$. The latter also observed that the depth is a function of wavelength but after observing ground wave velocities from a series of modelling exercises concluded that the depth of influence was not linearly dependent on wavelength as previously suggested by Du,1996 but was about $0.145\sqrt{\lambda}$. Boll et al. (1996) used GPR-derived soil water content estimates as a tool for detecting layers in the soil. They established several transects on a fine loamy soil throughout the growing season and the subsequent fall period to find the best time to reveal layer structures. This was made possible by actual measurements with soil samples and by the spatially varying apparent ground wave velocity from the CMP survey method. Lesmes et al. (1999) used 100 MHz antennas in the variable and CO modes to estimate small scale soil water content in a 17 m^2 study site using the apparent ground wave data. Soil water content values showed similar trends but their absolute values were less than those independently determined from conventional methods. This difference they assumed was likely due to a deeper zone of influence which was associated with the relatively lower frequencies used by the GPR method. Huisman et al. (2001) studied 24 variable offset ground wave data with antenna frequencies of 225 MHz and 450 MHz at various study plots of size 5 m × 2 m. The apparent ground wave-derived VWC estimates had an accuracy of 0.024 m^3m^{-3} and agreed well with both TDR and gravimetric VWC estimates. Grote *et al*, 2003 investigated the ground wave at GPR operational frequencies of 900 MHz and 450 MHz. They studied the ground wave travel times and their amplitudes to enable estimations of the VWC in the uppermost ∼ 15 cm of a vineyard. Their results from 29 multi-offset GPR-derived VWC estimates compared well with independent determinations from gravimetric and TDR techniques. Galagedara et al. (2005b) estimated the temporal soil water variability under uniform irrigation and drainage conditions with 200 MHz central frequency antenna in the CO mode. By comparing GPR-derived VWC estimates with conventional estimates from vertically and horizontally installed TDR probes at varying depths, they assessed the apparent ground wave sampling depth. Their results showed that GPR apparent ground wave sampling depth during drainage varied from ∼ 20 cm at high water content to ∼ 50 cm at the lowest water content.

Other researchers like Mayer et al. (1998); Seher (1998) and Mayer (2005) have through extensive modelling exercises explained the propagation and nature of the apparent ground wave. They observed that it rapidly decays and highly attenuates sharply both vertically and horizontally with a propagation velocity which equals that of the ground wave which generates it. Antennas must hence be well coupled to the ground in order to effectively record it.

Small scale variability in soil water content in the order of a few dm^3 based on the apparent ground wave have also been investigated by researchers such as Igel et al. (2006) using a 700 MHz central frequency antenna over an $2\,m \times 1\,m$ study area. They observed that heterogeneities in the VWC in the decimetre scale were caused partly by variations in the vegetative rooting intensities and the possible build up of hydrophobic and hydrophilic structures in the subsurface.

Since the last decade more researches are being focused in the use of other GPR-derived properties which are reliable and fast such as the signal amplitude or the amplitude spectra in the frequency domain and surface reflection coefficient to determine the VWC. Unlike the methods described so far which involve ground coupled antennas, a few papers have also discussed air-launched surface reflection methods in which the antennas are raised above the ground. This method which is quick and more suitable for field-scale application is based on the principle that the amplitude of the reflected wave depends on the amount of energy reflected. Thus, a high amplitude would correspond to a large dielectric contrast between two soil layers. Chanzy et al. (1996) employed the off-ground GPR technique. They used 200 MHz dipole GPR antennas elevated $5-15$ m above the soil surface to measure soil water content in the uppermost $10-20$ cm of the soil. They observed that the accuracy of the measurements was affected by other reflections from the antennas support structure due to the cylindrical radiation pattern of the dipole antennas used. Charlton 2000, discussed spatially distributed water content. The paper analysed the maximum amplitude and full profile amplitude spectra of the ground wave from GPR operated at frequencies 450 and 900 MHz and estimated the water content for a variety of earth materials and solutions in a series of laboratory controlled experiments. Serbin and Or (2003) deployed a suspended 1-GHz horn antenna over bare and vegetated soil surfaces and using surface reflection magnitudes and propagation times determined the bulk dielectric permittivity and water content of the soil. In a later discussion Serbin and Or (2004) used information from a suspended horn antenna to obtain continual observations of near-surface soil water content dynamics within a well-defined footprint. Water contents inferred from radar surface reflectivity (SR) measurements fitted gravimetric data for the top 1 cm soil layer. This observation was confirmed by comparison of SR data with deeper measurements (1−5 cm) obtained from the time-domain reflectometry method. Bano, 2006 modelled reflections from buried pipes on two simulated water tables at depths of 72 cm and 48 cm in a sand box by profiling with 1200 MHz antenna above sand box. He observed that the strength of GPR reflections, the modulus of the reflection coefficient and the thickness of the transition zone between the water tables decreased with increasing frequency. Ghose and Slob (2006), related seismic and GPR reflection coefficients to porosity and water saturation. The paper observes that this approach leads to a unique and more stable estimates of porosity and water saturation at a sublayer boundary than using either seismic and GPR data alone.

Structure Transillumination is a reflection based GPR survey method in which the transmitted signal is picked by a receiver placed on the opposite sides of the structure to be studied. In borehole transillumination surveys, for example, the signal may either be transmitted from the surface to a borehole or from one borehole to another. There are two methods of data acquisition here − the zero offset method where the midpoints of the antennas are placed at the same depths and the multi-offset methods where the depths to the antenna midpoints are variant (e.g. Gilson et al. (1996); Binley et al. (2001, 2002); Galagedara et al. (2003); Rucker and Ferré (2005)). Cross borehole radar tomography makes use of the radar wave travel time between boreholes. By studying anomalies associated with variations in the travel times, the amplitude or period of the transmitted wave through the structure, the soil water content variability as well as high resolution lithological information between the boreholes can be determined (e.g. Hubbard et al. (1997), Eppstein and Dougherty (1998); Parkin et al. (2000); Binley et al. (2001); Peterson (2001); Binley et al. (2002); Alumbaugh et al. (2002)).

Pettinelli et al. (2005) discuss a method which directly relates GPR to the conventional TDR and gravimetric measurements. Here, the amplitudes of instantaneous GPR signal envelope of the first 6 ns are compared with electrical properties (e.g. dielectric coefficient and dc conductivity) extracted from TDR measurements and also soil water content measured using conventional gravimetric technique. The results showed a good fit between the spatially varying GPR and TDR properties.

The GPR technique has a brilliant future in soil water research. It is fast, cost effective, portable and produces higher data resolution than the other known techniques. However, the technique is still young and the methodology and instrumentation are still in the development phase (Davis and Annan (2002)).

Chapter 2

Soil Water Content and Methods of its Determination

2.1 Definition of Soil Water

Liquid water (H_2O) is often thought of as a transparent, odourless, tasteless substance, which is ubiquitous in nature. The human being (composed of about 66 % water) cannot do without water, which plays a key role in a wide range of disciplines and industries and has a remarkable influence on climate, plant growth and our lives. Interestingly, droughts result in famines whereas floods cause disease and death. These characteristics make water perhaps the most studied material on our planet.

Soil water is hydrologically defined as that component of water in the soil, that may be evaporated from the soil by heating between 100 °C or 110 °C but usually 105 °C until there is no further weight loss (e.g. Gardner et al. (2001)). In the vadose zone soil water occurs under two classifications: Bound and free water. Bound water refers to water molecules which are found in the first few molecular layers surrounding the soil particles. They are tightly held to the surface of the soil particles due to the influence of matric and osmotic forces (Baver et al. (1997)). This water clings to the surface of the soil mineral grains so strongly that it does not flow under the influence of gravity and cannot be removed without destroying its structure. It is also not available to plants. This category of water comprises of capillary and adsorption water. Soil water occupies about 0.005 % of water on the earth's surface (Schlesinger (1997)). Matric and osmotic forces acting on the water molecules decrease with distance. Hence, water molecules located several molecular layers away are relatively free to move within the soil medium and are thus referred to as free water. Free water is held solely by gravity. It is available to plants and main source of groundwater. This division of water into bound and free fractions, however, describes only approximately the actual distribution of water molecules within the soil medium and is based on somewhat arbitrary criterion for the transition point between bound and free water layers (Hallikainen (1984)).

Soil water content which is the amount of water a porous medium contains is defined in most cases as the mass water content θ_m or the volumetric water content θ_v . These are defined by

$$\theta_m = \frac{M_w}{M_s} \tag{2.1}$$

$$\theta_v = \frac{V_w}{V_b} \tag{2.2}$$

where

M_w = mass of water evaporated for a minimum of 24 hours at 105°C
M_s = mass of dry soil
V_w = volume of water.
V_b = bulk volume of soil sample

Soil water content determinations by soil dielectric methods e.g. GPR and TDR are usually expressed in this form either in units [$\mathrm{cm^3cm^{-3}}$] or [$\mathrm{m^3m^{-3}}$]. At saturation, $\theta_v = \Phi$, where Φ is the soil porosity given by

$$\Phi = \frac{\text{volume of pores}}{\text{volume of soil}} = \frac{V_a + V_L}{V_s + V_a + V_L} = 1 - \frac{V_s}{V_b} \tag{2.3}$$

$$= 1 - \frac{\rho_b}{\rho_s} \tag{2.4}$$

where

V_L = volume of water + volume of non-aqueous liquid components e.g. oil, in sample
V_a = volume of air in sample
$V_b = V_a + V_s + V_L$
V_s = volume of matrix
ρ_s = density of dry sample
ρ_b = bulk density of soil sample

2.2 Methods of Soil Water Determination

There is a large number of methods available for assessing soil water content. The selection of a technique depends on weighing its advantages over disadvantages and the goal of the project. Cape (1997) and Charlesworth (2005) discuss various vital points to consider before selecting a particular technique. Direct methods e.g. gravimetric methods, involve the removal of soil water either through a physical or chemical process and subsequently determining the amount of water removed. Indirect methods, e.g. GPR, TDR, the nuclear magnetic resonance (NMR) and electrical resistance method (ERM) involve the monitoring of a soil property (e.g. relative dielectric coefficient, electromagnetic reflectivity, hydrogen nuclei content or electrical resistivity) as a function of the soil water content. Data may be acquired by placing the equipment in contact with the soil or remotely in which case the sensors are mounted on satellites or aeroplanes or on structures above the soil surface.

In this section I discuss methods of determining the soil water content in two basic categories-methods which depend on the relative dielectric coefficient of the soil and methods which are not directly dependent on this. The measurement resolution depends most cases on the soil type (e.g. texture), soil sampling frequency, precipitation and evapo-transpiration but also on the frequency used.

2.2.1 Dielectric Methods

The main quantity that is measured is the relative dielectric coefficient $\varepsilon_r (= \varepsilon/\varepsilon_0)$ of the soil. This is a measure of the polarizability of a medium in the presence of an electric field and its ability to sustain charge separations as stored potential energy. When electromagnetic waves propagate through the soil the electrons within the atoms and molecules of the soil become partially displaced creating a reverse electric field in the direction of propagation. This reduces the strength of the main field. As the relative dielectric coefficient increases the strength of the electromagnetic field as well as the propagating velocity is reduced. Thus, the stronger the dielectric permittivity the slower the electromagnetic wave propagates through the soil. The propagating velocity v can be approximately expressed as $v = c/\sqrt{\varepsilon_r}$ where c = 3.0×10^8 m/s, ε_0 = permittivity of free space.

Wet soil comprises of solid particles, water and air (Hillel (1973)) and the relative dielectric coefficient ε_r is a function of the operational frequency, temperature, porosity, lithology, water content and pore fluid composition. The relative dielectric coefficients of dry sand, air and water lies within the ranges $2-5$, 1 and 80 respectively (e.g. Davis and Annan (1989); Beres and Haeni (1991); Daniels (1996)). See section 5.1.1. The soil's permittivity is thus governed by the presence of water. The dielectric permittivity of a soil sample is hence related to it's water content. One of the most common empirical formulae widely used to determine volumetric water content (VWC or θ_v) [m^3m^{-3}] from measurements based on dielectricity is the formula due to Topp et al. (1980) which is discussed in section 5.1.3. Eq. (5.18) applies to most types of soil irrespective of composition and texture. However, for higher water content values e.g. above 50 %, probable for soils with considerable amount of clay content, other calibrated relationships have to be used as this calibration leads to wrong estimation of soil water content values. Charlesworth (2005) puts the range of validity of θ_v in the calibration equation of Topp et al. (1980) to be about $0.05 - 0.50 m^3m^{-3}$.

2.2.1.1 Time Domain Reflectometry (TDR)

The soil's relative dielectric coefficient ε_r is determined by measuring the two way reflection time t [s] taken by an electromagnetic wave to propagate along a transmission line of length l

[m] placed in the soil. If the electromagnetic energy encounters a discontinuity along its path of travel (e.g. end of line) part of the energy is reflected resulting in energy changes along the transmission line. The time t can be assessed from the run of the voltage curve. If c [m/s] and v [m/s] are the speeds of electromagnetic wave in vacuum and through the soil respectively, then

$$\varepsilon_r = \left(\frac{c}{v}\right)^2 = \left(\frac{ct}{2l}\right)^2 \tag{2.5}$$

A TDR probe usually comprises of two or three parallel metal rods which are inserted into the soil to act as wave guides for the propagating electromagnetic wave. Electrical conductivities values from about 0.8 – 1.0 S/m leads to overestimation of soil water content values (e.g. Dalton (1992); Vanclooster et al. (1993)). An example of time-domain TDR probe is the TRIME (Time reflectometry with intelligible microelements) which is discussed in section 7.2. The advantages of the conventional TDR are:

- They possess slender probes of various configurations for different probe depths with minimal soil disturbance.
- They can provide additional information about the soil conductivity.
- It is not very sensitive to normal saline soils.

The limitations are:

- The soil is disturbed during the installation of a TDR probe.
- It has relatively small sampling volume.
- The accuracy of probe depends on the coupling between it and the soil. Air gaps introduce errors.
- It has limited application in highly conductive clayey soils.
- Soil-specific calibration might in be necessary for soils with high bound water content e.g. volcanic soils.

2.2.1.2 Frequency Domain Reflectometry (FDR)

It operates on the principle that soil water content depends on the electrical capacitance of a capacitor that uses soil as a dielectric medium. The capacitor usually comprises of metal plates or rods which are buried in the soil. By connecting the capacitor as part of an electrical circuit with an oscillator changes in the soil water will reflect on changes in the operating frequency of the circuit. The frequency of the oscillator is adjusted until the resonant frequency is reached when the amplitude becomes highest. This frequency is a measure of the amount of soil water content in the soil. An example of an FDR probe is the simple soil water probe (SISOMOP). The advantages of FDR are:

- It is applicable in high saline soils where TDR normally fails.
- It has a better data resolution than TDR.
- Liquids may be used for its calibration resulting in very good contact between the probe and the soil (Jackson (1990)).

The limitations of FDR are:

- Small volumes of soil water content determined and method is not very suitable for field scale measurements (Dirksen and Dirksen (1999)).
- It needs soil specific calibration.
- It needs careful installation to avoid the occurrence of air gaps between sensor and soil.
- It has small measuring volume of about 10 cm radius.

2.2.1.3 Ground Penetrating Radar (GPR)

GPR measures the time taken by an electromagnetic wave to travel from the transmitting antenna through the subsurface to receiving antenna. The velocity and reflectivity of the electromagnetic wave are characterised by the soil's relative dielectric coefficient ε_r, conductivity σ, angular frequency ω and the relative permeability μ_r (see chapter 4, p. 39 for detail discussion). In a region of very low electrical conductivity and negligibly small change in the soil permeability (μ), the soil's relative dielectric coefficient ε_r is estimated from the electromagnetic wave velocity v and θ_v determined using Topp et al. (1980) calibration equation (section 5.1.3). GPR has among others the following advantages:

- It is a non invasive method and can also be operated remotely without necessarily being coupled to the surface of the soil.
- It has a large support volume for relatively more accurate measurements.
- It offers fast acquisition of data and is hence, appropriate for field scale measurements.
- It is highly sensitive to water. The tool can provide an accurate depth-structure model of the water bottom and sub-bottom sediments.
- Lithologic/facies units with thickness of the order of 0.1 m can be imaged with intermediate-frequency units (200 MHz).
- It detects both metallic and non-metallic objects.
- It has wide application e.g. groundwater research, geo-technical, environmental, archaeological, mine detection.

Its limitations are:

- The penetration depth and ability to resolve objects at depths is highly dependent on the electrical conductivity of the soil. A high conductivity causes great attenuation of the signal resulting in lower penetrating depths.
- The bandwidth of the antenna is broad. This makes it difficult for the technique to resolve two closely spaced targets.
- Data contamination may occur as a result of multiple reflections or spurious echoes (clutter) from buried objects such as boulders and metal scraps.
- The performance depends on the electrical contrast between the target and the surrounding medium. It does not perform very well in rain or soils saturated with water or in highly saline soils.
- It needs specialised user and software to evaluate the data.
- Results are sometimes subjective and the interpretation depends on the experience of the user because not all the techniques are standardised.
- Post-acquisition processing (migration) may be required in areas where significant structural relief is present.

2.2.2 Other Methods

2.2.2.1 Gravimetric Soil Sampling or Thermostat-Weight Technique

This method is very often used to determine the water content of a soil sample. The sample is first oven dried at 105° C for 24 hours. The gravimetric water content θ_m [kg/kg] of the sample is determined (DIN18121 (1988)) from the masses of the wet sample m_{wet} and dry sample m_s as

$$\theta_m = \frac{m_{\text{wet}} - m_s}{m_s} \tag{2.6}$$

The volumetric water content θ_v [m^3/m^3] of a soil sample is defined as the ratio of the volume of water V_w to the bulk volume of sample V_b i.e.

$$\theta_v = \frac{V_w}{V_b} = \frac{m_w}{\rho_w V_b} = \frac{m_{\text{wet}} - m_s}{\rho_w V_b} = \frac{\theta_m m_s}{\rho_w V_b} = \theta_m \frac{\rho_s}{\rho_w} \tag{2.7}$$

where V_b = volume of dry soil (V_s) + volume of air (V_a) + volume of water (V_w); ρ_b is the bulk density of the dry soil and ρ_w = 1000 kg/m^3 is the density of free water. The difference between θ_m and θ_v is that the former expresses a mass to mass ratio kg/kg i.e. kg water per kg dry soil whilst the latter expresses a volume ratio [m^3m^{-3}] i.e. m^3 water per m^3 bulk volume of soil. The bulk density may be determined by coating the soil clod with paraffin and measuring its mass in air and water respectively (Campbell and Henshell (2001)). It has the following advantages:

- The principle is simple and the equipment relatively less costly.
- It leads to high precision measurements of the soil water content and it is hence used as a standard reference against which other techniques are calibrated.

Some disadvantages are:

- The determination of the desired quantity θ_v requires the measurement of the soil bulk density ρ_b.
- The heating might destroy organic components of the soil sample due to oxidation effects leading to error in the mass.
- Repeating measurements in the same area through time may cause undesirable damage to the soil.
- It is labour intensive and procedure becomes more cumbersome if soil content information at great depths is required.
- V_b may change by heating the probe, so that ρ_s changes.

2.2.2.2 Neutron Moderation Measurements (NMM)

Fast moving neutrons emitted from a radioactive decay source $^{2}41\mathrm{Am}/^{9}\mathrm{Be}$ are slowed (thermalised) through elastic collisions with hydrogen particles present in the soil. Hydrogen is every effective in thermalising fast moving neutron by virtue of its high nuclear and scattering cross section (Vanclooster et al. (1952)). Water is the main source of hydrogen (H^+) in the soil. Hence, the change in the number of counts recorded by the NMM reflects the amount of water in the soil. NMM has the following advantages:

- It is not sensitive to soil salinity.
- It is not sensitive to air gaps in access tubes.
- It can measure large volumes of soil water.

The limitations are:

- Readings take a relatively long time.
- A radioactive source is used and this stirs the fear of radiation hazard.
- Readings become more difficult and errors increase as one get very close to the soil surface.
- Soils containing high amounts of organic matter and clay may require extra calibration as these are also good sources of hydrogen.

2.2.2.3 Neutron Magnetic Resonance (NMR)

This technique is based on the principle that nuclear spins undergo precession in a magnetic field at a frequency which is directly proportional to the magnitude of the local field. The technique principally measures the nuclear magnetisation of the spins of hydrogen nucleus (proton). The nuclear spins of the hydrogen nucleus are perturbed out of their equilibrium positions through the application of an external field. The relaxation times accompanying the signal decay as the spins return to their initial equilibrium state are measured. This contains vital information about the amount of soil water, the soil porosity, concentration of paramagnetic ions and the presence of ferromagnetic minerals. NMR has the following advantages:

- The technique is non-invasive.
- It responds only to protons present in water. Thus, no signal is observed if no water is present.
- There is a very good relation between liquid water, pore size and the NMR signal that often requires no or very little calibration.

The limitations are:

- The accuracy of the signal produced by the precessing protons is influenced by the strength of the signal, the ambient electromagnetic noise and the type of software used.
- The signal amplitude is often low (~ 10 nV - 600 nV) as compared to relatively higher ambient noises present. The presence of power lines are a major source of noise. Soundings, generally, need to be at least 1 km from any power line.
- The presence of ferromagnetic substances e.g. magnetite in the soil highly attenuates the NMR signal.

2.3 Conclusion and Outlook

I have discussed different techniques and methods of measuring soil water, their principles, advantages and limitations. There are certainly a large number of other methods e.g. tensiometer field methods (TFM) which measure soil water matric potential, suction measurement systems e.g. tensiometers which measure soil water suction and heat dissipation systems among many others which could not be discussed. The dominant controls surrounding the selection of a particular technique for a field campaign should not simply be the advantages and limitations that technique may have but also other considerations like the user's skill level and expertise required, the type of soil, the exploration depth, accuracy and soil water ranges expected as well as the cost should be looked at.

The gravimetric method is often set as a standard reference against which soil water estimates from the other methods e.g. GPR and TDR are compared. There is often a problem with this comparison. The gravimetric method with its thermal application liberates all the water from the soil sample until it records no change in mass. In effect, the soil water content registered by this method is the sum of both bound and free water whereas the electromagnetic methods measure only the free water component in the soil. Soil estimates from the gravimetric method are hence always expected to be higher than that measured by the other methods.

In many other cases it is usual to compare GPR estimates with the TDR. Here too, there are resulting disparities. TDR-derived VWC estimates are based on point to point observations that are later extrapolated over a whole survey region whereas GPR estimates principally covers a whole areal extent. Soil water content starkly varies spatially (e.g. Igel et al. (2006)) being influenced by the non-uniform vegetative root systems, soil texture, porosity and micro-fractures. In a heterogeneous environment where the VWC is highly variant such extrapolation of a local observation likely introduces large errors and might not at all be representative of the regional soil water trend. Besides, faulty coupling between the sensor and the soil generates an air pocket around the sensor which introduces errors (e.g. Stacheder (1996)). The length of cable may introduce further errors in TDR calibration (e.g. Logsdon (2000)). The TDR measures in the gigahertz region while the GPR measures in the frequency range of about 10 MHz to 1 GHz. Accompanying irregularities in the difference in operating frequencies are discussed further in section 7.8, p. 110.

One problem of comparing GPR derived water content information with other invasive dielectric techniques is the difficulty in setting data acquisition to a common sampling volume, frequency and data resolution. Perhaps the GWS method (discussed in chapter 7) answers part of these problems and may be used as an alternative to TDR in comparing GPR-derived soil water information.

Chapter 3

GPR Data Collection and Survey Design

This chapter discusses the factors that contribute to a successful field campaign and the basic methods used in GPR. A brief discussion is given on dipole antennas and their radiation characteristics.

Before embarking on a practical field campaign with the GPR a prior knowledge of the survey area with respect to the nature of the soil, the type of target to expect, the exploration depth sought after, the type of antennas to use and their resolutions are important elements to the logistics and success of the campaign. These factors are interdependent.

3.1 Factors Affecting the Performance of GPR

3.1.1 Nature of the Soil

The propagation of the signal depends on the nature of the soil and its water content. GPR performs poorly due to attenuation of the signal, especially, in wet soils with good proportions of organic and clay compositions. In soils of this nature it is often difficult for GPR to penetrate deeper than a few metres irrespective of the strength of the antenna. In dry soils, however, it is possible to record penetration depths as high as 100 m. The Topp et al. (1980) calibration equation, which I used to convert the relative dielectric coefficient into soil water content is based on a low loss porous medium whose electrical conductivity is less than 100 mS/m.

3.1.2 Frequency of the Antenna

The use of high frequency antennas results in higher data resolution and discrimination but the GPR signal is in this case highly attenuated. Lower frequencies give higher exploration depths but relatively poorer data resolution and discrimination. Antennas with frequency ranges between 300 MHz and 900 MHz were used in this work. For given survey sites antennas were also selected in such a way that the Nyquist frequency f_N was not exceeded (e.g. Keary and Brooks (1991)). The Nyquist frequency is defined by

$$f_N = \frac{1}{2\Delta t} = 2f_c \tag{3.1}$$

where Δt is the sampling interval and f_c is the central frequency of the antenna.

The Nyquist frequency is the highest frequency at which a signal can be sampled without any unwarranted distortions (*aliases*) in the data. The presence of frequencies higher than f_N on the data causes higher frequency components to be superimposed on the data within the Nyquist interval. For the work on the dike model at the Federal Waterways Research Institute in Karlsruhe (section 7.5) where a maximum depth of 3 m was envisaged, the 500 MHz antenna was employed using a sampling number of 256 samples per trace and a time window of 80 ns. This corresponds to a sampling interval

$$\Delta t = \frac{80}{256} = 0.3125 \text{ ns} \tag{3.2}$$

and from equation (3.1), $f_N = 1.6$ GHz. The choice of the 500 MHz antenna was better than that of the 900 MHz antenna. The latter would have given a frequency (= 2 × 900 MHz) of 1.8 GHz which, being greater than f_N, would have invited spectral aliases into the data.

3.1.3 The Length of the Time Window

The length of the time windows for the field work was always selected to be a little more that the expected target depth. For example with work on a dike model with a depth of 1.4 m using the 500 MHz antenna, a time window of 40 ns was employed based on an assumed average propagation velocity of 0.1 m/ns in the soil. Hagrey and Müller (2002) suggests that the optimal length of the time window should exceed the expected targeted depth by about a third.

3.1.3.1 The Sampling Interval

This refers to the rate at which the GPR signal reaching the receiver is sampled and it depends on the frequency of the transmitter. It is usual to sample with sample intervals of 256, 512 or 1024. As the frequency of the signal is increased the sampling interval should also be correspondingly increased, however, within the Nyquist sampling limit. A sampling interval of 256 was used for all data collections in this work. A way of improving the data quality (e.g. Hagrey and Müller (2002); Lutz et al. (2003)) has been to ensure very good coupling between the antennas and the ground especially for the work in Burkina the direct ground wave was of primary interest and as much as possible maintain a consistent configuration of the antennas throughout a survey.

3.2 Survey Methods

3.2.1 Modes of Measurement

GPR data can be acquired from two basic operational modes, namely, the fixed offset or the Common Offset (CO) and the variable offset modes (e.g. CMP and WARR).

3.2.1.1 Common Offset Mode

Fig. (3.1) shows reflection paths and resulting radargram of an ideal planar reflector for GPR operation in the CO mode.

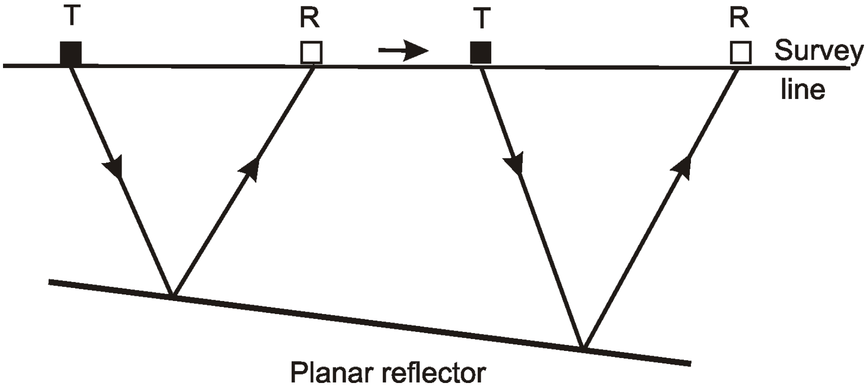

(a) Reflection paths of a planar reflector

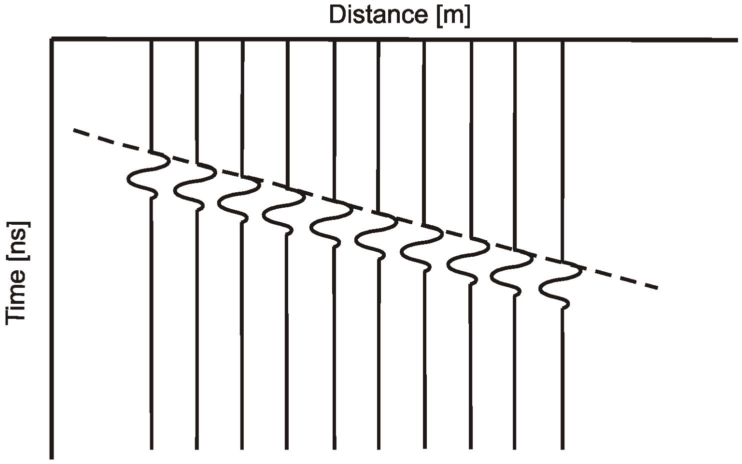

(b) CO radargram of a planar reflector

Figure 3.1: Schematic illustration of the CO field procedure showing reflection paths and corresponding radargram for an ideal planar reflector

In the Common Offset mode the separation between the transmitting and receiving antennas are fixed and both antennas are moved together as a unit either by pulling at constant pace or fixing aboard a vehicle or aeroplane and moved at constant speed. The CO profiling produces an image of subsurface dielectric variations (in the form of reflections) as a function of a two way travel time. The CO measurement mode is easy, fast and highly suited for field scale measurements. Fig. 3.2 shows reflection paths and the corresponding radargram for an isolated point reflector.

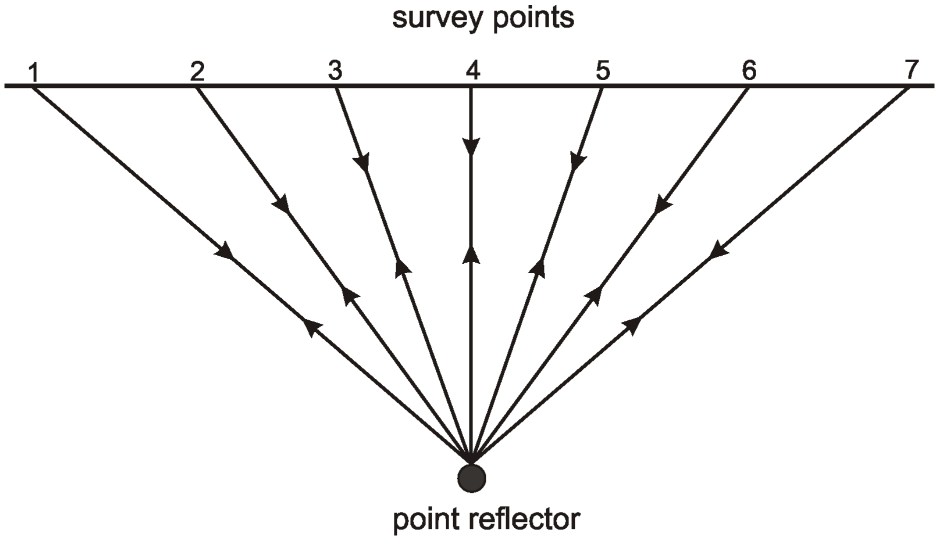

(a) Reflection paths of a point reflector

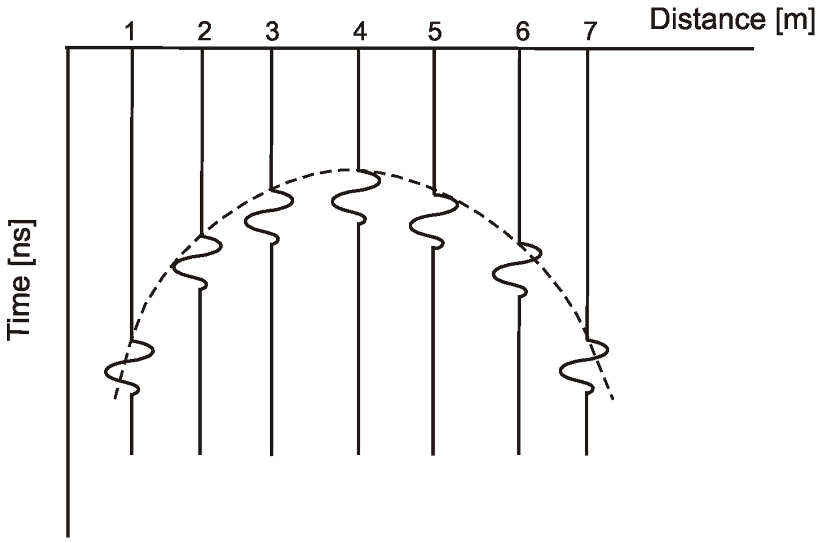

(b) CO radargram of a point reflector

Figure 3.2: Schematic illustration of the CO field procedure showing reflection paths to and from an isolated point reflector and corresponding radargram

3.2.1.2 Variable Offset Mode: CMP, WARR

Usually for sounding purposes, and to obtain a velocity-depth information about objects beneath the surface we operate the GPR in the variable offset mode. One of such modes is the Common Midpoint (CMP). Figs. 3.3 and 3.4 show the CMP procedure and resulting radargram respectively for the case of an ideal planar reflector.

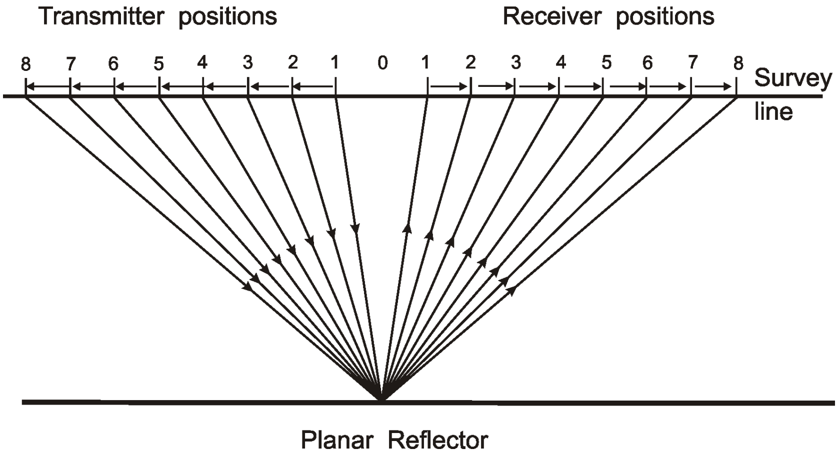

Figure 3.3: Schematic illustration of the Common Midpoint (CMP) field procedure.

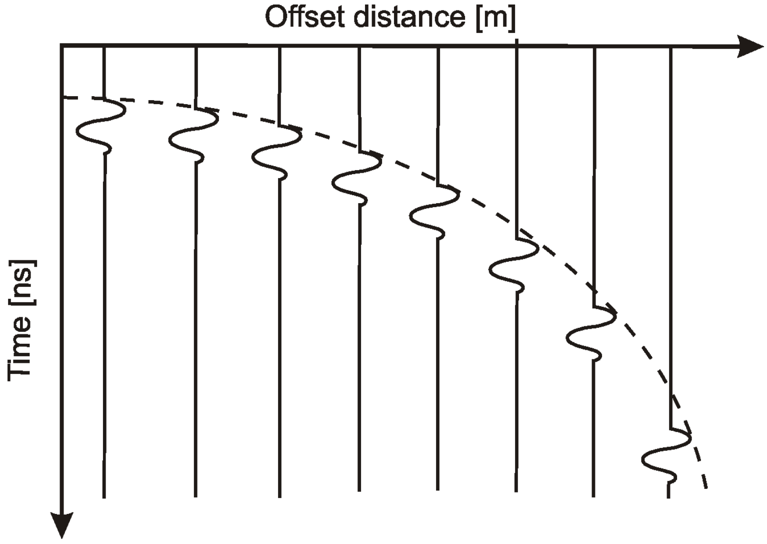

Figure 3.4: Schematic illustration of radargram from a buried planar reflector.

Here the common midpoint of the antennas is fixed at the point of observation and the antennas are moved apart in opposite directions at constant increments along a survey line. In this GPR mode electromagnetic wave reflections from the same reflectors below the surface are recorded by the receiver.

In the schematic radargram shown in Fig. 3.4, reflections below the common midpoint appear in the form of a diffraction hyperbola and from this information about the depth to the reflector and the propagation velocity of the electromagnetic wave can be determined. The CMP survey mode helps to acquire a first hand knowledge about the investigation site and it is reasonable to carry out a CMP prior to the major investigation. CMP was used for reconnaissance survey in Dano, Burkina Faso and was further used to acquire information of the soil water content distribution on a dike model at the University of Karlsruhe. In the Wide Angle Reflection and Refraction (WARR) mode, one of the antennas (in Fig. 3.5, the transmitter) is fixed in one location while the other is moved away at constant pace along the survey line. The WARR mode was used together with the CO mode to acquire data in Burkina Faso (see section 8.2.2, p. 119).

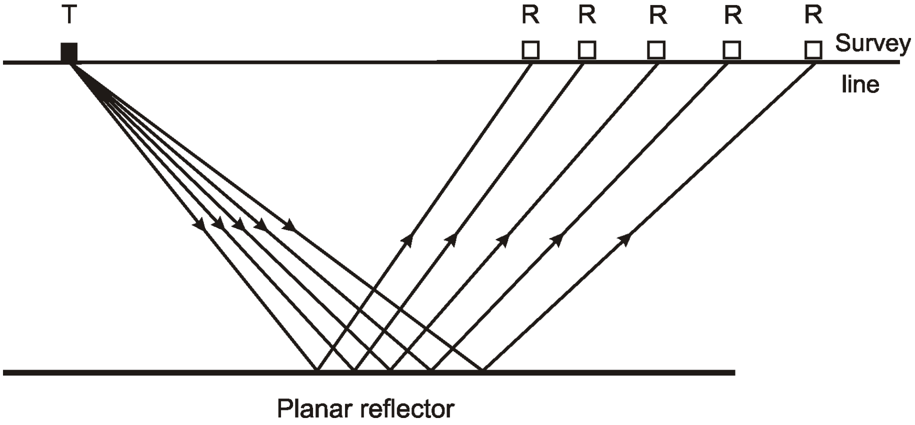

Figure 3.5: Schematic illustration of the field procedure of WARR. T and R are transmitter and receiver positions respectively.

3.3 Radiation Patterns of Antennas

The antennas used in this work are dipole antennas. These radiate and receive polarized electromagnetic wave fields in a complex 3-D elliptic-based cone, Fig. 3.6. Reflections recorded on the radargram may be from objects lying at anywhere along the GPR wavefront and not necessarily directly beneath the transmitter position (e.g. Yilmaz (1987); Keary and Brooks (1991)).

A dipole antenna (Fig. 3.7) comprises of a pair of insulated metal rods of lengths l with a gap between them. Usually the gap is positioned at the central point between the rods such that $2l = \lambda/2$. A high frequency (HF) voltage applied across the gap generates an HF current along the rods which in turn transmits electromagnetic waves into the ground. In the receiving mode electromagnetic waves reaching the rods (e.g. after reflection from the ground) induce a current

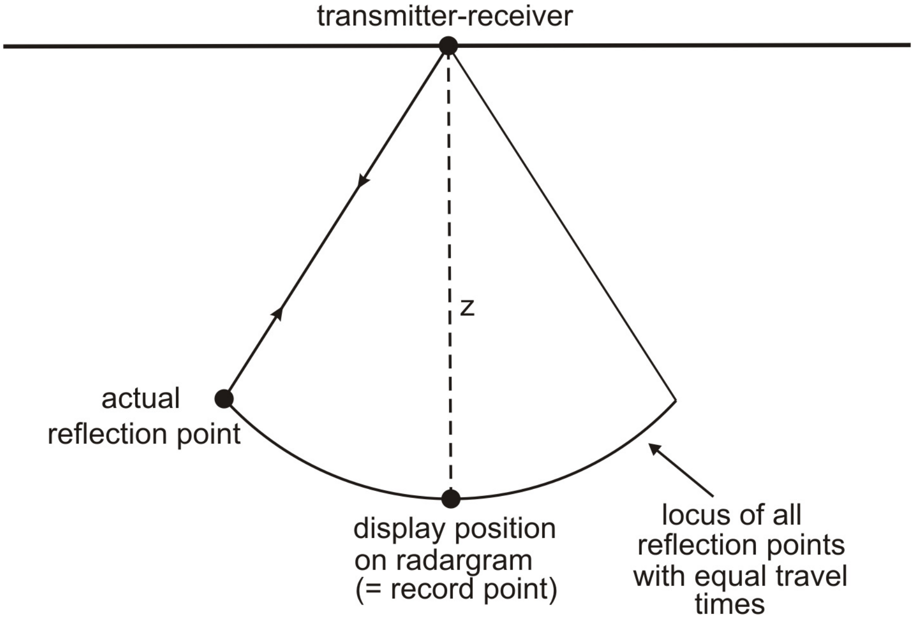

Figure 3.6: Complex 3-D elliptic-based cone radiation of the radar antenna (Modified from Neal, 2004)

and a corresponding voltage across them. The transmitted GPR signal often induces a slow-decaying wow which interferes with the waves reaching the receiver depending on the depth of the reflector, the electrical properties of soil and the proximity of the transmitting and receiving antennas. The wow should first be corrected for before processing the data further. This was done help of the Reflexw software tool *dewow*, Sandmeier (2007). The electrical waves produced on the rods have fixed wavelength. Periodic reflected waves incident on the antenna are the prime cause of antenna resonances.

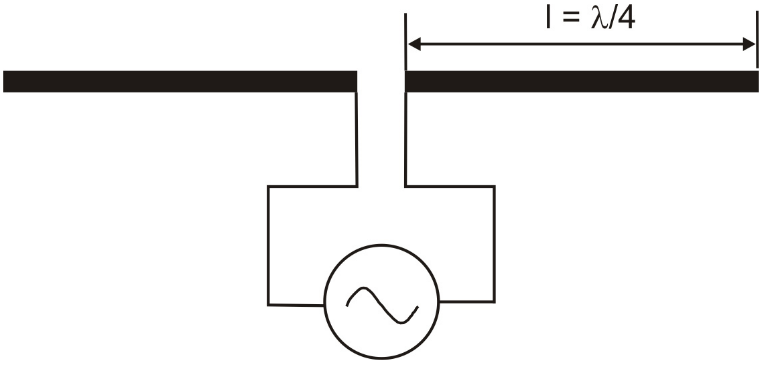

Figure 3.7: Schematic illustration of a dipole antenna.

The radiation pattern of the antenna depends on the distance from the dipole. There are three major regions (Fig. 3.8):

- The **reactive near field** is the region closest to the antenna where the reactive field predominates. For most antennas this region is defined by
  $$r_i < \frac{\lambda}{2\pi} \tag{3.3}$$
  where r_i is the distance from the source and λ is the wavelength. The wave fields predominantly decay by a factor of $1/{r_i}^3$.
- The **radiating near field** (Fresnel Zone). This region is defined by
  $$\frac{\lambda}{2\pi} < r_i < \frac{2D^2}{\lambda} \tag{3.4}$$
  where D is the largest dimension of the antenna. The angular distribution of energy depends on the distance of the observer from the antenna and the wave field predominantly decay by $1/{r_i}^2$.
- The **radiating far field**. Here, the angular field distribution of the antennas is approximately independent of distance from the antenna and this region is defined by
  $$r_i > \frac{2D^2}{\lambda} \tag{3.5}$$
  For small antennas (with $D \leq \lambda$) the far-field begins at about $r_i = 10\lambda$ (Balanis (1997); Schubert (1999)).

A GPR antenna placed in a homogeneous isotropic ground-air interphase radiates symmetrical spherical waves into the air and ground. Fig. 3.9 illustrates the spatial distribution of the various types of wavefronts radiated by a transmitter as seen in the far field of the dipole antenna. The air wave propagates along the air side of the ground-air interphase. Part of the energy travelling along the ground-air interphase below the ground (i.e. the ground wave) becomes transformed into an inhomogeneous airwave whose amplitude decreases rapidly with increasing distance from the interphase. This is the phase recorded by the receiving antenna and I refer to it as the *apparent ground wave* (see section 6.4, p. 66). Still another part gives rise to a lateral wave, the so-called head wave. The picture presented here is only an idealised case to explain the various types of wavefronts radiated by the antenna. The medium is in fact heterogeneous due to the contrasting material properties.

Knowledge of the form of radiation pattern of an antenna gives information about the antenna's resolution in a medium. The main energy from the antenna is usually transmitted into the ground in the form of an elliptical lobe with its tip at the position of the transmitter. Part of the energy degenerates into secondary lobes in the vicinity of the main lobe (Fig. 3.10)

In order to reduce energy losses from the transmitter, radiations into the upper half-space (air) should be reduced. Furthermore, interferences from other radiation sources such as mobile phones and televisions and reflections from objects in the upper half space should be minimised. A way of doing this is to carefully shield the antennas without reducing their performance. The antenna systems used in this work were all shielded.

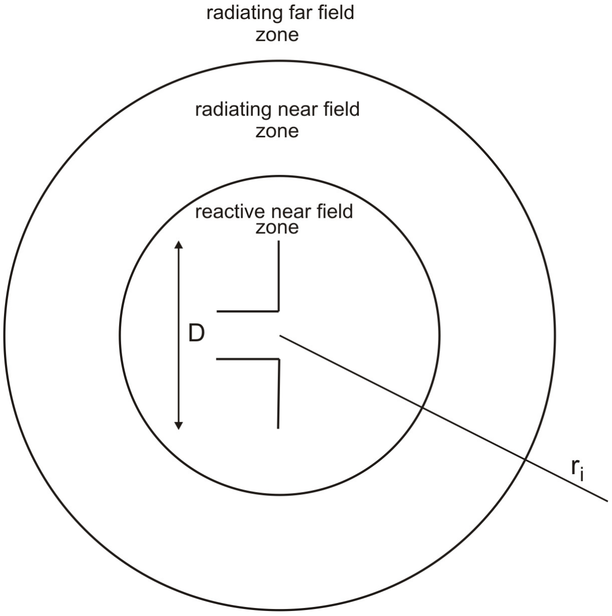

Figure 3.8: Radiation zones of a dipole antenna.

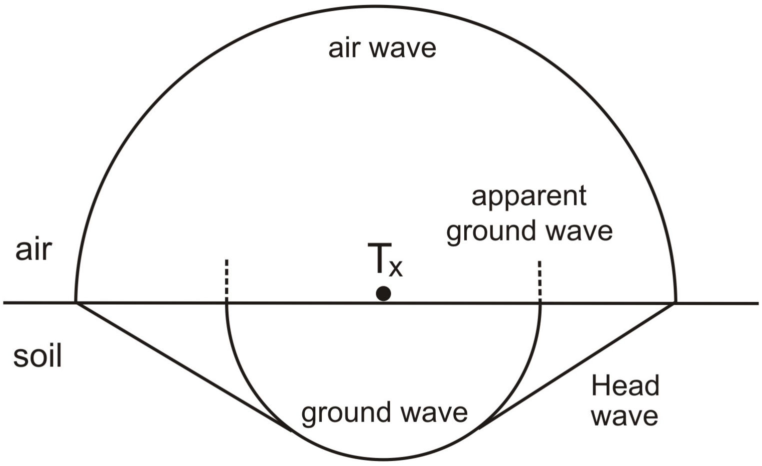

Figure 3.9: Radiated wavefronts close to a transmitter T_x

3.3.1 Antenna Resolution

The resolution of the antenna is defined in two ways:

- The ability of the antenna to determine the exact location of a subsurface reflector in space and time and
- the ability of the antenna to resolve two closely spaced subsurface structures.

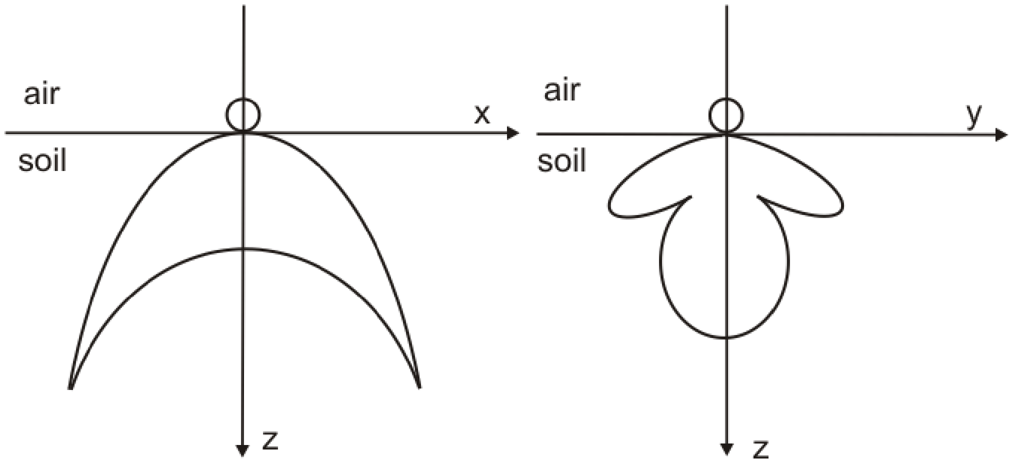

(a) perpendicular to dipole axis (b) parallel to dipole axis

Figure 3.10: Radiation characteristics of a dipole placed on a homogeneous isotropic half space perpendicular and parallel to dipole axis respectively (modified after Tsang et al. (1973).

The vertical resolution is controlled by the wavelength $\lambda = v/f$. From the wave theory two structures are optimally resolved if they are separated by a distance given by $\frac{1}{4}$ of the central wavelength (e.g. Sheriff 1977, Yilmaz (1987), Reynolds (1997)). For reflectors whose separation is within this distance reflections interfere constructively producing a distinctive observed reflection. Features that are closely apart can be best imaged by using high frequency antennas. The dike model at the University of Karlsruhe comprised of thin soil layers of thickness ranging from 0.01 m to 0.02 m. The use of antennas of central frequencies 500 MHz and 900 MHz meant that I worked within a dominant wavelength range of 0.1 – 0.2 m rendering the individual soil layers whose thickness were less than 0.025 m unresolved. However, from the GWS method used here (see chapter 6.3) reflections from the end of a metal rod positioned at intervals of 0.025 m could be vividly resolved. In the modelling exercises using the GWS the plastic sheath of the metal rod of about 0.001 m thick and the air pocket of corresponding thickness were too thin against the dominant wavelength of the 500 MHz antenna used. They were hence not considered in the modelling.

3.4 Conclusion and Open Questions

We have discussed the various factors like soil type, antenna frequency (and Nyquist frequency), sampling interval and length of time window that influence both the operation and quality of data registered by GPR. We have also discussed the commonly used GPR operational methods of CO, CMP and WARR. These methods were applied in chapter 8 to estimate soil water content in the Dano region of Burkina Faso, West Africa.

The method to apply in the field will depend on the description of the target, its expected depth and the frequency of the antennas. The coupling between the ground and antennas contributes to data quality. In all applications of GPR there exists a trade off between the depth of penetration and the resolution. The use of HF antennas gives a higher data resolution, however, the depth of penetration in this case becomes low due to the high attenuation of the signal.

The success of GPR in field campaigns depends (besides factors mentioned above) on effective planning (taking into consideration resources like budget, personnel and other additional equipment which might be useful), right data acquisition, processing (including logical checking and editing of raw data) and right data interpretation. These depend on the expertise of the user, the type of equipment as well as the software used.

Now there remain open questions to be answered in the future. Will it be possible to develop a standardised GPR technique by which right from data acquisition through processing to interpretation not a whit of the expert know-how of the user will be required? Will such a standard permit in-situ field measurements of soil texture and porosity? Would it be possible through a single measurement to acquire information about the dielectric coefficient and electrical conductivity of the soil?

Chapter 4

Theoretical Background of GPR

In this chapter I discuss the fundamental equations underlying the application of GPR. In particular I discuss the phase velocity approximation of electromagnetic waves propagating through media assumed to be non-magnetic with negligible losses.

GPR uses high frequency pulsed electromagnetic waves (typically from 10 MHz to 1 GHz) to acquire subsurface information. A transducer generates a broadband electromagnetic wave (impulse). This wave is radiated from a transmitting antenna, travels through the ground at a velocity, which is determined primarily by the electrical properties (the dielectric coefficient, conductivity, and magnetic permeability) of the ground, to a receiving antenna. The latter registers the travel time and amplitude of the signal. Part of the energy, known as the airwave, travels directly through the air from the transmitter to the receiver. Part of the transmitted energy known as the direct ground wave travels through the soil along the air-ground interface (Berktold et al. (1998)) to the receiver. Another part reaches the receiver after reflection from a medium with contrasting material properties.

4.1 Propagation of Electromagnetic Wave through Material

The propagation of electromagnetic waves through material is described by Maxwell's equations. GPR waves are electromagnetic with frequency range of about 10 - 1000 MHz and obey Maxwell's equations. In the differential form these equations are written as

$$\begin{aligned}
\nabla \times \mathbf{H}(\mathbf{r},t) &= \mathbf{j}(\mathbf{r},t) + \frac{\partial \mathbf{D}(\mathbf{r},t)}{\partial t} && (4.1)\\
\nabla \times \mathbf{E}(\mathbf{r},t) &= -\frac{\partial \mathbf{B}(\mathbf{r},t)}{\partial t} && (4.2)\\
\nabla \cdot \mathbf{D}(\mathbf{r},t) &= \rho(\mathbf{r},t) && (4.3)\\
\nabla \cdot \mathbf{B}(\mathbf{r},t) &= 0 && (4.4)
\end{aligned}$$

where

$\mathbf{H}(\mathbf{r}, t)$: magnetic field intensity [A/m]
$\mathbf{E}(\mathbf{r}, t)$: electric field intensity [V/m]
$\mathbf{D}(\mathbf{r}, t)$: electric displacement [AS/m^2]
$\mathbf{B}(\mathbf{r}, t)$: magnetic induction [Vs/m^2]
$\mathbf{j}(\mathbf{r}, t)$: current density [A/m^2]
$\rho(\mathbf{r}, t)$: free charge density [As/m^3]
$\mathbf{r}$: position vector [m]
t : time [s]

The medium propagated by the electromagnetic wave is considered under the following assumptions in order to simplify our analysis:

- The medium is isotropic i.e. the material properties ε, μ, and σ are scalar.
- The material properties ε, μ and σ are real and spatially variable.
- Changes in the field vectors are linear.

Eqs. (4.1-4.4) are coupled in the time domain by the following constitutive relations

$$\mathbf{D}(\mathbf{r}, t) = \varepsilon(r)\mathbf{E}(\mathbf{r}, t) = \varepsilon_0\varepsilon_r(r)\mathbf{E}(\mathbf{r}, t) \tag{4.5}$$

$$\mathbf{B}(\mathbf{r}, t) = \mu(r)\mathbf{H}(\mathbf{r}, t) = \mu_0\mu_r(r)\mathbf{H}(\mathbf{r}, t) \tag{4.6}$$

$$\mathbf{j}(\mathbf{r}, t) = \sigma(r)\mathbf{E}(\mathbf{r}, t) \tag{4.7}$$

Eqs. (4.1-4.4) can now be written using Eqs. (4.5-4.7) as

$$\nabla \times \mathbf{H}(\mathbf{r}, t) = \sigma(\mathbf{r})\mathbf{E}(\mathbf{r}, t) + \varepsilon_0\varepsilon(\mathbf{r})\frac{\partial \mathbf{E}(\mathbf{r}, t)}{\partial t} \tag{4.8}$$

$$\nabla \times \mathbf{E}(\mathbf{r}, t) = -\mu_0\mu(\mathbf{r})\frac{\partial \mathbf{H}(\mathbf{r}, t)}{\partial t} \tag{4.9}$$

$$\nabla \cdot \varepsilon(\mathbf{r})\mathbf{E}(\mathbf{r}, t) = \frac{\rho(\mathbf{r}, t)}{\varepsilon_0} \tag{4.10}$$

$$\nabla \cdot \mu(\mathbf{r})\mathbf{H}(\mathbf{r}, t) = 0 \tag{4.11}$$

where

ε_0 : permittivity of free space = [As/Vm]
$\mu_0 = 4\pi \times 10^{-7}$: magnetic permeability of free space [Vs/Am]

However, if the material properties ε, μ and σ are dependent on frequency (respectively on time), i.e. if the medium is dispersive, then, the constitutive relations are expressed as convolution integrals

$$\mathbf{D}(\mathbf{r},t) = \varepsilon_0 \int_{-\infty}^{t} \varepsilon_r(\mathbf{r},\tau)\mathbf{E}(\mathbf{r},t-\tau)d\tau \tag{4.12}$$

$$\mathbf{B}(\mathbf{r},t) = \mu_0 \int_{-\infty}^{t} \mu_r(\mathbf{r},\tau)\mathbf{H}(\mathbf{r},t-\tau)d\tau \tag{4.13}$$

$$\mathbf{j}(\mathbf{r},t) = \int_{-\infty}^{t} \sigma(\mathbf{r},\tau)\mathbf{E}(\mathbf{r},t-\tau)d\tau \tag{4.14}$$

So far the Maxwell's equations have been expressed in the time domain only. All time dependent variables expressed as $f(t)$ can then be transformed into the frequency dependent variables $F(\omega)$ through Fourier transformation integrals (Eqs. (4.15) and (4.16)):

$$\mathbf{F}(\omega) = \int_{-\infty}^{+\infty} \mathbf{f}(t)e^{-i\omega t}\,dt \tag{4.15}$$

$$\mathbf{f}(t) = \frac{1}{2\pi}\int_{-\infty}^{+\infty} \mathbf{F}(\omega)e^{i\omega t}\,d\omega \tag{4.16}$$

where $\omega = 2\pi f$ [rad/s] is the angular frequency. We make the following additional assumptions to simplify our analysis:

- It is homogeneous i.e material properties ε, μ and σ are independent of position.
- The medium is source-free i.e. $\rho(\mathbf{r},\omega) = 0$
- The medium is non-magnetic and the magnetic permeability μ is assumed to be that of free space i.e. $\mu(\omega) = \mu_0$.
- The medium is conductive, non-dispersive and possess electrical properties which are independent of temperature, pressure and time.
- A harmonic wave $\mathbf{E}(\mathbf{r},\omega) = \mathbf{E}_0\, e^{i(\mathbf{k}\cdot\mathbf{r}-\omega\, t)}$ propagates through the medium.

Maxwell's equations expressed in the frequency domain are

$$\nabla \times \mathbf{H}(\mathbf{r},\omega) = \mathbf{j}(\mathbf{r},\omega) - i\omega\mathbf{D}(\mathbf{r},\omega) \tag{4.17}$$

$$\nabla \times \mathbf{E}(\mathbf{r},\omega) = i\omega\mathbf{B}(\mathbf{r},\omega) \tag{4.18}$$

$$\nabla \cdot \mathbf{D}(\mathbf{r},\omega) = \rho(\mathbf{r},\omega) \tag{4.19}$$

$$\nabla \cdot \mathbf{B}(\mathbf{r},\omega) = 0 \tag{4.20}$$

The constitutive relationships that describe the material properties of the medium simplify to

$$\mathbf{D}(\mathbf{r},\omega) = \varepsilon(\omega)\mathbf{E}(\mathbf{r},\omega) = \varepsilon_0\varepsilon_r(\omega)\mathbf{E}(\mathbf{r},\omega) \tag{4.21}$$

$$\mathbf{B}(\mathbf{r},\omega) = \mu(\omega)\mathbf{H}(\mathbf{r},\omega) = \mu_0\mu_r(\omega)\mathbf{H}(\mathbf{r},\omega) \tag{4.22}$$

$$\mathbf{j}(\mathbf{r},\omega) = \sigma(\omega)\mathbf{E}(\mathbf{r},\omega) \tag{4.23}$$

where

$\varepsilon_r(\omega)$: relative permittivity (dielectric coefficient) of medium
$\varepsilon(\omega) = \varepsilon_0\varepsilon_r(\omega)$: permittivity of medium [As/Vm]
$\mu(\omega) = \mu_0\mu_r(\omega)$: magnetic permeability [Vs/Am]
$\mu_r(\omega)$: relative magnetic permeability
$\sigma(\omega)$: electrical conductivity [S/m]

We make use of the vector identity

$$\nabla \times \nabla \times \mathbf{V} = \nabla(\nabla \cdot \mathbf{V}) - \nabla^2\mathbf{V} \tag{4.24}$$

for any vector $\mathbf{V}$. Taking the curl of Eq (4.18) and considering $\nabla \cdot \mathbf{E}(\mathbf{r},\omega) = 0$ for a homogeneous medium and also the constitutive Eqs. (4.21-4.23), we have

$$\begin{aligned} \nabla^2\mathbf{E}(\mathbf{r},\omega) &= [i\omega\mu(\omega)\sigma(\omega) - \omega^2\mu(\omega)\varepsilon(\omega)]\mathbf{E}(\mathbf{r},\omega) \\ &= -\omega^2\mu_0\mu_r(\omega)\varepsilon_0\left(\varepsilon_r(\omega) - i\frac{\sigma(\omega)}{\varepsilon_0\omega}\right)\mathbf{E}(\mathbf{r},\omega) \end{aligned} \tag{4.25}$$

The differential Eq. (4.25) can be solved by considering the ansatz of a plane wave solution

$$\mathbf{E}(\mathbf{r},\omega) = \mathbf{E}_0 e^{i(\mathbf{k}\cdot\mathbf{r}-\omega t)}, \quad t = t_0 \tag{4.26}$$

The Fourier transformation of Eq. (4.26) is

$$\mathbf{E}(\mathbf{r},t) = \mathbf{E}_0 e^{i\mathbf{k}\cdot\mathbf{r}}\delta\,(t - t_0) \tag{4.27}$$

with the impulse function $\delta(t - t_0)$

Eqs. (4.26) and (4.25) give

$$k^2(\omega) = \varepsilon\mu\omega^2 + i\sigma\mu\omega \tag{4.28}$$

Eq. (4.28) shows that in a conductive lossy medium the wave number k is a complex quantity.

Let us consider a plane wave propagating in the z-direction, and make the ansatz

$$k_z(\omega) = \beta(\omega) + i\alpha(\omega) \tag{4.29}$$

for the z-component of the wave vector.

Now, substituting Eq. (4.29) in the equation of a plane wave propagating in the $\vec{e_z}$-direction, $\mathbf{E}(r,\omega) = \mathbf{E}_0 e^{i(k_z r - \omega t)}$, we have

$$\mathbf{E}(r,\omega) = \mathbf{E}_0 e^{-\alpha z} e^{i(\beta z - \omega t)} \tag{4.30}$$

where β the real part of k is termed the phase or propagation constant, and α the imaginary part is referred to as the attenuation constant of the wave.

Taking the square of Eq. (4.29) gives

$$k_z{}^2(\omega) = \beta^2 + 2i\beta\alpha - \alpha^2 \tag{4.31}$$

Comparing Eqs. (4.28) and (4.31),

$$\beta^2 - \alpha^2 = \varepsilon\mu\omega^2 \quad \text{and} \quad \beta\alpha = \frac{\sigma\mu\omega}{2} \tag{4.32}$$

Solving Eq. (4.32) gives

$$\beta(\omega) \;=\; \left[\frac{\omega^2\mu\varepsilon}{2}\left(\sqrt{1+\left(\frac{\sigma}{\omega\varepsilon}\right)^2}+1\right)\right]^{\frac{1}{2}} \tag{4.33}$$

$$\alpha(\omega) \;=\; \left[\frac{\omega^2\mu\varepsilon}{2}\left(\sqrt{1+\left(\frac{\sigma}{\omega\varepsilon}\right)^2}-1\right)\right]^{\frac{1}{2}} \tag{4.34}$$

The skin depth Λ corresponding to the attenuation α is given by

$$\Lambda(\omega) = \frac{1}{\alpha(\omega)} \tag{4.35}$$

The phase velocity $v(\omega)$ [m/s] of the wave is

$$v(\omega) = \frac{\omega}{\beta(\omega)} \tag{4.36}$$

Substituting Eq. (4.33) into (4.36) gives

$$v(\omega) = \left[\frac{\mu\varepsilon}{2}\left(\sqrt{1+\left(\frac{\sigma}{\omega\varepsilon}\right)^2}+1\right)\right]^{-\frac{1}{2}} \tag{4.37}$$

The quantity $\sigma/\omega\varepsilon$ expresses the ratio of the conduction current $\mathbf{j} = \sigma\mathbf{E}$ to the displacement current $\partial\mathbf{D}/\partial t = -i\omega\varepsilon\mathbf{E} = \mathbf{j}_d$ in material.

The conduction and displacement currents are out of phase with the applied electric field through a phase angle ϕ. The tangent of the angle ϑ (= dielectric loss angle) which is the complement of ϕ is termed the *material loss tangent*. Thus,

$$\tan\vartheta = \left|\frac{\mathbf{j}}{\mathbf{j}_d}\right| = \frac{\sigma}{\omega\varepsilon} \tag{4.38}$$

In a very low conductive medium where $\sigma \ll \varepsilon\omega$ and at relatively low frequencies (0.01 - 1 GHz) which is the typical operative frequency of GPR, the conduction current is negligibly small compared with the displacement current i.e. $\sigma/\varepsilon\omega \ll 1$. Eq. (4.37) then simplifies to

$$v = \frac{1}{\sqrt{\varepsilon\mu}} = \frac{1}{\sqrt{\varepsilon_0\varepsilon_r\mu_0\mu_r}} = \frac{c}{\sqrt{\varepsilon_r\mu_r}} \tag{4.39}$$

where c (= 3.0×10^8 m/s) is the speed of electromagnetic wave in vacuum and

$$c = \frac{1}{\sqrt{\varepsilon_0\mu_0}} \tag{4.40}$$

The velocity of GPR waves in a low conductive medium under these conditions is hence, mainly controlled by the dielectric coefficient ε_r i.e. with $\mu_r = 1$,

$$v = \frac{c}{\sqrt{\varepsilon_r}} \tag{4.41}$$

Eq. (4.41) represents the phase velocity approximation of electromagnetic waves in non-magnetic low loss media. This approximation is used in throughout this work to determine electromagnetic wave velocities in the soil. The wavelength λ of the GPR operating at a central frequency f [Hz], then, becomes

$$\lambda = \frac{v}{f} = \frac{c}{f\sqrt{\varepsilon_r}} \tag{4.42}$$

However, for GPR operating in a more conductive medium at frequencies such that $\sigma/\omega\varepsilon \gg 1$ Eq. (4.37) becomes

$$v(\omega) = \sqrt{\frac{2\omega}{\mu\sigma}} = \sqrt{\frac{2\cdot 2\pi f}{4\pi\cdot 10^{-7}\sigma}} = \sqrt{\frac{10^7 f}{\sigma}} \tag{4.43}$$

Now, as it is evident from Eqs. (4.41) and (4.43) the velocity of the GPR wave is mainly controlled by ε, σ and f. The quantities ε_r and σ at particular frequencies are themselves complex functions of frequency. Eq. (4.41) is applicable to most materials within the average conductivity range of 0.003 – 0.3 S/m (Du 1996).

Fig. 4.1 shows a plot of the phase velocity against frequency for a medium with $\varepsilon = 9$ (see Table 5.1, p. 50). At frequencies below 0.1 MHz the velocity is influenced by both the conductivity and frequency. Within the GPR operative frequency range of 10 MHz - 1 GHz, the velocity is nearly independent of frequency for conductivities below 0.1 S/m. At higher frequencies above about 1 GHz the velocity once again becomes frequency-dependent as a result of relaxation effects of water.

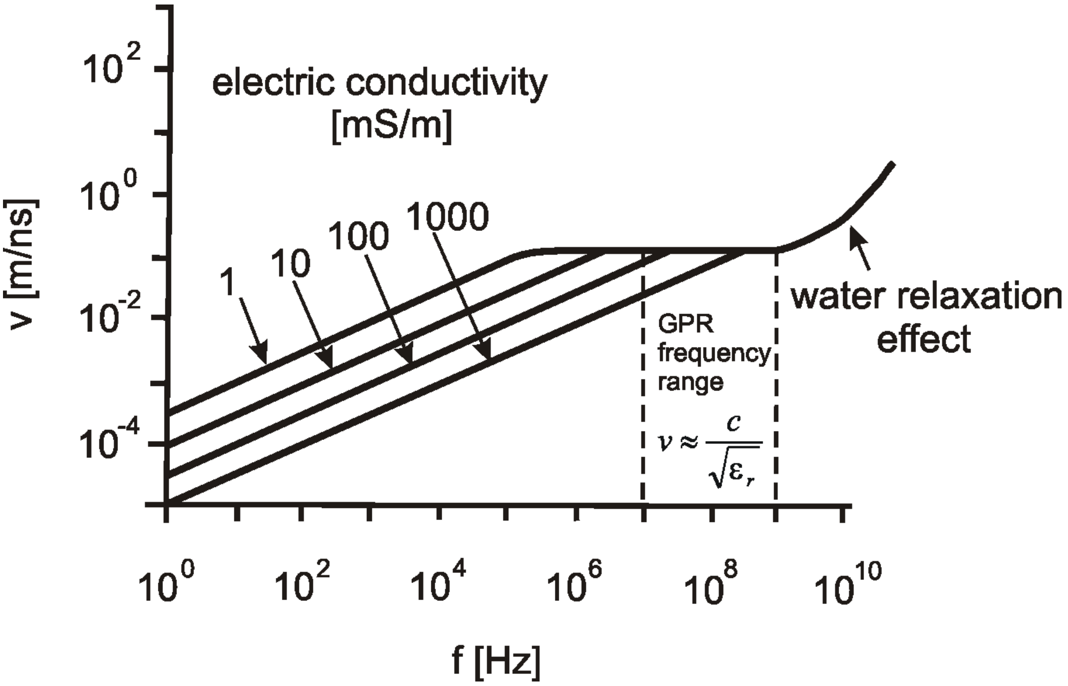

Figure 4.1: Frequency dependence of the phase velocity in a medium with $\varepsilon_r = 9$ at different electrical conductivities (modified after Annan, 1989).

In a similar way we obtain a simplified attenuation constant α from Eq. (4.33) as

$$\alpha = \frac{\sigma}{2}\sqrt{\frac{\mu}{\varepsilon}} \tag{4.44}$$

The attenuation of the GPR signal is governed mainly by σ and ε. This relationship is valid only for a homogeneous soil without impedance contrasts (Theimer et al. (1994)). Where the signal comes across an impedance contrast, part of the energy which is proportional to the magnitude of change (Reynolds (1997)) is reflected back. If Z_1 and Z_2 are the impedances of soil layers immediately above and below the impedance contrast, then the reflection coefficient RC is given as (e.g. Brewster and Annan (1994); Hagrey and Müller (2000); Lunt et al. (2005)):

$$RC = \frac{Z_2 - Z_1}{Z_2 + Z_1} \tag{4.45}$$

The impedance Z is characterised by the ratio of the magnetic to the electric energy density. Considering a harmonic electromagnetic wave $\mathbf{D}(x,t) = \mathbf{D}_0 e^{-i(\omega t - kx)}$, then, it follows from Eqs. (4.1) and (4.8) that

$$\nabla \times \mathbf{H} = \mathbf{j} + \frac{\partial D}{\partial t} = (\sigma - i\omega\varepsilon_r\varepsilon_0)\mathbf{E} \tag{4.46}$$

$$-i\omega\left(\varepsilon_r + \frac{i\sigma}{\varepsilon_0\omega}\right)\varepsilon_0\mathbf{E} = -i\omega\widetilde{\varepsilon}_r\varepsilon_0\mathbf{E} = -i\omega\widetilde{\mathbf{D}} \tag{4.47}$$

and

$$\widetilde{\varepsilon_r} = \varepsilon_r + \frac{i\sigma}{\varepsilon_0\omega} \tag{4.48}$$

$$\Rightarrow \qquad \frac{\mathbf{B}\cdot\mathbf{H}}{\widetilde{\mathbf{D}}\cdot\mathbf{E}} = \frac{\mu\mathbf{H}^2}{\widetilde{\varepsilon_r}\varepsilon_0\mathbf{E}^2} = \frac{\mu_r\mu_0\mathbf{H}^2}{\widetilde{\varepsilon_r}\varepsilon_0\mathbf{E}^2} = Z^2\frac{\mathbf{H}^2}{\mathbf{E}^2} \tag{4.49}$$

$$Z = \sqrt{\frac{\mu_r\mu_0}{\widetilde{\varepsilon_r}\varepsilon_0}} = \sqrt{\frac{\mu_r\mu_0}{\varepsilon_0\left(\varepsilon_r + \frac{i\sigma}{\varepsilon_0\omega}\right)}} = \sqrt{\frac{\mu}{\left(\varepsilon + \frac{i\sigma}{\omega}\right)}} = \sqrt{\frac{\mu}{\varepsilon\left(1 + \frac{i\sigma}{\varepsilon\omega}\right)}} \tag{4.50}$$

For $\sigma/\varepsilon\omega \ll 1$ and $\mu_r = 1$, Eq. (4.50) simplifies to

$$Z = \sqrt{\frac{\mu_0}{\varepsilon}} = \sqrt{\frac{\mu_0}{\varepsilon_0\varepsilon_r}} \tag{4.51}$$

Eq. (4.45) can then be written with Eq. (4.41) as

$$RC = \frac{Z_2 - Z_1}{Z_2 + Z_1} = \frac{\frac{1}{\sqrt{\varepsilon_{r2}}} - \frac{1}{\sqrt{\varepsilon_{r1}}}}{\frac{1}{\sqrt{\varepsilon_{r2}}} + \frac{1}{\sqrt{\varepsilon_{r1}}}} = \frac{\sqrt{\varepsilon_{r1}} - \sqrt{\varepsilon_{r2}}}{\sqrt{\varepsilon_{r1}} + \sqrt{\varepsilon_{r2}}} = \frac{v_2 - v_1}{v_2 + v_1} \tag{4.52}$$

where ε_{r1} and ε_{r2} are the dielectric permittivities of the soil layers immediately below and above the impedance contrast (transition zone) and v_1 and v_2 are the corresponding electromagnetic wave propagation velocities. RC determines how sharp a boundary reflection may be. A well-defined change in ε_r with depth gives in a sharp signal reflection whereas pulse widening results from gradual change in ε_r (van Dam et al. (2002)). Eq. (4.52) shows that the phase of the electromagnetic wave velocity at a soil layer boundary remains unaltered for $v_2 > v_1$. There is, however, a phase shift of 180 ° when $v_2 < v_1$. Thus, the value of RC ranges between +1 and −1. I used this criterion to correctly pick and process the reflected phases of the GPR signal from the radargram in experiments Common Midpoint (CMP) method of GPR.

Chapter 5

Dielectric Properties of Soil

Two electrical properties of the soil, the dielectric permittivity ε and the electrical conductivity σ, and a property of the electromagnetic signal i.e. its frequency, $\omega = 2\pi f$, control the propagation of electromagnetic waves in the soil. These are of prime interest in GPR measurements. They (ε and σ) control two importance processes - energy dissipation and storage in the dielectric material - and influence the amplitude and propagation speed of radar waves. At high frequencies ε controls the phase velocity while σ controls the attenuation and the penetration depth of the electromagnetic wave. These two properties are strongly dependent on the volumetric water content. It should be mentioned that ε and σ are also controlled by the hydraulic properties of the soil such as porosity, permeability, retention capacity, sorptivity, salinity, transmissivity, infiltration rate and soil water tension. However, this discussion is only restricted to the relative dielectric coefficient, electric conductivity and signal frequency which I see as most vital controls in GPR soil water measurements. For a detailed description of the electric and hydraulic properties of rocks and soils the reader is kindly referred to sources like Parkhomenko (1967); Hasted (1973); Schön (1996); Olhoeft (1987, 1994, 1998); Terzaghi et al. (1996); Singh (1997); Bell (2000); Smoltczyk (2001); Hull et al. (2003), Pansu and Gautheyrou (2006) for more information.

5.1 Dielectric Permittivity of Materials

The dielectric permittivity is characteristic of the material polarization which describes the response of bound displacement charges to the applied alternating electric field. With increasing ω the bound charges fail to keep pace with the fast changing field resulting in an out of phase polarization component. The dielectric permittivity is hence, also written in the complex notation

$$\varepsilon(\mathbf{r}, \omega) = \varepsilon'(\mathbf{r}, \omega) + i\varepsilon''(\mathbf{r}, \omega) \tag{5.1}$$

The related electric displacement flux density $\mathbf{J}_d$ (for a dependence $e^{-i\omega t}$) is given by

$$\mathbf{J}_d(\mathbf{r}, \omega) = -i\varepsilon(\mathbf{r}, \omega)\omega\mathbf{E}(\mathbf{r}, \omega) \tag{5.2}$$

The corresponding current density $\mathbf{J}_c(\mathbf{r}, \omega)$ [A/m^2] is given by

$$\mathbf{J}_c(\mathbf{r}, \omega) = \sigma(\mathbf{r}, \omega)\mathbf{E}(\mathbf{r}, \omega) \tag{5.3}$$

The electrical conductivity describes the flow of current resulting from free charge movement in a material when an electric field $\mathbf{E}(\mathbf{r}, \omega)$ is applied. At relatively low frequencies ω the current flows in phase with the applied field but as the frequency increases the time taken for the charges to respond to the field increases giving rise to an out-of-phase current component. The electrical conductivity s may thus be expressed in the complex notation as

$$\sigma(\mathbf{r}, \omega) = \sigma'(\mathbf{r}, \omega) + i\sigma''(\mathbf{r}, \omega) \tag{5.4}$$

Eqs. (5.1)−(5.4) give the total electric current density $\mathbf{J}(\mathbf{r}, \omega)$ as

$$\begin{aligned} \mathbf{J}(\mathbf{r}, \omega) = \mathbf{J}_c(\mathbf{r}, \omega) + \mathbf{J}_d(\mathbf{r}, \omega) &= (\sigma(\mathbf{r}, \omega) - i\varepsilon(\mathbf{r}, \omega)\omega)\mathbf{E}(\mathbf{r}, \omega) \\ &= \sigma_{\text{eff}}(\mathbf{r}, \omega)\mathbf{E}(\mathbf{r}, \omega) \qquad (5.5) \\ &= -i\omega\varepsilon_{\text{eff}}(\mathbf{r}, \omega)\mathbf{E}(\mathbf{r}, \omega) \qquad (5.6) \end{aligned}$$

where $\sigma_{\text{eff}}(\mathbf{r}, \omega)$ and $\varepsilon_{\text{eff}}(\mathbf{r}, \omega)$ are defined by

$$\begin{aligned} \sigma_{\text{eff}}(\mathbf{r}, \omega) &= \sigma(\mathbf{r}, \omega) - i\omega\varepsilon(\mathbf{r}, \omega) \qquad (5.7) \\ \varepsilon_{\text{eff}}(\mathbf{r}, \omega) &= \varepsilon(\mathbf{r}, \omega) + i\frac{\sigma(\mathbf{r}, \omega)}{\omega} \qquad (5.8) \end{aligned}$$

Substituting Eqs. (5.4) and (5.1) into (5.7) and (5.8) respectively gives

$$\begin{aligned} \varepsilon_{\text{eff}}(\mathbf{r}, \omega) &= \underbrace{\left(\varepsilon'(\mathbf{r}, \omega) - \frac{\sigma''(\mathbf{r}, \omega)}{\omega}\right)}_{\varepsilon'_{\text{eff}}(\mathbf{r},\omega)} + i\underbrace{\left(\varepsilon''(\mathbf{r}, \omega) + \frac{\sigma'(\mathbf{r}, \omega)}{\omega}\right)}_{\varepsilon''_{\text{eff}}(\mathbf{r},\omega)} \qquad (5.9) \\ \sigma_{\text{eff}}(\mathbf{r}, \omega) &= \underbrace{(\sigma'(\mathbf{r}, \omega) + \omega\varepsilon''(\mathbf{r}, \omega))}_{\sigma'_{\text{eff}}(\mathbf{r},\omega)} + i\underbrace{(\sigma''(\mathbf{r}, \omega) - \omega\varepsilon'(\mathbf{r}, \omega))}_{\sigma''_{\text{eff}}(\mathbf{r},\omega)} \qquad (5.10) \end{aligned}$$

where $\varepsilon'_{\text{eff}}(\mathbf{r}, \omega)$ and $\sigma'_{\text{eff}}(\mathbf{r}, \omega)$ are the real parts of the effective relative dielectric coefficient and conductivity respectively. The properties $\varepsilon'(\mathbf{r}, \omega)$ and $\sigma''(\mathbf{r}, \omega)$ contribute to the in-phase component of the total current while $\varepsilon''(\mathbf{r}, \omega)$ and $\sigma'(\mathbf{r}, \omega)$ produce out-of-phase component. Hence, it is customary to introduce the concept of *effective dielectric permittivity* and *effective dielectric conductivity* since only the in-phase and out-of-phase components of the total current are of most practical interest.

At the GPR operational frequency range and at conductivities (< 10 mS/m) the imaginary component $\sigma''(\mathbf{r}, \omega)$ of the effective conductivity is very small i.e.

$$\varepsilon'_{\text{eff}}(\mathbf{r}, \omega) = \varepsilon'(\mathbf{r}, \omega) - \frac{\sigma''(\mathbf{r}, \omega)}{\omega} \approx \varepsilon'(\mathbf{r}, \omega) \tag{5.11}$$

Eq. (5.11) leads to the phase velocity approximation $v = \frac{c}{\sqrt{\varepsilon_r}}$ at low conductivities (< 10 mS) and frequencies (10−1000 MHz). Hence, in this work, unless otherwise stated, the dielectric permittivity refers to the real part of the effective dielectric permittivity.

5.1.1 The Relative Dielectric Coefficient ε_r

The dielectric coefficient is a measure of the extent to which a material traversed by an electromagnetic field becomes polarized and it describes the frequency response of the material.This process involves energy storage and dissipation. Hence, it is customary to write $\varepsilon_r(\mathbf{r}, \omega)$ as a complex quantity with real and imaginary parts. The in-phase component ε_r' results in dispersion. The physical meaning of this is that an electromagnetic wave packet is dispersed due to the frequency dependence of the phase velocity of its spectral components as it passes through the medium. The out-of-phase component $\varepsilon_r''(\mathbf{r}, \omega)$ describes the attenuation and energy loss of the signal (Davis and Annan (1989)). For many materials of geological relevance only the real part of the dielectric coefficient $\varepsilon_r'(\mathbf{r}, \omega)$ is of practical importance (Schmugge, 1985). A frequency dependent attenuation also causes a dispersion of the signal in addition (Mayer (2005)).

For an isotropic medium this dimensionless parameter $\varepsilon_r(\omega)$ is expressed as

$$\varepsilon_r(\mathbf{r}, \omega) = \varepsilon_r'(\mathbf{r}, \omega) + i\varepsilon_r''(\mathbf{r}, \omega) = \frac{\varepsilon(\mathbf{r}, \omega)}{\varepsilon_0} \tag{5.12}$$

$\varepsilon_0 = 8.854 \times 10^{12}$ F/m. In the literature a number of authors e.g. (McCann et al. (1988); Davis and Annan (1989); Ulaby et al. (1990); Daniels (1996); Zeng and McMechan (1997)) discuss the relative dielectric coefficients of different soils and minerals. For a porous granular material it is a function of its composition and more importantly the amount of water it contains as seen from Table (5.1). Such values of the dielectric coefficient help in the GPR soil data interpretation. They give information about the amount of water present in the soil as well as the speed, reflectivity and attenuation of propagating GPR signal.

5.1.2 Dielectric Mixing Models of Soil

Soil as medium is electromagnetically considered to be a four-component dielectric mixture which consist of air, soil particles, bound water and free water (Hallikainen et al. (1984). Due to the differences in the intensity of the forces acting on the bound and free water fractions an incident electromagnetic wave is variably dispersed between these fractions. The effective dielectric permittivity of the fractions depend on frequency, temperature and salinity. In effect this makes the dielectric permittivity of a soil mixture functions of frequency, temperature, salinity, relative fractions of bound and free water, bulk soil density, shape of the soil particles and shape of water inclusions. Several models have been proposed over the past years (e.g. Wang and Schmugge (1980); Hoekstra and Delaney (1974); Dobson et al. (1984); Hallikainen et al. (1984), Heimovaara (1994)) to provide a convenient means of predicting the dielectric behaviour of the soil. A few of these models are discussed briefly.

In a two component model the soil is assumed to comprise of soil particles and free water. This model may produce the right trend for a soil's dielectric permittivity-soil water content relationship but it fails to explain the dependence of θ_v on soil texture. For example, Topp

Material	$\varepsilon_r(\mathbf{r}, \omega)$ (Daniels (1996))	$\varepsilon_r(\mathbf{r}, \omega)$ (Davis and Annan (1989))
Air	1	1
Asphalt: dry	2 – 4	
Asphalt: wet	6 – 12	
Clays	2 – 40	5 – 40
Clay: dry	2 – 6	
Clay: wet	15 – 40	
Coal: dry	3.5	
Coal: wet	8	
Concrete: dry	4 – 10	
Concrete: wet	10 – 20	
Granite		4 – 6
Granite: dry	5	
Granite: wet	7	
Limestone: dry	7	
Limestone: wet	8	
Permafrost	4 – 8	
Salt (rocksalt): dry	4 – 7	5 – 6
Sand: dry	4 – 6	3 – 5
Sand: wet	10 – 30	20 – 30
Sandstone: dry	2 – 3	
Sandstone: wet	5 – 10	
Seawater		80
Seawater: ice	4 – 8	
Shales		5 – 15
Shale: wet	6 – 9	
Silts		5 – 30
Snow	8 – 12	
Soil: sandy dry	4 – 6	
Soil: sandy wet	15 – 30	
Soil: loamy dry	4 – 6	
Soil: loamy wet	10 – 20	
Soil: clayey dry	4 – 6	
Soil: clayey wet	10 – 15	
Water: distilled		80
Water: fresh	81	80
Water: fresh ice	4	3 – 4

Table 5.1: Relative dielectric coefficients of some geological material measured at 100 MHz (culled from Davis and Annan (1989); Daniels (1996)).

et al. (1980) reported from their investigations that the soil texture has very little influence on the dielectric coefficient of a wet soil. On the contrary, investigators like Wang and Schmugge (1980) and Newton (1977) reported that for the same θ_v, different soil types show differences in the magnitudes of their soil permittivities.

More elaborate models which take into account the effect of the bound water fraction have been suggested by e.g. Dobson et al. (1984) and Wang and Schmugge (1980). These models fit $\varepsilon_{\text{soil}} - \theta_v$ experimental observations better than the two component models do due to soil specific parameters in the models which can be adjusted.

Dobson et al. (1984) introduce a four-component model consisting of dry soil solids as the host with inclusions (of bound water, free water and air) which are assumed to be disc-shaped based on an earlier model suggested by de Loor (1968). However, not all the input quantities for this theoretical four-component model are readily available or remain constant over time for specific soils. Hence, for many applications simple empirical models which use the volume fractions V_i and the dielectric permittivities ε_i of the soil components to calculate the effective dielectric permittivity ε_{eff} of the soil (e.g. models suggested by Lichtenecker and Rother (1931); Birchak et al. (1974)) are more convenient. For such a four-component model

$$\varepsilon_{\text{eff}}^{\kappa} = V'_s\varepsilon_s^{\kappa} + V'_a\varepsilon_a^{\kappa} + V'_{fw}\varepsilon_{fw}^{\kappa} + V'_{bw}\varepsilon_{bw}^{\kappa} \tag{5.13}$$

where the subscripts s, a, fw and bw refer to soil solids, air, free water and bound water, and V' the corresponding volume fractions respectively.

$$V'_s + V'_a + V'_{fw} + V'_{bw} = 1 \tag{5.14}$$

with $0 \leq \kappa \leq 1$; κ depends on the geometry of the medium with respect to the applied electric field. This model is effective in predicting the dielectric permittivity for a low-loss ($\sigma < 10$ mS/m) non-magnetic (with $\mu_r \approx 1$) medium (e.g. Martinez and Byrnes (2001)).

Like the other models discussed above, it describes the dielectric behaviour of soil-water mixtures in the microwave region ($f > 1$ GHz) well. However, I see it to be of little practice significance vis-a-vis GPR observations due to the use of operational frequencies (> 1 GHz) that are above the GPR range. Besides there are inconsistencies in the reported observations from different investigators due probably to the differences in experimental procedures, sample preparation and sample composition.

5.1.3 Dielectric Permittivity and Soil Water Content

When we reconsider Eq. (5.13) with $\kappa = 0.5$ (e.g. Roth et al. (1990)) and the the assumption that the soil comprises of the three components: soil particles, free water and air we describe the CRIM model.

$$\varepsilon_{\text{eff}} = \left[V'_s\sqrt{\varepsilon_s} + V'_a\sqrt{\varepsilon_a} + \theta_v\sqrt{\varepsilon_{fw}}\right]^2 \tag{5.15}$$

Substituting $V'_a = 1 - (\theta_v + V'_s)$ into Eq. (5.15) and arranging gives

$$\theta_v = \frac{\sqrt{\varepsilon_{\text{eff}}}}{\sqrt{\varepsilon_{fw}} - \sqrt{\varepsilon_a}} - \frac{V'_s(\sqrt{\varepsilon_s} - \sqrt{\varepsilon_a}) - 1)}{\sqrt{\varepsilon_{fw}} - \sqrt{\varepsilon_a}} \tag{5.16}$$

which can be expressed in the form

$$\theta_v = a\sqrt{\varepsilon_{\text{eff}}} - b \tag{5.17}$$

where a and b are constants. This relation is identical to a relation also suggested by Ledieu et al. (1986); Herkelrath et al. (1991); and Wensink (1993) at frequencies below 1 GHz. The dielectric permittivity varies along a curve which is approximately parabolic from values of about 4 – 30 as the soil water content varies from 0 to about 50 % (Parkhomenko (1967)).

This model was based on the assumption that soil water exists in the free state without taking into consideration the vital role which could be played by bound water especially in soils which contain a good amount of clay. For such a soil, in one case, the soil water might exist as free water in the pores of the porous medium at high frequencies of about 1 GHz due to relaxation effects. In another case, it might exist as bound water due predominantly to polarization effects at low frequencies of about 25 MHz. This behaviour results from a double layer formed at the boundary between the soil particles and liquid phases (e.g. Parkhomenko (1967); Saint-Amant and Strangway (1970); de Loor (1983); King et al. (1981)).This makes the soil water content relation with dielectric permittivity dependent on the nature of the soil.

5.1.3.1 The Empirical Formula by Topp et al. (1980)

The empirical equation given by Topp et al. (1980) showing the relationship between relative dielectric coefficient ε_r and the volumetric water content θ_v was based on a series of experiments on a number of soil specimens of different textures, water contents (0 – 55 m^{3}m^{-3}), temperatures (10 – 40°C) and at different frequencies ranging between (20 MHz – 1 GHz):

$$\theta_v = -5.3 \cdot 10^{-2} + 2.92 \cdot 10^{-2}\varepsilon_r - 5.5 \cdot 10^{-4}\varepsilon_r^2 + 4.3 \cdot 10^{-6}\varepsilon_r^3 \tag{5.18}$$

The relationship between ε_r and θ_v based on Eq. (5.18) is shown in Fig. (5.1). Under normal soil conditions Eq. (5.18) is found to be almost independent of soil texture, temperature, bulk density and fluid salinity. The formula has its limitations in soil water content evaluation e.g. Miyamoto and Chikushi (2006) reports that it underestimates soil water content for mineral soils of low bulk density. Logsdon (2000) reports of overestimated values of the actual water content for dispersive soils. Besides, the equation seems to be very ideal for non-magnetic ($\mu_r = 1$) soils with low clay content (bound water content which is about proportional to the amount of clay in the soil was not considered in the model) and conductivity ($\sigma < 10$ mS/m). It is not suitable for measuring water content values above 0.55 m^{3}m^{-3} and it might lead to errors for soils of high organic matter or very low water content values below 0.05 m^3/m^3. Irrespective of these limitations the formula has been *universally* accepted for volumetric water content evaluations, hence, I used it throughout this work for all soil water content determinations.

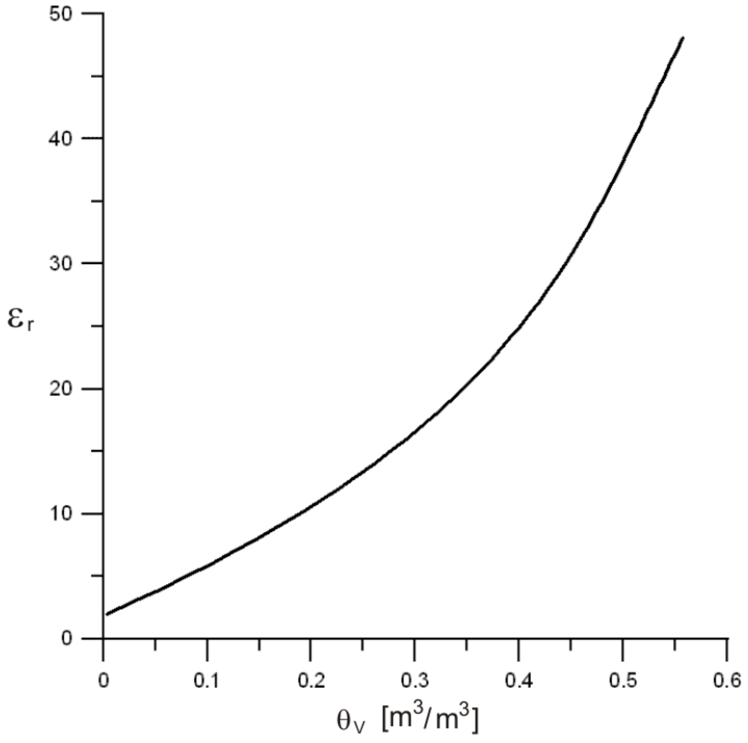

Figure 5.1: Relationship between the relative dielectric coefficient ε_r and the volumetric water content θ_v (calculated from the empirical formula of Topp et al. (1980))

5.1.4 Frequency Dependence of Dielectric Permittivity

At low frequencies the effective complex dielectric permittivity of a soil is very high (see Fig. 5.3). The cause of this high values is usually attributed to two mechanisms - polarization and relaxation effects associated with ionic clusters around soil solids especially clay minerals. The presence of adsorbed water on the surface of soil solids catalyses soil solid-ionic interactions (Maxwell-Wagner effect) (e.g. Hilhorst (1998)). The solid interface is characterised by a double layer with different charge carriers. On application of an electromagnetic field charge separation of positive and negative charges occurs resulting in polarization.

In the GPR frequency range ($10^7 < f < 10^9$) Hz and at conductivities below 10 mS/m the relative dielectric coefficient is approximately independent of frequency (Annan (1996)). At higher frequencies > 10^9 Hz dipolar relaxation of soil water produces dispersive effects. The empirical Debye equation (Debye (1945)) which describes only a single relaxation phenomenon is usually used to describe the frequency dependence of polarization:

$$\varepsilon_{\text{eff}}(f) = \underbrace{\varepsilon_{\text{eff},\infty} + \frac{\varepsilon_{\text{eff},0} - \varepsilon_{\text{eff},\infty}}{1 + \left(i\frac{f}{f_0}\right)}}_{\text{relaxation term}} - \frac{i\sigma_{\text{dc}}}{2\pi f \varepsilon_0} \tag{5.19}$$

where

$\varepsilon_{\text{eff},0}$ = static permittivity i.e. the permittivity value at zero frequency.
$\varepsilon_{\text{eff},\infty}$ = permittivity at infinite frequency i.e. the permittivity value at a frequency that is so high that polar molecules do not have time to contribute to polarization (see section 5.2).
f = frequency [Hz].
f_0 = relaxation frequency.
σ_{dc} = dc conductivity [S/m]

The imaginary part of the relaxation term (see Eq. 5.19) has its maximum at f_0. It should be mentioned that due to the fact that soil is a porous medium with many other possible components, besides water, the idea of mixing models (e.g. Wang and Schmugge (1980); Hoekstra and Delaney (1974); Dobson et al. (1984); Hallikainen et al. (1984)) which could describe the effective permittivity with more than one relaxation phenomenon would give a better description of dispersion in soils than the Debye model.

5.1.5 Dielectric Permittivity and Soil Salinity

Parkhomenko (1967) describes the relative dielectric coefficient of a solution of a binary electrolyte as

$$\varepsilon_r = \varepsilon_w + 3.79\sqrt{c_i} \tag{5.20}$$

where ε_r, ε_w and c_i [mole/l] are the relative dielectric coefficients of electrolyte and pure water and the ionic concentration of the electrolyte respectively.

At low frequencies below 10 MHz the ionic concentration c_i might have an influence on ε_r (Olhoeft (1987)). There is, however, no significant increase in the relative dielectric coefficient for low concentrations between $1 - 5$ g/l. However, with increasing conductivity there occurs a significant increase in ε_r with salinity (Parkhomenko (1967)). Garrouch and Sharma, 1994 observed that the dielectric permittivity of Ottawa-bentonite pack varied ≈ 80 % from $200 - 20,000$ ppm, however, at low frequencies below 10 MHz. Marquart (2000) describes stark variations in the imaginary part of ε_r with increasing salinity between frequency ranges of 25 MHz and 2 GHz (Fig 5.2). The implications of this in the GPR frequency range are energy dissipation leading to damping and low penetration depth of the GPR signal. A series of experiments on both clean and sorted sand using GPR with 500 and 900 MHz antennas together with electrical techniques by Hagrey and Müller (2000) revealed that the amplitude of the reflection coefficient increased with salinity.

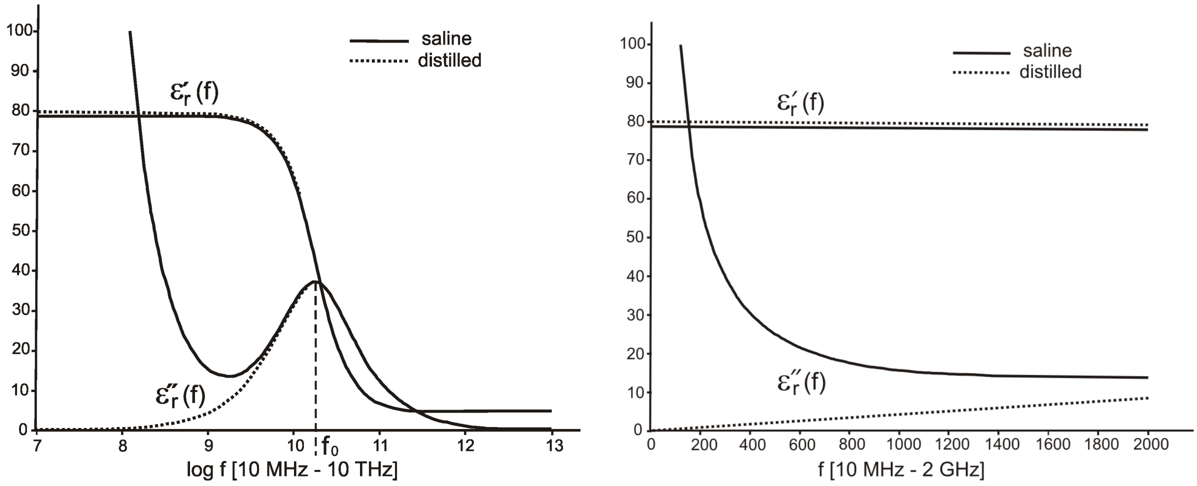

(a) Trend at general frequencies (b) Trend at GPR frequencies

Figure 5.2: Complex dielectric permittivity of saline water with salinity of 4 % and distilled water at 21 ° C (modified after Marquart, 2000)

5.2 Dielectric Polarization of Material

When an alternating electric field is incident on a material bound electric charges in the material are displaced in response to the applied field. Material charges are accelerated and decelerated depending on the sign of the applied field. The mechanical response of the material depends on the frequency f of the applied field. Thus, the applied electric field induces electric dipoles in the material and tries to align them in the direction of the field and at the same time tries also to align the dipoles that are already present in the material. When the resulting electric field within the material balances that of the applied external field the movement of charges comes to a halt. This kind of charge separation is termed polarization. There are of different types: electronic polarization, molecular polarization, orientation polarization and interfacial polarization. (e.g. Powers (1997), Olhoeft (1998)) . If the frequency is very high the mechanical system will not be able to follow the changes. At very high frequencies all polarization mechanisms *cease* or the system fails respond to a field at high frequency. Thus, the relative dielectric coefficient $\varepsilon_r \rightarrow 1$ as $f \rightarrow \infty$. If the applied electric field E is not too strong many substances show that the polarization $\mathbf{P}(\mathbf{r},\omega)$ is directly proportional to the applied field $\mathbf{E}(\mathbf{r},\omega)$ (e.g. Forster and Schwan (1989); Griffiths (1999)) and

$$\mathbf{P}(\mathbf{r},\omega) = \varepsilon_0 \chi_e(\mathbf{r},\omega)\mathbf{E}(\mathbf{r},\omega) \tag{5.21}$$

where χ_e is the electric susceptibility of the medium. It depends on temperature and the microscopic structure of the substance concerned. The attached ε_o, the permittivity of vacuum is to render χ_e dimensionless. The electric susceptibility can be measured as the relative change in capacitance of a capacitor due to the presence of a dielectric material i.e.

$$\chi_e(\mathbf{r},\omega) = \frac{C - C_0}{C} = \varepsilon_r(\mathbf{r},\omega) - 1 \tag{5.22}$$

For a linear dielectric medium which obeys Eq. (5.21),

$$\begin{aligned}
\mathbf{D}(\mathbf{r},\omega) &= \varepsilon_0\mathbf{E}(\mathbf{r},\omega) + \mathbf{P}(\mathbf{r},\omega) && (5.23)\\
&= \varepsilon_0\mathbf{E}(\mathbf{r},\omega) + \varepsilon_0\chi_e(\mathbf{r},\omega)\mathbf{E}(\mathbf{r},\omega) = \varepsilon_0(1+\chi_e(\mathbf{r},\omega))\mathbf{E}(\mathbf{r},\omega) && (5.24)\\
&= \varepsilon(\mathbf{r},\omega)\mathbf{E}(\mathbf{r},\omega) && (5.25)
\end{aligned}$$

where $\varepsilon(\mathbf{r},\omega) = \varepsilon_0(1+\chi_e(\mathbf{r},\omega))$ is the permittivity of the material and the relative dielectric coefficient is expresses as

$$\varepsilon_r(\mathbf{r},\omega) = \frac{\varepsilon(\mathbf{r},\omega)}{\varepsilon_0} = 1 + \chi_e(\mathbf{r},\omega) \tag{5.26}$$

For a lossy medium it is customary to use the complex susceptibility $\chi_e^*(\mathbf{r},\omega)$

$$\chi_e^*(\mathbf{r},\omega) = \chi_e'(\mathbf{r},\omega) + i\chi_e''(\mathbf{r},\omega) \tag{5.27}$$

5.2.1 Types of Dielectric Polarization

Polarization is influenced by the structure of the material and the kind of density defects in the material. The dielectric polarization of rocks and soils involves the following principal mechanisms discussed by (Parkhomenko (1967); Topp et al. (1980); Dobson et al. (1984); Olhoeft (1984); Schön (1996)):

5.2.1.1 Electronic Polarization χ_e

This is caused by the displacement of the nuclear and the electron cloud of a an atom under the application of an external electric field or as in the case of GPR by an electromagnetic field. This causes one part of the atom to be more positive and the other part more negative than in the normal case. The centre of electronic negative charge then no longer coincide with the positive nuclear charge giving rise to a dipole. The electrons are very light and respond quickly to changes in the field. This art of polarization is the most widely observed type of polarization, being found in all materials, solid, liquid, or gaseous. The periodic time required for electronic polarization to occur is about 10^{-15} s which is below the period of the GPR electromagnetic waves which is about $10^{-6} - 10^{-9}$ s. Hence, over the frequency range of the GPR a dielectric medium does not show any dispersion caused by electronic polarization.

5.2.1.2 Molecular Polarization χ_m

This is the distortion of an entire molecule under the influence of an external electric field resulting in the unequal distribution of electric charges within the molecule. It occurs at a frequency of about 10^{13} Hz which is beyond the normal frequency range of GPR.

5.2.1.3 Ionic Polarization χ_i

This involves the redistribution of ions in the ionic lattice due to the presence of an applied electric or electromagnetic field. In such a case the field causes ions of one sign to be displaced relative to ions of the opposite sign. A coulombic force of attraction and repulsion then exists between ions of opposite and like signs respectively. This interaction depends on the distances of the ions in the lattice, the magnitude of the displacement and thus the polarizability, the ionic radii, density and texture of the rock or soil. It is observed in amorphous materials as well as crystalline materials. Polarization by ionic displacement requires a time of about 10^{-13} – 10^{-12} s. The relative dielectric coefficients of such materials fall within the range $4 - 15$. This gives rise to a resultant dipole moment for the entire body.

5.2.1.4 Orientation Polarization χ_d

This is also called dipole polarization or relaxation polarization. It occurs in materials having naturally charged dipole molecules which can rotate freely such as water. The applied electric or electromagnetic field tends to realign these permanent dipoles (without distorting their shape) to some extent in its direction and thereby induces a polarization in the material. In the presence of the driving force the system attains an equilibrium state with a net dipole moment. If the driving force were to disappear suddenly the dipole moment or polarization would decrease till the ensemble of dipoles attain a new equilibrium state (with random distribution of dipoles). This is done within some characteristic *relaxation time* τ. Thus, the system does not undergo any resonance phenomena. Instead, it is characterised by a relaxation time. As the movement of molecules in solids is restricted orientation polarization is more often observed in liquids and gases. Materials exhibiting this type of polarization have high values of dielectric permittivity. The excitation and relaxation time of orientation polarization is about 10^{-9} – 10^{-11} s. Dispersive effects are observed from dielectric permittivity for frequencies of about 10^9 – 10^{11} Hz which is beyond the operational frequency range of GPR used in this work.

5.2.1.5 Interfacial Polarization χ_{in}

This type of polarization is also termed structural or induced polarization. For a material which contain inclusions of a conductor or semiconductor, local variations in electric field properties at interfaces cause non-uniform charge distribution at interfaces when charges move across them under the influence of an external electric or electromagnetic field. This polarization occurs at relatively lower frequencies ($< 10^5$ Hz) than the GPR operational frequency range (of order 10^8 Hz) used and hence does not influence the observations.

A schematic diagram showing the dependence of relative dielectric coefficient on frequency is shown in Fig. (5.3). It is seen from Fig. (5.3) that the real part of the relative dielectric coefficient ε_r' is approximately constant and independent of frequency within the frequency range of the GPR. This means that, approximately, the propagation velocity of GPR waves which is pivotal in soil water content determinations is not influenced by the dispersive effects of the applied electromagnetic field.

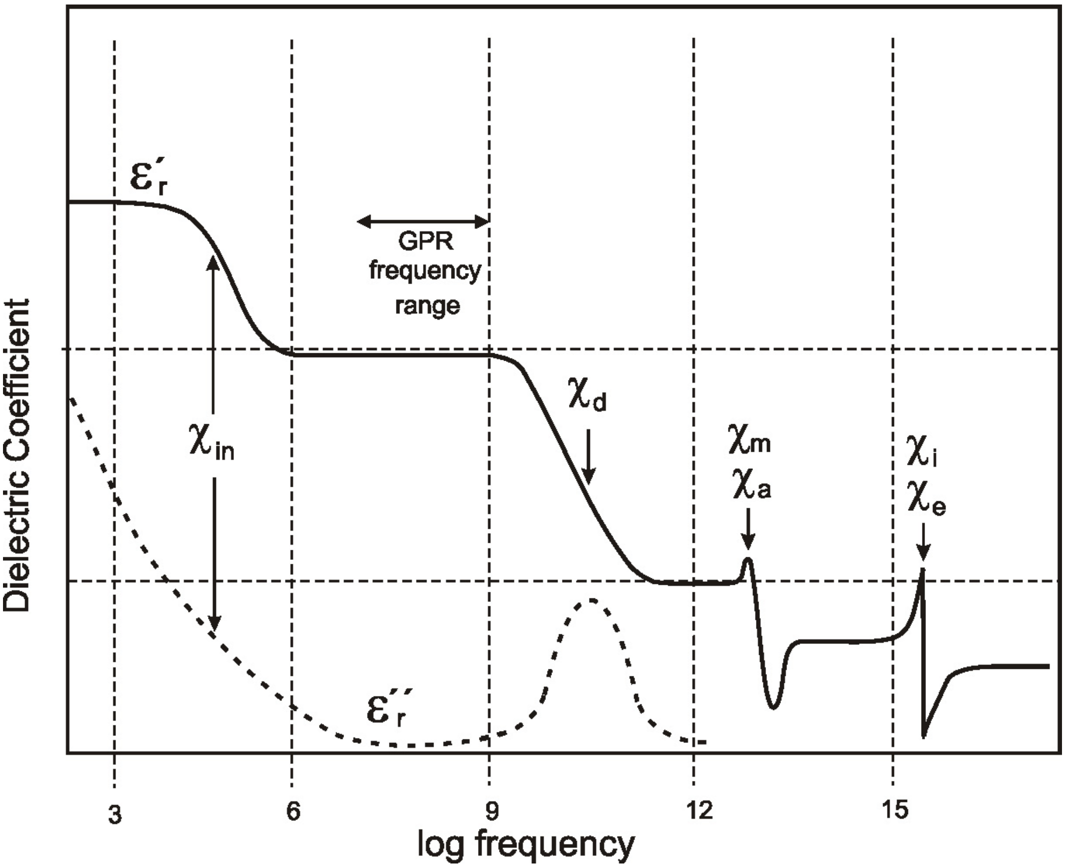

Figure 5.3: Schematic diagram showing the contribution of the different polarization mechanisms [interfacial (χ_{in}), orientation (χ_d), ionic (χ_i), electronic (χ_e), atomic (χ_a), and molecular (χ_m) polarization respectively] to the frequency dependence of relative dielectric coefficient. (Modified after Parkhomenko (1967), and King et al. (1981)).

Chapter 6

The GPR Ground Wave

Introduction

In this chapter I discuss reflection and refraction of homogeneous and inhomogeneous plane waves in a two-layer medium with different optical properties and the condition for inter-transformations between these two. The ground wave is a homogeneous wave transformed from an inhomogeneous wave. The nature of the ground wave, its mode of propagation and the factors that influence its amplitude, velocity and exploration depth are further discussed. This discussion is aimed at introducing the reader to the use of the ground wave in determining VWC. The field work of this application is discussed, however, in chapter 8.

The use of the ground wave in estimating the VWC of the soil as compared with the other methods involving the reflected and refracted phases has the following advantages:

- The VWC of the soil can be determined by the use of the ground wave even in the absence of a reflecting medium in the subsurface.
- The ground wave propagates directly from the transmitter to the receiver and the travel path is relatively easier to predict along the survey profile than the other electromagnetic phases.
- Though the wave is attenuated like the other phases for example in the presence of highly clayey conductive medium, its velocity is hardly affected by inhomogeneities within the near surface especially where these have dimensions less than the wavelength of the ground wave.

6.1 The Electromagnetic Field of a Unit Electric Dipole

Fig. 6.1 shows an assumed dipole in the x-direction and situated at the origin of a coordinate system in infinite space. The electrical and magnetic field of this dipole in two coordinate systems (cartesian and cylindrical) at a point $P(x, y, z) = P(\rho, \varphi, z)$ are described here.

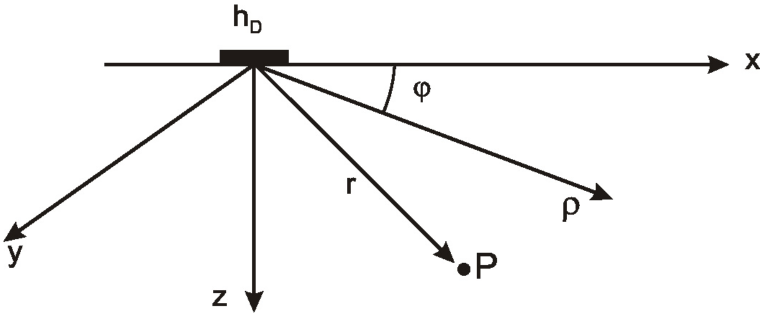

Figure 6.1: Radiation from a unit horizontal dipole h$_\mathrm{D}$ placed at the origin of coordinates (0,0) in an infinite space.

The vector potential **A** and the scalar potential Θ in the Lorentz gauge are defined by (King et al. (1992)):

$$\begin{aligned} \nabla \times \mathbf{A} &= \mathbf{B} && (6.1) \\ -\nabla\Theta &= \mathbf{E} - i\omega\mathbf{A} && (6.2) \\ \nabla \cdot \mathbf{A} &= \frac{ik^2\Theta}{\omega} && (6.3) \end{aligned}$$

The vector dipole satisfies the second-order equation:

$$\nabla^2\mathbf{A} + k^2\mathbf{A} = -\mu\mathbf{j} \tag{6.4}$$

An x-directed unit infinitesimal electric dipole placed at the origin of coordinates in an infinite medium (Fig. 6.1) is defined by

$$\mathbf{j} = \hat{\mathbf{x}}\delta^3(\mathbf{r}) \tag{6.5}$$

where $\delta^3(\mathbf{r})$ represents the 3D delta function. Eqs. (6.4) and (6.5) give

$$\mathbf{A} = \mu\hat{\mathbf{x}}\frac{e^{ikr}}{4\pi r}Idl \tag{6.6}$$

where $r = \left(x^2 + y^2 + z^2\right)^{\frac{1}{2}}$ and I is the current flowing through a current element of length dl. Eqs. (6.1), (6.2) and (6.3) give

$$\mathbf{E} = -\nabla\Theta + i\omega\mathbf{A} = \frac{i\omega}{k^2}(\nabla\nabla \cdot \mathbf{A} + k^2\mathbf{A}) \tag{6.7}$$

In Cartesian coordinates the **B** and **E** components are, according to Eqs. 6.1 and 6.7, omitting the common source factor $1dl = 1\ \mathrm{m}^2$,

$$B_x = 0 \tag{6.8}$$

$$B_y = \frac{\partial A_x}{\partial z} = \frac{z}{r}\frac{\partial A_x}{\partial r} = \frac{\mu_0}{4\pi}\frac{z}{r}\left(\frac{ik}{r} - \frac{1}{r^2}\right)e^{ikr} \tag{6.9}$$

$$B_z = -\frac{\partial A_x}{\partial y} = -\frac{y}{r}\frac{\partial A_x}{\partial r} = -\frac{\mu_0}{4\pi}\frac{y}{r}\left(\frac{ik}{r} - \frac{1}{r^2}\right)e^{ikr} \tag{6.10}$$

$$E_x = \frac{i\omega}{k^2}\left(\frac{\partial B_z}{\partial y} - \frac{\partial B_y}{\partial z}\right) \tag{6.11}$$

$$= \frac{i\omega\mu_0}{4\pi k^2}\left[\frac{k^2}{r} + \frac{ik}{r^2} - \frac{1}{r^3} - \frac{x^2}{r^2}\left(\frac{k^2}{r} + \frac{3ik}{r^2} - \frac{3}{r^3}\right)\right]e^{ikr} \tag{6.12}$$

$$E_y = -\frac{i\omega}{k^2}\frac{\partial B_z}{\partial x} = -\frac{i\omega\mu_0}{4\pi k^2}\frac{xy}{r^2}\left(\frac{k^2}{r} + \frac{3ik}{r^2} - \frac{3}{r^3}\right)e^{ikr} \tag{6.13}$$

$$E_z = \frac{i\omega}{k^2}\frac{\partial B_y}{\partial x} = -\frac{i\omega\mu_0}{4\pi k^2}\frac{xz}{r^2}\left(\frac{k^2}{r} + \frac{3ik}{r^2} - \frac{3}{r^3}\right)e^{ikr} \tag{6.14}$$

By restricting to the far field we neglect the terms $\frac{1}{r^2}$ and $\frac{1}{r^3}$.

In cylindrical coordinates (ρ, φ, z),

$$\rho = (x^2 + y^2)^{\frac{1}{2}}; \quad \varphi = \tan^{-1}\left(\frac{y}{x}\right) \tag{6.15}$$

$$\cos\varphi = \frac{x}{\rho}; \quad \sin\varphi = \frac{y}{\rho} \tag{6.16}$$

$$E_\rho = E_x\cos\varphi + E_y\sin\varphi \tag{6.17}$$

$$E_\varphi = -E_x\sin\varphi + E_y\cos\varphi \tag{6.18}$$

Hence, for the x-directed electric dipole we have

$$E_\rho = -\frac{i\omega\mu_0}{4\pi k^2}\left[\frac{2ik}{r^2} - \frac{2}{r^3} - \frac{z^2}{r^2}\left(\frac{k^2}{r} + \frac{3ik}{r^2} - \frac{3}{r^3}\right)\right]e^{ikr}\cos\varphi \tag{6.19}$$

$$E_\varphi = -\frac{i\omega\mu_0}{4\pi k^2}\left(\frac{k^2}{r} + \frac{ik}{r^2} - \frac{1}{r^3}\right)e^{ikr}\sin\varphi \tag{6.20}$$

$$E_z = -\frac{i\omega\mu_0}{4\pi k^2}\frac{\rho z}{r^2}\left(\frac{k^2}{r} + \frac{3ik}{r^2} - \frac{3}{r^3}\right)e^{ikr}\cos\varphi \tag{6.21}$$

$$B_\rho = \frac{\mu_0}{4\pi}\frac{z}{r}\left(\frac{ik}{r} - \frac{1}{r^2}\right)e^{ikr}\sin\varphi \tag{6.22}$$

$$B_\varphi = \frac{\mu_0}{4\pi}\frac{z}{r}\left(\frac{ik}{r} - \frac{1}{r^2}\right)e^{ikr}\cos\varphi \tag{6.23}$$

$$B_z = -\frac{\mu_0}{4\pi}\frac{\rho}{r}\left(\frac{ik}{r} - \frac{1}{r^2}\right)e^{ikr}\sin\varphi \tag{6.24}$$

$$\tag{6.25}$$

6.2 Reflection and Refraction of Electromagnetic Waves at an Interface

We consider here a plane wave $\mathbf{E}(r,t) = \mathbf{E}_0 e^{-i(\omega t - \mathbf{k}\cdot\mathbf{r})}$ incident on a planar interface $z = 0$ in the $x - z$ plane (Fig. 6.2). A part of the energy is reflected as $\mathbf{E}_r$ at the interface while another part is transmitted as $\mathbf{E}_t$. The two media propagated by the wave are assumed to be non-magnetic (i.e. $\mu_1 = \mu_2 = \mu_0$). The tangential components of $\mathbf{E}$ and $\mathbf{H}$ as well as the normal components of $\mathbf{B}$ and $\mathbf{D}$ are assumed continuous. Thus, for the tangential components of $\mathbf{E}$

$$\mathbf{E}_{\|} = \mathbf{E}_r\| + \mathbf{E}_t\| \tag{6.26}$$

where $\mathbf{E}_{\|}$, $\mathbf{E}_r\|$ and $\mathbf{E}_t\|$ are the incident, reflected and refracted tangential components respectively. This means that the wave's frequency ω remains unaltered after reflection and refraction from the interface. Hence,

$$\omega_i = \omega_r = \omega_t \tag{6.27}$$

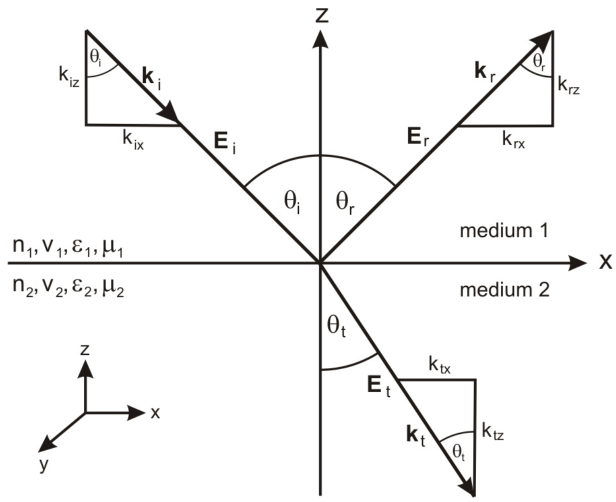

Figure 6.2: Schematic diagram showing the transmission and reflection of a wave at an interface ($v_1 > v_2$, $\varepsilon_1 < \varepsilon_2$, $\mu_1 = \mu_2$).

6.2.1 Snell's Law

For a plane wave propagating with a constant phase velocity across the interface $z = 0$, Eq. (6.27) gives

$$\mathbf{k}_i \cdot \hat{\mathbf{x}} = \mathbf{k}_r \cdot \hat{\mathbf{x}} = \mathbf{k}_t \cdot \hat{\mathbf{x}} \tag{6.28}$$

where $\hat{\mathbf{x}}$ is a unit vector in the $x-$direction. From Snell's laws, at the point of incidence, the incident wave, the reflected wave and the transmitted wave all lie in the same plane (Fig. 6.2).

This implies

$$k_{ix} = k_{rx} = k_{tx} \tag{6.29}$$

$$k_{ry} = k_{ty} = 0 \tag{6.30}$$

and

$$\begin{aligned} k_{ix} &= k_i \sin\theta_i \\ k_{rx} &= k_r \sin\theta_r \\ k_{tx} &= k_t \sin\theta_t \end{aligned} \tag{6.31}$$

Hence, Eq. (6.28) with (6.31) can be written as

$$k \sin\theta_i = k \sin\theta_r = k \sin\theta_t \tag{6.32}$$

where $k = |\mathbf{k}|$. With $\theta_i = \theta_r$, $k = \omega/v$ and $v = c/\sqrt{\varepsilon_r}$, Eq. (6.32) gives

$$\frac{\sin\theta_i}{\sin\theta_t} = \frac{\sqrt{\varepsilon_2}}{\sqrt{\varepsilon_1}} = \frac{v_1}{v_2} = \frac{n_2}{n_1} = {}_2n_1 \tag{6.33}$$

where n_1 and n_2 are the refractive indices of medium 1 and medium 2 respectively and ${}_2n_1$ is the refractive index of medium 2 with respect to medium 1 (Fig. 6.2).

6.2.2 Fresnel's Equations

The fraction of the incident energy reflected from the interface is given by the reflection coefficient R, and the fraction transmitted by the transmission coefficient T. The Fresnel equations, which are based on the assumption that the two media propagated by the wave are non-magnetic, can be used to calculate the parallel $\|$ and perpendicular $\perp$ components of R and T (e.g. Schröder and Treiber (2002)):

$$R_{\|} = \frac{n_2 \cos(\theta_i) - n_1 \cos(\theta_t)}{n_2 \cos(\theta_i) + n_1 \cos(\theta_t)} \tag{6.34}$$

$$R_{\perp} = \frac{n_1 \cos(\theta_i) - n_2 \cos(\theta_t)}{n_1 \cos(\theta_i) + n_2 \cos(\theta_t)} \tag{6.35}$$

$$T_{\|} = \frac{2n_1 \cos(\theta_i)}{n_2 \cos(\theta_i) + n_1 \cos(\theta_t)} \tag{6.36}$$

$$T_{\perp} = \frac{2n_1 \cos(\theta_i)}{n_1 \cos(\theta_i) + n_2 \cos(\theta_t)} \tag{6.37}$$

For the unpolarized wave

$$R = \frac{R_{\|} + R_{\perp}}{2} \tag{6.38}$$

For an angle of incidence perpendicular to the interface (i.e. $z = 0$), $\theta_i = 0$ and $\cos\theta_i = \cos\theta_t = 1$ the interface becomes undefined and $R = R_{\|} = R_{\perp}$.

6.3 Homogeneous and Inhomogeneous Waves

Spherical waves are generated from a dipole antenna source. In the far field of the dipole antenna these waves may be considered as homogeneous plane waves when we assume it to be source-free. When these waves are incident at an interface between two contrasting media with an angle of incidence greater than the critical angle necessary for total internal reflection between the two media, complex refracted waves that are exponentially attenuated with distance from the source are generated. These waves that are described taking into consideration the source field are *inhomogeneous plane waves*. They propagate in one direction with a wave vector **k** while its amplitude falls off in one of the perpendicular directions (Brekhovskikh (1980)).

6.3.1 Generation of Inhomogeneous Waves from Homogeneous Waves

A homogeneous wave is a free wave propagating into a 3D space with real wave vector **k** and an inhomogeneous wave is a boundary surface wave with a complex wave vector. The refracted wave for a homogeneous plane wave travelling from a more dense (n_1) to less dense medium (n_2) with $n_1 > n_2$, travels away from the normal at ordinary angles of incidence to the interface. Now, if the angle of incidence is gradually increased to a critical incidence $\theta_i = \theta_c$, the refracted wave travels along the interface at $\theta_t = 90°$ with

$$\frac{\sin\theta_c}{\sin\theta_t} = \frac{\sin\theta_c}{1} = \frac{n_2}{n_1} = {}_2n_1 \quad \Rightarrow \quad \theta_c = \sin^{-1}\, {}_2n_1 \tag{6.39}$$

If the angle of incidence θ_i is further increased, then generally,

$$\sin\theta_t = \frac{n_1}{n_2}\sin\theta_i = \frac{\sin\theta_i}{{}_2n_1} = \frac{\sin\theta_i}{\sin\theta_c} \tag{6.40}$$

It follows from Eq. (6.40) that with $n_1 > n_2$, if $\sin\theta_i > \sin\theta_c = {}_2n_1$, then $\sin\theta_t > 1$. This means that θ_t is complex and the refracted wave is inhomogeneous, i.e. it has a complex wave number. Such a case occurs and it is made use of in refraction seismic (Fig. 6.3(a)).

Now from Eq. (6.40), if this time $n_1 < n_2$ i.e. for a wave travelling from an optically faster medium with velocity c to a slower medium velocity with v_1, then, $\sin\theta_t < 1$ (see Fig. 6.3(b)). For inhomogeneous plane waves due to the complex angles of incidence refraction angles of $\theta_t > \theta_c$ are possible. In addition if $\sin\theta_i < {}_2n_1$, then it follows that $\sin\theta_t < 1$ and the refracted wave is homogeneous. This case occurs in GPR where the ground wave is transformed from an inhomogeneous wave (Fig. 6.3(b)).

Now, if we consider a homogeneous wave

$$\mathbf{E} = \mathbf{E}_0 e^{-i(\omega t - \mathbf{k}\cdot\mathbf{r})} \tag{6.41}$$

in a lossless medium, the wave vector **k** is real and its components along the coordinate axes k_x, k_y and k_z are related by

$$k^2 = {k_x}^2 + {k_y}^2 + {k_z}^2 \tag{6.42}$$

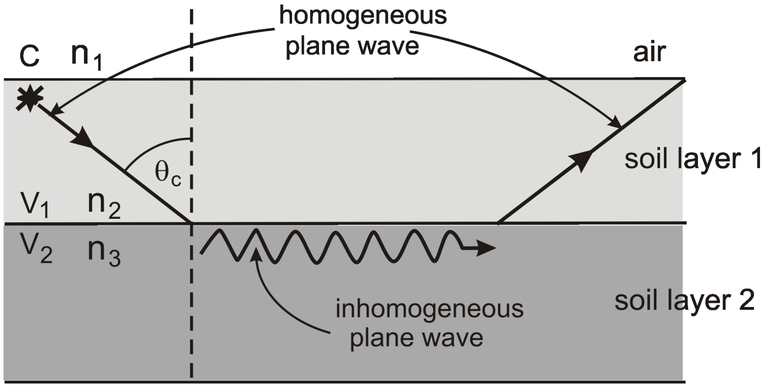

(a) case of seismic refraction ($c < v_1 < v_2$, $n_1 < n_2 < n_3$)

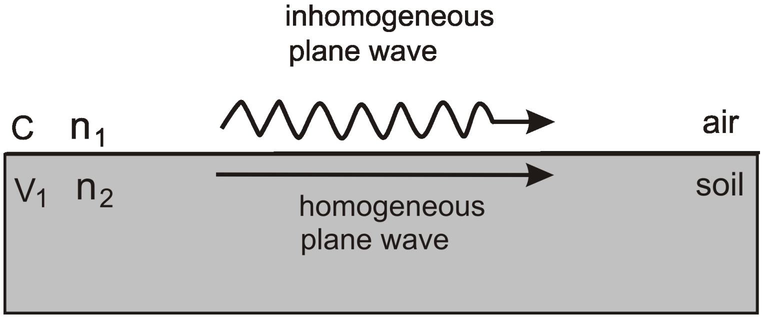

(b) case of GPR refraction ($c > v_1$, $n_1 < n_2$)

Figure 6.3: Transformation of inhomogeneous and homogeneous waves

An inhomogeneous plane wave has a complex wave number $\mathbf{k} = \mathbf{k}' + i\mathbf{k}''$ i.e.

$$\begin{aligned} k_x &= k'_x + ik''_x \\ k_y &= k'_y + ik''_y \\ k_z &= k'_z + ik''_z \end{aligned} \tag{6.43}$$

Substituting Eqs. (6.43) into (6.41) gives the corresponding inhomogeneous plane wave as

$$\mathbf{E} = \mathbf{E}_0 \underbrace{e^{-i(\omega t - k'_x x - k'_y y - k'_z z})}_{\phi} \underbrace{e^{-(k''_x x + k''_y y + k''_z z})}_{A} \tag{6.44}$$

Eq. (6.44) describes an attenuated wave whose planes of equal phase $\phi = c_1$ do not coincide with its planes of equal amplitude $A = c_2$. These planes are described by

$$k'_x x + k'_y y + k'_z z = c_1 \tag{6.45}$$

$$k''_x x + k''_y y + k''_z z = c_2 \tag{6.46}$$

In a lossless medium $k^2 = \varepsilon\mu\omega^2$ (from Eq. (4.28)). This implies that

$$\mathrm{Im}(k^2) = 0 \tag{6.47}$$

Substituting Eqs. (6.43) into (6.42) gives

$$k_x'^2 - k_x''^2 + k_y'^2 - k_y''^2 + k_z'^2 - k_z''^2 = \mathrm{Re}(k^2) = \varepsilon\mu\omega^2 \tag{6.48}$$

$$2(k_x'k_x'' + k_y'k_y'' + k_z'k_z'') = \mathrm{Im}(k^2) = 0 \tag{6.49}$$

$$\Rightarrow \quad \mathbf{k}' \cdot \mathbf{k}'' = 0, \quad \text{i.e.} \quad \mathbf{k}' \perp \mathbf{k}'' \tag{6.50}$$

Eqs. (6.47) and (6.49) imply that planes of constant phase are perpendicular to planes of constant amplitude. Thus, as the wave propagates in the direction $\mathbf{k}'(k_x', k_y', k_z')$ its amplitude decays in a direction perpendicular to $\mathbf{k}'(k_x', k_y', k_z')$ i.e. $\mathbf{k}''(k_x'', k_y'', k_z'')$ (Brekhovskikh (1980)). If the medium is lossy the planes of constant phase and amplitude are no longer perpendicular to each other because then

$$\mathrm{Im}(k^2) = \sigma\omega\mu \neq 0 \tag{6.51}$$

$$\mathbf{k}' \cdot \mathbf{k}'' = \sigma\omega\mu \neq 0 \tag{6.52}$$

and the wave is damped also in the direction of propagation.

6.4 The GPR Ground Wave

For a homogeneous wave travelling from a less to a more dense medium, the largest angle of refraction $\theta_t = \theta_c$ with $\sin\theta_c < 1$ (Fig. 6.4). The wave travels from an optically faster medium

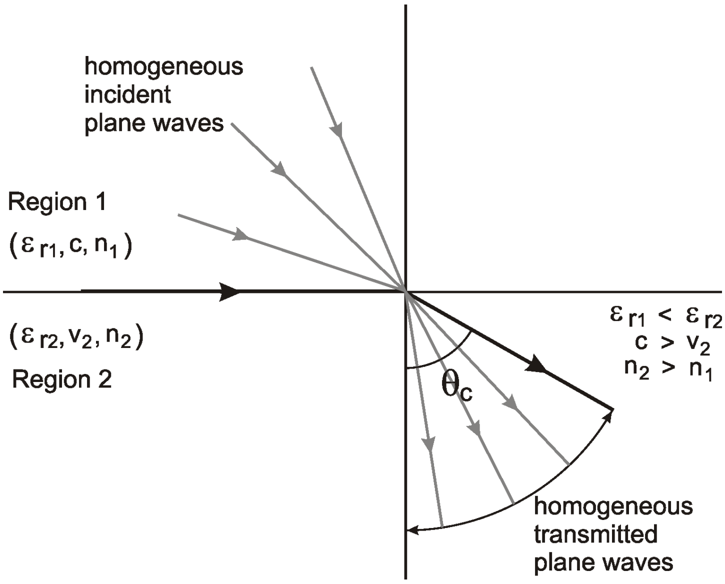

Figure 6.4: Refraction of electromagnetic waves at an interface: Homogeneous waves in region 1 are transmitted into the range $\theta_t < \theta_c$ in region 2 (modified after Sperl, 1999).

(air) to a slower medium (soil) of relative permittivities ε_{r1} and ε_{r2}, refractive indices n_1 and n_2 and velocities c and v_2 respectively.

For an inhomogeneous wave due to the complex angles of incidence, angles of refraction $\theta_t > \theta_c$ with $\sin\theta_t > 1$ occur as seen in section 6.3.1 do occur (Fig. 6.5). One of such waves (propagating with $\theta_t > \theta_c$) is converted into a homogeneous wave with the velocity $c/\sqrt{\varepsilon}$ which travel along the air-ground interface below the ground surface. This is the ground wave in GPR terminology. A corresponding inhomogeneous air wave propagating in the air side along the air-ground interface is generated by the ground wave. This wave propagates with the same velocity as the ground wave. It is the ground wave analogue that is recorded by the GPR receiver placed above the ground surface. This wave is the *apparent ground wave*. It is highly attenuated with distance away from the interface.

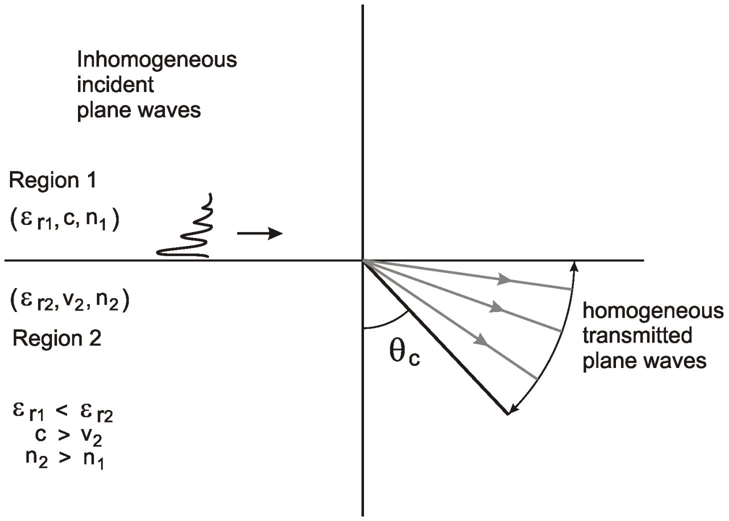

Figure 6.5: Refraction of electromagnetic waves at an interface: Inhomogeneous waves from region 1 are transmitted as homogeneous waves into the range $\theta_c < \theta_t < 90°$ in region 2 (modified after Sperl, 1999).

The receiving antenna must hence be well coupled to the ground surface in order to record it effectively (Fig. 6.6).

The GPR antenna is considered as a horizontal Hertzian dipole which radiates spherical waves. The various electromagnetic phases radiated by the antenna are illustrated in Fig. (6.6). The spherical waves can be decomposed in a series of homogeneous and inhomogeneous plane waves (Du (1996)) which can be described as shown before.

A GPR source radiates different phases A,B,C and D. In air A and C are recorded and in the ground B and D. The receiving antenna is not able to record B directly but rather C, a highly attenuated inhomogeneous wave with same propagation velocity as B. C propagates along the air-ground interface. The receiving antenna must be very close to the ground to record C effectively. On a radargram the travel times of the air wave and ground wave picks appear as straight

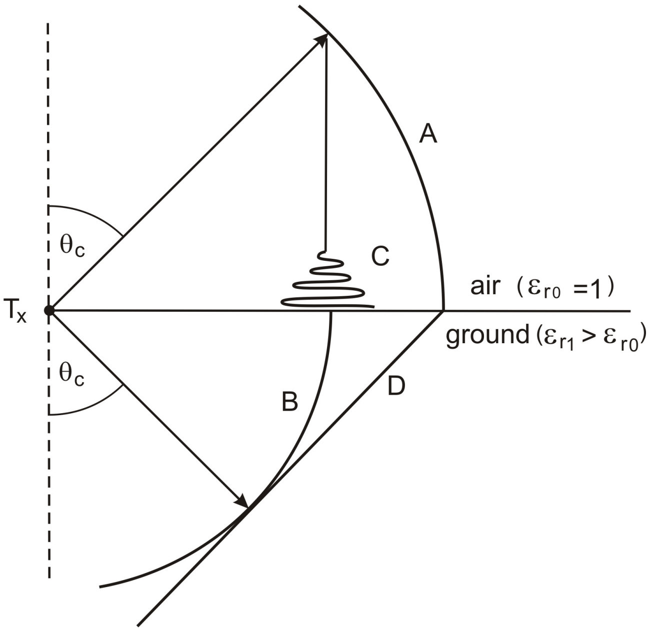

Figure 6.6: Schematic diagram illustrating the various electromagnetic phases radiated by the GPR antenna. A is the air-wave, B = ground wave, C = apparent ground wave and D is the head wave (modified after Annan, 1973).

lines and the propagation velocities are calculated from the inverse of their slopes. The various electromagnetic wave types radiated by the GPR antenna are shown schematically in Fig. 6.7.

6.4.1 Propagation of the Ground Wave

Based principally on the previous works done by Brekhovskikh (1960), Annan (1973) and Du (1996), the mathematical expression of the apparent ground wave radiated from a horizontal electric dipole (HED) is:

$$E_y = \frac{i\omega\mu_0 Idl}{2\pi(k_1^2 - k_0^2)}\frac{1}{\rho^2}(k_0 e^{ik_0\rho} - k_1 e^{ik_1\rho}) \tag{6.53}$$

where I is the current in a current element of length dl, ρ is the antenna separation and k_0 and k_1 are the complex wave numbers in air and ground respectively. The y-component of the electric field in Eq. (6.53) is normal to the air-ground interface (Fig. 6.1). The amplitude decay of the apparent ground wave with height h above the air-ground interface is given by (Du (1996)):

$$E_y(h) = E_y(0)e^{-(k_0\sqrt{\varepsilon_r - 1})h} \tag{6.54}$$

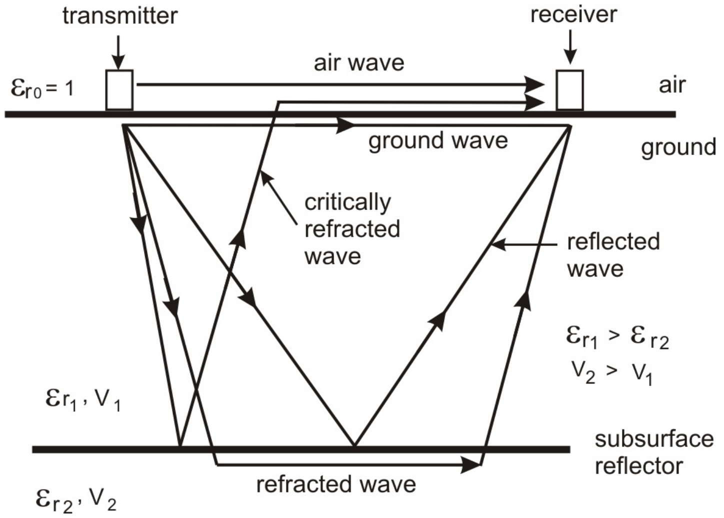

(a) Travel paths of the various GPR wave types.

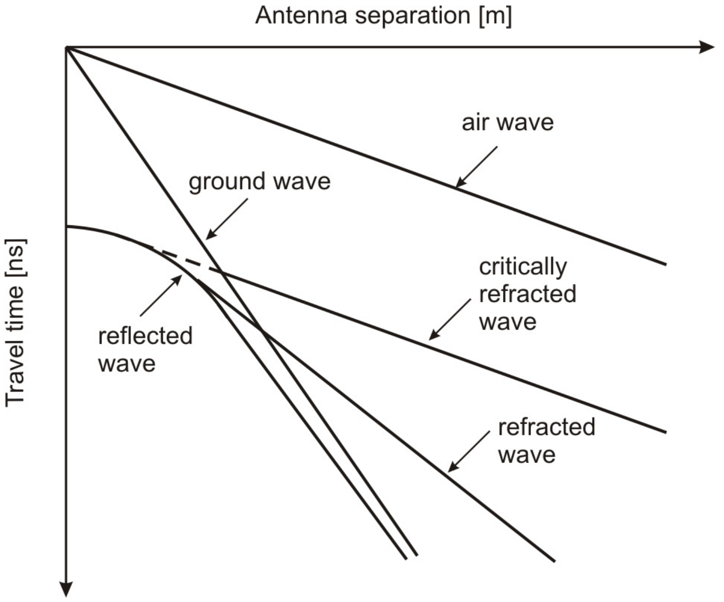

(b) Travel time diagram of the various electromagnetic phases in a layered medium

Figure 6.7: Schematic illustration of the various phases radiated by a GPR antenna.

6.4.2 Depth of Influence of the Ground Wave

The depth of influence, z, of the ground wave, i.e. the thickness of the zone between the surface of the ground and the maximum penetration depth of the ground wave, is not distinctly defined and authors present different formulae to quantify it. This depth is expressed as a function of wavelength of the GPR signal and it is dependent on the VWC of the soil (Berktold et al. (1998);

Du and Rummel (1996); Grote et al. (2003); Galagedara et al. (2004)).

Du (1996), considered a two-layer soil model with a much thicker lower layer and observed that under the application of a moderately high central frequency of 225 MHz that the ground wave propagation velocity was effectively influenced by dielectric coefficient of the thicker lower layer. In addition to further observations from laboratory experiments carried out on a two layer model comprising of a water layer of varying thickness over a lower concrete layer Du (1996) suggested this depth range to be $\approx (0.5 - 1.0)\lambda_s$ confirming in a way a proposition previously made by Brewster and Annan (1994) that this depth is about $1.0\lambda_s$ where $\lambda_s = c/(f\sqrt{\varepsilon_r})$ is the wavelength and f the central frequency of the wave propagating through the soil. This would mean that for $\varepsilon_r = 6$, the depth of influence would be $\approx 0.122 - 0.245$ m and $\approx 0.068 - 0.136$ m for 500 MHz and 900 MHz antennas respectively.

Sperl, 1999 after a series of modelling exercises over a two-layer model using 5 different central frequencies between 35 MHz and 660 MHz in a Wide Angle Reflection and Refraction (WARR) measuring mode suggested the empirical formula $d = 0.145\sqrt{\lambda_s}$ for the calculation of the depth of influence. He further observed that the apparent ground wave might travel selectively either with the velocity of the upper or the lower layer depending on the layer thickness for a two-layer model, and not conditionally with the velocity of the lower layer as proposed by Du (1996). Using Sperl's formula and taking $\varepsilon_r = 6$, the depth of influence would be ≈ 0.072 m and ≈ 0.053 m for the 500 MHz and 900 MHz antennas respectively. Grote *et al*, 2003, invoked a formula from Hagedoorn 1954, an approximation also used by van Overmeeren *et al*, 1997 and put this depth to be approximately equal to one-half of the first fresnel zone for seismic waves. For this approximation, the depth of influence $d = 0.5\sqrt{vs/f}$ where v is the velocity of the electromagnetic wave in the soil, s is the separation between the antennas. This approximation gives for the 500 MHz antenna (with $s = 0.16$ m) $d \approx 0.100$ m and $d \approx 0.082$ m for the 900 MHz antenna (with $s = 0.2$ m) for GPR signal propagation velocity $v = 0.122$ m/ns.

The differences in the frequency dependence of the depth of influence as presented by the different authors might be due to the variance in the experimental methods used. Irrespective of this, it should be mentioned that the depth of influence is not yet universally quantified and its approximation will also depend on the experimenter's methodology and experience. May be replacing the term with *depth range of influence* would give it a better physical interpretation than the term *depth of influence*. In chapter 8 p. 113 where soil water content determination in Burkina Faso using the ground wave method is discussed Sperl's empirical relation is evoked to estimate the ground wave exploration depth.

6.4.3 Calculation of the Ground Wave Velocity

Fig. 6.8 shows the schematic travel times of the ground and air waves. The ground wave velocity v_{gw} is calculated from the information of the WARR and CO data (see sections 8.2.2 and 8.2.3).

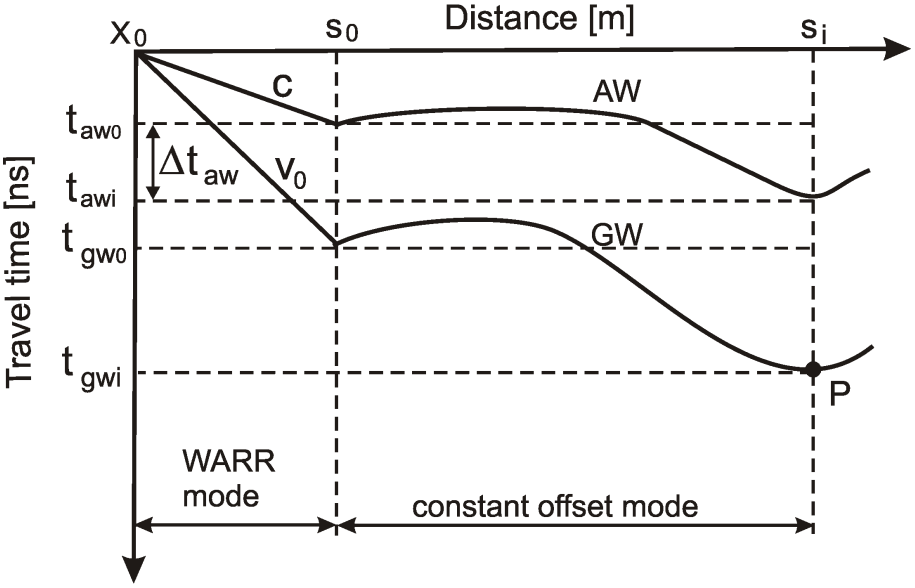

Figure 6.8: Schematic illustration of ground wave velocity calculation.

X_0:	travel time cross point for the air wave (AW) and ground wave (GW).
S_0:	optimal separation of antennas.
t_{aw0}:	time taken by AW to travel the distance S_0.
t_{awi}:	time taken by AW to travel the distance S_i.
t_{gw0}:	time taken by GW to travel the distance S_0.
t_{gwi}:	time taken by GW to travel the distance S_i.
c:	velocity of AW from WARR data.
v_0:	velocity of GW from WARR data.
P:	arbitrary point at distance S_i along survey line.

In a case where the survey line and where the antennas experience no drifting, the ground wave velocity v_{gwi} at point P is given by

$$v_{gwi} = \frac{S_0}{t_{gwi}} \tag{6.55}$$

For an uneven surface, it might be difficult to keep the antenna separation constant at S_0 due to the possibility of drifting. In such a case Wollny (1999) suggests that time fluctuations Δt_{aw} in the air wave travel time resulting from variations in the antenna separation should be subtracted from the ground wave travel time.

Thus,

$$\Delta t_{aw} = t_{awi} - t_{aw0} \tag{6.56}$$

The corrected time t_{gwic} of the ground wave at the point P is

$$t_{gwic} = t_{gwi} - \frac{c}{v_0}\Delta t_{aw} \tag{6.57}$$

where c and v_0 are determined from the WARR data.

The corrected ground wave velocity v_{gwic} at the point P becomes

$$v_{gwic} = \frac{S_0}{t_{gwic}} = \frac{S_0}{t_{gwi} - \frac{c}{v_0}\Delta t_{aw}} \tag{6.58}$$

Chapter 7

Soil Water Content Determination on Dike Models with Guided Wave Sounding (GWS) Method

7.1 Previous Work with Guided Waves

In this section, I discuss the application of guided electromagnetic waves in the determination of soil water content. Guided electromagnetic waves represent waves that are guided by e.g. conductors and/or dielectrics to propagate in a particular direction usually through a limited region around the waveguides in the transverse plane. For electromagnetic waves propagating through the soil a guided wave may be generated when a low velocity medium is sandwiched between two media of relatively higher velocity. This might occur in cases where a wet soil lies on a dry sediment (e.g. Arcone et al. (2003) or with the presence of permafrost at depth beneath unfrozen or wetter sediments (e.g. Arcone et al. (1998)) or when a soil layer underlain by a low porosity bedrock (e.g. Arcone et al. (2003); van der Kruk et al. (2006); Strobbia and G. (2005)). A guided wave may also be generated when a high velocity medium is sandwiched between media of relatively low velocities, especially, in cases where the lower medium is a strong reflector e.g. dry soil lying on top of wet clay or ice on top of water (e.g. Arcone et al. (2003)).

Transmission characteristics along conductors have already been analysed by authors like Sommerfeld (1899, 1948); Harms (1907); Hondros (1909); Goubau (1950) and Piefke (1959). In the present case guided waves propagate along a metal rod placed erect in the soil (see appendix B for mathematical analysis of this). For this case the GPR signal from the transmitting antenna travels through the air and soil and couples to the metal rod. Part of the signal is refracted, scattered, absorbed or reflected to the receiver upon reaching the lower end of the rod. This wave is analysed for information about the material properties of the soil, in particular the dielectric coefficient ε_r. Igel et al. (2001) used this technique to determine the VWC of the soil. Deep seated hydrocarbon accumulations have been successfully detected through guided wave sounding from active electromagnetic sources (e.g. Johansen et al. (2005); Navarkhele and Nakade (2006)). Other applications include the detection of fractures and defects (Olsson et al. (1992); Yeh and Zoughi (1994); Sato and Miwa (2000); Hayashi (2005)); location of underground tunnels (e.g. Deryck (1978), Olhoeft (1993)); interpretation of geologic features (e.g. Nickel et al. (1983); Dubois (1995) and also in soil water investigations. Soil water has usually been investigated through the application of the conventional TDR technique (e.g. Topp et al. (1980); Topp and Annan (1982); Topp and Davis (2005); Ledieu et al. (1986); Roth et al. (1990); Scheuermann et al. (2001); Becker et al. (2002); Becker et al. (2005); Wraith et al. (2006)) or with TDR-based equipment like TAUPE, a French word for mole, (e.g. Königer et al. (2005)) or with the FDR e.g. Simple Soil Moisture Probe - SISOMOP, which have been used by authors like Schlaeger et al. (2005). TAUPE and SISOMOP were developed by the SMG (Soil Moisture Group), Karlsruhe, Germany.

Guided wave sounding (GWS) is an invasive application of the GPR technique in an operational mode similar to that of the conventional TDR. This application was first used by Igel et al. (2001).

7.2 Comparing GWS with TRIME-TDR in Soil Water Content Estimation

7.2.1 Materials and Methods

I carried out experiments with GWS on two different dike models referred to here as dike models A and B:

- **Dike Model A**. This dike model is built in the Theodor-Rehbock Laboratory of the Institute for Water and River Basin Management at the Department of Water Resources Management and Rural Engineering, University of Karlsruhe, Karlsruhe, Germany (Fig. 7.1). I performed controlled flooding experiments here.
- **Dike Model B**. This is a full scale dike model situated at Federal Waterways and Research Institute, Karlsruhe, Germany (Fig. 7.24). I performed controlled precipitation experiments here.

7.2.1.1 Site Description of Dike Model A and Flooding Experiments

I performed these experiments on dike model A from April 23 - May 5, 2007. This is an experimental dike model of dimensions 2.3 m × 8 m × 1.4 m constructed from soil of the textural class loamy sand (USDA, 1975) and commonly called *Waldstadt lehm*. It has a height of 1.4 m with two planes inclined at 1:2.5, a crest of approximate length 2.2 m and a base width of 8.0 m. On the wet plane of the dike is a water basin with adjustable water level. The experimental model is enclosed by external walls inclined at low angles of 2 ° to reduce the bypath of water along the boundary as much as possible. The experiments were performed on the crest of the dike model (Fig. 7.1).

Figure 7.1: Dike model A at the Theodor-Rehbock-Laboratory, Institute for Water and River Basin Management, University of Karlsruhe, Karlsruhe, Germany. Picture shows the operation of the GPR in the GWS mode from the crest of the dike.

Table 7.1 shows the thickness of the various soil layers used in the construction of the dike model.

Soil Layer	Thickness [m]	Depth [m]
1	0.115	0.115
2	0.085	0.200
3	0.120	0.320
4	0.085	0.405
5	0.100	0.505
6	0.200	0.615
7	0.115	0.730
8	0.120	0.850
9	0.110	0.960
10	0.110	1.070
11	0.105	1.175
12	0.110	1.285
13	0.115	1.400

Table 7.1: Construction of the dike model A with soil layers of varying thickness.

It comprised of 13 loamy sand layers of varying layer thickness. The depths indicated represent distances measured from the dike's crest.

7.2.1.2 GWS Experiments with Metal Rod

From the crest of the dike to its base, a borehole of about 45 mm diameter was drilled at the point G (Fig. 7.2) about its central position.

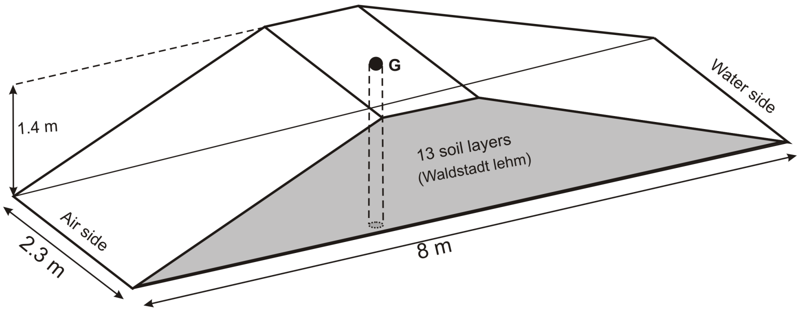

Figure 7.2: Schematic diagram of the dike model A showing sampling point G for GWS and TRIME-TDR measurements. The borehole was sunk at G.

A hollow insulating tube of about 42 mm diameter and 1.3 m length was then inserted through the borehole to the base of the dike. This was an access tube for a metal rod of length 1.4 m and external diameter 38 mm. The lower end of this rod served as a reflector for the transmitted GPR signal.

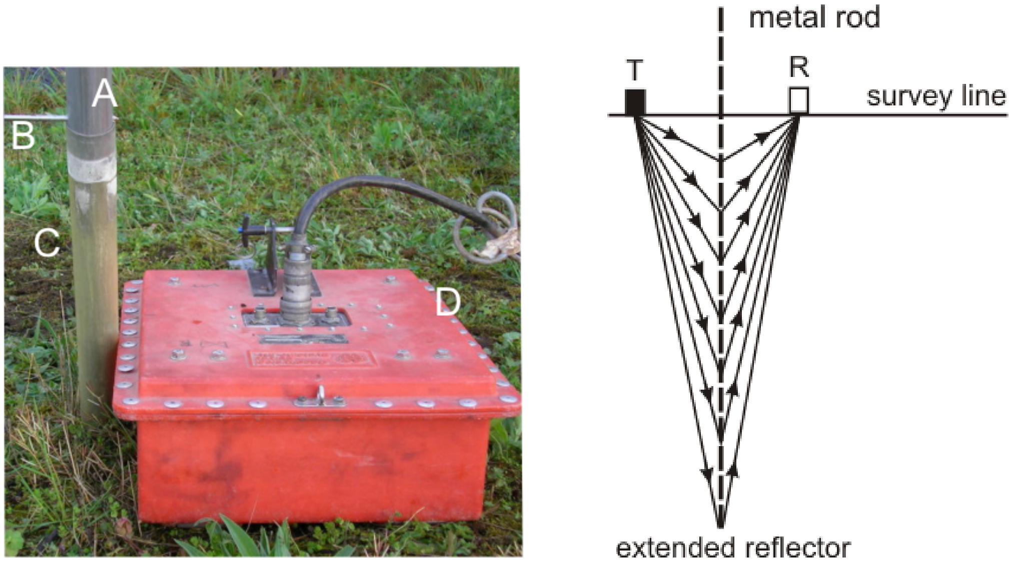

(a) Metal rod with 500 MHz antenna. (b) Reflections from lower ends of rod

Figure 7.3: GWS field procedure with a graduated metal rod (A: metal rod, B:stop, C: access tube for metal rod, D: 500 MHz antenna. Each point of reflection on Fig. 7.3(b) illustrates a position of the lower end of metal rod. T and R are at the same level with metal rod in the middle.

The antennas (500 MHz and 900 MHz) were positioned in turn at about 1 cm close to the borehole with the metal rod located midway between the transmitter and receiver (Fig. 7.3(a)).

This position was maintained throughout experiment I lowered the metal rod graduated at intervals of 2.5 cm down the borehole. The experiment comprised of 6 phases in which the dike was flooded from its waterside with different volumes of water to levels of 0.00 m, 0.30 m, 0.60 m, 0.80 m, 1.00 m and 1.25 m above its base. After each flooding phase the dike was rested 24 hrs, after which time, according to short term measurements by Wörsching et al. (2006) using TDR probes distributed in the dike, I expected it to have approximately attained a hydrostatic equilibrium condition. I then took data with GPR operated in the GWS mode using the 500 MHz and 900 MHz antennas. I also took co-located measurements with the TRIME-TDR for comparison and repeated each experiment for at least two other times. At the water level 1.25 m the flood water was almost at the brink of the dike's crest (Fig. 7.4).

During the operation of the GPR in the GWS mode, guided waves from the transmitter travelled along the metal rod and were reflected back from the lower edge of the metal rod to the receiver due to the impedance contrast between this end of the rod and the medium below in a time *t* (Fig. 7.3(b)).

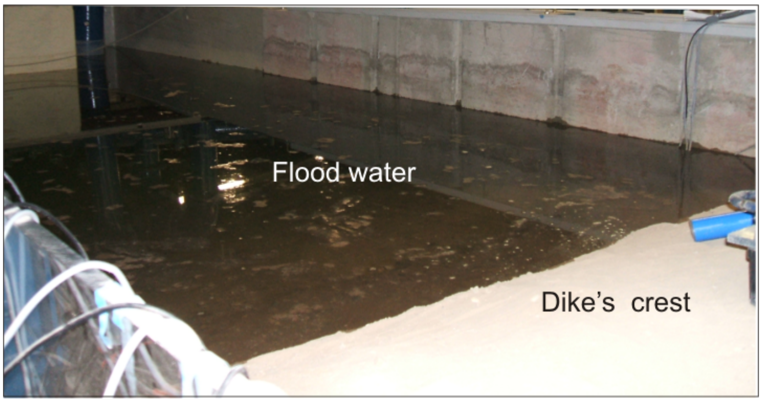

Figure 7.4: Flooding experiment at flood level 1.25 m. At this flood level the dike's crest was almost covered with flood water.

If the corresponding length of rod beneath the surface to this time is d, then, the interval velocity v corresponding to d is given by the relation

$$v = \frac{2d}{t} \tag{7.1}$$

The velocity of the guided wave so calculated was related to the relative permittivity of the soil and eventually the soil water content with the help of Eq. (5.18). Through this process, I determined the soil moisture content distribution in the dike model as a function of depth. I repeated the experiment with the 900 MHz antenna.

7.2.1.3 TRIME-TDR Experiments with TRIME T3 Probe

7.2.1.4 Previous Work with TRIME-TDR

The TRIME-TDR technique has been used by a number of investigators to study soil water content e.g. (Stacheder et al. (1994), Stacheder et al. (1997); Debruyckere et al. (1996); Beldring et al. (1999); Laurent et al. (2001), Laurent et al. (2005); Evett et al. (2002)). The authors Evett et al. (2002) and Laurent et al. (2005) reported of RMS deviations of $(0.1 - 0.7)\ \mathrm{m^3m^{-3}}$ with the TRIME-TDR.

7.2.1.5 TRIME-TDR Measuring Principle

The TRIME-TDR system uses an algorithm that records the arrival times of specific voltage levels (Stacheder et al. (1994, 1997); IMKO (2001)) unlike the conventional analogue which records the entire voltage trace, and determines the two way travel time of the reflected pulse based on the trace shape. The TRIME T3 tube access probe from the manufacturer IMKO (IMKO GmbH, Ettlingen, Germany) which was used for the measurement, is a hand-held battery operated commercial TDR equipment. It comprises of a probe of about 18 cm length fitted with a high frequency cable about 2.5 m long. The probe was inserted vertically at constant increments of 10 cm down the plastic access tube installed vertically on the landside and waterside of the dike at the point G (Fig. 7.2). The device generates a high-frequency pulse (up to 1 GHz) which propagates along the metal shells, generating an electromagnetic field around the probe (Fig. 7.5(b)). The metal shells are used as wave-guides for the transmission of the TDR-signal. At the end of the shells, the pulse is reflected back to its source. By measuring the resulting transit time (3 ps...2 ns) the propagating velocity which is primarily dependent on the water content was determined. The equipment is operated by just pressing a start-button after the probe has been well embedded in the access tube. The VWC which is calculated from the propagation velocity of the signal was readily read from the display panel (IMKO (2000)).

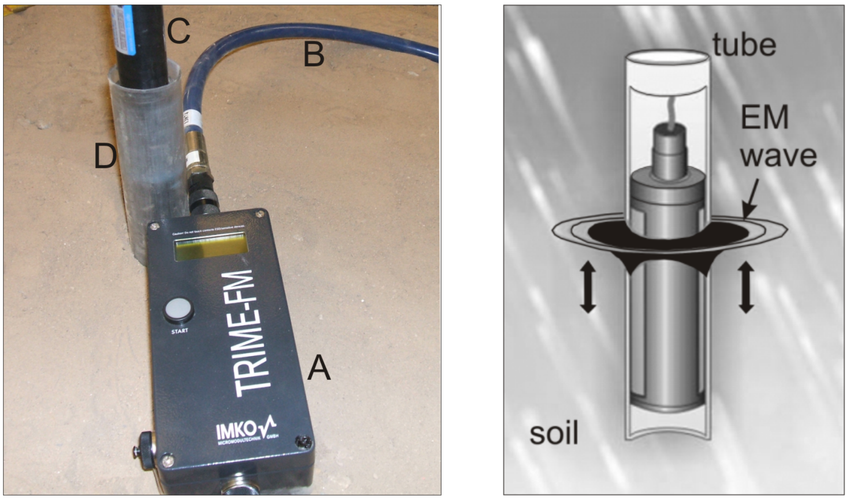

(a) TRIME T3 system

(b) Operational principle

Figure 7.5: Overview of TRIME T3 system and operational principle: TRIME FM (A), coax cable (B), probe (C) and access tube (D) (IMKO (2000)).

7.2.2 Calibration of TRIME T3 Probe, Gravimetric Soil Samples

The TRIME T3 tube access probe uses a standard calibration to determine the VWC. The use of the access tube for the probe in a way serves as a coating for the soil. After the measurements the probe then needed to be calibrated to the material specific properties of the dike material (Fig. 7.6).

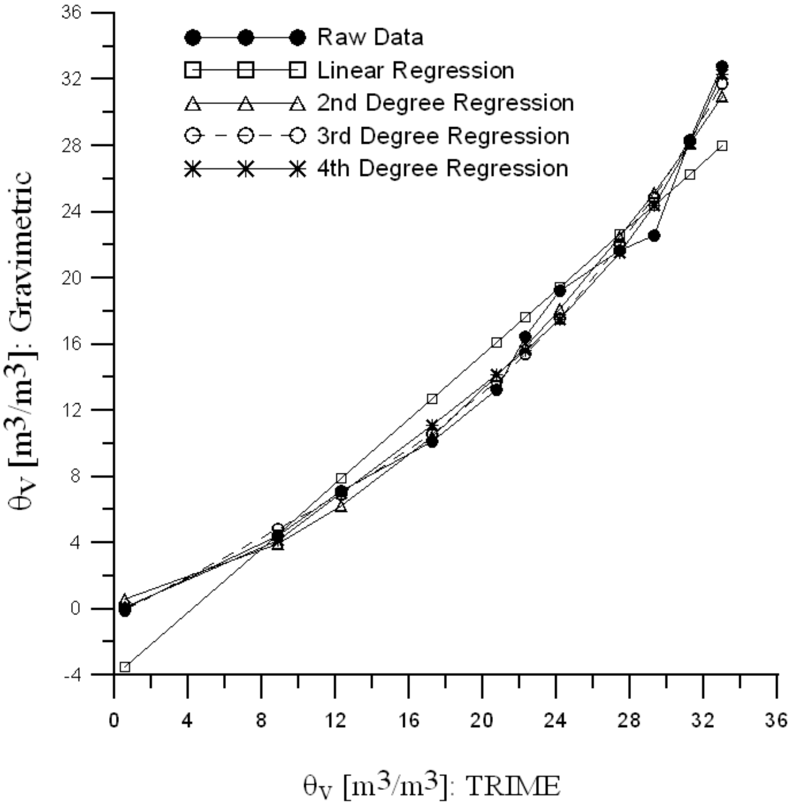

Figure 7.6: Material specific calibration of the TRIME-TDR to the *Waldstadt lehm*. The third degree regression polynomial yielded the best fit to the raw data.

I performed the calibration experiment with the help of the conventional gravimetric method. Water was added in quantities of about 400 g to a volume of the soil sample in a measuring cylinder of known volume. After thoroughly mixing the contents I first determined the VWC with the TRIME T3 probe and then gravimetrically using guidelines described in DIN 18 121. I determined the gravimetric water content θ_g, from the masses of the wet and dry soil samples m_w and m_d respectively as: $\theta_g = (m_w - m_d)/m_d$ and the volumetric water content $\theta_v = \theta_g \rho_s / \rho_w$ where $\rho_w = 1\text{g/cm}^3$ as the density of water. I determined the density of the dry soil, ρ_s from the mass of dry soil that fills a measuring cylinder of known volume. Finally, I fitted the calibration data with the third order polynomial equation:

$$\theta_v = -4.29 \cdot 10^{-1} + 6.47 \cdot 10^{-1}\theta_T - 1.21 \cdot 10^{-2}\theta_T^2 + 6.65 \cdot 10^{-4}\theta_T^3 \tag{7.2}$$

where θ_v and θ_T are the volumetric water contents [%] from the gravimetric and TRIME-TDR measurements respectively.

7.2.3 Data Processing

I processed GWS data with the software package Reflexw (Sandmeier (2007)) Each observation from the end of the metal rod at a given depth comprised of a minimum of 120 traces. A complete survey from the crest to the base of the dike for any flood level comprised of 53 observation points. The 120 traces from each observation point were first stacked into a single trace and stored as a file. Subsequently, all 53 files were merged into a single radargram. I corrected for static errors and performed a *background removal* and *f-k filtering* to make desired reflections from the lower end of the metal rod very distinct.

I loaded zero-crossing distance-time picks from the radargram (indicated by hatched lines in Figs. 7.8 and 7.9) into an ASCII-format and determined interval velocities (over every 0.025 m) and subsequently harmonic velocities (from every 3 interval velocities). Finally, I used Eq. (7.1) to calculate the corresponding relative dielectric permittivities and Eq. (5.18) to eventually determine the VWC. The root mean square deviation (RMSD) of GWS compared to TRIME-TDR was calculated by

$$\mathrm{RMSD} = \sqrt{\frac{1}{n}\sum_{i=1}^{n}[\theta_{i(\text{TRIME-TDR})} - \theta_{i(\text{GWS})}]^2} \tag{7.3}$$

for co-located GWS and TRIME-TDR soil water content values of $\theta_{i(\text{GWS})}$ and $\theta_{i(\text{TRIME-TDR})}$ respectively.

7.2.3.1 Data Processing with and without f-k Filter

Spurious reflections in the signal, contributed in part to reading errors from the equipment components and the surroundings, interfere with reflections from the lower part of the metal rod reducing signal quality and introducing errors in the arrival times of the reflections. In the time-space domain it is relatively difficult to separate true reflections (from the lower end of the metal rod) from noise. Hence, I filtered the data from noise with the help of the Reflexw tool *f-k filter*. The signal acquired by the GPR in the x-direction is a 2D signal in t and x which can be represented as $f(t, x)$. The *f-k filter* performs a 2D Fourier transformation of $f(t, x)$ from the *t-x* (time-space) domain into the *f-k* (frequency-wavenumber) domain (Eqs. 7.4 and 7.5). A 2D Fourier transformation and inverse transformation of the raw data in *t-x* domain $f(t, x)$ can be defined by

$$F(\omega, k_x) = \iint f(t, x)e^{-i(\omega t - k_x x)}\, dtdx \tag{7.4}$$

$$f(t, x) = \frac{1}{(2\pi)^2}\iint F(\omega, k_x x)e^{i(\omega t - k_x x)}\, d\omega dk_x \tag{7.5}$$

If v_a is the apparent velocity of the wave travelling in the $x-$direction then, the wave number k_x and angular frequency ω are related by

$$\omega = v_a k_x \tag{7.6}$$

A line of constant apparent velocity in the *t-x* domain transforms to a line of constant slope in the *f-k* domain. A dipping line in the *t-x* domain thus transforms into a line through the origin

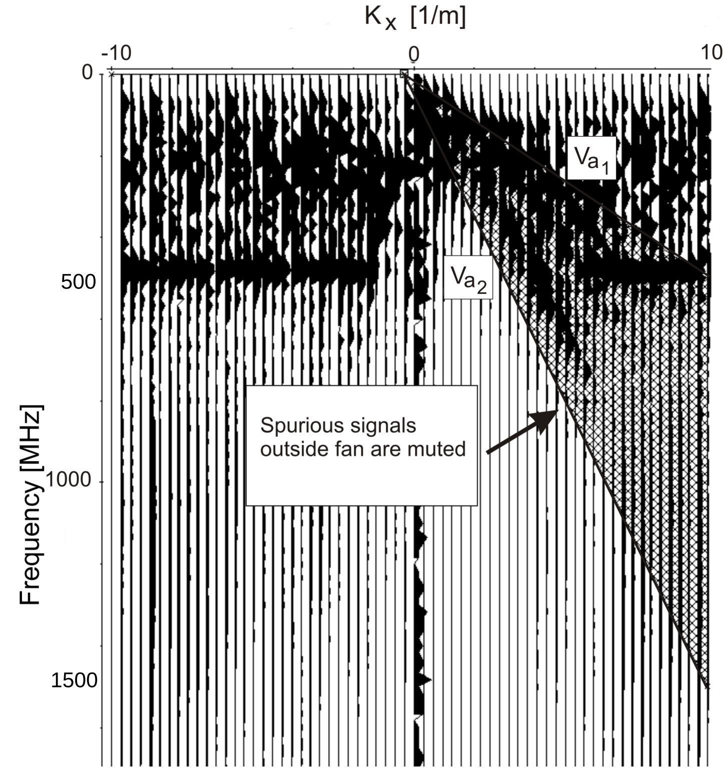

Figure 7.7: Diagram of an f-k spectrum F(f, kx). V_{a1}(= 0.15 m/ns) and V_{a2}(= 0.05 m/ns) define the range of the apparent velocity filter. Signals outside this fan are suppressed while signals with velocities between 0.15 and 0.05 m/ns are retained.

in the *f-k* domain, the orientation of the latter being perpendicular to the former. Horizontal lines in the *t-x* domain will correspondingly map to vertical lines in the *f-k* domain and dipping features that overlap in the *t-x* domain can be identified by their dips in the *f-k* domain and thus separated. The *f-k filter* is hence, effective in separating linear coherent noise from the GPR signal. I selected an apparent velocity filter range of 0.05 − 0.15 m/ns which is a reasonable propagation velocity range for an electromagnetic wave in a geological structure to filter out spurious signals from the *f-k* spectrum. On the *f-k* spectrum this velocity range defines a fan with velocity limits v_{a1} and v_{a2} (Fig. 7.7). After this operation the data were transformed back to the *t-x* domain (Eq. 7.5). Through this process spurious signals were suppressed from the original data and reflections from the lower part of the metal rod were enhanced (Fig. 7.9). Figs. (7.8) and (7.9) show the difference in data quality between data processed without and with an *f-k filter*. Without the application of the *f-k filter* reflections from the lower end of the metal rod are of poor quality and contain spurious reflections from other sources which result in spikes in the interval velocities with attendant errors in the interval VWC (Figs. 7.8(a) and 7.8(b)). For example, before applying *f-k filter*, the interval velocity between picks *a* and *b* resulted in a negative value while that between picks *c* and *d* resulted in a value far greater than the velocity of electromagnetic wave in air i.e. > 0.3 m/ns (Fig.7.8(b)).

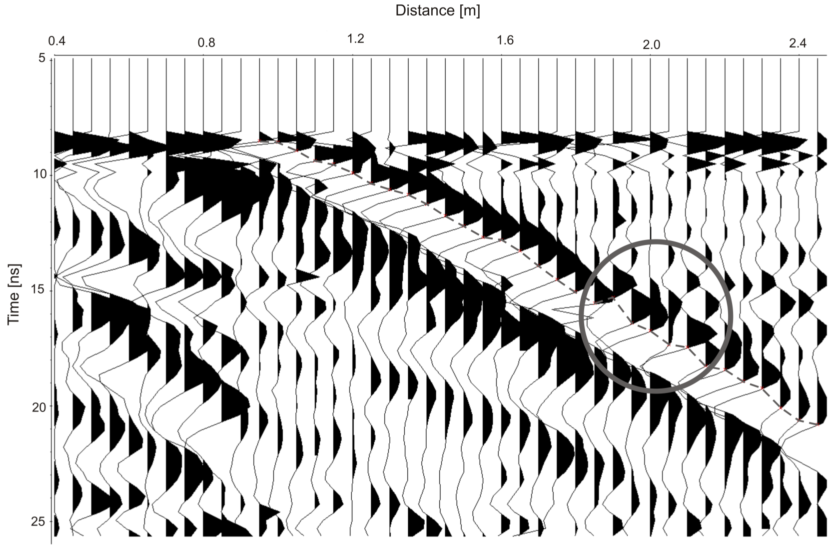

(a) Processed data without *f-k filter*

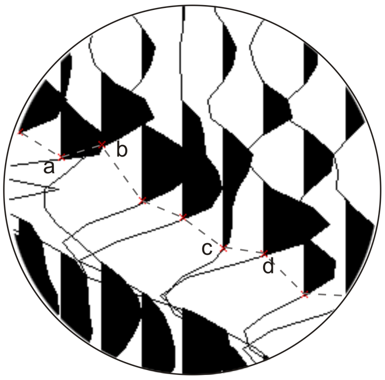

(b) Stark irregularities in picks

Figure 7.8: Data processed without an *f-k filter*. Interference of spurious reflections with reflections from the lower part of the metal rod cause irregularities in the calculated interval velocities. Region in Fig. 7.8(a) indicated by a circle is highlighted in Fig. 7.8(b). Picks *a*, *b* and *c*, *d* are discussed in text.

However, with the application of the *f-k filter* (Fig. 7.9) the zero-crossing picks indicated by a hatched line are much improved and stark irregularities in interval velocities caused by spurious reflections are relatively suppressed (Figs. 7.9(a) and 7.9(b)). For this case the interval velocity between picks *a* and *b* is positive and that between *c* and *d* fall reasonably within the propagation velocities of electromagnetic waves in porous media.

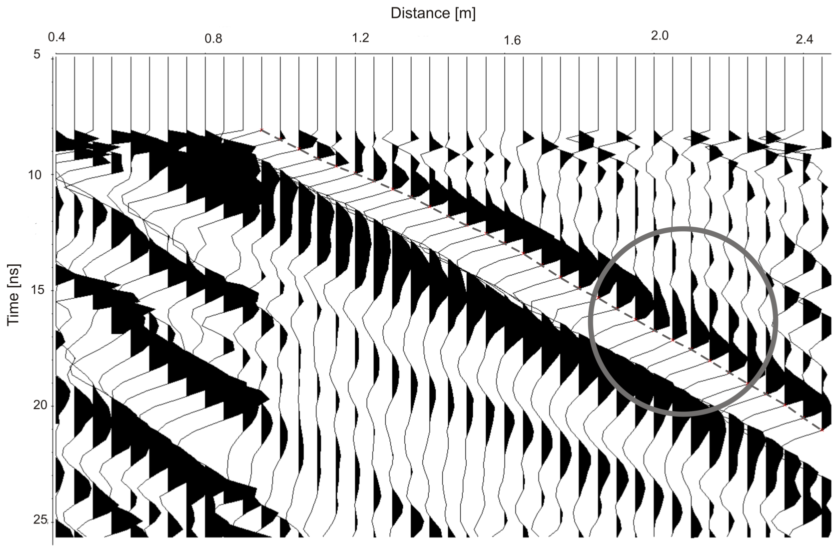

(a) Processed data with *f-k filter*

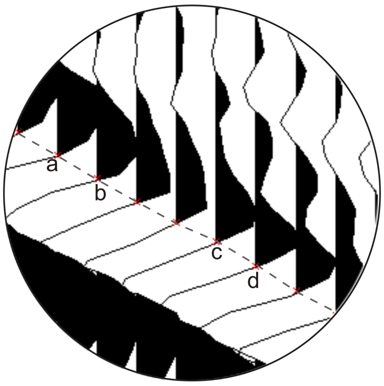

(b) Much improved picks

Figure 7.9: Data processed with *f-k filter*. The much improved picks are indicated by a hatched line. Irregularities in interval velocities caused by spurious reflections are relatively suppressed. The region indicated by a circle in Fig. 7.9(a) is highlighted in Fig. 7.9(b). Improved picks *a*, *b* and *c*, *d* are discussed in text.

7.3 Results of GWS and TRIME-TDR Measurements on Dike Model A

- Figs. 7.10, 7.11 and 7.12 show GWS and TRIME-TDR derived soil water content distribution with depth in dike model A for the 500 MHz antenna. Two distribution properties of the interval VWC, the raw data and harmonic means are shown in Fig. 7.10 for GWS while distribution shown for TRIME-TDR represents the interval VWC. In subsequent plots only the harmonic means of GWS interval soil water content are shown along with TRIME-TDR. The 13 soil layers used for the dike construction are indicated by vertical hatched lines and marked 1-13 in Fig. 7.10. TRIME-TDR and GWS show almost identical trends, however, GWS shows a much higher depth resolution. Comparison of GWS with TRIME-TDR shows a RMSD of 0.018 m^3m^{-3}.

- There is hardly any remarkable change in the soil water content distribution for the distributions before and after flood level 0.30 m (7.11(a)). There is still only a marginal change in the VWC distribution after flood level 0.60 m (7.11(a)).

- There is a general increase of soil water content with increasing flooding as expected. The different soil layers display variation in their water storage capacities. The graphs display three main zones which come more into play at higher flood levels beyond 0.8 m. These are:

  - A zone of unsaturation marked by continuous increase in VWC with depth. This is indicated by the soil layers 1-6 (Fig. 7.10, 7.11(a) and 7.11(b)). The soil water content rises to a maximum at higher flood levels reaching a maximum at depths between 0.6-0.7 m i.e. between the 6th and 7th soil layers.
  - A zone of sharp decrease in VWC with depth. This is indicated by the soil layer 7 (Figs. 7.12(a) and 7.12(b)).
  - A zone of apparent water saturation. This is indicated by the soil between the 8th and 12th soil layers where the soil water content reaches an approximate constant value of about 0.22 m^3m^{-3} between 0.8-1.4 m depth. (Figs. 7.11(c) - 7.12(a)]

Other graphs showing VWC distribution with depth with the 900 MHz antenna and co-located TRIME-TDR measurements are shown in appendix A. They show identical trends with soil water content values measured with the 500 MHz antenna.

Fig. 7.10 is a graph of soil water content distribution on the dike model using 500 MHz antenna before flooding. It is the only graph that shows both the harmonic means and raw data of the GWS-derived soil water content. In subsequent graphs the raw data are not shown. The 13 soil layers of the dike model are indicated with vertical hatched lines and numbered from 1 to 13.

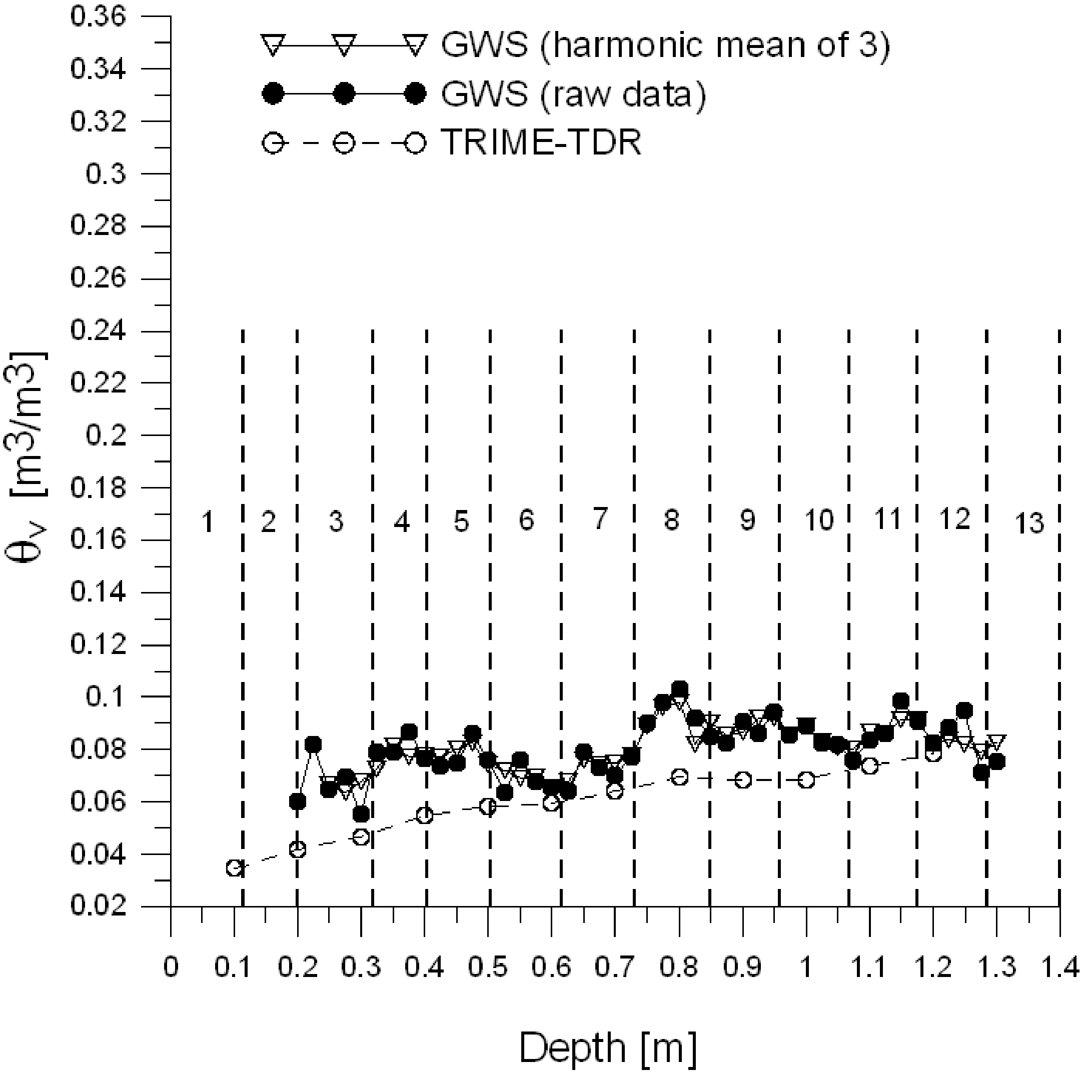

Figure 7.10: Comparison between GWS and TRIME-TDR VWC distribution in dike model A before flooding.

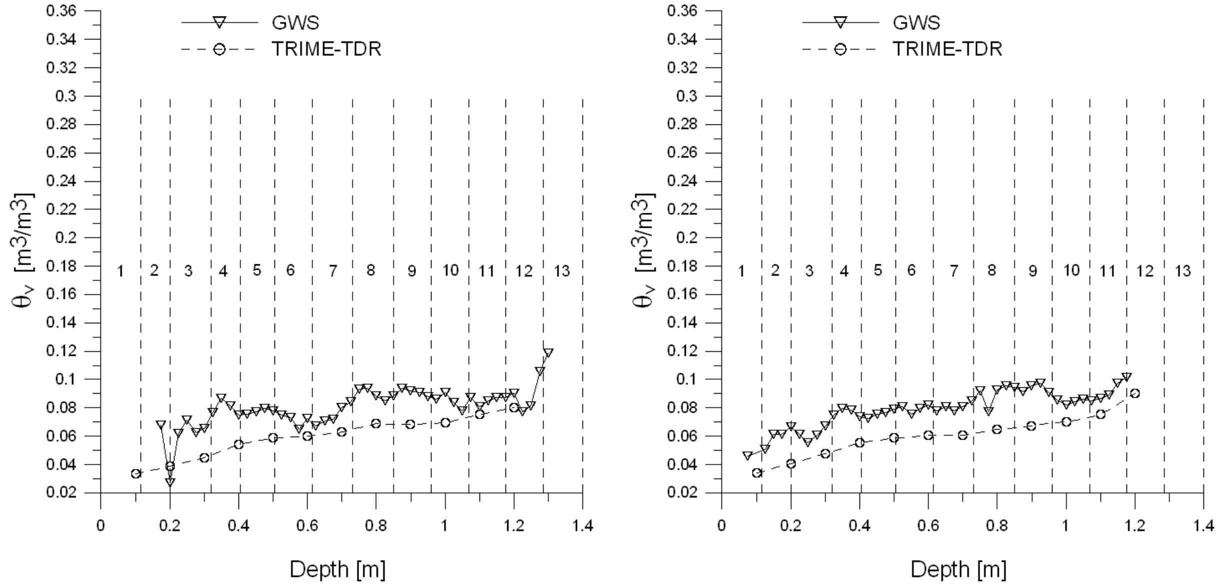

(a) Soil water distribution at 0.3 m flood level

(b) Soil water distribution at 0.6 m flood level

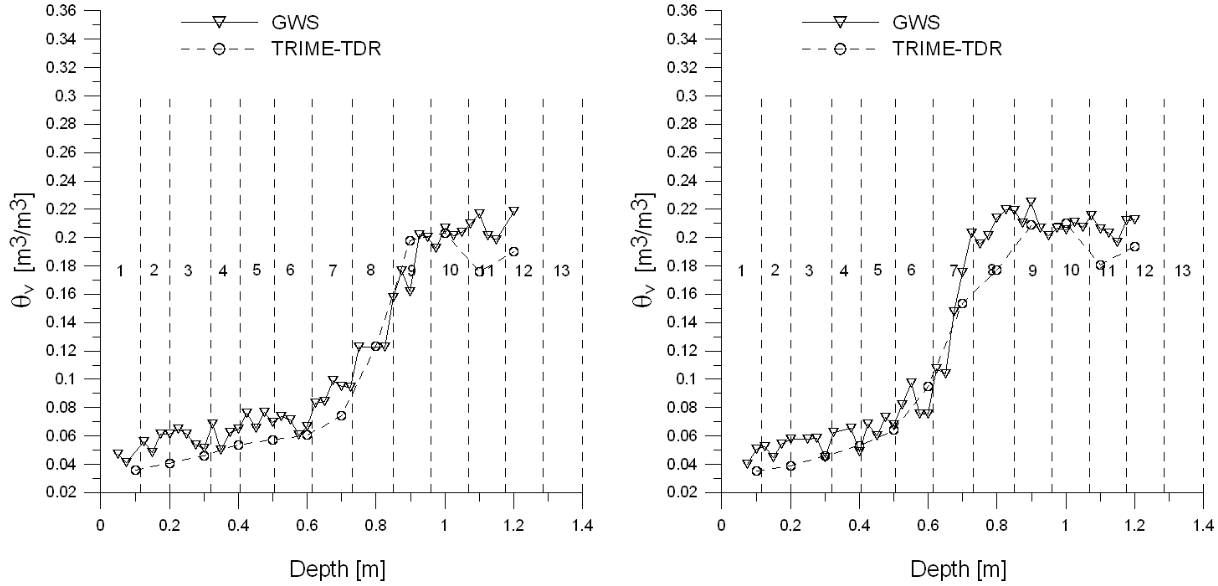

(c) Soil water distribution at 0.8 m flood level

(d) Soil water distribution at 1.0 m flood level

Figure 7.11: Comparison of GWS and TRIME-TDR derived VWC distribution in dike model A for flood levels 0.3 - 1.0 m.

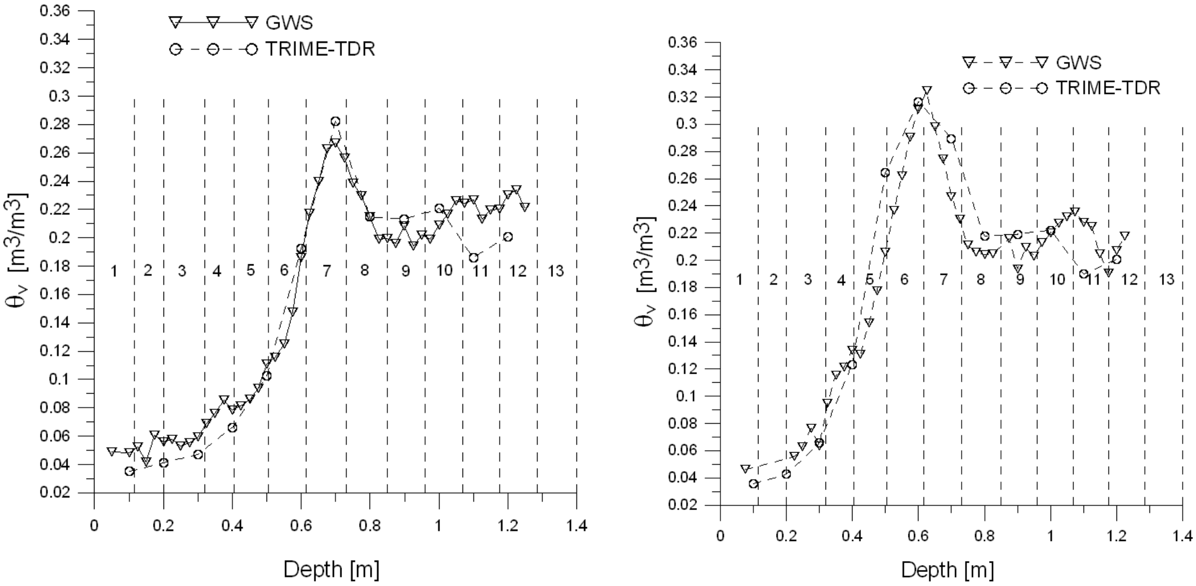

(a) Soil water distribution at 1.2 m flood level

(b) Soil water distribution at 1.25 m flood level

Figure 7.12: Comparison of GWS and TRIME-TDR derived VWC distribution in dike model A for flood levels 1.20 m and 1.25 m. The soil layers are indicated with vertical hatched lines and marked 1-13.

7.3.1 Discussion of Results

- The interval VWC was determined from the average interval velocity over a distance of 2.5 cm, a distance which corresponds to a displacement of the lower end of the metal rod. Over such a small displacement any error in the velocity created peaks in the interval VWC. The use of the running harmonic mean velocities (calculated from 3 interval velocities) helped to smoothen the GWS-derived VWC data and remove these peaks. This process was not required for TRIME-TDR.
- GWS shows a higher depth resolution. The method calculates the interval soil water content over average distance range of 2.5 cm. TRIME-TDR determines the soil water content over an average distance which corresponds to the length of the sensor (≈ 20 cm). This gives GWS a much higher depth resolution than TRIME-TDR.
- Apart from a minimum change in the soil water content in the 12th layer the distribution trend before flooding and after 30 cm and 60 cm of flooding levels hardly changes. This is due to the point of observation and the position of the slowly rising wetting front. All measurements were made from the crest of the dike model. The wetting front moved gradually upwards with flooding. At lower flood levels of 30 and 60 cm this mobile front had only reached the 12th and 13th soil layers as seen from the centre line of the crest (Fig. 7.14). With increasing flood levels the dike has ample time to store water, the pores become more filled from previous flooding, the wetting front gradually rises reaching the upper soil layers and the flood waters easily infiltrates the opposite plain.
- The VWC distribution anomaly occurs at the border zone between the 6th and 7th soil layers (Fig. 7.12) . The dike was constructed with homogeneous loamy sand with minor differences in the soil layer densities as a result of compaction. The transition zone between soil layers 6 and 7 is seen to record the highest soil water content than the layers below it. This region is highlighted in Fig. 7.13.

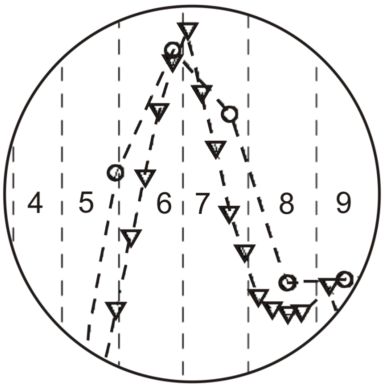

Figure 7.13: Soil water content distribution anomaly in soil layers 6 and 7.

This may take place especially when a fine grained material with greater porosity overlies a coarse grained in an unsaturated condition. For such a case more water is drawn from the coarse grained material into the fine grained material through the effect of capillarity. However, close examination of the VWC distribution reveals a sharp increase followed by an abrupt decrease. This anomaly occurs at the boundary between layers 6 and 7. This is likely due to the break in cohesion between the soil particles of the two adjacent soil layers giving way to preferential water flow along the boundary. This occurrence might have resulted from local grain re-arrangement from the hydraulic load due to the flooding. The flood water accumulates along this preferential infiltration path and easily reaches the other plain. It is not observed for flood levels below 1.2 m till the rising wetting front (Fig. 7.14) reaches the soil layers 6 and 7. Such dike breaches occur in dikes of granular soils, in particular soils without cohesion e.g. (Mohamed et al 2000, Zhu, 2006). A breach of this nature weakens the dike model and when not detected and checked may lead to its eventual collapse. The breaching of dikes and other levee structures are often accompanied by huge losses of human lives as well as property. A solution to a breach of this kind might be to construct the dike with more cohesive material e.g. clay. However, the application of GPR will be limited here due to strong attenuation of GPR waves in clay.

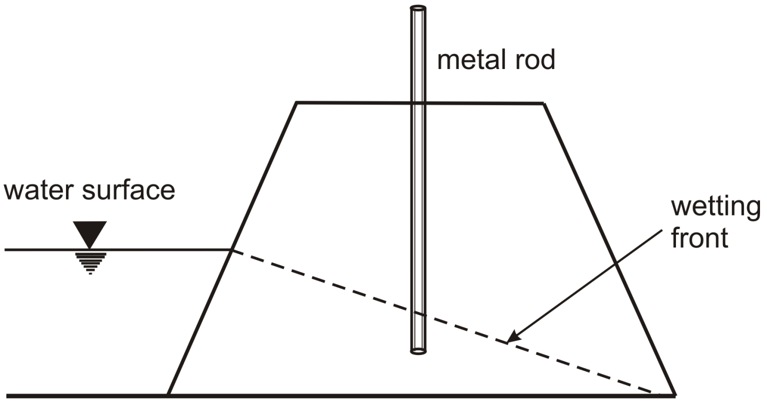

Figure 7.14: Schematic illustration of the wetting front from flooding.

7.4 Comparison of GWS with CMP in Soil Water Content Estimation

The common midpoint (CMP) is a data acquisition method of GPR. We have already discussed the method in section 3.2, p. 29. Data acquisition with the CMP method is time-consuming, but necessary. This is because this method yields a subsurface velocity-depth model. The model can then be used to infer the dielectric properties of the soil and hence, the soil water content.

7.4.1 Previous Work with CMP

Tillard and Dubois (1994) and Greaves et al. (1996) reported of errors of the order of 10 % with the CMP method. Grote et al. (2003) used the CMP method with 900 MHz and 450 MHz antennas to estimate the VWC with a root mean square value of about $0.11 - 0.17 \mathrm{m}^3\mathrm{m}^{-3}$. Other investigators who used the CMP method to estimate the VWC of the soil include Davis and Annan (1989); Fischer et al. (1992); Greaves et al. (1996); Du (1996); van Overmeeren et al. (1997); Berktold et al. (1998); Endres et al. (2000); Nakashima et al. (2001); Huisman et al. (2003a) and Galagedara et al. (2004).

7.4.2 Materials and Methods

I performed the experiments from March 1 - 10, 2006 on dike model A. With the GPR in the CMP mode I collected data using two bistatic antennas of central frequencies 500 and 900 MHz in two configurations. In one configuration the 500 MHz antenna transmitted while the 900 MHZ antenna received. In another configuration the 900 MHz antenna served as the transmitter with the 500 MHz antenna as the receiver. I placed the antennas parallel to each other and initially 0.2 m apart with an orientation perpendicular to the profile and moved them stepwisely away in

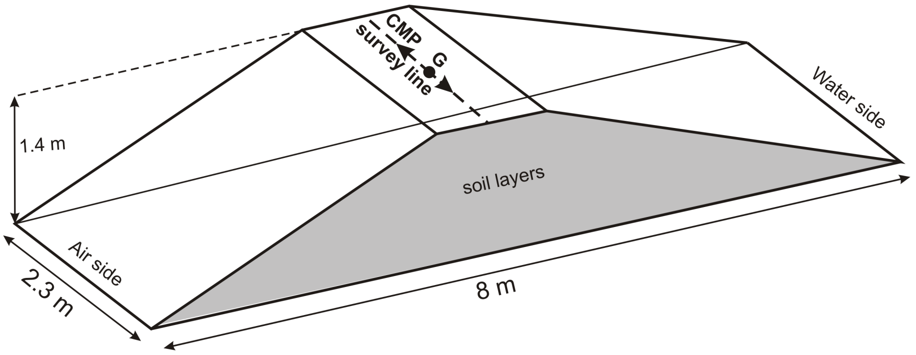

Figure 7.15: Sketch of dike model showing CMP survey line.

opposite directions at constant increments of 0.1 m. These experiments were performed at the crest of the dike at a single location which was the midpoint G of the crest of the dike (Fig. 7.15). The CMP method which employs the use of the apparent ground wave allowed the computation of the radar wave velocities through the soil at regular intervals along the profile even in the absence of a reflecting surface. I took data with the CMP and GWS methods from the same point G for 5 different flood levels between 0 and 1.2 m. Unlike GWS experiments described in section (7.2.1), p. 74, where the raw data for each observation point of the GWS experiment comprised of a minimum of 120 traces, for this experiment the equipment was programmed for a single trace (which represented reflection from the lower end of the metal rod) per observation point with he help of a specially mounted trigger button. The field exercise here was thus less time intensive.

7.4.3 Data Processing

The key to this analysis is the correct distinction between the air wave and the apparent ground wave and the proper calibration of the *zero time* which is the point of intersection of the air wave and the apparent ground wave on the radargram. I processed CMP data with Reflexw (Sandmeier (2007)) in two two main steps:

- I calibrated the zero time and used the Reflexw tools *subtract mean (dewow)* and *bandpassbutterworth* to remove low frequency induction effects and high frequency noise from the radargram.
- I performed a velocity *semblance analysis* (Yilmaz (1987)) of the Reflexw processed raw CMP data. The Reflexw tool *semblance analysis* allows the calculation of the semblance or unnormalised correlation for each data point within the zero-offset section based on a summation over a calculated hyperbola *x*-*t* range. This means that an unweighted summation for each point of the profile is performed over a calculated hyperbola of preset *bandwidth* (i.e. the area in the *x*-direction over which the summation is done). The choice of a larger bandwidth increases the computing time significantly, however, this helps the formation of clearly visible diffraction hyperbolas that extend over a large trace range (Sandmeier (2007)). I picked reflection events on the semblance diagrams and obtained a 1D depth-velocity model of the dike. The 1D depth-velocity models display both the root mean squared (RMS) and interval velocities (Figs. 7.16- 7.18).

The root mean velocity v_{rms} allows a time migration and depth conversion of the travel time profile. Mayer (1994) defines v_{rms} as

$$v_{\mathrm{rms}}^2 = \frac{\sum_{i=1}^{n} v_i^2 \Delta t_i}{\sum_{i=1}^{n} \Delta t_i} \tag{7.7}$$

where

v_{rms} : root mean square velocity
v_i : velocity within the i-th soil layer.
Δt_i : travel time for the i-th soil layer, $\Delta t_i = \frac{2d_i}{v_i}$
d_i : i-th soil layer thickness.

The interval velocity v_i of the soil layers is defined by Mayer (1994):

$$
{v_{i,n}}^2 = \frac{v^2_{\mathrm{rms},n} \sum_{i=1}^{n} \Delta t_i - v^2_{\mathrm{rms},n-1} \sum_{i=1}^{n-1} \Delta t_i}{\Delta t_n} \tag{7.8}
$$

where

$v_{i,n}$: interval velocity in the n th soil layer
$v_{\mathrm{rms},n}$: average velocity between the surface and the n-th reflector.
$v_{\mathrm{rms},n-1}$: average velocity between the surface and the $n-1$-th reflector.
Δt_i : travel time for the ith soil layer.
Δt_n : travel time for the n-th soil layer.

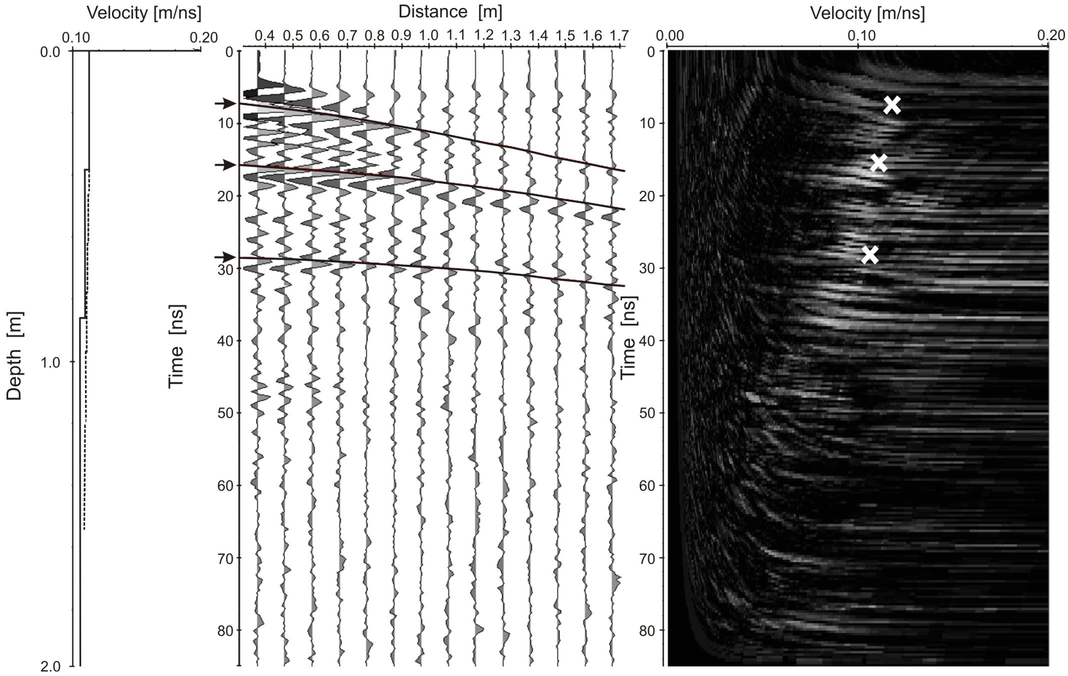

(a) Before flooding

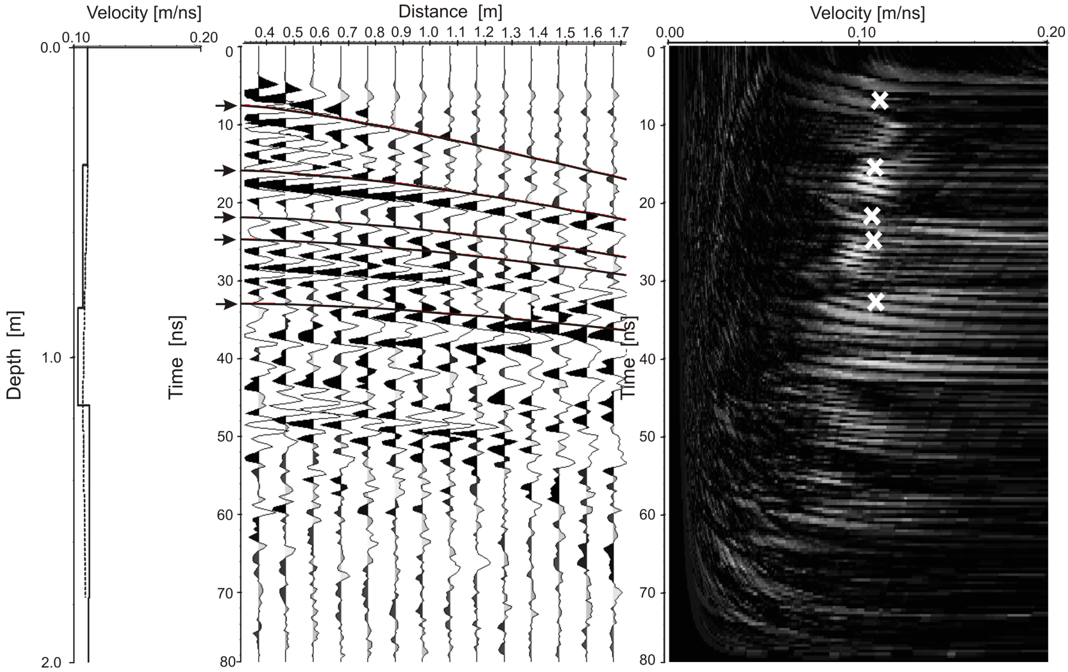

(b) After flood level 0.3 m

Figure 7.16: CMP velocity analyses showing 1D velocity models (continuous line:interval velocity, dotted line: RMS velocity), hyperbolic adaptations (indicated by arrows) and semblance images before and after flood level 0.3 m.

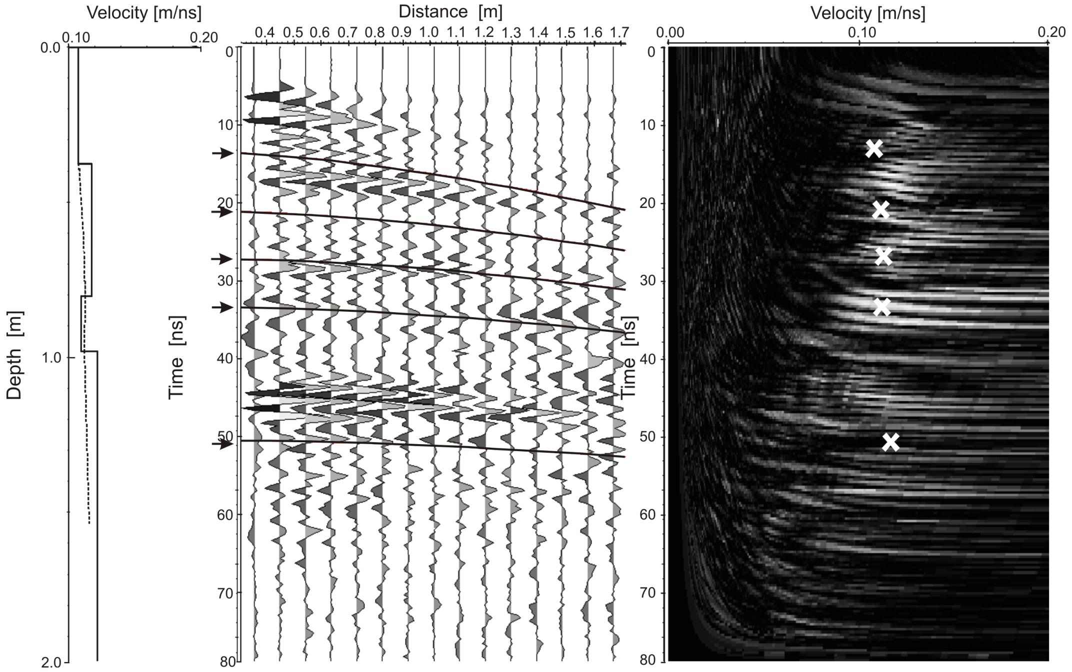

(a) After flood level 0.6 m

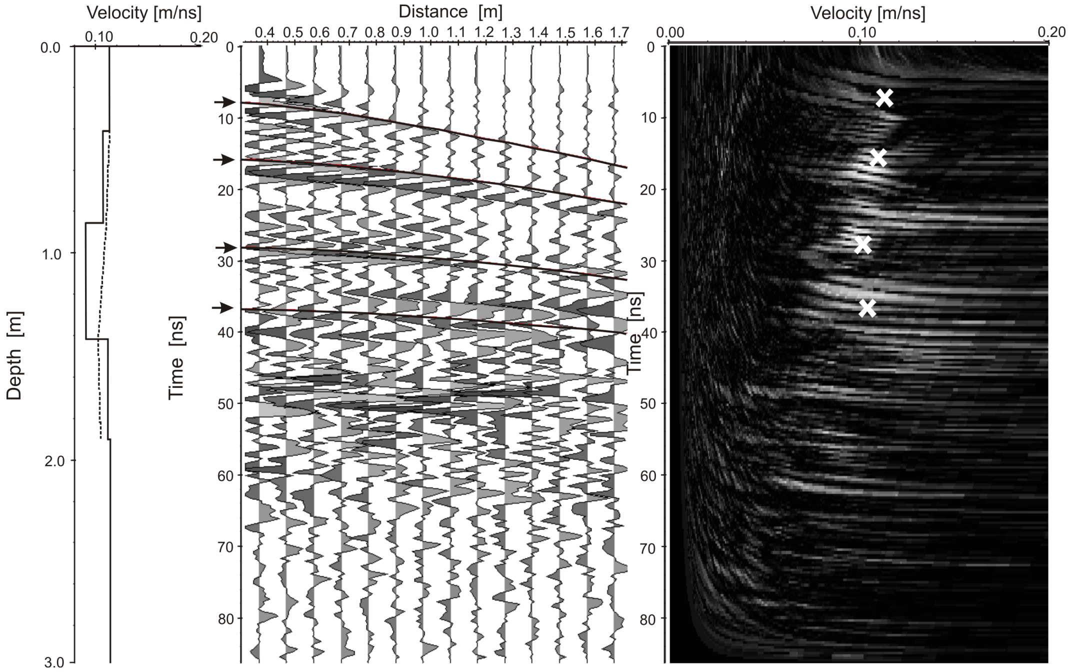

(b) After flood level 0.9 m

Figure 7.17: CMP velocity analyses showing 1D velocity models (continuous line:interval velocity, dotted line: RMS velocity), hyperbolic adaptations (indicated by arrows) and semblance images after flood levels 0.6 m and 0.9 m.

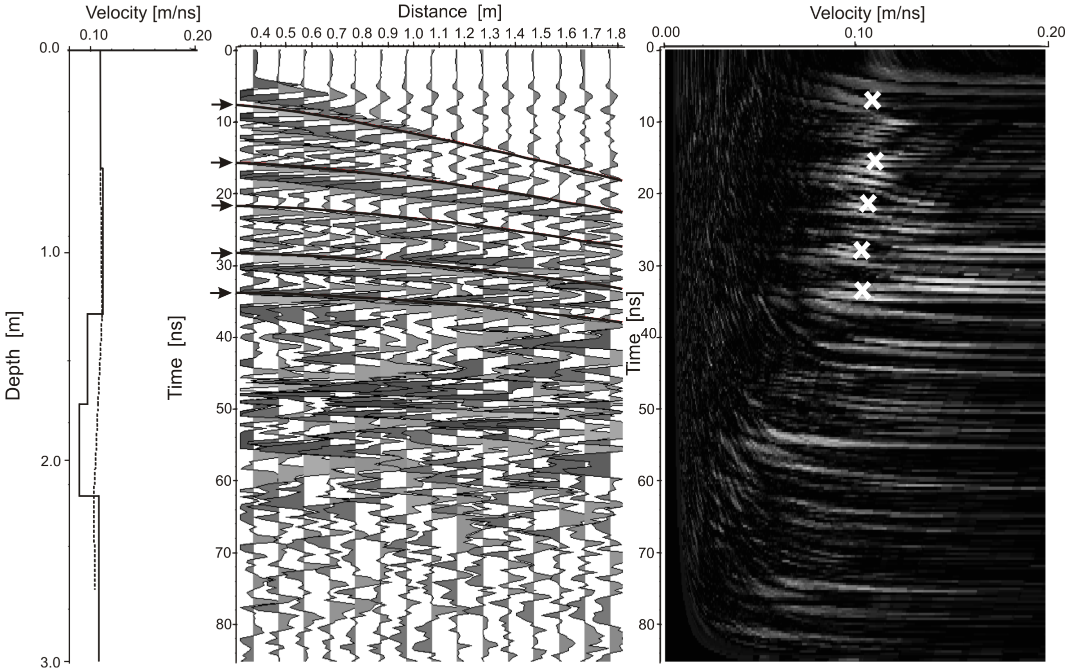

Figure 7.18: CMP velocity analyses showing 1D velocity models (continuous line:interval velocity, dotted line: RMS velocity), hyperbolic adaptations (indicated by arrows) and semblance images after flood level 1.2 m.

I stored the 1D depth-interval velocity model as an ASCII file and for GWS matching depth intervals, determined corresponding interval ε_r and θ_v. As a help in picking up the right phases of the reflected waves between two contrasting layers I made use of Eq. 4.52 on p. 46. The apparent ground wave velocity was estimated from the travel times of the airwave and apparent ground wave. If Δt is the time difference between the two waves, then, by adding this time difference to the calculated travel time of the airwave the travel time of the apparent ground wave could be calculated. Thus, if t_{GW} and $t_{AW}(= c/\Delta_x)$ represent the travel times for the ground and air waves respectively with $t_{GW} - t_{AW} = \Delta t$, $c = 3.0 \cdot 10^8$ m/s, then for two antennas of separation Δx, the apparent ground wave velocity v is calculated as

$$v = \frac{\Delta x}{\Delta t + t_{AW}} \tag{7.9}$$

and from Eq. (7.9) the soil permittivity ε_r is given by

$$\varepsilon_r = \left(\frac{c}{v}\right)^2 = \left[\frac{c(\Delta t + t_{AW})}{\Delta x}\right]^2 \tag{7.10}$$

The dielectric coefficient ε_r from Eq. (7.10) was then eventually related to the soil water content with the help of Eq. (5.18). A guide for identifying the airwave, apparent ground wave and reflected wave is that the airwave travels at the highest velocity of 0.3 m/ns and the amplitude of the apparent ground wave decays with distance at a faster rate than that of the reflected waves (Du (1996)). Besides, the air wave and ground wave have opposite phases. Generally, as the distance of separation of the antennas increased the more time it takes for the radar signal to travel from the transmitter to the receiver and the deeper the signal probes into the soil. I processed co-located GWS data using Reflexw as described under section 7.2.3 and calculated running harmonic means (from 3 interval velocities) and determined corresponding VWC values for all flooding experiments. For the case before flooding I calculated in addition running harmonic means from 5 interval velocities.

7.4.4 Results and Discussion

Distribution of VWC with depth as derived from GWS and CMP methods are shown in Figs. 7.19 - 7.23. For all the figures the harmonic means (calculated from 3 interval velocities) as well as the interval VWC from the raw data are shown for GWS. The use of harmonic means helped to removed peaks and smoothen the data. Irrespective of this the distribution still shows peaks even after the application of the harmonic mean. The peaks partly result from errors in picking the reflection over the small distance range of 2.5 cm. The trigger button mounted on the equipment had periodic contact problems. This might have contributed to errors in the GWS data. Despite these problems the VWC distribution trends displayed by both methods are quite comparable. In Fig. 7.19(b), I have shown an additional distribution property, the harmonic mean calculated from 5 interval velocities. This was discontinued in the other graphs because the process apart from being very time intensive did not yield much difference from the distribution indicated by the harmonic mean of 3.

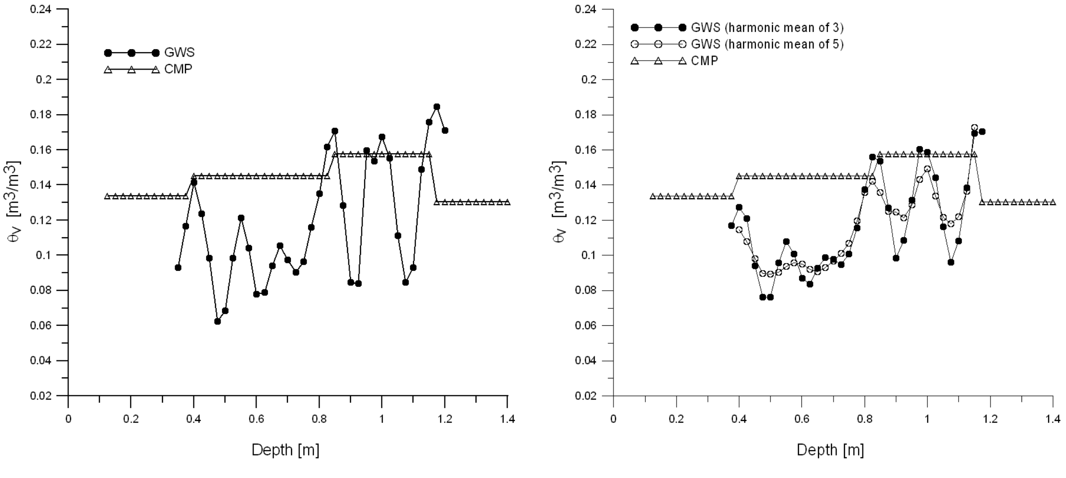

(a) GWS (interval VWC), CMP

(b) GWS (harmonic means of 3 and 5), CMP

Figure 7.19: Comparison of GWS and CMP plots before flooding.

CMP shows a much poorer depth resolution than GWS. This large difference is likely due to the poor depth resolution of the CMP method or the use of two different antennas - the 500 MHz antenna as transmitter and the 900 MHz antenna as receiver. Data acquired with the 900 MHz antenna as transmitter with 500 MHZ antenna as receiver were of much poorer quality and hence were not further processed. Comparison of GWS with CMP shows a relatively large RMSD of 0.06 m^3m^{-3}. Other investigators like Tillard and Dubois (1994) and Greaves et al. (1996), reported of deviations of the order of 10 % with CMP-derived VWC measurements. A problem which I encountered with the CMP experiment was that the crest ($\approx$ 2 m) of the dike was not long enough to permit free movement with the CMP method. For a dike crest of such dimensions with the CMP method only antennas with small dimensions would have been more reasonable. Thus, I was restricted to select 900 MHz and 500 MHz antennas from the number of antennas I had. The best combination would have been for example, the use of two 900 MHz antennas which I did not have. I had only one of 900 MHz and 500 MHz antennas. The best way out was to combine 900 MHz and 500 MHz antennas with the former as transmitter which I did.

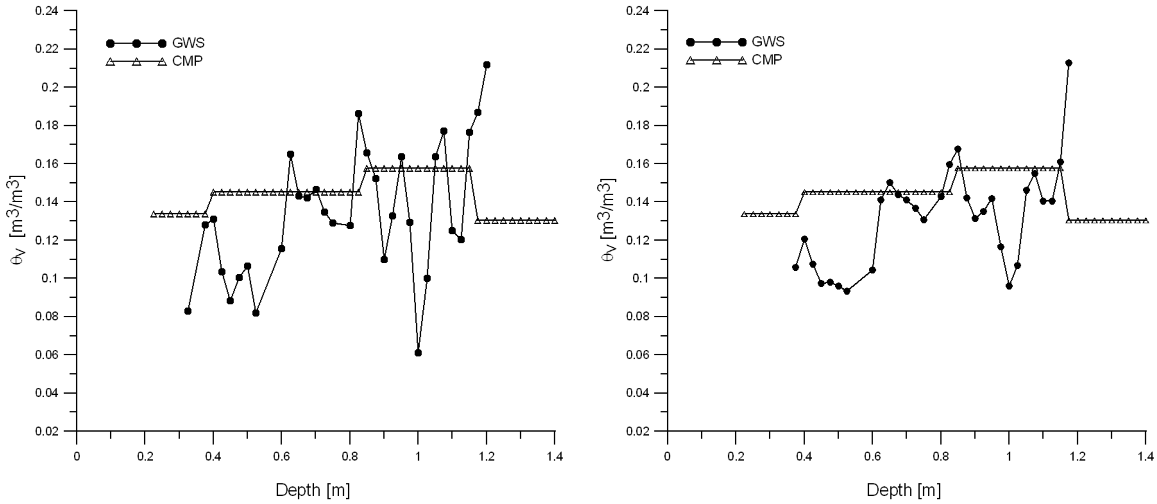

(a) GWS (interval VWC), CMP

(b) GWS (harmonic mean of 3), CMP

Figure 7.20: Comparison of GWS and CMP plots after a flood level of 0.3 m.

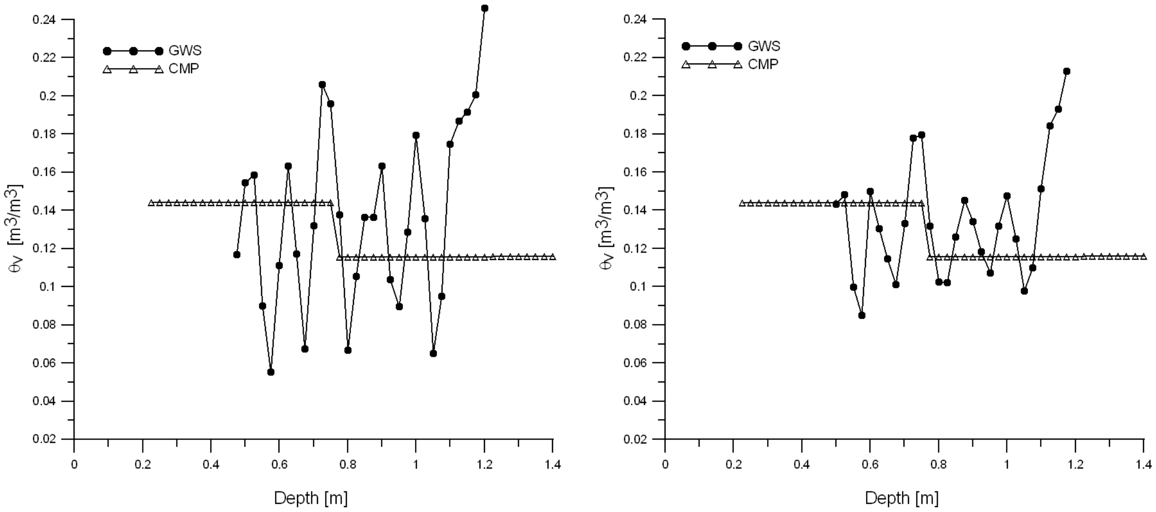

(a) GWS (interval VWC), CMP (b) GWS (harmonic mean of 3), CMP

Figure 7.21: Comparison of GWS and CMP plots after a flood level of 0.6 m.

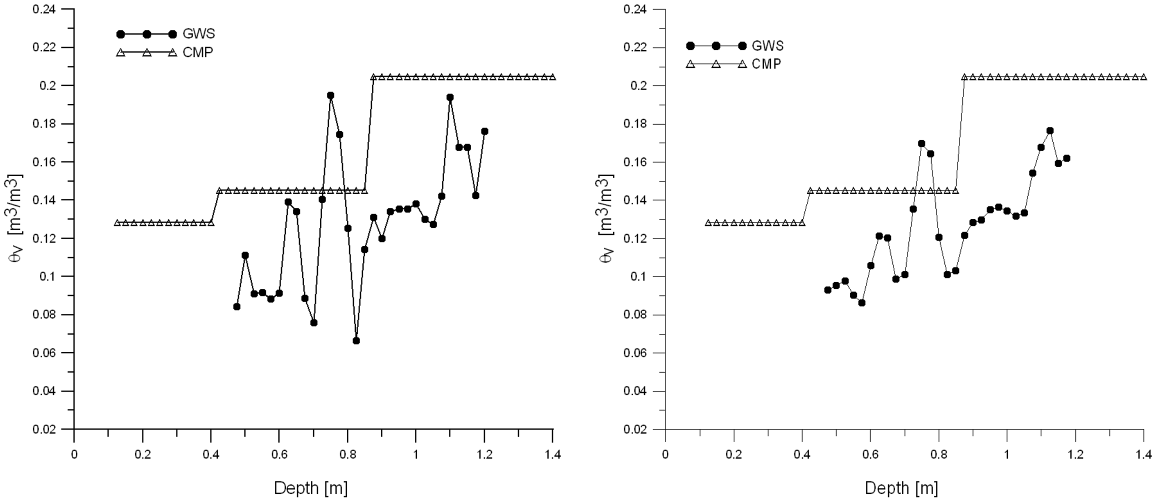

(a) GWS (interval VWC), CMP (b) GWS (harmonic mean of 3), CMP

Figure 7.22: Comparison of GWS and CMP plots after a flood level of 0.9 m.

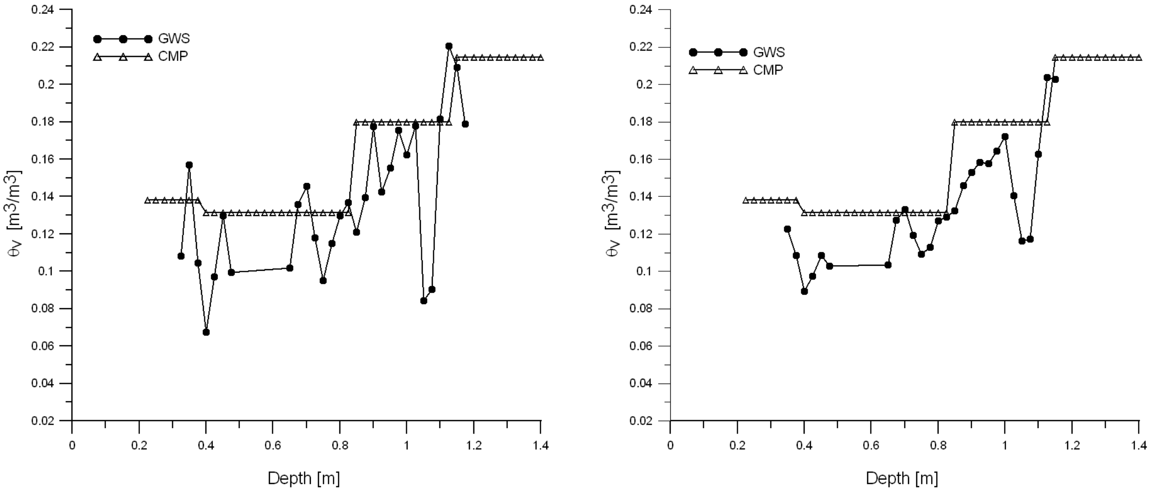

(a) GWS (interval VWC), CMP (b) GWS (harmonic mean of 3), CMP

Figure 7.23: Comparison of GWS and CMP plots after a flood level of 1.2 m.

The survey procedure and data processing for CMP are labour and time intensive. This makes the method of little practical use especially in field scale monitoring of soil water content distribution. However, the method is necessary because it provides a depth-velocity model of the subsurface from which the soil water content could be inferred.

7.5 GWS Experiments on Dike Model B

The dike model B is a full-scale experimental dike model situated at the Federal Insitute of Engineering and Waterways, Karlsruhe. Fig. 7.24 shows an overview of the dike model. An exhaustive description of this model and its detailed instrumentation has been given by Scheuermann (2005).

Figure 7.24: Dike model B of the Federal Waterways and Research Institute, Karlsruhe, Germany. Picture shows the data acquisition point of GWS (P), the waterside (W) and the landside (L) of the dike model.

7.5.1 Site Description and Precipitation Experiments

The dike model B comprises of a homogeneous sand with grain sizes distribution from 0.2 to 2.0 mm with an organic overburden of about 25 cm thickness. It has a height of 3.6 m, a crest length of 22.4 m and two plains with inclinations 1:2 and 1:2.25 on the waterside and landside respectively. It is built on a waterproof plastic sealing so that infiltrating water easily gathers into access drains at its foot. The experiments described in this section comprised of four consecutive days of simulated precipitation. Two sprinklers were installed on the crest of the dike and operated for 8.5 hours on the first day, 19 hours on the second, 16 hours on the third and 12.5 hours on the fourth day. Directly before and immediately after the rain phases, I took measurements with the GWS and the TRIME-TDR techniques.

7.5.2 Experiment with Suspended Metal Rod

Figure 7.25: Experiment with suspended metal rod. String (A), Metal rod (B), Access tube (C)

Through one of the access tubes installed on the dike, I lowered a short metal rod of length 25 cm and diameter 4.5 cm suspended on a light inextensible string at intervals of 5 cm down to the base of the dike. For each position of the lower end of the metal rod in the access tube, I operated the GPR in the CO mode along a 1 m long traverse with the position of the access tube at its mid-point. I used the 500 MHz antenna for this exercise. The experiment was designed to measure the VWC distribution in the dike by measuring the velocity of electromagnetic wave in the soil.

The experiment, however, failed to yield the expected results. I encountered two main problems: Reflections from the metal even after careful processing contained noise. This might be due to stronger reflections from other sources such as conventional TDR components and piezometers installed in the dike body. The second problem was that at certain depths the radargram showed no reflections at all from the metal. This might be due to the following reason: The wavelength of the electromagnetic signal transmitted with the 500 MHz antenna was of about the same order as the depth of the upper surface of the metal rod. Destructive interference between the incident and reflected waves from the upper surface of the rod is likely to be the cause of zero reflections registered on the radargram. The quest for a solution to this problem turned my attention to the use of a long metal rod with a single reflecting end, the methodology of the GWS which has been the subject of discussion in this chapter.

7.5.3 Comparison of GWS with TRIME-TDR on Dike Model B

I performed these experiments on dike model B from April 23 - 27, 2007 at common locations through access tubes installed vertically on the landside and waterside of the dike model. There are 2 basic differences between the measurements on dike model A and that on dike model B:

- For the dike model B the experiments were performed on the inclined plane of the waterside, rather than from on the crest as in dike model A. Since the inclination here was quite substantial I performed depth corrections on the data (Fig. 7.26).
- Water was introduced into the dike model B by simulated precipitation with the help of installed water sprinklers. Simulated flooding method was used in dike model A.

Apart from these measurement procedures, data processing and calibration of TRIME-TDR are similar to procedures already discussed under sections (7.2.1.3) and (7.2.3). I fitted the TRIME-TDR calibration data with the first order linear regression:

$$\theta_v = 1.015\theta_T - 2.49 \tag{7.11}$$

where θ_v and θ_T are the volumetric water contents [%] from the gravimetric and TRIME measurements respectively.

7.5.3.1 Depth Correction of GWS Data

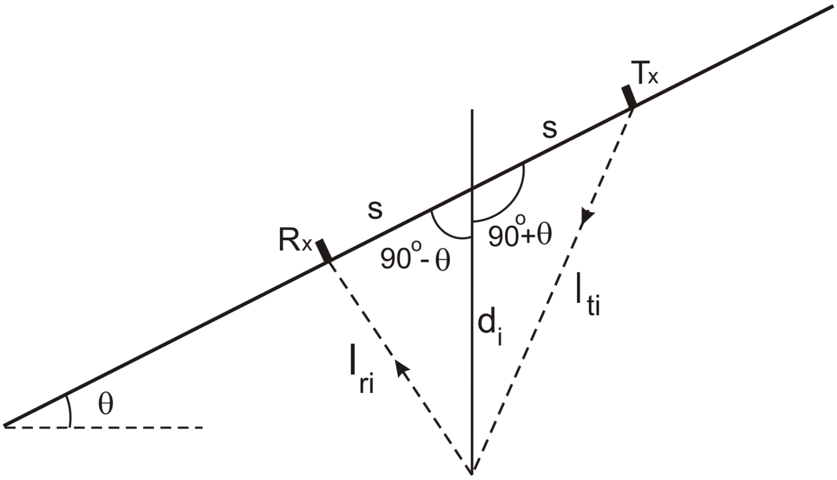

Figure 7.26: Correction for depth of metal rod in soil.

Due to sloping nature of the plane on which I took data, I made depth corrections for the depths of the metal rod beneath the surface. If θ is the inclination of the plane with the horizontal and

l_{ti} and l_{ri} are the distances travelled by the electromagnetic wave from the transmitter T_x to the lower edge of the metal rod and from lower end to the receiver R_x, then the total path length L from transmitter to receiver is given by

$$L = l_{ti} + l_{ri} \tag{7.12}$$

$$l_{ri}^2 = d_i^2 + s^2 - 2d_i s\cos(90^\circ + \theta) \tag{7.13}$$

$$l_{ti}^2 = d_i^2 + s^2 - 2d_i s\cos(90^\circ - \theta) \tag{7.14}$$

Eqs. (7.13), (7.14) and (7.14) give the depth d_i of the metal rod beneath the inclined plane as

$$d_i = \left(\frac{L^4 - 4L^2 s^2}{16s^2 C_0 + 4L^2}\right)^{\frac{1}{2}} \tag{7.15}$$

where $\theta = 26.57^\circ$ and $C_0 = \cos(90^\circ + \theta)\cos(90^\circ - \theta) = -0.199$. For the 500 MHz antenna used throughout the experiment $s = 0.105$ m.

7.5.4 Results of GWS and TRIME-TDR Measurements on Dike Model B

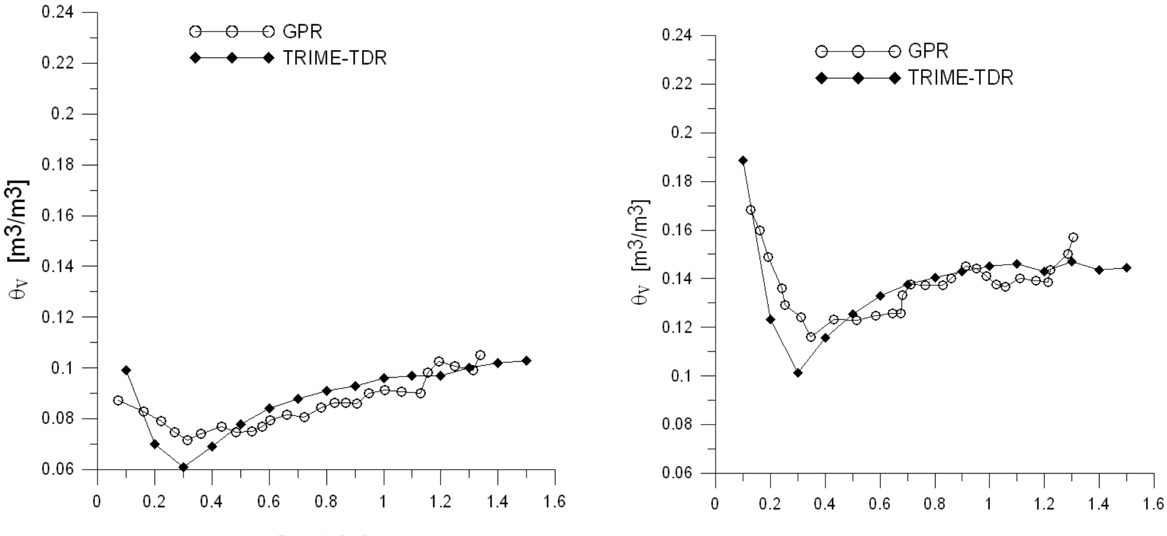

(a) Before precipitation (b) After Precipitation

Figure 7.27: Measurements with TRIME-TDR and GWS before and after precipitation from the water side of the dike model.

I summarise the results of the measurements on dike model B as follows:

- The VWC distribution for TRIME-TDR and GWS experiments in the dike model (Figs. 7.27(a) and 7.27(b)) show almost similar trends. The GWS-derived soil water data showed a relatively small RMSD of 0.011 m^3m^{-3} as compared to TRIME-TDR.

- There is a decrease in VWC with depth from about 0.09 m^3m^{-3} to about 0.07 m^3m^{-3} before and from about 0.17 m^3m^{-3} to about 0.12 m^3m^{-3} after precipitation between the surface and 0.3 m depth. TRIME-TDR follow almost identical trend.
- Between depths of 0.3 m and 1.6 m there is an increase in VWC from about 0.07 m^3m^{-3} to about 0.11 m^3m^{-3} before precipitation and from about 0.12 m^3m^{-3} to 0.16 m^3m^{-3} after precipitation.
- The soil layer between the surface and about 0.3 m depth represents the inhomogeneous organic overburden. The sand layer begins after 0.3 m. The overburden is able to hold more water than the sand and hence records a higher VWC than the sand after precipitation. The increase in VWC in the sand layer is due to water infiltration from the top.

7.6 Estimation of Errors in θ_v and ε_r

7.6.1 Estimation of $\Delta\theta_v$ and $\Delta\varepsilon_r$ from CMP Data

The focal point for the correct evaluation of θ_v lies in the correct distinction between the air wave and the ground wave from the radargram and the right calculation of their velocities. Due to the use of shielded antennas and the short length of the crest of dike model A (resulting in superposition of the air wave with the other phases) it was in most cases very difficult to recognise the air wave in the radargram. This resulted in errors in the zero-time calibration of which the point of intersection of the air wave and ground wave play a vital role. Consequently, this created errors in the calculation of the VWC.

I calculated a RMSD of $\Delta v = 0.03$ m/ns in the ground wave velocity from the radargram by repeating the process several times. Considering a typical propagation velocity of $v = 0.12$ m/ns with corresponding dielectric coefficient $\varepsilon_r = 6.25$, Eqs. (4.41, p. 44) and (7.1) give

$$|\Delta\varepsilon_r| = \frac{|-2c^2|}{v^3} \cdot |\Delta v| = \frac{2 \times 0.3^2}{0.12^3} \cdot 0.03 = 3.125 \tag{7.16}$$

and

$$|\Delta\theta_v| = e \cdot |\Delta\varepsilon_r| \approx 0.07\,\mathrm{m^3m^{-3}} \tag{7.17}$$

where

$$e = 2.92 \times 10^{-2} - 1.1 \times 10^{-3}\varepsilon_r + 1.29 \times 10^{-5}\varepsilon_r^2 = 0.0228 \tag{7.18}$$

7.6.2 Estimation of $\Delta\theta_v$ and $\Delta\varepsilon_r$ from GWS Data

Several exercises of picking the travel times of the reflected phase from the radargram reveal an error of about 1.2% in picking the travel times. From Eqs. (4.41) and (7.1)

$$|\Delta v| = \frac{|-2d|}{t^2} \cdot |\Delta t| = v\frac{\Delta t}{t} \tag{7.19}$$

and

$$|\Delta\varepsilon_r| = \frac{|-2c^2|}{v^3} \cdot |\Delta v| = \frac{|-2c^2|}{v^2}\frac{\Delta t}{t} = 2\varepsilon_r\frac{\Delta t}{t} \tag{7.20}$$

From Eq. (5.18, p. 52)

$$|\Delta\theta_v| = e \cdot |\Delta\varepsilon_r| = 2e\varepsilon_r\frac{\Delta t}{t} \approx 0.00342\,\mathrm{m^3m^{-3}} \tag{7.21}$$

with $\varepsilon_r = 6.25$ and $|\Delta t|/t = 1.2\,\%$.

Now, when we compare the errors in θ_v from Eqs. 7.17 and 7.21 we see that the error in estimating soil water content from CMP data is about 10 times higher than the case of GWS. The CMP method has a relatively poor depth resolution and the volume of data acquired by this method too is far below that of GWS. These result in large errors as compared with GWS. See Figs. 7.19 - 7.23.

7.7 Guided Wave Modelling

I did the modelling and analysis of guided wave propagation through the soil with the help of the **F***inite* **D***ifference* **T***ime* **D***omain* (FDTD)(Yee (1996)) modelling tool of Reflexw. I considered a simplified model with air layer above the soil surface for soil of constant dielectric coefficient ε_r. With this model the source is placed 0.02 m below the surface and about 0.08 m away from the metal rod. For the soil, I selected the parameters $\mu_r = 1$, $\sigma = 0.001$ S/m and $\varepsilon_r = 9$ the latter of which approximates to a propagation velocity of 0.1 m^3m^{-3}. For the metal rod, I selected $\mu_r = 1$, $\sigma = 9$ S/m and $\varepsilon_r = 1$ (Fig. 7.28). The selected value $\sigma = 9$ S/m was the highest conductivity possible with the software packet (Reflexw) used. The source T_x transmits an electromagnetic wave of central frequency 500 MHz which is polarized in the x-direction. Results of the modelling are shown in Fig 7.29. Transmitted spherical waves from the source get coupled to the metal rod and travels along it. The guided wave reaches the lower end of the metal rod after a travel time of 14.73 ns and the reflected wave is recorded by the receiver after 29.49 ns (Fig 7.29). By knowing the depth of the lower end of the metal rod and the corresponding reflection times recorded by the receiver the average velocities of the guided wave for various depths of the metal rod can be deduced. From these, interval velocities for each 0.025 m change in depth can be deduced. This leads to the determination of corresponding interval ε_r and finally interval VWC. The about 1 mm thick plastic sheathing and the corresponding thin air column

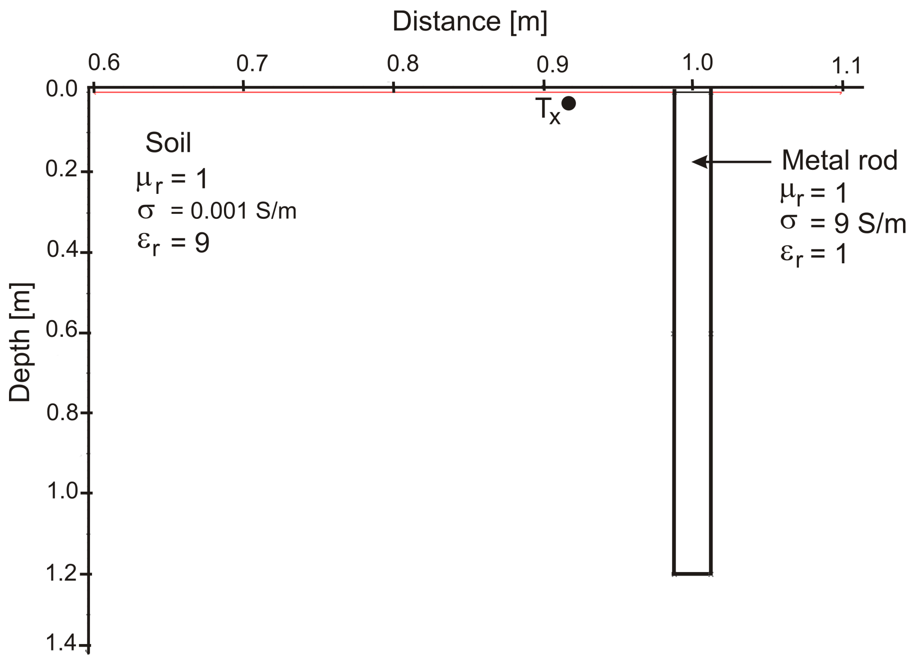

Figure 7.28: Model of the metal rod in the soil. Rod was positioned about the midpoint of the crest which was about 2 m wide.

between the metal rod and the soil were not overseen in the modelling. The sheathing is very thin ($\approx$ 1 mm thick) vis-à-vis the much larger wavelengths ($100\,\mathrm{mm} < \lambda < 300\,\mathrm{mm}$) of the GPR signals employed, and thus has insignificant influence on the reflections from the metal rod. The inclusion of the air column on the other hand would have rendered the modelling very complicated making the snapshots hardly recognisable. I excluded this for the sake of clarity.

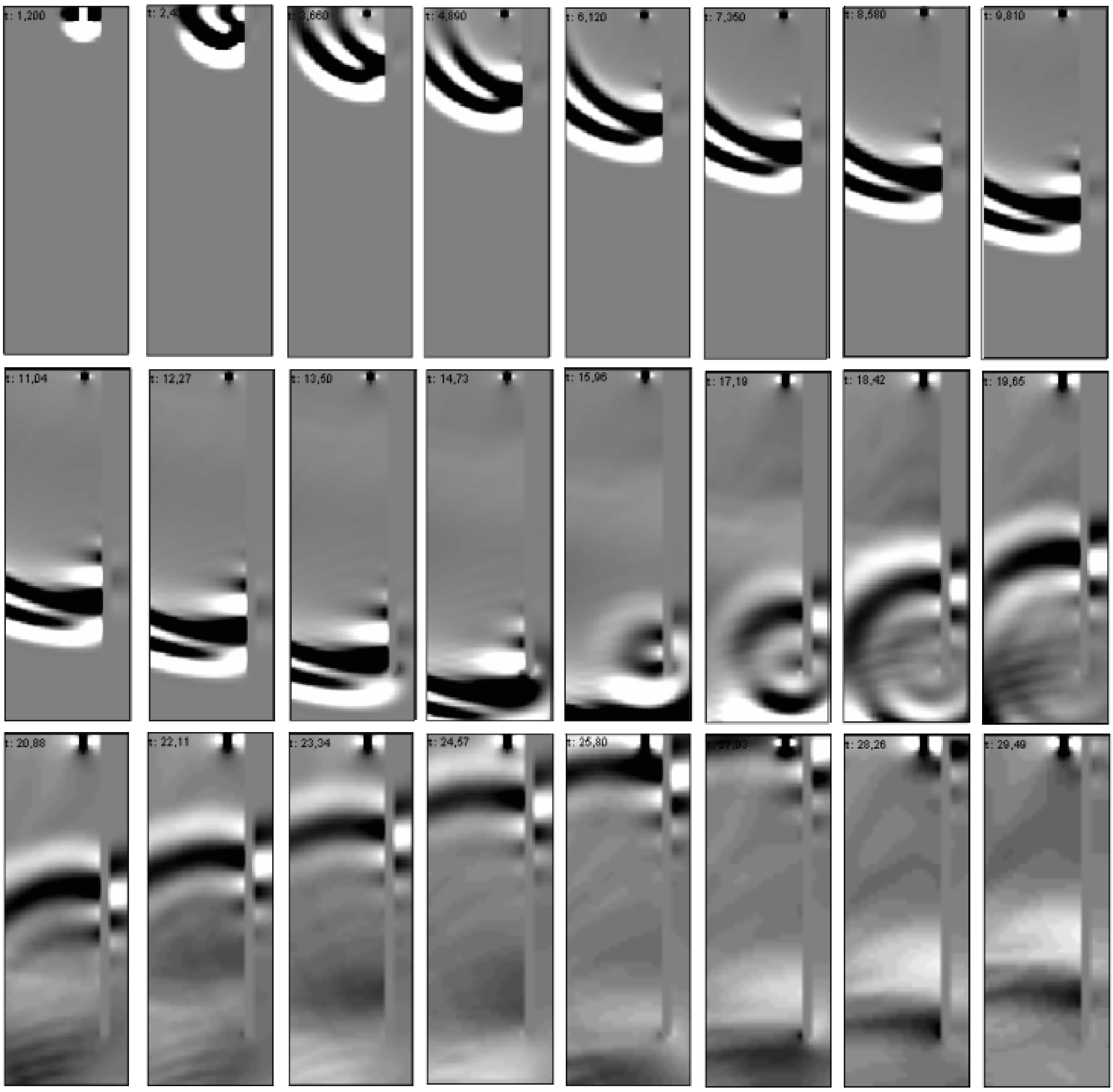

Figure 7.29: Snapshots in time intervals of 1.23 ns from FDTD modelling.

7.8 Discussion and Outlook

Soil water content monitoring in the vadose zone has vital applications for dam surveillance in hydrology. One major cause of damage to embankment dikes is internal leakage and erosion. In order to overcome this problem and to ensure the safety of dikes a good monitoring and leakage detecting system has to be installed. One way of doing this is to periodically check the water content distribution in the dike body.

Conventionally, this is done by observation the water level in boreholes sunk in the ground close to the dike body or the installation of piezometers to monitor pore water pressure and compare them with values designed for the dike. There are many attendant problems with such conventional monitoring systems. Such systems themselves soon give in through aging or could also be destroyed through the destructive strike of lightning. Their results too might not be very reliable because such point monitoring systems might not necessarily tell the whole story of the state of the art anomalous behaviour of the dike.

Other monitoring techniques include temperature measurements. Here, local temperature anomalies which might result from seepage and erosion are mapped (e.g. Merkler et al. (1985, 1989); Theune (1999)).

The electrical resistivity tomography (ERT) technique yields vital information about changes in the soil water content in the subsurface and has proven successful in detecting early leakage in dike structures (e.g. Johansson and Dahlin (1996); Johansen et al. (2005); Daily et al. (1992); Ellis and Oldenburg (1994); Li et al. (1992); Loke and Barker (1995); al Hagrey and Michaelson (2002); Hauck (2002); Rings et al. (2006)). However, the reliability of the technique continues to be debated due to the non-standardised inversion algorithms between electrical resistivity and soil moisture. Other techniques based on measurement of change in the soil's dielectric permittivity, a property influenced by the water content and thus the porosity are the conventional TDR (e.g. Scheuermann et al. (2002); Scheuermann and Bieberstein (2006); Scheuermann (2005)) or the use of the GPR technique (e.g. Xu et al. (2006)).

I have shown through measurements with GWS on dike models and comparison with co-located measurements with CMP and TRIME-TDR that the method can be used to reasonably measure the volumetric soil water content. Results and procedures used in the experiments can hence be applied usefully in the monitoring of infiltration and water flow in embankment dikes and other levee structures to ensure their stability and safety. In the low season where precipitation is low the amount of water in the dike is low. We may have large precipitation and flooding during the whole year except for the real cold season. When snow melts quickly in the Alps we may have flooding courts either in late February, March or April. In such a season with increasing precipitation and attending flooding over long periods, the dike's dielectric permittivity increases and it stores more water resulting in high degree of water distribution and seepage. GWS can thus provide a way of ensuring the stability and safety of embankment dikes by measuring the spatial VWC distribution based on dielectric permittivity measurements.

The experiments discussed so far described phases of controlled precipitation and flooding and consequent VWC determinations on dike models constructed with different soil layer types. These methods could be applied usefully in the field of agriculture to help improve agricultural practices. Water content distribution in the soil before the onset of irrigation can be estimated. Furthermore, the intensity of irrigation can be well planned across the field non-uniformly as may be desired.

One difficulty and lack of fairness in the experiments is having to compare data acquired from sources with different operational frequencies and support volumes. This is the case with co-located TRIME-TDR and GWS measurements. The quantity that plays decisive role in the material characterisation of soil is the conduction current-displacement current ratio or $\frac{\sigma}{\omega\varepsilon}$ (with $\varepsilon = \varepsilon_r \varepsilon_0$). At very high frequencies and low conductivities the soil behaves more as a dielectric (because the displacement current then dominates over conduction current) and the phase velocity and the depth of penetration of the electromagnetic wave become independent of frequency. However, at low frequencies and moderately large conductivities the phase velocity and penetration depth are frequency dependent and this gives way to dispersion and high attenuation effects. My experiments on the dike models were performed in very many cases with the 500 MHz antenna. A practical analysis given below shows that at high frequencies above 1 GHz, GPR is simply not applicable to moist and wet soils. Table 7.2 illustrates three standard cases of soils.

Soil Type	ε_r	σ [S/m]
dry	7	10^{-3}
moist	15	0.012
wet	30	0.3

Table 7.2: Illustration of three cases of dry, moist and wet soil (modified after King et al. (1981), Wilhelm and Brandelik (1998)).

The values of $p = \frac{\sigma}{\omega\varepsilon_r\varepsilon_0}$ for GPR frequencies in two main regions $0 < p < 1$ and $0 < p < 25$ are illustrated in Fig. (7.30) for electromagnetic wave at normal incidence with $k = \beta + i\alpha$ where $\beta = k_0\sqrt{\varepsilon_r} f(p)$ = wave number, $\alpha = k_0\sqrt{\varepsilon_r} g(p)$ = attenuation constant and $k_0 = \frac{\omega}{c}$. The relationship between the loss tangent $p = \frac{\sigma}{\omega\varepsilon}$ and the functions $\beta \propto f(p)/p$ and $\alpha \propto g(p)/p$ and frequency for the three types of soil are also shown. At high frequencies, p varies between 0 and 2 while $p > 5$ at low frequencies. This means that the high frequency case applies to dry soils for frequencies > 15 MHz while for moist and wet soils the high frequency case applies for minimum frequencies of 100 MHz and 900 MHz. Thus, working in wet soil between the frequency range 1 GHz and 100 MHz one operates in the intermediate range between $p = 0.2$ and $p = 0.5$. The dielectric coefficient is thus frequency dependent and the best way of comparing two techniques which are dependent on this quantity is to take co-located measurements also in the same frequency range.

The gravimetric method which is used as a standard against which other methods are calibrated and which was used to calibrate the TRIME-TDR (section 7.2.2) measures soil water content in the mass unit [g/g] instead of the desired volumetric unit [m^3m^{-3}]. It is usually converted to the volumetric water content using the density of water (taken as $1\,g/cm^3$). This has its accompanying errors due to the varying densities of water.

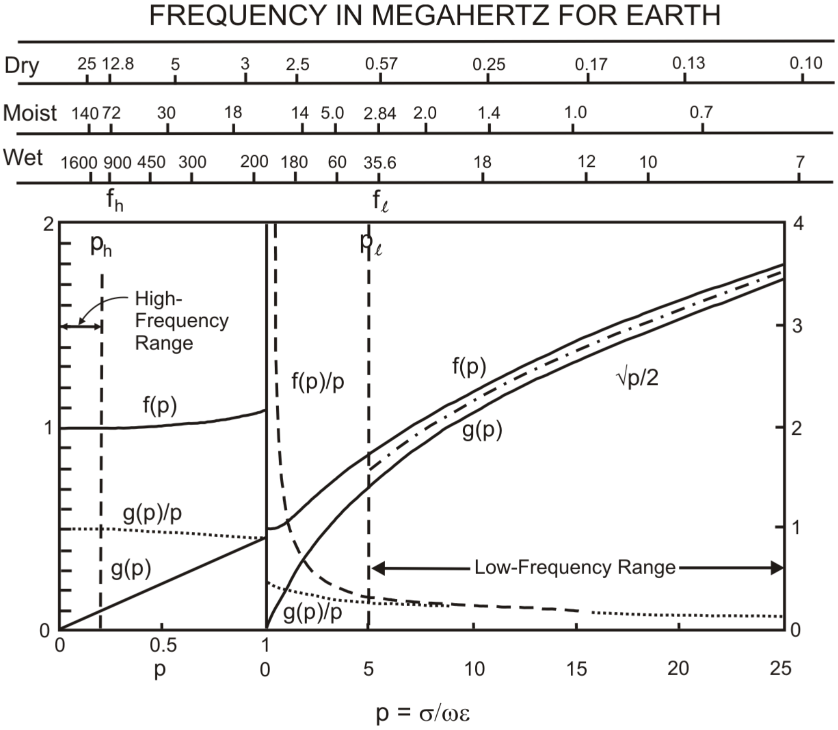

Figure 7.30: Frequency dependence of the phase velocity and attenuation of the electromagnetic waves for three types of soils for separate two cases - frequencies $p < 1$ with border case $p < 0.2$ for high frequencies and frequencies $0 < p < 25$ with border case $p > 5$ for low frequencies. (modified after King et al. (1981); Wilhelm and Brandelik (1998)).

Comparison of GWS with co-located measurements using TRIME-TDR and CMP on dike models showed almost identical trends with RMSD values of 0.011-$0.018\,m^3m^{-3}$ and $0.056\,m^3m^{-3}$ respectively. The relatively small RMSD of GWS means that the method can be creditably used to measure VWC of the soil. GWS has in addition many other advantages over the CMP and the other methods. For example, it has a much higher depth resolution and besides, the method enables the investigator to have a feeling of the level of attenuation and damping of the phase velocity of the electromagnetic wave in soil. The latter advantages are highlighted in the modal guided wave analysis for GWS method which is exhaustively discussed in appendix B.

Chapter 8

Soil Water Content Estimation in Semi-arid Burkina Faso Using the Ground Wave Method

8.1 Introduction

The CO and GWS methods which have been already discussed require knowledge of the depth to a reflecting medium. The apparent ground wave is the wave that travels directly between the transmitter and the receiver through the air side of the soil-air interface. The use of the apparent ground wave does not require information about a reflecting medium (Du (1996); Berktold et al. (1998); Sperl (1999)) and it is suitable for measuring the soil water content in the upper 10 cm of the soil (e.g. Huisman et al. (2001)). The apparent ground wave is the only wave whose propagation path length (i.e. the transmitter-receiver separation) can be predicted even before the start of the measurement. Soil water content determination using the apparent ground waves comes under various survey methods. These are the CMP and WARR in combination with CO.

The multi-offset CMP method of measuring soil water content has been used by a number of authors. For example, Huisman et al. (2001) analysed a 24 multi-offset data collected using 225 MHz antennas together with independent gravimetric soil samples and reported an accuracy of 0.024 m^3m^{-3}. Grote et al. (2003) reported of RMSD of 0.022 and 0.015 m^3m^{-3} compared to independent gravimetric soil sampling method in their multi-offset GPR measurements performed using 450- and 900-MHz. Du (1996) reported that the combination of the WARR and CO methods overcame limitations of the Radar Surface Arrival Detection (RSAD) technique in soil water content estimation. RSAD considers the first wave arrival after the air wave to as the apparent ground wave and uses this to determine the relative permittivity of the soil and subsequently the water content. Du (1996) pointed out that in a layered underground a critically refracted signal is always radiated and reaches the receiver earlier than the apparent ground wave. Hence, the apparent ground wave may in such a case be the third observed signal in the radargram. Galagedara et al. (2004) conducted GPR measurements with the WARR and CO methods with the 450 MHz antenna and reported that an optimal antenna separation of at least 1.5 m was needed to identify the apparent ground wave clearly. Other authors who have successfully used the ground wave method to retrieve soil water content information are Du and Rummel (1996); Lesmes et al. (1999); Sperl (1999), Huisman et al. (2003a,b); Hubbard et al. (2002); Grote et al. (2003); Galagedara et al. (2005a,c) and Weihermüller et al. (2007) among many others.

Soil water variability is effected by changes in the soil's electric properties, mineral and ionic content as well as the hydraulic properties both on the scale in the decimetre region (e.g. Igel et al. (2006)) and on the large scale in kilometre region (e.g. Jackson and Le Vine (1996)). Weihermüller et al. (2007) used the ground wave and off-ground GPR methods to monitor field scale soil water content at environmentally relevant soil depths of 0-10 cm.

In this section I discuss the application of the ground wave method to determine the spatial variation of soil water content in the upper ~10 cm depth of the soil. I relate the measured soil water content to rainfall along a 1 km long transect in semi-arid Burkina Faso. This project was funded by AMMA (African Monsoon Multidisciplinary Analyses) and was a co-operation between the Institute for Meteorology and Climate Research (IMK), Forschungszentrum GmbH, Karlsruhe (FZK) and the Geophysical Institute (GPI), University of Karlsruhe, Germany.

8.1.1 Motivation and Project Objectives of AMMA

The economies and lives of West African societies strongly depends on the West African Monsoon (WAM) which is responsible for rainfall in the region. Over the last 30 years due to dramatic changes in the WAM the region experienced one of the strongest climatic fluctuations and trends: from wet conditions in the 1950s and 1960s to much drier conditions from 1970s to 1990s. With a large rural population depending on rain-fed agriculture, the abrupt decrease of water resources had devastating effects on both the population and the economy.

The vulnerability of West African to the adverse effects of climate variability is likely to increase to critical heights in the next decades as demands on the resources increase with her rapidly growing population rate if nothing is done to address the situation.

The integrated European project AMMA (www.amma-eu.org) is motivated by the need to develop strategies of arresting the socio-economic impacts of climate variability and change in the WAM and improve the ability to forecast the weather and climate in the West African region. The objectives of AMMA for the West African project are:

- Improving weather forecasting in West Africa to create early warning system for food security, risk management and civil protection in West Africa.
- Improving climate forecasting for food security and the development of agronomic adaptation strategies at longer time scale.

- Managing food security, water resources and public health by studying both the direct effect of the monsoon on the human activities and the possible adaptive strategies.
- Implementation of a multi-scale and integrated environmental monitoring network by upgrading radiosonde network and providing the personnel with the appropriate training to maintain them over the long term.
- Offering training and education for african students and scientists to make them competent enough to maintain and develop forecasting and early warning systems by integrating new knowledge and user feedback.

8.1.2 IMK's Contribution to AMMA's Project Objectives

1. To study by observation and also through modelling with the Local Model (LM) of the German Weather Service (DWD) the triggering, propagation and modification of the life cycle of precipitating convective systems in relation to regional to large-scale meteorological conditions, boundary layer conditions and energy exchange at the Earth's surface resulting from spatial differences in land-use and soil water.
2. To perform two Special Observation Periods (SOPs) in Dano to thoroughly investigate the onset and the fully developed monsoon.

As contribution to the above mentioned AMMAs project objectives and targets IMK and GPI in collaboration with FZK undertook two field campaigns in Dano, Burkina Faso. The first Special Observation Period (SOP1) was from 1 to 15 June 2006 to investigate the onset of the monsoon. During SOP1, measurements of soil water, energy balance as well as boundary-layer and tropospheric conditions in the Dano area (Burkina Faso) were performed. The second Special Observation Period (SOP2) took place from July to August 2006 to investigate the fully developed monsoon. During the SOP2, ground based soil water measurements were conducted with TDR, FDR and GPR techniques. Measurements with GPR were done by me while that with TDR and FDR (using the SISOMOP) were performed by IMK.

8.1.3 Problem Statement

Rainfall, soil water, and evaporation are key elements in meteorological weather forecast models. Many research findings (e.g. Houser, 1996) have shown that soil water forms the main link between the hydrologic cycle and the energy balance of the ground surface. Hence, in addition to the field of meteorology soil water data find useful applications in fields such as water resources management, agriculture, soil science and civil engineering. In a semi arid region (e.g. Dano) soil water forms the main control of a number of hydrologic models and may exert a greater influence on the atmospheric boundary layer than vegetation (e.g. Franks et al 1997). For field scale measurements in the km region the spatial water variability influences meteorological and climatic processes (e.g. Chanzy (2003)), and also controls water runoff (e.g. Kirby (2001)) and evapo-transpiration rates (e.g. Wetzel and Chang (1987)).

Despite this importance of soil water, long term soil water variability data are difficult to come across. This is because conventional point measurements like gravimetric soil sampling, TDR and FDR are restricted to the mapping of small areas and their application are time consuming and labour intensive especially when field scale applications are envisaged. Field scale applications with point measurements therefore often result in a scanty data representation of the survey area. Furthermore, these techniques are invasive and may disturb the soil during the course of mapping, thus, preventing more accurate in-situ soil water measurements (e.g. Lunt et al. (2005)). In a region where the soil water content distribution is strongly heterogeneous, interpretation of results might lead to the wrong evaluation of the soil water content distribution pattern. Aircraft and satellite remote sensing methods provide fast and effective method for mapping soil water content data over large areas (e.g. Jackson et al. (1995, 1999); D'Urso and Minacapilli (2006)). However, their disadvantage is that they retrieve soil water data at large scales with coarse resolutions. On such scales the small scale-variability in soil water content (e.g. in the centimetre region) is usually masked.

The spatial soil water variability is linked to the variability in the soil hydraulic properties at small scale (e.g. Ritsema and Dekker (1998); Igel et al. (2006); Igel (2007); Schmalholz (2007) as well as the variability at field scale (e.g. Jackson and Le Vine (1996)). The effects of small-scale heterogeneity in land surface characteristics on the large-scale fluxes of water and energy in the land-atmosphere system has become a central focus of many climatology research experiments and it is a critical variable that controls the non-linear behaviour of land-atmospheric interactions (Wood (1997)).

Information on small scale spatial soil water variability is essential for calibrating, validating and downscaling satellite-retrieved soil water data. For meteorological modelling purposes it is essential to establish a relationship between the spatial water variability in the inputs and model parameters, the scale being modelled and the proper representation of the hydrologic processes at that scale (Wood (1997)).

In order to characterise satellite-retrieved soil water data in the Dano region of Burkina Faso a number of ground-based field measurements were carried out with TDR, FDR and the GPR. The satellite equipment used by IMK, Karlsruhe, had a spatial resolution of 25 km. Ground-based experiments were taken along a 1 km long transect to help characterise soil water information within the footprint of the satellite equipment. TDR and FDR probes were planted every 200 m along the transect while GPR retrieved soil water information at every 0.1 m along the transect.

An energy balance station was positioned at about 650 m along the transect. This provided information like latent and sensible heat fluxes, net radiation, soil heat flux, rainfall, wind direction, evapo-transpiration, air and sonic temperature and relative humidity for the earth-atmosphere feedback and boundary layer growth.

8.2 Materials and Methods

8.2.1 Description of Project Site

The experiments were conducted in the neighbourhood of the Bontioli Faunal Reserve near Bontioli (11 ° 10′ N, 03 ° 05′ W) close to Dano in Burkina Faso (8.1(a)). The soil is dominated by highly weathered ferruginous, pebbly and quartzitic sandstones. This type soil is commonly called laterite. Oxidation of its iron components gives it a typical reddish-brown colour (Fig. 8.1(b)).

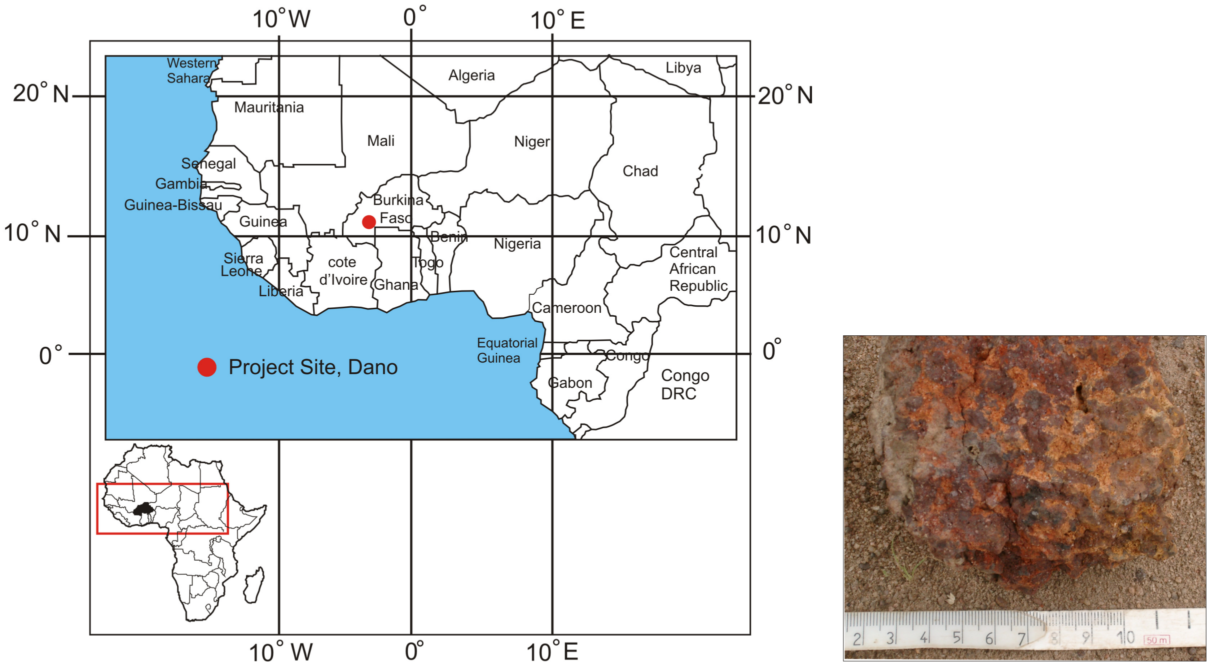

(a) Project site location (scale: 1:50 000 000)

(b) A laterite

Figure 8.1: Project site with a laterite rock sample in a pebbly quarzitic sandy soil.

Table 8.1 gives a summary of texture [μm] and mineral composition for soil samples taken between depths of 0 and 25 cm at Dano.

This soil type comes under the textural class loamy sand according to Soil Taxonomy (Soil Survey Staff (1975)). The relief of the area is on the average flat and the vegetation is savannah grass with open shrubs of acacia trees.

Grain Size	Fraction [%]	Mineral Composition	Fraction [%]
>2000	34.18	Quartz	75.03
500-2000	23.78	Goethite	12.10
250-500	12.57	Kaolinite	5.80
63-250	14.26	Muscovite	3.24
20-63	14.90	Haematite	2.97
2-20	0.00	Rutile	0.78
<2	0.31		

Table 8.1: Summary of texture and mineral composition for soil samples between depths of 0-25 cm.

8.2.2 GPR Data Collection

I used a Subsurface Interface Radar (SIR) System-3 from Geophysical Survey Systems Inc. (GSSI) with two bistatic antennas of central frequencies 300 MHz for the data collection and operated the GPR in the WARR and CO modes. As reference measurements IMK installed TDR and SISOMOP probes every 200 m along the transect (Fig. 8.2).

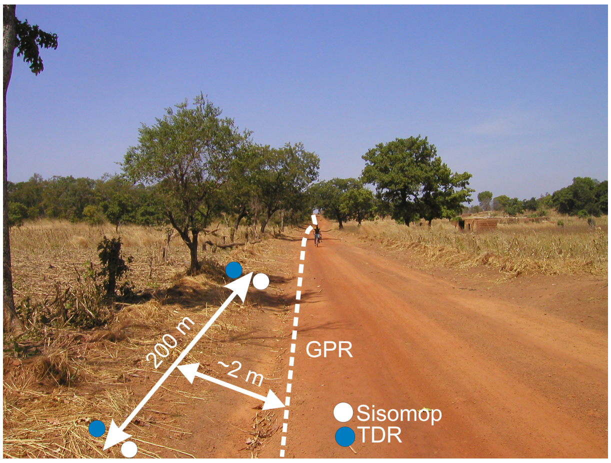

Figure 8.2: Schematic diagram illustrating the observation points for the ground measurements at Dano, Burkina Faso: GPR (hatched line), TDR (blue circle) and SISOMOP (white circle).

These methods have been described by Du (1996), Huisman et al. (2003a,b) and Galagedara et al. (2005a,c). Initially, I kept the receiver position fixed and gradually moved away the transmitter along the transect until an optimal transmitter-receiver separation was found at which the apparent ground wave could be best identified on the radargram. The optimal separation was found to be 1.2 m. This is the WARR method. In the second part of the experiment I kept the antennas fixed at the optimal separation with the aid of supporting wooden frames and moved the system as a unit at pace speed along the 1 km long transect. This is the CO method. An odometer wheel connected to the GPR system (Fig. 8.3) triggered data collection every 0.1 m.

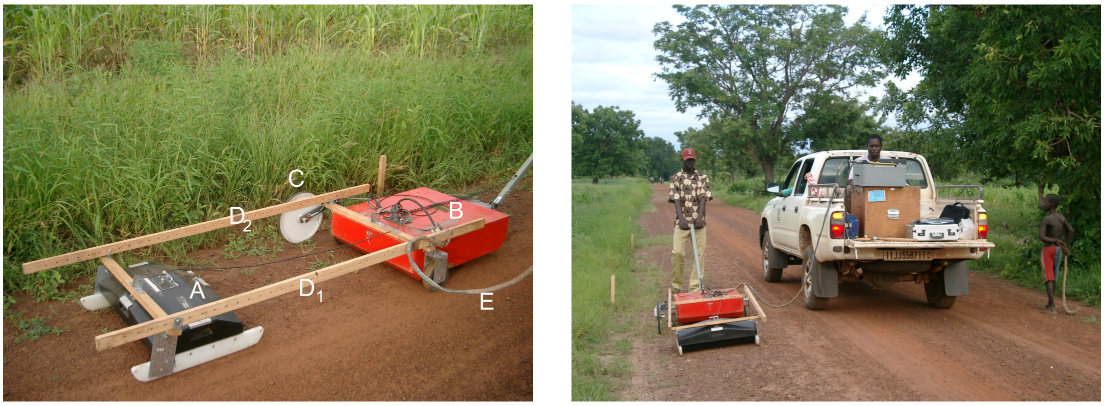

(a) Antenna configuration with wooden support system

(b) Operation of GPR in CO mode

Figure 8.3: The CO field operation: Antennas(A,B), Odometer (C), Wooden supports ((D_1,D_2,), Cable (E) to radar system.

8.2.3 GPR Data Processing

In order to estimate the soil water content from the ground wave data the *zero-time* (i.e. the start of the signal, indicated by the crossing point of the air and apparent ground wave on the radargram) has to be first calibrated (Fig. 8.4).

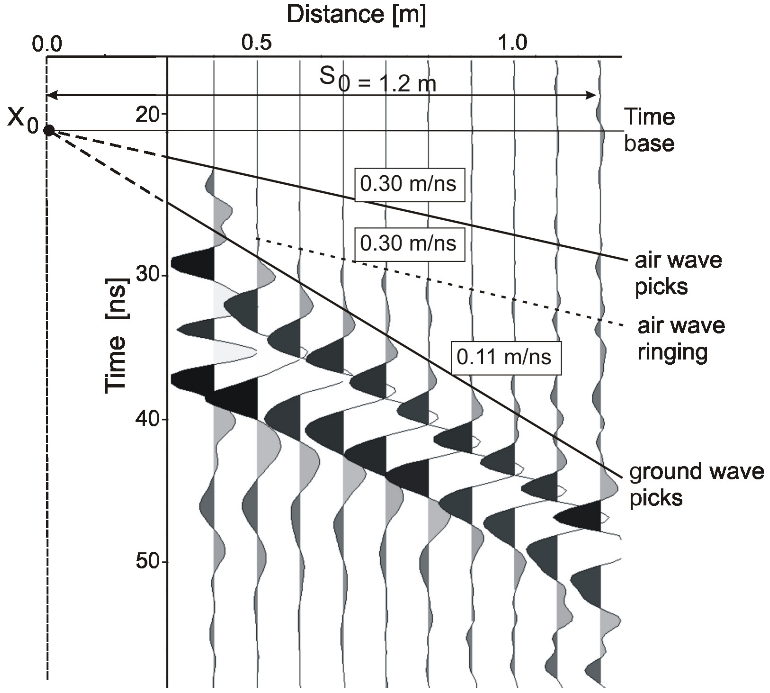

Figure 8.4: Radargram (WARR mode) showing air and ground wave picks.

I calibrated the *zero-time* from the WARR data and then determined the ground wave velocities from the CO data (Fig. 8.5). The air wave has a higher velocity (3×10^8 ms^{-1}) than the apparent ground wave ($\sim 1 \times 10^8$ ms^{-1}) and hence, reaches the receiver earlier. The air wave arrival time was used as a reference in calculating the *zero-time*. The apparent ground wave velocity was then calculated from the CO data by dividing the transmitter-receiver separation by the travel time of the ground wave. With the Reflexw software package (Sandmeier (2007)). I determined the soil water content from the WARR and CO data by doing the following:

- I determined the velocities of the air wave ($c = \frac{S_0}{t_{\text{aw0}}}$) and ground wave ($v_0 = \frac{S_0}{t_{\text{gw0}}}$) from the WARR data where S_0, t_{aw0} and t_{gw0} are the optimal antenna separation, air wave and ground wave travel times from transmitter to receiver respectively (see section 6.4.3, p. 70). On the radargram the air wave and ground wave picks appear as straight lines and their velocities are the inverse of their slopes (Fig. 8.4). The apparent ground wave is often difficult to distinguish from the other waves on the radargram in most cases due to superposition with the other waves or the weak radiation of the signal which may result from the poor

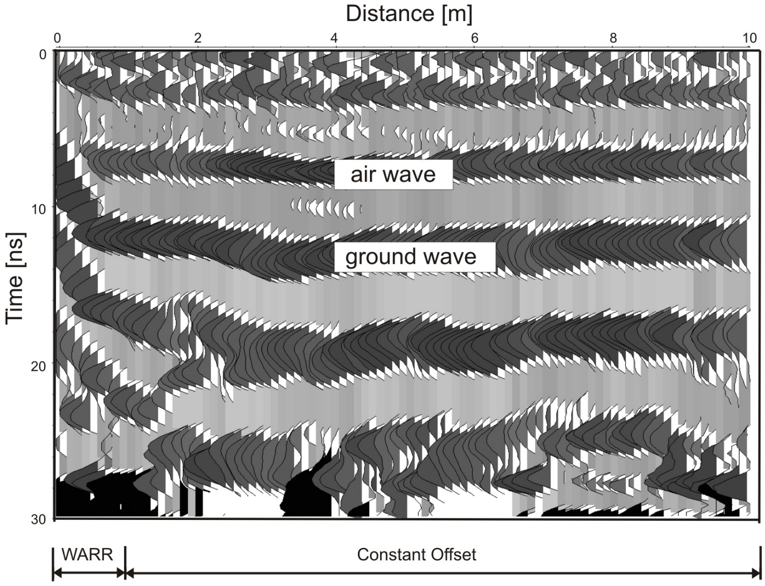

Figure 8.5: Radargram showing the WARR and CO modes.

coupling of the antenna with the ground surface. On the radargram the ground wave has the following distinguishing characteristics:

1. It travels slower than the air wave and its slope from the WARR data is higher than that of the air wave.
2. Its amplitude decays much faster with distance than that of the reflected waves.

- I located the point X_0 on the radargram (see Figs. 6.8 and 8.4) where the air wave and the ground wave travel times crossed and used the Reflexw tool *static correction* to calibrate the zero time. The *static correction* tool defines a reference time base (corresponding to the time at point X_0) for calculating the times of travel for the ground wave.
- From the CO data I picked the travel times (t_{GW}) of the apparent ground wave phase (Fig. 8.5). The was partly done with the help of the Reflexw tool *phase follower* and stored them in an ASCII format.
- The velocity of the ground wave v_{gwi} is then calculated by Eq. (6.55), p. 71 and the dielectric coefficient by $\varepsilon_r = c^2/v_{gwi}^2$.
- The soil dielectric coefficients calculated in this way were converted to water content by using the empirical relation from Topp et al. (1980).

The survey profile was planar (and antenna-ground coupling was very good), hence, corrections due to the drifting of the antennas for uneven surfaces during the course of the CO experiment as discussed by Wollny (1999) were not needed.

8.2.4 Exploration Depth of GPR Ground Wave

We have already discussed various relations in section 6.4.2 p. 69 for the calculation of the exploration depth (or the depth of influence) of the ground wave. The pure empirical relation established by Sperl (1999) is used here for the calculation of the exploration depth because I find it most convincing. Sperl thoroughly made investigations the behaviour of the ground wave through various numerical models and to come up with the equation $d/d_1 = 0.145\sqrt{\lambda_s/\lambda_1}$ where d [m] and λ_s [m] are the exploration depth and wavelength of electromagnetic wave in soil respectively. The parameters d_1 and λ_1 are to render d and λ_s dimensionless. If we consider an extreme velocity range $0.05\,\text{m/ns} < v < 0.15\,\text{m/ns}$, for the propagation of an electromagnetic wave through soil then, Sperl's empirical relation gives the exploration depth range d as $0.06\,\text{m} < d < 0.1\,\text{m}$. In the analysis following, the exploration depth is taken as the upper 0.1 m of the soil.

8.2.5 Conversion of GPR-derived Soil Water Content into [mm] of Water

I converted the soil water content [m^3m^{-3}] determined from the WARR-CO method into mm of water by

$$\theta_v\,[\text{mm}] = \frac{\theta_v\,[\text{m}^3\text{m}^{-3}] \times s\,[\text{m}^2] \times d\,[\text{m}] \times 1000\,[\text{mm}]}{[\text{m}^3]} \tag{8.1}$$

where θ_v is the mean soil water content, s is the surface area of the antenna configuration, d is the approximate exploration depth, T is the transmitter and R is the receiver. Eq. (8.1) is an approximation since d is an approximate value. Fig. 8.6 shows a schematic illustration of the measuring volume of the GPR. The optimal antenna separation was 1.2 m and the width of the configuration was 0.645 m (see also Fig. 8.3(a)). This conversion fascilitated easier comparison of GPR-derived soil water content with rainfall and evapo-transpiration rates (see Fig. 8.9).

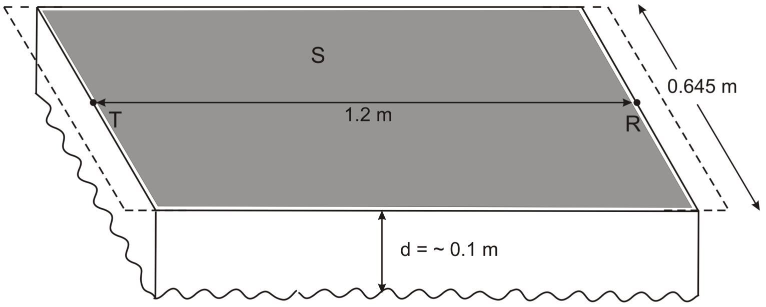

Figure 8.6: Schematic illustration of antenna configuration and measured volume.

8.2.6 R^2 and F Tests

I used the R^2 and F tests to evaluate the degree of fit of my regression equations. Hence, I briefly discuss these tests.

The R^2 (called *R-squared* or *coefficient of determination*) test measures the degree to which an estimated regression equation fits the sample. The R^2 of the regression equation is defined by Pindyck and Rubinfeld (1991) as

$$R^2 = 1 - \frac{\text{ESS}}{\text{TSS}} = \frac{\text{RSS}}{\text{TSS}} \tag{8.2}$$

where ESS is the residual sum of squares; TSS is the total sum of squares and RSS is the regression sum of squares. R^2 is often considered informally as a goodness-of-fit statistic and used to compare the validity of regression results under alternative specifications of the independent variables in the model (Pindyck and Rubinfeld (1991)). However, the goodness of fit is relative. In other words, there is no simple method of determining how high R^2 must be in order to be considered satisfactory. The F test can be formally used to test the significance of the R^2 statistic and the overall fit regression equation. In order to do this a critical F value based on the level of significance is selected. This critical value takes into account the number of independent variables $(k - 1)$ and the degrees of freedom $(N - k)$ as well as the sample size N. The F test is defined by

$$F_{k-1,N-k} = \frac{R^2}{1 - R^2}\frac{N - k}{k - 1} \tag{8.3}$$

The result of the F test enables us to *accept* or *reject* the null hypothesis.

8.3 Results

Results of the experiment are discussed in different ways: First the influence of soil water on the ground wave amplitude is discussed (section 8.3.1). I then discuss the temporal and spatial distribution of soil water using classical statistics (sections 8.3.2 and 8.3.3). Furthermore, geostatistical analyses are applied to the data with discussion on the correlation lengths and nugget effects to help evaluate the spatial pattern of soil water content with infiltration (section 8.3.3). Next, I discuss the effect of GPR operational frequency on the apparent ground wave through modelling (section 8.3.4) before comparing GPR with TDR and FDR techniques in soil water content determination (section 8.3.5). Finally, the relation of soil water content to ground surface-atmosphere feedbacks is discussed (section 8.3.6).

8.3.1 The Influence of Soil Water on the Ground Wave

Water in the soil influences the ground wave velocity as well as its amplitude. The experiment reveals the following behaviour of the ground wave with soil water:

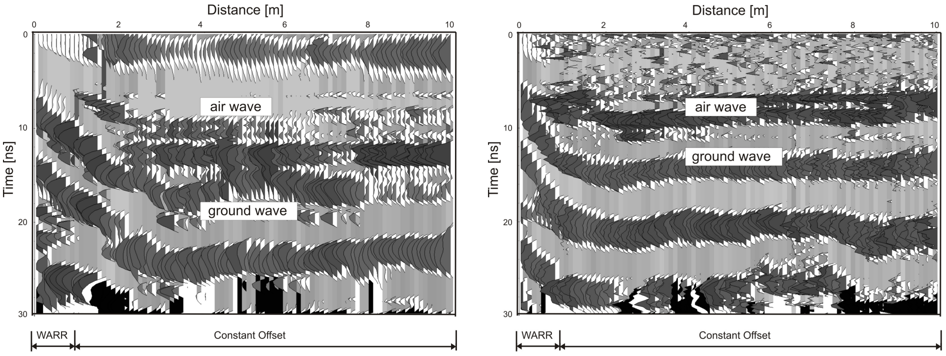

(a) 1st August: after heavy downpour (b) 3rd August: (no rain)

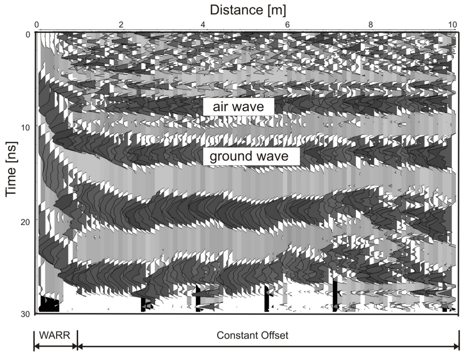

(c) 5th August: (no rain)

Figure 8.7: Influence of soil water on the ground wave radiation in August 2006: (a) after heavy downpour, (b) after 2 days of no rain, (c) after 4 days of no rain.

- It is more strongly radiated in a wet soil than in a dry one (Figs. 8.7(a), 8.7(b) and 8.7(c)). This might be due to the better capacitive coupling between the antennas and the ground when the soil surface is wet than when dry. The ground wave which is recorded by the antennas travels in the near-surface and it is highly attenuated both with distance above the surface and from the transmitter. The capacitive coupling between the ground and the antennas must be very good in order to register it effectively. A high capacitive coupling (which is usually the case for a wet soil) leads to a higher dielectric coefficient. Subsequently a greater amount of energy is radiated between the transmitting and receiving antennas. Fig. [8.7(a)] shows a radargram picked after a heavy downpour and Fig. (8.7(b)) and Fig. (8.7(c)) show radargrams taken two and four days later respectively, without rain. The apparent ground wave amplitude is seen to decay from wet to dry soil. It is thus easier to identify the ground wave in the radargram when the soil is wet than when it is dry. There are other factors, however, such as surface roughness, frequency, type of soil, height of antenna above the ground which jointly influence the amplitude of the ground wave. For example, where the ground surface is highly undulating most of the energy from the transmitter might be lost due to the poor capacitive coupling between the antennas and the ground surface. In such a case soil water may contribute very little to the ground wave amplitude.

- As the amount of water in the soil increases the velocity of the GPR wave decreases due to the effect of electrical conductivity which usually increases with increasing water content.

8.3.2 Temporal Variability of Soil Water Content

From my GPR measurements, I determined the mean soil water content [m^3m^{-3}] between 600-700 m along the transect. This was to help me closely relate results of GPR-derived soil water content to rainfall and evaporation data taken by the energy balance station which was positioned about 650 m along the transect. I converted the VWC to [mm] of water as discussed in section 8.2.5. Fig. 8.8 shows the temporal variability of GPR-derived soil water content at Dano, Burkina Faso between August 1-19, 2006.

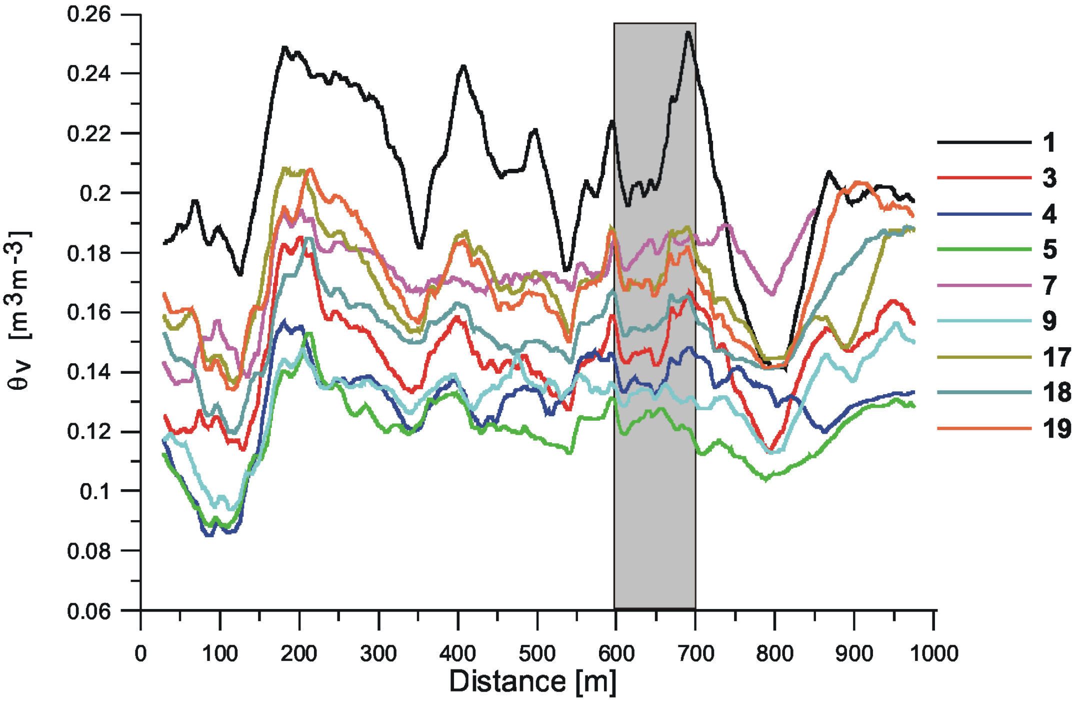

Figure 8.8: Spatial variability of GPR-derived soil water content between August 1-19, 2006.

The graphs show means of 500 values i.e. means over a distance of 50 m. The vertical column highlights the distance between 600-700 m along the transect and means of soil water content values between August 1-19, 2006. I converted mean soil water values in this zone from [m^3m^{-3}] to [mm] to enable direct comparison with rainfall and evapo-transpiration rates. This comparison is displayed graphically in Fig. 8.9 which shows the temporal variation of GPR-derived soil water content, rainfall and evapo-transpiration rates in [mm]. Rainfall and evapo-transpiration rates were determined by IMK.

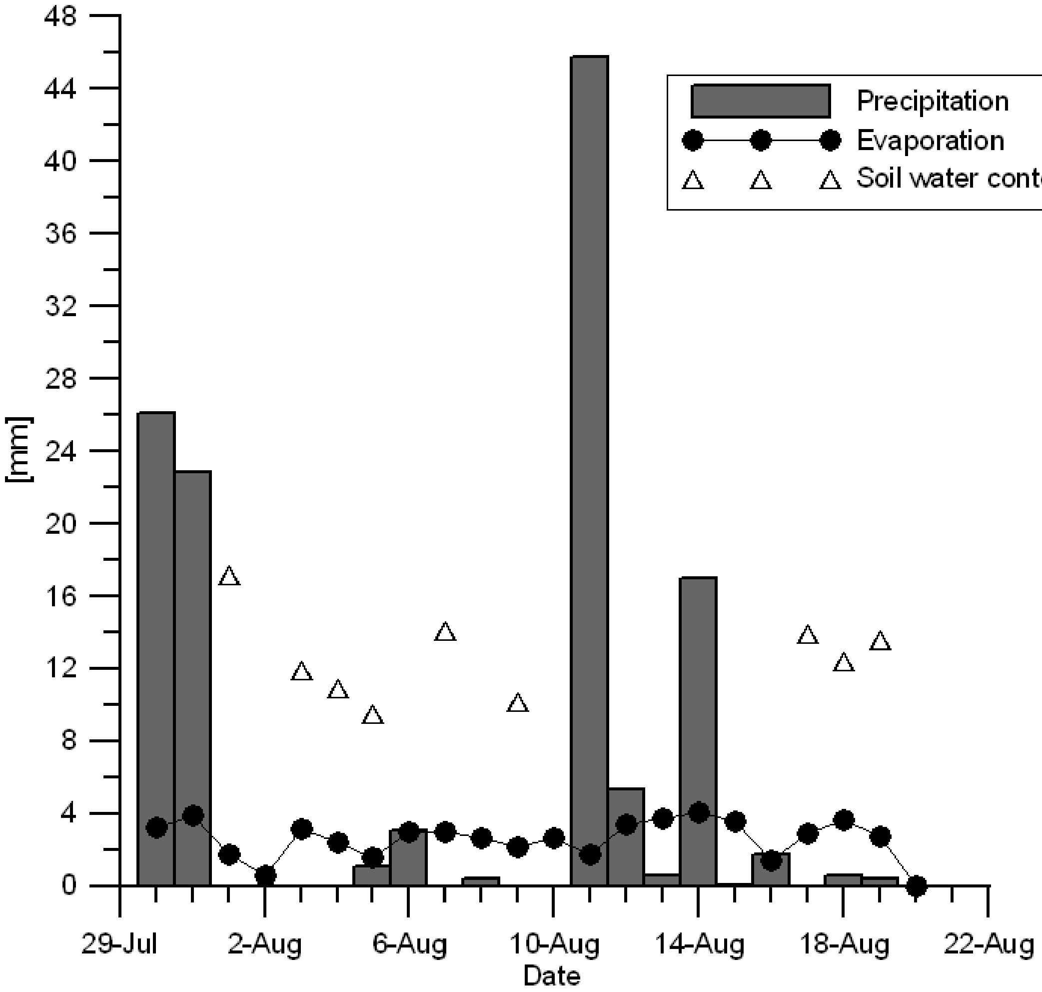

Figure 8.9: Temporal variation of GPR-derived soil water content, the influence of rainfall and evapo-transpiration.

It is seen from Fig. 8.9 that the temporal variation of GPR-derived soil water content is dominated by rainfall and that evapo-transpiration plays an insignificant role in the wet season at which measurements were taken. The amount of rainfall reaching the soil is divided into soil water content, run-off, seepage and evaporation. A list of rainfall rates, evaporation rates and soil water content with dates of measurement is provided in appendix C.3.

8.3.2.1 Scatter Diagrams of Soil Water Content Distribution

In this section I discuss the relation between soil water content values measured on two separate days graphically with the help of scatter diagrams. The horizontal axis of each scatter diagram defines GPR-derived soil water content values for a particular day and the vertical axis defines co-located values taken a day or two later. These scatter diagrams help to visualise any correlations that may occur in the temporal soil water content distribution and also provide statistical information such as the mean, standard deviation (std), coefficient of variation (CV), range and median of the distribution.

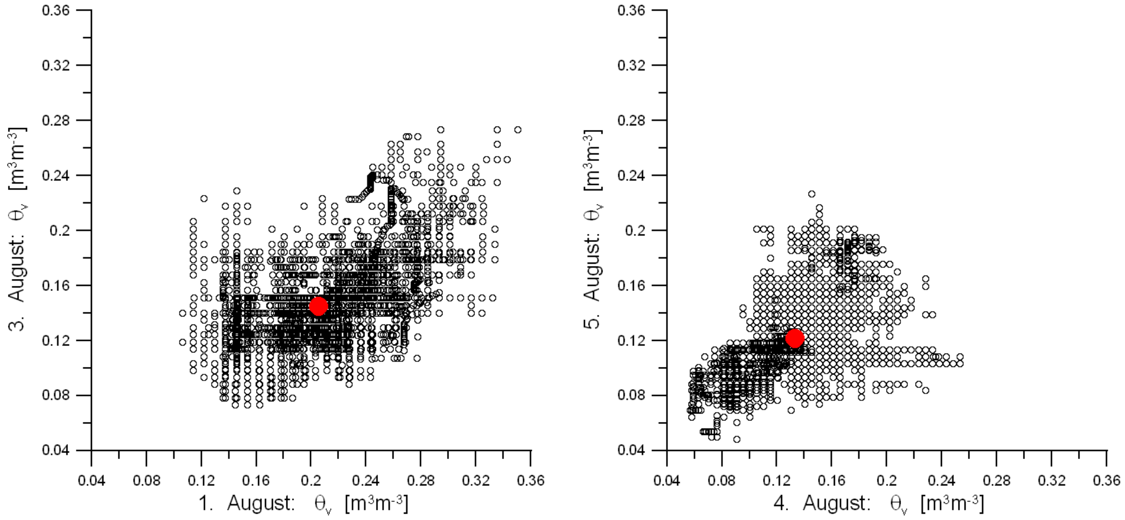

(a) 1 August-3 August (b) 4 August-5 August

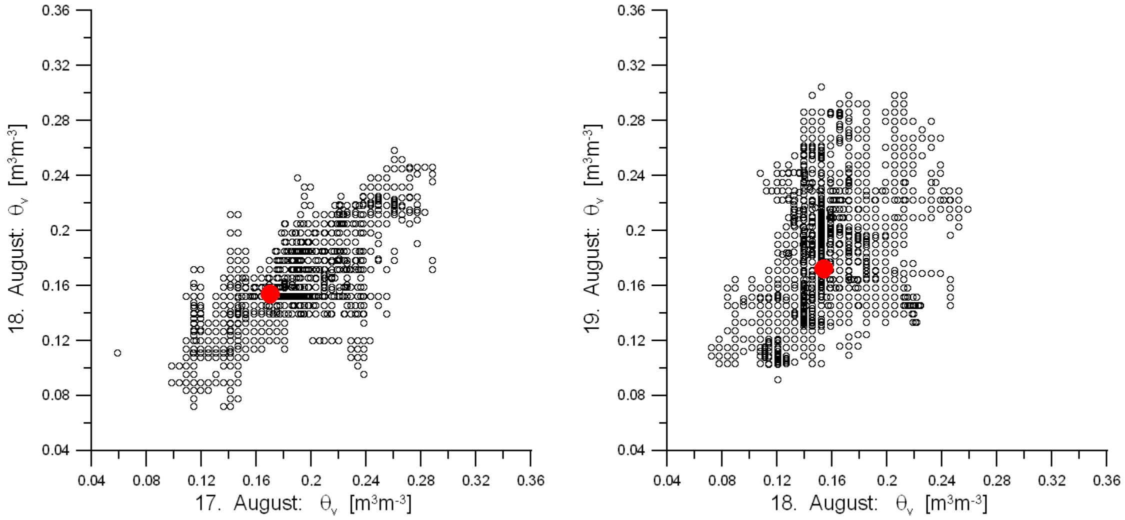

(c) 17 August-18 August (d) 18 August-19 August

Figure 8.10: Scatter plots of soil water content for two successive days of observation.

As seen from Fig. 8.9 soil water content decreases from August 1 to August 5 and from August 17 to August 18. It increases from August 18 to August 19. Fig. 8.10 shows scatter diagrams of soil water content distribution between two successive days of observation. The figures show that GPR is able to detect both large (e.g. Fig. 8.10(a)) and minute changes (e.g. Fig. 8.10(b)) in the soil water content as influenced mainly by the effect of rainfall. The mean of the distribution for each diagram is indicated by a large red circle. From the coordinates of the means the difference in the mean soil water content between successive days of observation can be deduced. This difference, being highest between August 1 and August 3 and lowest between August 4 and August 5 follows after the the pattern of rainfall. Table 8.2 gives a summary of statistical properties of soil water distribution pattern in the surveyed area.

Date	Mean VWC [m^3m^{-3}]	Std [m^3m^{-3}]	CV	Range [m^3m^{-3}]	Median [m^3m^{-3}]
1 Aug 06	0.2032	0.0411	0.2025	0.2439	0.2032
3 Aug 06	0.1443	0.0286	0.1978	0.2002	0.1457
4 Aug 06	0.1297	0.0234	0.1809	0.1963	0.1302
5 Aug 06	0.1197	0.0203	0.1694	0.1788	0.1134
9 Aug 06	0.1308	0.0219	0.1678	0.1582	0.1370
17 Aug 06	0.1686	0.0274	0.1627	0.2296	0.1666
18 Aug 06	0.1567	0.0232	0.1481	0.1866	0.1522
19 Aug 06	0.1716	0.0298	0.1734	0.2306	0.1645

Table 8.2: Summary of statistical soil water distribution pattern at Dano, Burkina Faso between 1st-19th August 2006.

8.3.2.2 Trend of Soil Water Content for 5 Days without Rainfall

The heterogeneity in the soil water distribution in Dano is further indicated by the soil water content difference plots shown in Fig. 8.11. Differences in soil water content for 5 days of no rainfall after rainfall on 31st July 2006 are plotted. For the distribution over two days *day 1* and *day 2*, co-located soil water values of *day 2* are subtracted from that of *day 1*. On the graphs (Fig. 8.11), soil water values above the line $\Delta\theta_v = 0$ represent soil water values of *day 1* in excess of *day 2*. Soil water values below $\Delta\theta_v = 0$ are values of *day 2* in excess of *day 1*. Generally, (as seen from Fig. 8.11) the difference in soil water content increases from 1st August to 5 August 2006 indicating conditions of dryness.

However, isolated zones contrary to expectation, are seen to be relatively wet (see Fig. 8.11(d) for zones below the line $\Delta\theta_v = 0$). The nature of the soil and the possible preferential water infiltration paths in these zones might be contributory to this heterogeneous distribution trend.

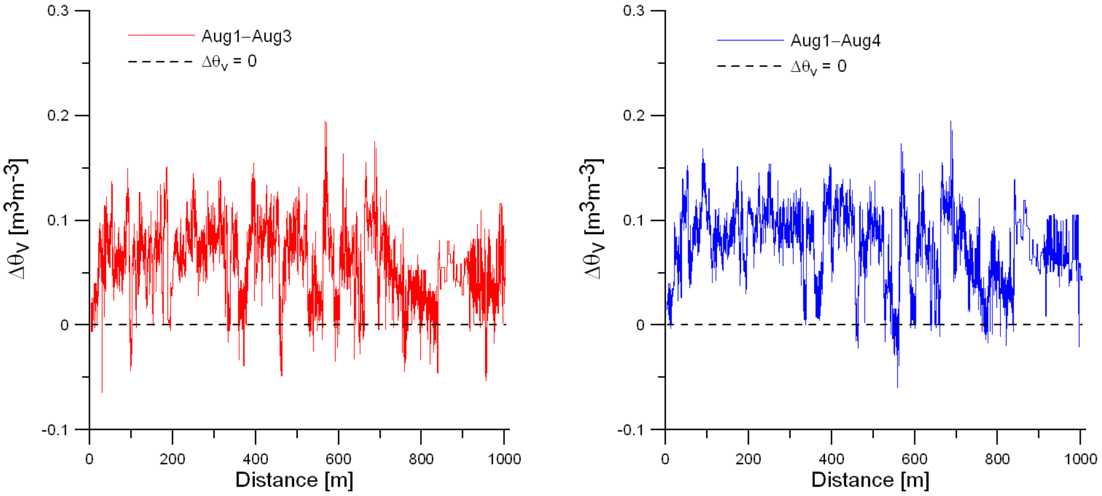

(a) Difference: August 1, August 3, 2006.

(b) Difference: August 1, August 4, 2006.

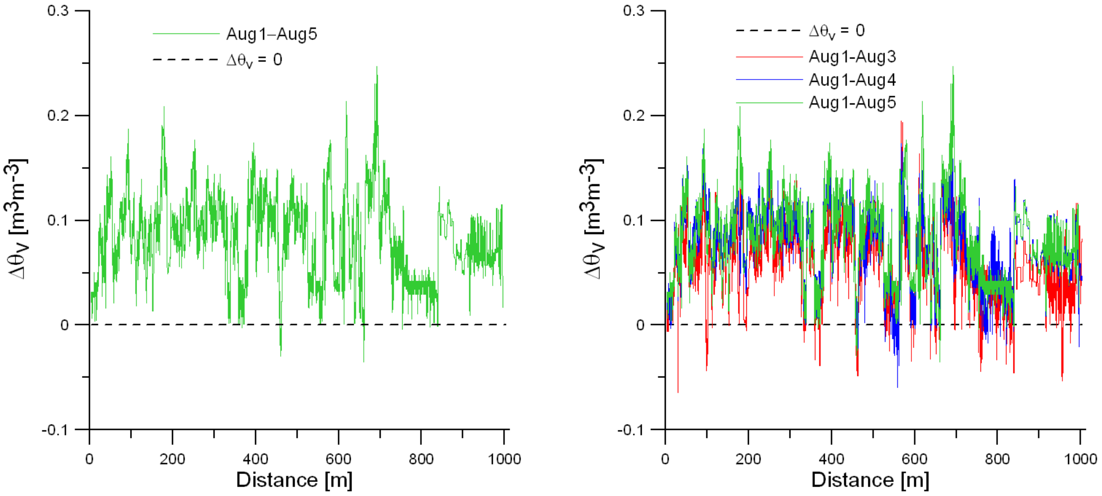

(c) Difference: August 1, August 5, 2006.

(d) Summary of differences: August 1 to August 5, 2006.

Figure 8.11: Differences in soil water content between August 1-5, 2006 after antecedent rainfall on July 31, 2006. Soil water data for 1st August 2006 are used as reference.

8.3.2.3 Histograms of Soil Water Content Distribution

A histogram helps to visualise graphically the shape of a set of data e.g. how far it spreads out and where its centre is. Figs. 8.12 and 8.13 show histograms of the soil water content distribution in Dano, Burkina Faso between August 1-5, 2006. Other histograms of the soil water content distribution between August 7-19, 2006 are shown in appendix C.

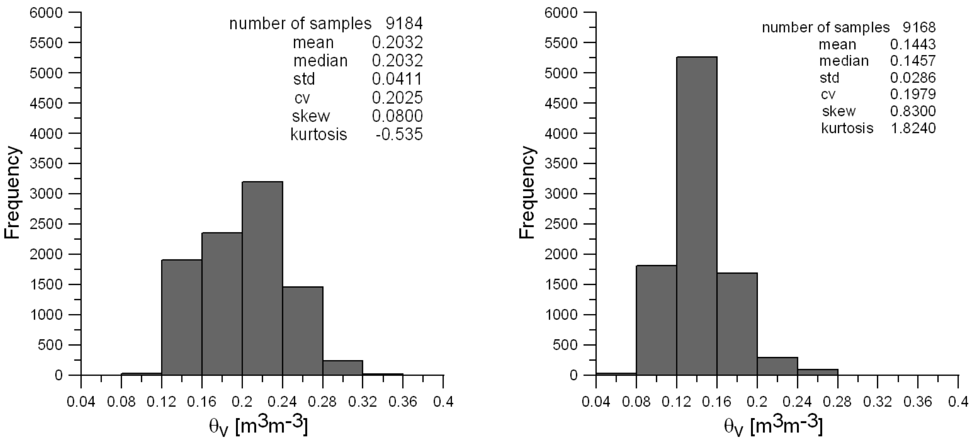

(a) 1st August 2006.

(b) 3rd August 2006

Figure 8.12: Histograms of soil water content from August 1-3,2006.

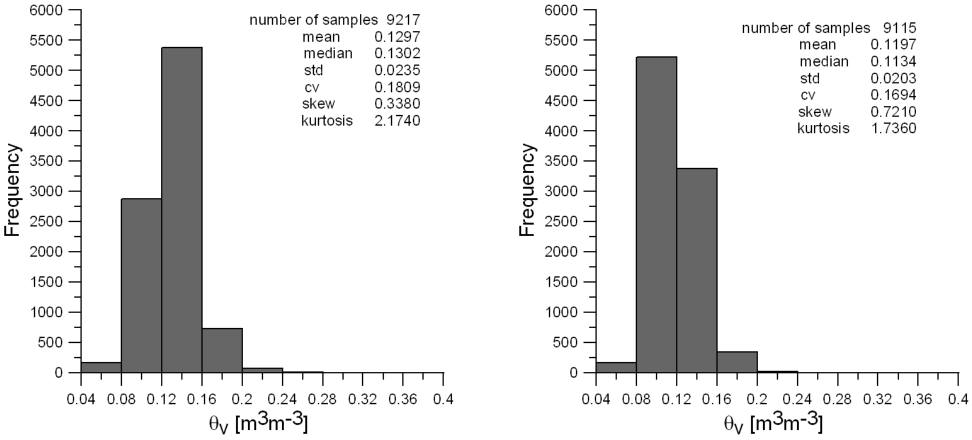

(a) 4th August 2006

(b) 5th August 2006

Figure 8.13: Histograms of soil water content from August 4-5,2006.

A histogram in addition, provides statistical information on the number of samples, mean, median, standard deviation, coefficient of variation (ratio of the standard deviation to the mean), skewness (skew) and kurtosis of the distribution. The skewness characterises the degree of asymmetry of the distribution around the mean. Positive values of skewness mean that the distribution is asymmetric with the right tail longer than the left. Negative skewness indicates that the distribution is asymmetric with the left tail longer than the right. A normal distribution has a skewness of zero. The kurtosis characterises the relative peakness or flatness of the distribution relative to the normal distribution. A normal distribution produces a kurtosis of 3. A negative kurtosis indicates a relatively flat distribution while a positive kurtosis indicates relatively peaked distribution. For detail description of these statistical properties the reader is kindly referred to statistics books like Pindyck and Rubinfeld (1991), Salvatore and Reagle (2001), Rumsey (2003), McClave and Sincich (2006), Spiegel and Stephens (2007),

From the distribution pattern displayed by these histograms, it is seen that the distribution is not a normal one. As the soil dries up from 1st August towards 5th August, 2006 due to lack of rains and the effect of evaporation, the means and also the medians of the distribution gradually shift towards left (i.e. lower values) This produces positive skewness. Furthermore, generally, for the drying-up soil the higher water classes (bins) diminish while the lower bins build up. This pattern yields the displayed peaked distribution.

In addition to Fig. 8.13, Table 8.3 summarises the frequency distribution pattern of the soil water content classes expressed in [%] as the soil dries up from August 1 to August 5, 2006.

Date	Class Interval [m^3m^{-3}]							
	0.04-0.08	0.08-0.12	0.12-0.16	0.16-0.2	0.2-0.24	0.24-0.28	0.28-0.32	0.32-0.36
	Class Frequency [%]							
1	0	0.4	20.8	25.7	34.8	15.7	2.6	0.4
3	0.4	19.8	57.3	18.3	3.2	1.0	0	0
4	1.9	31.1	58.2	8.0	0.8	0	0	0
5	1.9	57.0	37.0	3.8	0.3	0	0	0

Table 8.3: Summary of soil water distribution pattern from August 1-5, 2006. The class frequency is expressed in [%].

Between August 4 and August 5, for the class 0.04-0.08 [m^3m^{-3}], the frequency remains constant at 1.9 [%] though the soil apparently dries up further. This occurrence likely reflects the lower limit of my GPR equipment. The range of validity of soil water estimation from the Topp et al. (1980) calibration formula used in this work is about 0.05-0.50 [m^3m^{-3}] (Charlesworth (2005)). TDR and FDR techniques will be likewise limited when the Topp calibration equation is used.

8.3.2.4 Relationship of Mean Soil Water Content to Coefficient of Variation

Fig. 8.14 shows the relationship between the mean soil water content and the coefficient of variation (CV).

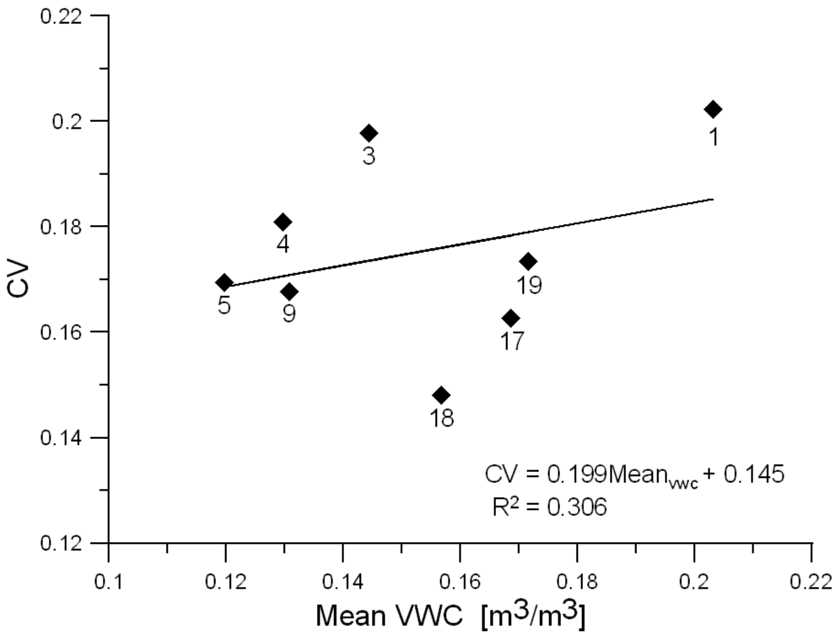

Figure 8.14: Relating mean soil water content to CV. The numbers in the figure indicate dates in August 2006.

The regression equation fitting the data yields a coefficient of determination, $R^2 = 0.306$. This shows that there is a correlation between the mean soil water content and CV, the degree of this correlation is, however, determined by the F test. Using Eq. (8.3), for $N = 8$ and $k = 2$, the F test gives $F_{1,6} = 2.64$. This value is below the critical value of 5.99 at 95 % significance. Hence, there is a poor correlation between the mean soil water content and CV. It is thus difficult to predict the behaviour of the dispersion of soil water indicated by CV as the mean soil water increases or decreases.

Literature, also presents no conclusive relationships between the two. Hubbard et al. (2002) reported from investigations made on soil water content using GPR on California vineyards that the highest soil water content variability occurred in a wet soil with the lowest in a dry soil. Miyamoto et al. (2003) reported rather of a decrease of CV with soil water content analysed with TDR under vegetation conditions. They attributed spatial trend to micro-topographic features resulting from tillage. Other investigators (e.g. Western et al. (1998); Famiglietti et al. (1999); Hupet and Vanclooster (2002)) reported of an increase in variability with decreasing soil water content. Western et al. (2004) characterised the geostatistical properties of soil water patterns from different sites in Australia and New Zealand using TDR. They reported of an increase in variance with soil water at the Australian sites and a decrease at the New Zealand sites. They attributed the differences to be partly due to differences in meteorological impacts between the sites and also differences in soil properties. Gravimetric soil water measured at depths 0-0.40 m by Junior et al. (2005) showed spatial structure at all depths except 0-0.10 m. The spatial character of soil water in a region seems then to be controlled by intrinsic factors like soil heterogeneity (e.g. Trangmar et al. (1985, 1987)) as well as extrinsic factors like climate and agricultural practices.

8.3.3 Spatial Variability of Soil Water Content

For discussion of the spatial soil water variability I have selected water data taken on August 1, 2006 when the soil was most wet after a heavy downpour (Fig. 8.15(a)) and August 5, 2006 when the soil was most dry after 4 days of no rainfall (Fig. 8.15(b)). As seen in these figures the spatial variability is highly heterogeneous. The highest soil water content variability was observed on August 1, 2006 while the lowest was observed on August 5, 2006. Spatial variability of soil water content in the near surface on scales ranging from a few centimetres to several hundred metres has been studied by many authors like Jackson and Le Vine (1996), Grayson et al. (1997); Ritsema and Dekker (1998); Famiglietti et al. (1999); Hupet and Vanclooster (2002), Huisman et al. (2003a); Igel et al. (2006); Weihermüller et al. (2007) among many others. The effect of topography was contributory to soil water spatial variability in most of these investigations. However, in my case topography seems not to play any significant contribution to soil water content variability due to the averagely flat nature of the survey region. The heterogeneity in the soil water content distribution might be due to a number of factors including the spatial variation of soil hydraulic properties, the effect of plant root distribution, the influence of earth worms and the spatial variability of soil water-holding capacities along the transect.

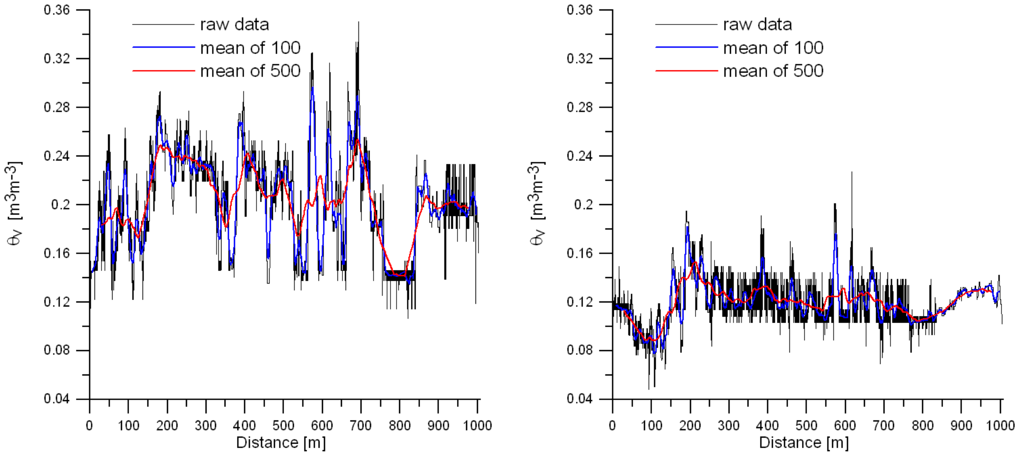

(a) Wet soil (1 Aug 06, after heavy downpour) (b) Dry soil (5 Aug 06, after 4 days of no rain)

Figure 8.15: Spatial soil water content variability.

Fig. 8.16 shows the temporal soil water content between August 1-19, 2006. Running means of 500 values are plotted to show the general trend of soil water content distribution. Near surface heterogeneities and the varying local water-holding capacities of the soil play vital roles in the distribution trend. The strong spatial variability of soil water content makes it difficult to extrapolate values of discrete point measurements from TDR and FDR to field scale. The distribution pattern can be characterised by 3 main zones: peaks marked by H_1 to H_4, zone of low water content marked L_1 and L_2 and moderately low zones marked ML. Point-based measurements placed every 200 m along the transect missed soil water information at L_1 (124 m), ML_1 (351 m) and ML_2 (535 m) as well as H_3 (595 m) and H_3 (688 m). This makes it less reasonable to extrapolate local pont measurements to field scale in an area marked by such strong spatial soil water variability.

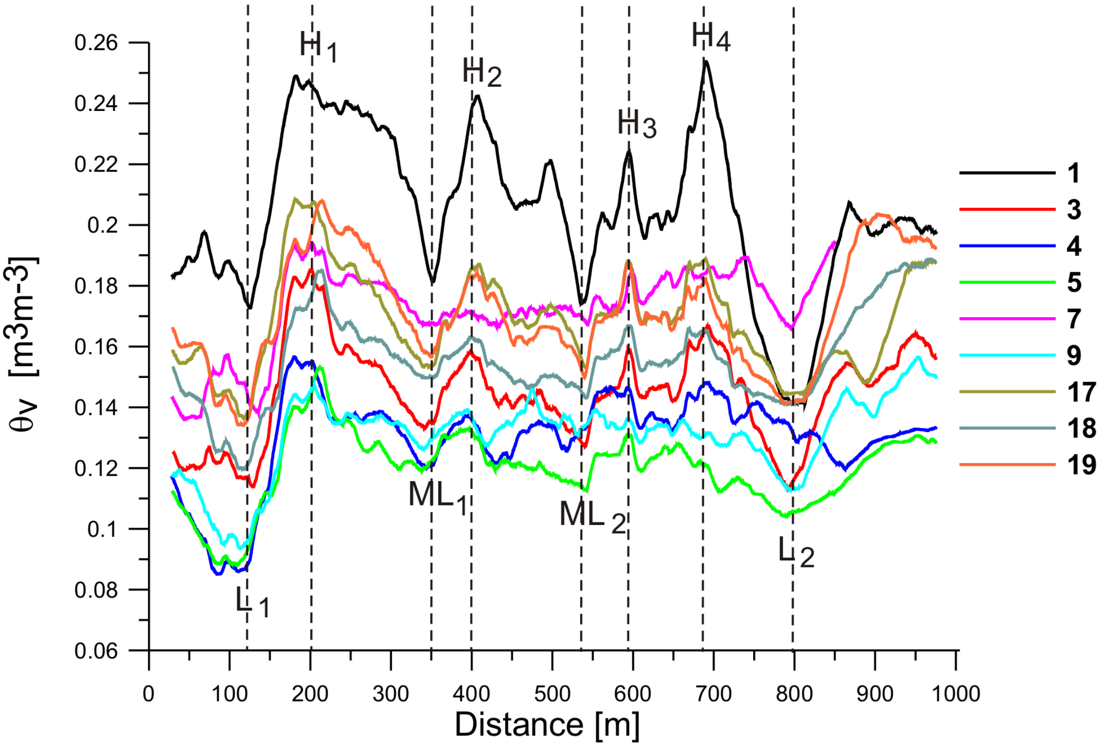

Figure 8.16: Spatial variability of soil water content:running means of 500 values (50 m). The numbers in the legend represent dates between August 1-19, 2006.

Soils such as those at locations marked H_1-H_4 with very high water contents are not ideal for crop yield due to poor respiration they provide for plants. On the other hand soils with very low water content such as occur at locations L_1 and L_2 are hardly reached by plants.

I now apply geostatistical methods to characterise the spatial soil water content variability between August 1-19, 2006.

8.3.3.1 Application of Geostatistics to Soil Water Content Distribution

Geostatistical techniques are a collection of statistical methods which describe spatial relationship between sample data values in a region. These techniques have often been used to characterise the spatial distribution of soil water content (e.g. Entin et al. (2000); Liu (2001); Huisman et al. (2002); Western et al. (2002)). As an illustration to the significance of geostatistics let us assume that the soil water content values θ_{v1}, θ_{v2}, θ_{v3}, θ_{v4} and θ_{v5} have been measured at five locations $\mathbf{x}_1$, $\mathbf{x}_2$, $\mathbf{x}_3$, $\mathbf{x}_4$ and $\mathbf{x}_5$ respectively (Fig. 8.17).

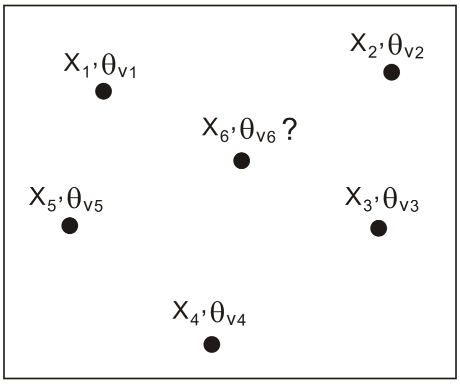

Figure 8.17: Schematic illustration of the application of geostatistics to determine the unknown value θ_{v6} at the location $\mathbf{x}_6$.

Geostatistics focuses on finding the unknown value θ_{v6} at the known location $\mathbf{x}_6$. The advantages of geostatistical methods over the other data processing methods are that:

- It enables appropriate data estimations within given limits at locations where no observations were made i.e. it is used to interpolate (by the method of *kriging*) isolated data and to map this into a continuous space. Furthermore, it can be used to assess the level of confidence which can be put in such estimation assuming that it is subject to errors. This is done by estimating the probability density function $f_{\theta v}(\theta_{v6}, \mathbf{x}_6)$. This probability gives the level of uncertainty about the unknown value θ_{v6} at $\mathbf{x}_6$.
- The spatial correlation of geological and geophysical data can be quantitatively described with the help of spatial models e.g. variograms, correlograms or covariance functions.

Geostatistics has its history in the estimation of ore grades of mining blocks along outcrops [Krige (1951)]. This application later extended to statistical theory of spatial data [Matheron (1970)]. In the last few years geostatistics has been usefully applied in the fields of agriculture and hydrology to investigate the spatial soil water content variability (e.g. Nielsen et al. (1973); Anderson and Burt (1978); Kachanoski et al. (1985); Moore et al. (1988); Barling et al. (1994); Merz and Plate (1997); Western et al. (1998); Bárdossy and Lehmann (1998); Western and Blöschl (1999); Qiu et al. (2001); Täumer et al. (2006)). Quite a number of papers have also reported that although the soil water content varies with time and field location, the trend of the spatial variability is independent of time when the field observations are scaled against the mean soil water content, a phenomenon known as *temporal stability* (e.g. Kachanoski and de Jong (1988); Jaynes and Hunsaker (1989) Goovaerts and Chiang (1993); van Pelt and Wierenga (2001); Martinez-Fernandez and Ceballos (2003); Ya et al. (2005); Lin (2006)). The knowledge of the spatial variability of soil water content is important for managing soil water and understanding plant growth as well as a number of soil processes controlled by soil water such as erosion, chemical exchange, microbial activity and soil-plant energy balance systems.

The application of geostatistics helps in modelling/understanding the spatial variability of the soil water content θ_v.

8.3.3.1.1 The Semivariogram The central theme of geostatistical methods is the application of the variogram which describes the variance between data points as a function of their separation. A variogram (often called semivariogram because of the factor "$\frac{1}{2}$" in the Eq. (8.4)) is a cross plot that illustrates the correlation between the data as the distance between them increases. Let us consider as a way of illustration a parameter θ_v that varies throughout a region. In order to determine the experimental variogram (Fig. 8.18) that quantitatively describes the spatial variation of θ_v throughout the region of interest we go through the following procedure:

- Select two locations x_i and $x_i + h$ separated by a lag distance h and determine the difference $\theta_v(x_i) - \theta_v(x_i + h)$. This is done for all data pairs N.
- The procedure above is repeated for many other values of h.
- The experimental semivariogram which is a plot of the semivariogram function $\gamma(h)$ is defined by

  $$\gamma(h) = \frac{1}{2N(h)} \sum_{i=1}^{N(h)} [\theta_v(x_i) - \theta_v(x_i + h)]^2 \qquad (8.4)$$

  The function $\gamma(h)$ is a measure of the lack of dependence between $\theta_v(x_i)$ and $\theta_v(x_i + h)$ (e.g. Journel and Huijbregts (1978)).

The basic components of the semivariogram are schematically illustrated in Fig. 8.18.

- The **sill** represents the spatial variance. The variogram flattens symbolising the absence of spatial correlation at all values of $h > h_L$ (h_L = correlation length).
- The **correlation length** or **range** is the distance at which the variogram becomes constant or reaches the sill. It is the maximum distance from which sample pairs are drawn for interpolation by kriging and indicates the spatial continuity of the valuable under consideration. Values of a given property separated by distance larger than the range can be considered as

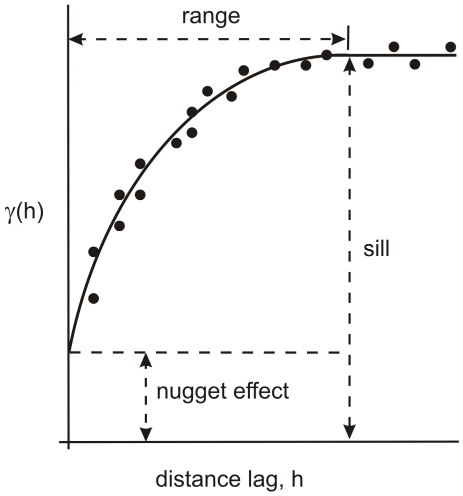

Figure 8.18: Schematic illustration of the basic components of a variogram. The solid line is the result of the model fitted to the experimental data.

purely random and uncorrelated. Sample pairs separated by distance closer than the range are spatially related. A large range implies that the major variation takes place over large distances while a short range means that short-range variation dominates.

- The **nugget effect** is the measurement error attributed to microscale variation (i.e. variability at distances smaller than the sample spacing used). It represents the discontinuity of $\gamma(h)$ at the origin (Cressie (1993)). A nugget variance of 0 % implies that there are no short-range variations or measurement errors. A pure effect (i.e. 100 % of sill) represents a total absence of spatial correlation at the sampling scale used and this arises from very large variations at short distances. Errors in the measurement or the location of the measurement lead to a higher nugget effects. A high nugget effect may also result from sparse data. If the effect is far higher than the local variation then the data might be too noisy to effect any sensible interpolation exercise.

- The semivariance function $\gamma(h)$ is related to the autocovariance function $C(h)$ by $\gamma(h) = C(0) - C(h)$. The autocovariance decreases with increasing distance while the semivariance increases. The relationship between $\gamma(h)$ and $C(h)$ is shown graphically in Fig. 8.19.

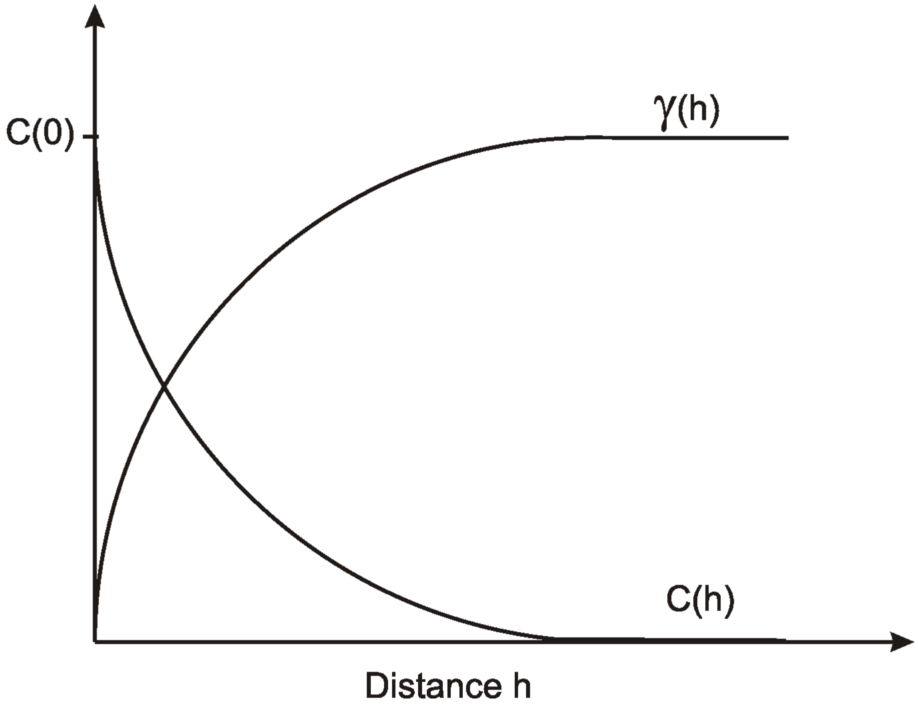

Figure 8.19: Comparison of covariance and semivariance functions.

8.3.3.1.2 Variogram Modelling After plotting the experimental semivariogram we seek to construct a model that characterises the spatial structure of the variable under study using the kriging algorithm. A reason for this is that the kriging algorithm assesses additional distances (lags) besides those represented by the experimental semivariogram. Another reason is that the experimental semivariogram is only an empirical estimator of the covariance of a gaussian process and hence, may not be directly used in kriging without further constraints or processing. Geostatisticians, therefore choose from a palette a limited number of acceptable models (e.g. linear, spherical, exponential, gaussian, rational quadratic etc.) to fit experimental semivariograms. From such a model the behaviour of the semivariogram function close to the origin may be estimated from the data. Generally, models which increase linearly close to the origin (for small lags) are adequate for most geoscience applications. The trial and error exercise of fitting a model curve to the data points on the radargram is termed *Variogram modelling*.

Principally, the model chosen should be as simple as possible, yet adequate. The semi-variance spherical model (Carr (1995)), which is characterised by an increase in variation along a slope until a point is reached where the variation is maximum was found most appropriate in fitting my experimental data. The semi-variance of the spherical model is defined by

$$\gamma_m(h) = \begin{cases} C\left[\frac{3}{2}\left(\frac{h}{a}\right) + \frac{1}{2}\left(\frac{h}{a}\right)^3\right] & \text{if } h < a \\ 2C & \text{if } h \geq a \end{cases} \tag{8.5}$$

where $\gamma_m(h)$, a, C and h are the fitted variogram model, the range, sill and lag respectively and $h \geq 0$; and $a, c > 0$.

I characterised the quality of the variogram model fits by the RMSD calculated as:

$$\mathrm{RMSD} = \sqrt{\frac{1}{n_h}\sum_{i=1}^{n_h}[\gamma_m(h) - \gamma(h)]^2} \tag{8.6}$$

where n_h represents the number of lag bins of the experimental semivariogram.

8.3.3.1.3 Results of Geostatistical Modelling of Soil Water Content Fig. 8.20 shows semivariogram models of soil water content distribution at Dano between August 1-5, 2006.

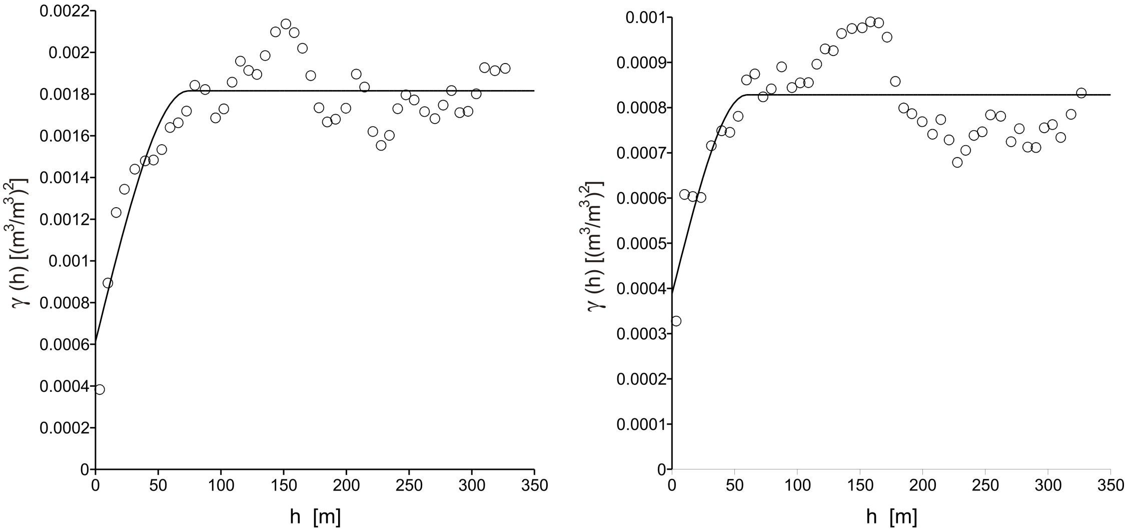

(a) 1st August 2006 (b) 3rd August 2006

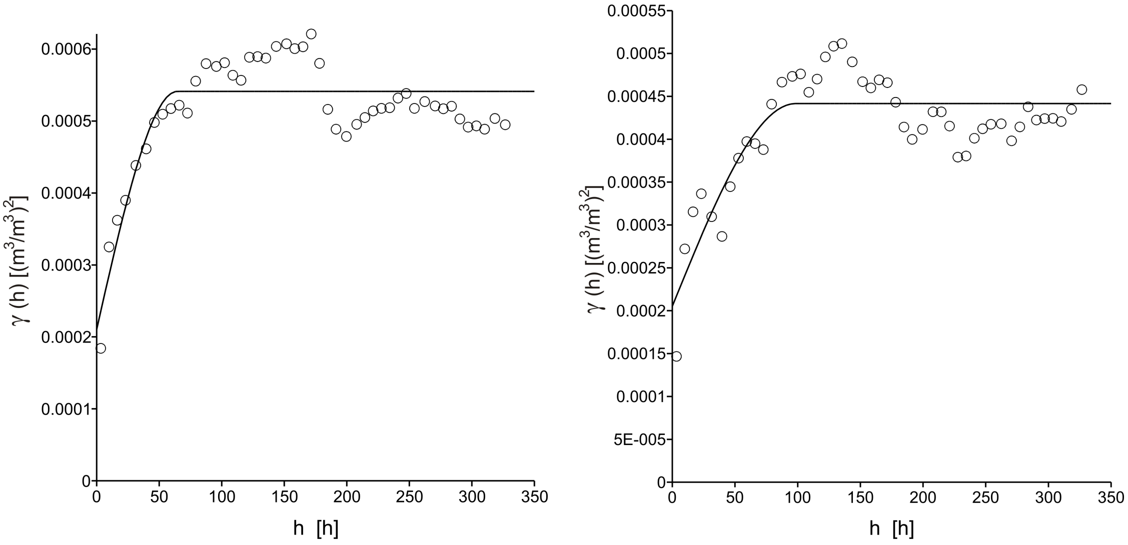

(c) 4th August 2006 (d) 5th August 2006

Figure 8.20: Semivariograms of volumetric soil water content. Solid lines represent spherical models fitted to experimental values.

The plots show consistency in shape and display an oscillatory behaviour about the sill. The oscillation is likely due to the heterogeneous nature of the soil which can cause the development of preferential flow paths resulting in such development. This is called the *whole* or *wave effect*. This occurrence is often prevalent in agricultural fields especially in areas of rows and furrows. The correlation between observation points in a row or in a furrow may be low while that between rows may be higher and this gives rise to alternating patterns of low and high correlations whose amplitudes decrease with increasing lag distance. Other graphs showing semivariograms of soil water content between August 9-19, 2006 are shown in appendix C.4.

Fig. 8.21 relates the correlation length to the mean soil water content.

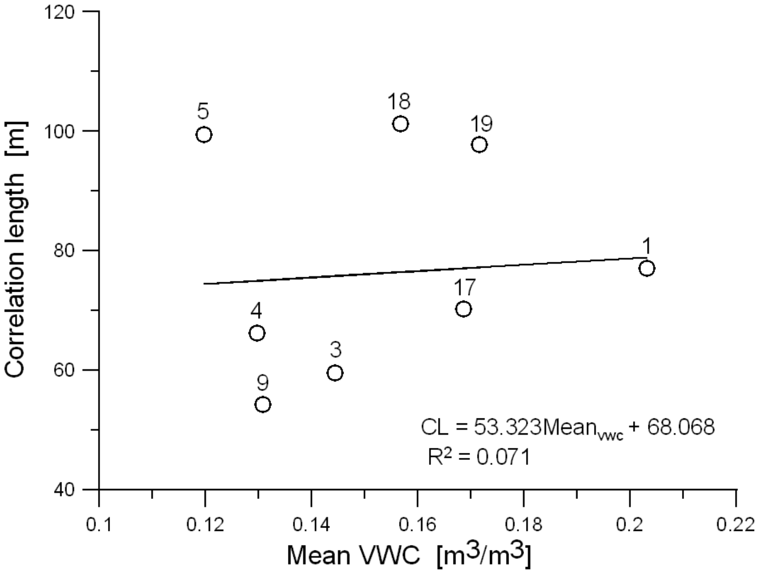

Figure 8.21: Relationship between mean soil water and correlation length (CL). The numbers in the figure indicate dates in August 2006.

The mean soil water content seems not to be related to the correlation length (R^2 = 0.071, $F_{1,6}$ = 0.46 < 5.99 at 95 % significance). The property is perhaps controlled by many composite processes operating on a single scale.

From the results of this analysis (for soil water content in the near-surface for depths 0-0.1 m), this means that the soil water content as measured by TDR and SISOMOP which were placed at 200 m apart along the 1 km long transect were uncorrelated. Optimal positions for the TDR and SISOMOP points would have been say every 50 m. This could be determined first after a reconnaissance campaign with GPR.

The correlation lengths were found to be between 54 - 102 m (Table 8.4).

Date	Mean VWC	Nugget	Correlation length	Sill	RMSD
	$[m^3m^{-3}]$	$[(m^3m^{-3})^2]$	[m]	$[(m^3m^{-3})^2]$	$[(m^3m^{-3})^2]$
	$\times10^{-2}$	$\times10^{-4}$		$\times10^{-4}$	$\times10^{-5}$
1 Aug 06	20.32	6.14	77.05	18.0	7.93
3 Aug 06	14.43	3.88	59.57	8.4	5.11
4 Aug 06	12.97	2.10	66.20	5.4	2.48
5 Aug 06	11.97	2.05	99.45	4.4	1.95
9 Aug 06	13.08	2.34	54.27	4.5	1.24
17 Aug 06	16.86	3.28	70.28	8.0	4.25
18 Aug 06	15.67	2.30	101.25	5.3	2.53
19 Aug 06	17.16	4.25	97.78	9.5	4.91

Table 8.4: Summary of geostatistical soil water distribution pattern at Dano, Burkina Faso (August1-19,2006).

Fig. 8.22 shows the relation between the mean soil water content and the nugget.

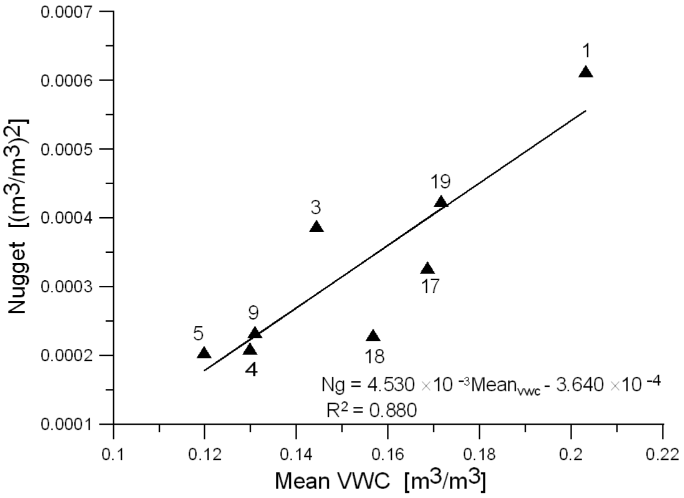

Figure 8.22: Relationship between mean soil water and nugget (Ng). The numbers in the figure indicate dates in August 2006.

Regression analysis shows that there is a strong tendency for the nugget to increase during wetter soil conditions (R^2 = 0.88, $F_{1,6}$ = 44 > 5.99 at 95 % significance). This is also indicated by the strong relationship (R^2 = 0.87) between RMSD and the mean soil water content (Table 8.4).

8.3.4 Modelling of Ground Wave Propagation in Soil

Experiments with WARR show possible geometric dispersion of the ground wave as it propagates through an inhomogeneous layered medium with varying dielectric coefficients, electric conductivity and water content with a phase velocity different from the group velocity.

For this section I invoke ideas and deliberations of ground wave propagation as described by the authors Du (1996); Wollny (1999); Sperl (1999) and Voss (2006) to help explain the dispersive behaviour of the apparent ground wave in a layered wet soil.

Two different soil models A and B of a two-layer soil column Fig. 8.23 are discussed:

- **Model A**: A relatively dry soil layer of thickness 0.2 m with constant relative dielectric permittivity $\varepsilon_r = 8$ (which corresponds to VWC of 0.15 m^3m^{-3} using Topp et al. (1980) calibration equation) overlying a water-saturated layer of relative dielectric permittivity $\varepsilon_r = 25 \equiv \theta_v = 0.40$ m^3m^{-3} (Fig. 8.23(a)).
- **Model B**: A soil layer of thickness 0.5 m of linearly increasing relative dielectric permittivity between $\varepsilon_r = 8$ and $\varepsilon_r = 25$ overlying a water-saturated layer relative of dielectric permittivity $\varepsilon_r = 25$ (Fig.8.23(b)).

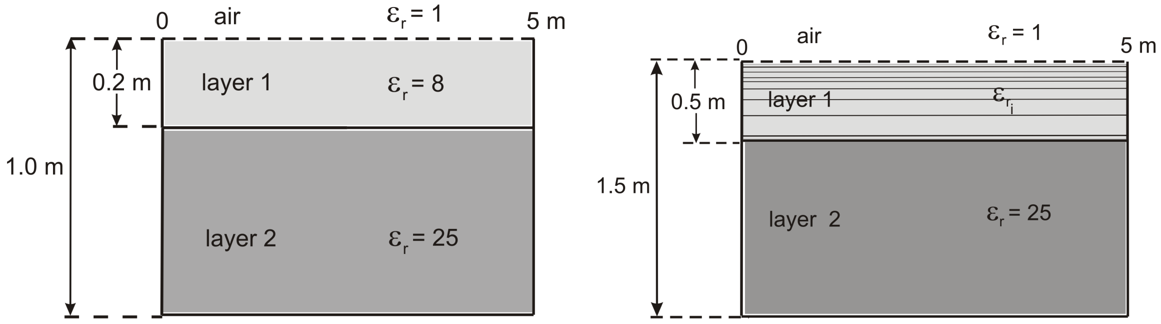

(a) Model A (b) Model B

Figure 8.23: Schematic illustration of soil layer models A and B (modefied after Sperl, 1999).

With this two-layer soil model the ground wave is expected to propagate either with the velocity of the upper or lower layer or with a velocity which is a superposition of both. The exploration depth of the ground wave varies depending on the soil water content and the frequency of the transmitting antenna. The signal registered by the receiver placed at the air-ground interface is a superposition of the waves generated by the lateral waves propagating along the layer interfaces. Where the soil water content contrast between the interfaces is very sharp it is possible for the ground wave to split along the interfaces and propagate as two different waves. This condition is schematically illustrated in (Fig. 8.24). A similar occurrence is expected for model B.

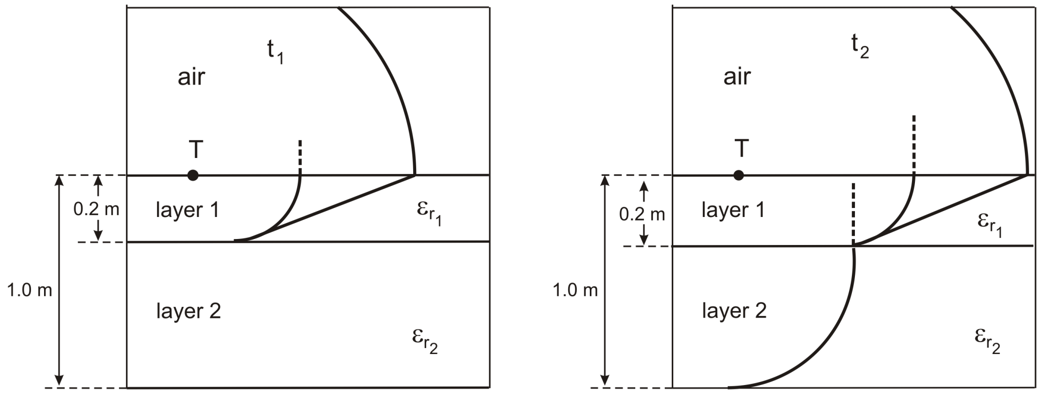

(a) Ater time t_1 (b) After time $t_2 > t_1$

Figure 8.24: Schematic illustration of the propagation of the ground wave in a two-layer medium with $\varepsilon_{r1} < \varepsilon_{r2}$ after times t_1 and $t_2 > t_1$. T is transmitter. (modified after Wollny (1999); Voss (2006).).

8.3.4.1 Simulation of Radargram Models

Based on soil layer models described in Fig. 8.23 radargram models of electromagnetic wave propagation from transmitters of different frequencies 50, 100, 200 and 400 MHz placed on the air-ground surface are discussed. The soil permeability is assumed to be constant ($\mu_r = 1$). The soil is assumed lossless and a time interval of 60 ns is considered. The resulting models are discussed below. The models were created and the simulations calculated with the modelling tool of Reflexw (Sandmeier, 2007).

8.3.4.1.1 Simulated Model A The exact depth of influence of the ground wave remains unknown. Values given are more or less a matter of conjecture. At a very low frequency of 50 MHz the receiver registers principally the ground wave with a velocity of 0.060 m/ns from the deeper layer (Figs. 8.25(a) and 8.25(b)). For the 100 MHz antenna the receiver on the ground surface records both slower phase of 0.060 m/ns from the deeper layer and the faster phase of 0.106 m/ns from the upper layer (Figs. 8.25(a) and 8.25(b)). For higher frequencies of 200 MHz and 400 MHz the ground wave recorded by the receiver is principally the faster phase from the upper layer (Figs.8.25(c) and 8.25(d)).

8.3.4.1.2 Simulated Model B At higher frequencies of 200 MHz and 400 MHz the ground wave signal recorded by the receiver is principally from the upper 0.2 m (Figs. 8.26(c) and 8.26(d)). At a frequency of 100 MHz the signal reaching the receiver is a superposition of ground waves propagating both the upper and lower layers. At the frequency of 50 MHz the receiver principally records the phase propagating in the lower layer (Figs.8.26(a) and 8.26(b)).

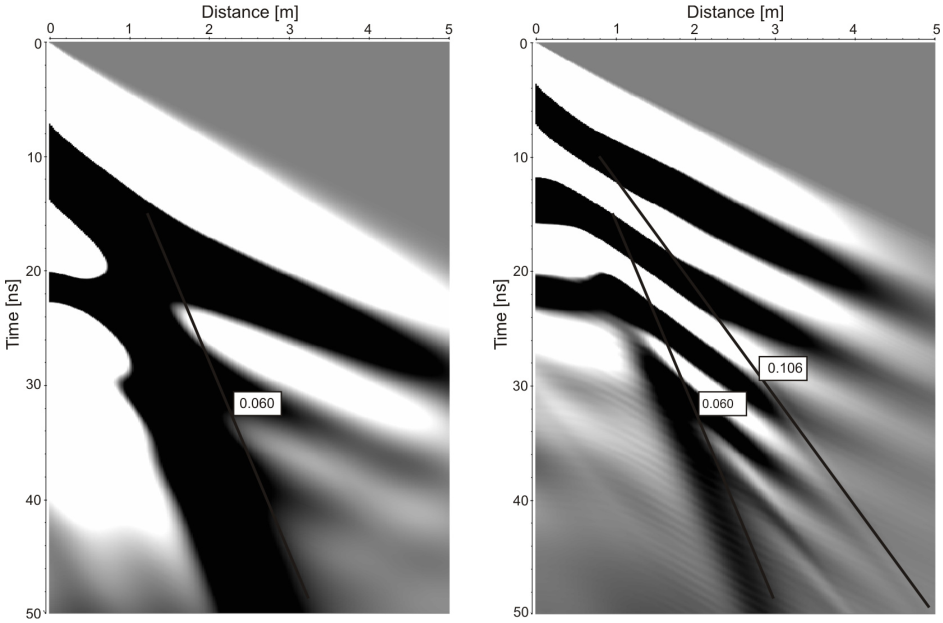

(a) 50 MHz (b) 100 MHz

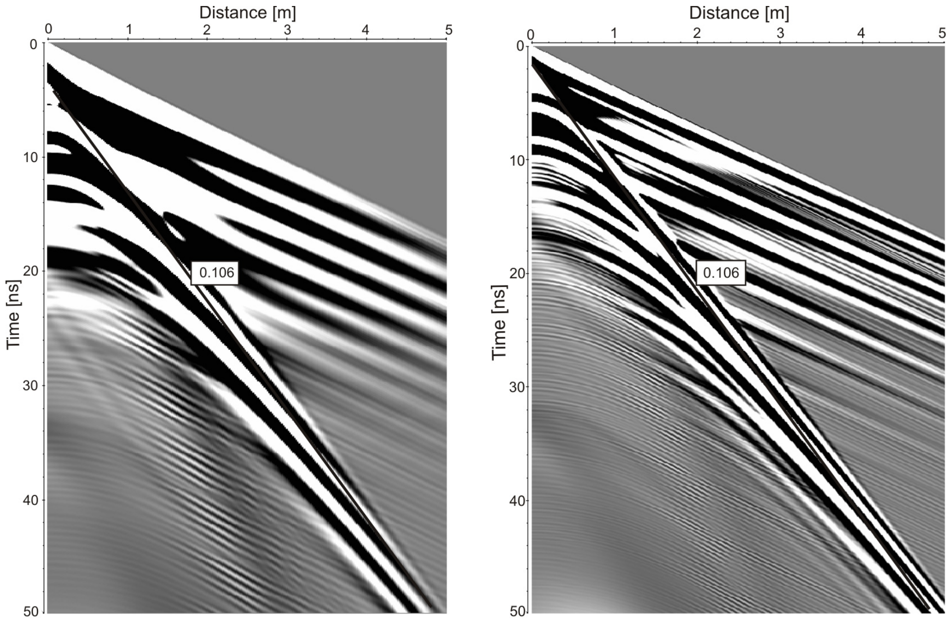

(c) 200 MHz (d) 400 MHz

Figure 8.25: Simulation of the ground wave at 50 MHz,100 MHz, 200 MHz and 400 MHz for model A.

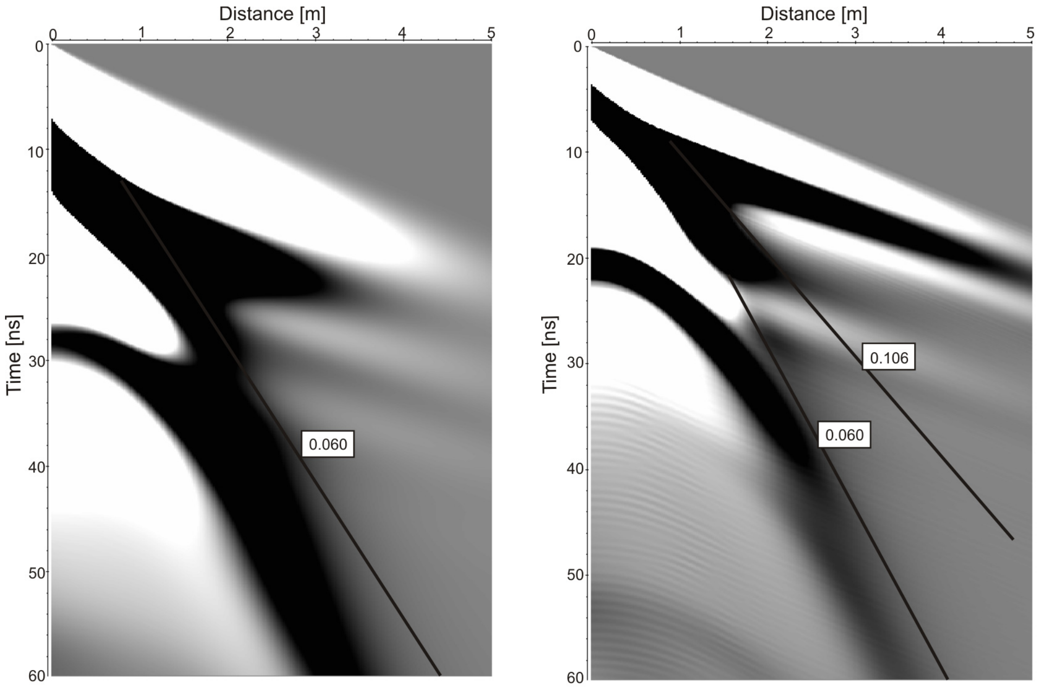

(a) 50 MHz

(b) 100 MHz

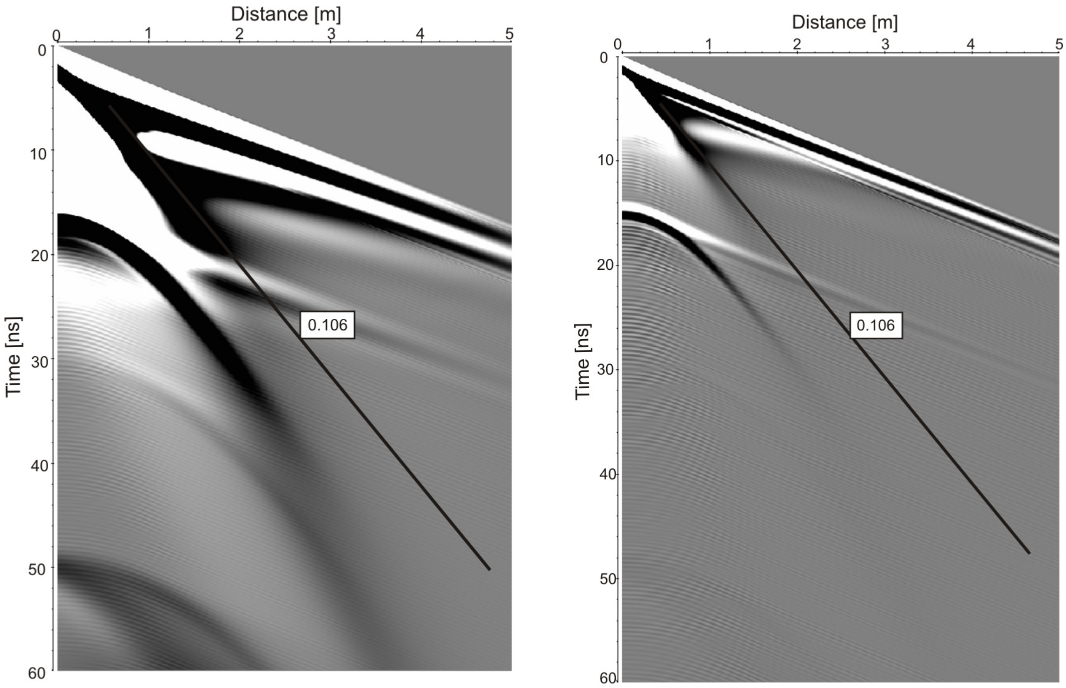

(c) 200 MHz

(d) 400 MHz

Figure 8.26: Simulation of the ground wave at 50 MHz,100 MHz, 200 MHz and 400 MHz for model B.

8.3.5 Comparison of GPR with TDR and SISOMOP

Fig. (8.27)[1] shows plots of the dielectric coefficient of the soil as measured by GPR, TDR and FDR (i.e. SISOMOP) techniques. The results displayed by GPR which registered soil water content every 0.1 m along the profile show strong heterogeneities in the distribution, a trend which is not well displayed by the point measurements. GPR has additional advantages of being quasi-continuous, non-invasive and fast. Geostatistical analyses (see section 8.3.3.1, p. 138) show further advantages of GPR over TDR and FDR.

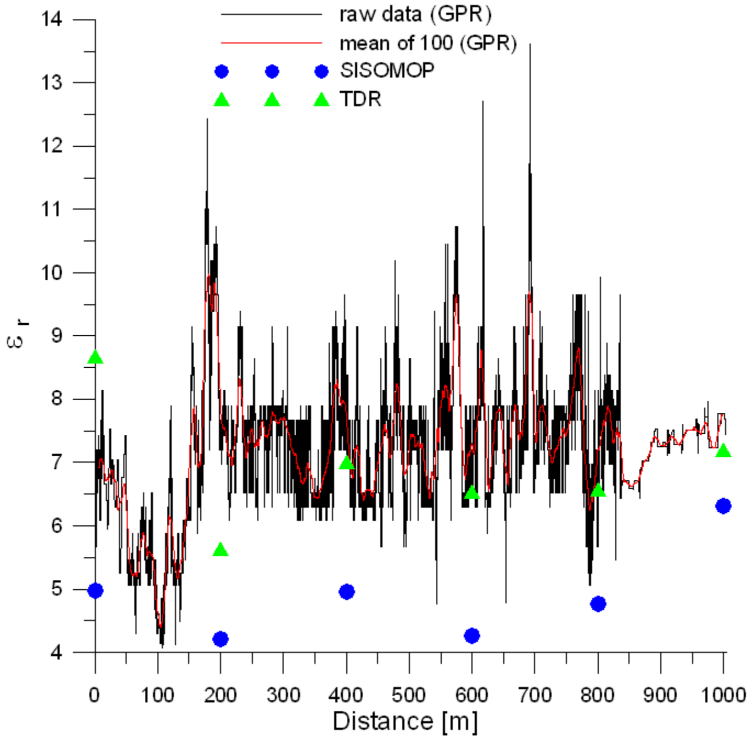

Figure 8.27: Comparison of GPR-derived soil dielectric coefficient with that of TDR and SISOMOP for 4th August 2006.

The GPR-derived relative dielectric coefficient shows a relatively small RMSD of 0.86 with TDR and a moderately large value of 2.10 with SISOMOP. The relatively low values registered by SISOMOP might be due to the deeper depth at which it acquires soil water content information. Whereas the GPR and TDR soil water data refer to the upper 0.1 m of the soil SISOMOP measures about the upper 0.2 m. Near-surface water content decreases with depth and fluctuations of soil water content are most predominant in the upper layer (~0.1 m) of the soil. Deeper soil layers show less variable behaviour (e.g. Ramos and Mulligan (2005)). SISOMOP is thus expected to register relatively lower soil water content values than that registered by GPR and TDR.

---

[1] The apparent ground wave phase of the last ~150 m of this and subsequent figures were manually picked due to problem with the automatic *phase follower* tool from Reflexw. This portion thus displays a different resolution.

The discrete point measurements have the disadvantage of being invasive. Soil water values may hence, be influenced through the process of digging and planting of the probes in the soil. GPR does not have this problem. Furthermore, from its much larger data volume ($N > 9000$ as compared to $N = 6$ for discrete point measurements) one builds a more reliable statistical mean for comparison with satellite measurements.

Other graphs comparing relative dielectric coefficients of the three techniques are shown in appendix C.

8.3.6 Soil Water Content and Surface-Atmosphere Feedbacks

The impact of soil water on albedo, turbulent fluxes and evapo-transpiration influence atmosphere-landsurface interactions. Differences in the thermal and hydrological status of soil characterise the heterogeneities in land surface which tend to enhance convective phenomena, affecting the Bowen ratio (i.e. the ratio of *sensible heat* to *latent heat*) and inducing atmospheric circulations, therefore modulating the variability of the climate system (D'Odorico et al. (2000)). In the rainy season higher soil water content resulting from rainfall leads to lower albedo (i.e. the fraction of incident electromagnetic radiation reflected by a surface) while in the dry season low soil water values lead to higher albedo. Soil water also influences the Bowen ratio. Rainfall leads to a higher reservoir of water and thus a higher *latent* heat flux with a corresponding decrease in the Bowen ratio. Dry periods are accompanied by higher *sensible* heat flux with a corresponding increase in the Bowen ratio.

The Bowen ratio reaches a value of 1 in the dry season in the Dano (Burkina Faso) area. The increase in the latent heat flux after rainfall leads to a high evapo-transpiration rate [4 mm/day]. Evapo-transpiration rate decreases to 1.5 mm/day for the dry soil[2].

8.4 Discussion and Conclusions

I have discussed the use of the ground wave method of GPR in retrieving near surface (~0.1 m) soil water information in the semi-arid region of Dano, Burkina Faso with 300 MHz antennas. As reference measurements SISOMOP (to sample soil water content of the top ~0.2 m of the soil) and TDR (to measure soil water of the top ~0.1 of the soil) probes were positioned at intervals of 200 m along the 1 km long transect. Soil water content in Dano, Burkina Faso during the raining season varies both temporally and spatially and it is dominated by rainfall rate. Evaporation plays an insignificant role in the soil water content variability. GPR-derived dielectric coefficients of the soil were compared with parallel measured by TDR and FDR (i.e. SISOMOP) probes. GPR showed a RMSD of 0.86 and 2.10 with TDR and FDR respectively. The high RMSD of SISOMOP might be due to the relatively deeper depth at which it retrieves soil water information. Geostatistical analyses show that 200 m distant TDR and SISOMOP

---

[2] Personal communication with Martin Kohler

probes are not correlated. The GPR technique has advantages over TDR and FDR techniques for being quasi-continuous, non-invasive and fast.

Simulated radargram models of the apparent ground wave propagation show that the apparent ground wave is more easily registered with high frequency antennas than low one. High frequency antennas (e.g. 900 MHz), however, have the disadvantage of having attenuation and low penetration depths. At moderately low frequencies of 100 MHz the apparent ground wave recorded by the receiver is a superposition of apparent ground waves propagated along the interfaces of the lower media.

The apparent ground wave was found to be more strongly radiated in a wet soil than a dry one. The increase in amplitude during wet conditions might be due to the better capacitive coupling between the between the antennas for the wet soil.

Classical statistics was used to describe the soil water distribution pattern. Frequency plots of soil water revealed that the distribution deviates from that of a normal distribution. No concrete relationship could be established between the mean soil water content and the coefficient of variation (CV). A regression equation fitted to the CV-mean soil water data yielded $R^2 = 0.306$. The F-test on the significance of the regression equation for $N = 8$ and $k = 2$ produced $F_{1,6} = 2.64$ which is less than the critical value of 5.99 at 95 % significance.

Soil water was also characterised geostatistically through semivariogram modelling. The models displayed a hole-effect, a sequel to the probable occurrence of preferential water infiltration pathways in the soil. Correlation lengths determined from geostatistical analyses of soil water content were found to be between 50 and 102 m. This means that soil water data acquired by TDR and SISOMOP which were placed every 200 m in the soil were not correlated. Furthermore, there was no correlation between the mean soil water content and the correlation length ($R^2 = 0.071$, $F_{1,6} = 0.46 < 5.99$ at 95 % significance). However, the nugget and the coefficient of variation showed a strong dependency on rainfall ($R^2 = 0.88$ $F_{1,6} = 44 > 5.99$). The surveyed area was on the average a flat land, hence, topography played no significant role in the spatial variation of soil water content.

Remote sensing of soil water is based on the analysis of electromagnetic dielectric properties of the soil. Satellite equipments emit radiation pulses through space to the target (usually soil) and records the pulse that reflects from the target. From this information, the backscatter coefficient (i.e. the ratio of received to transmitted power) is then related to the dielectric properties of the soil and the latter to the soil water. Some satellites passively record thermal emission from the ground for soil moisture determination. Remote sensing equipment can be operated in the dark and also during bad weather.

Despite these advantages they have their drawbacks. Where the surface is rough or where the spatial soil dielectric coefficient is highly heterogeneous (as it is in Dano), the transmitted wave tend to scatter in all directions and may rebound back over the boundary surface (e.g. Ulaby et al. (1982)). For such a case back scattering models display distortions and poor results (e.g. Altese et al. (1996)). This is because remotely sensed soil water models are highly sensitive to soil heterogeneities and satellite equipment are unable to correctly measure these (e.g. Davidson et al.

(2000)) especially where the spatial soil water pattern is strongly non-homogeneous. The radiation which is observed by the satellite sensor is affected by a variety of factors, e.g. soil physical properties, soil temperature, surface roughness, vegetation, and also the sensor characteristics (Owe et al. (2001)).

For this reason the estimation of soil water with satellite equipment requires very detailed knowledge of soil surface parameters (e.g. spatial dielectric coefficient pattern) to create appropriate soil water models. This information could be best obtained through continuous ground-based soil water measurements such as provided by the GPR. The microwave satellite system, Advanced Microwave Scanning Radiometer-Earth Observing System (AMSR-E), used by IMK has a frequency of 10.7 GHz and an exploration depth of ~ 0.01 m (using Sperl's empirical formula, see section 8.2.4, p. 123) with the assumption that the soil has no vegetative cover.

Discrete point scale measurements (as offered by TDR and FDR) do not correctly present the full-scale soil water picture due to their low data density basis ($N = 6$ as compared to $N > 9000$ for GPR). Extrapolating soil water content within this low data volume to field scale, as is usually the case with discrete point measurements, often results in errors and aliasing effects. Reynolds (1970) characterises soil water variability from two sources - static properties (e.g. type of soil) and dynamic properties (e.g. rainfall). These two properties vary both spatially and temporally in the investigated region. Hence, in the Dano region point scale-fed satellite soil water models are more likely to be erroneous. The mean GPR-derived soil water content values are built from a large data density basis and are thus more appropriate for comparison with the satellite measurements and as input data for meteorological modelling.

Soil water content influences the Bowen ratio which reaches a value of 1 when the soil becomes dry due to lack of rainfall. The increase in latent heat flux after rainfall leads to a high evapotranspiration rate of 4 mm/day.

Chapter 9

Summary and Conclusions

The main theme of this work has been the characterisation of soil water content in the vadose zone with the help of the ground penetrating radar (GPR). Experiments were performed under controlled conditions on two dike models and also in the field at Dano, Burkina Faso. GPR measures the propagation velocity of electromagnetic waves through the soil and from this makes estimation of the dielectric coefficient of the soil and eventually the soil water content through a suitable calibration equation. The calibration equation by Topp et al. (1980) which is universally recognised was used to estimate soil water content from dielectric coefficient measurements. All data were processed with Reflexw software Sandmeier (2007).

I performed controlled flooding experiments on a dike model (of dimensions $8.0\,\mathrm{m}\times 2.2\,\mathrm{m}\times 1.4\,\mathrm{m}$) constructed with soil of the textural class loamy sand and situated in the Theodor-Rehbock Laboratory, Institute of Water and River Basin Management, University of Karlsruhe, Karlsruhe. These experiments were performed at the crest of the dike model with the guided wave sounding (GWS) method, which is an invasive application of the GPR, with 500 MHz and 900 MHz bistatic antennas. I analysed guided wave reflections from the lower end of a 1.2 m long metal rod which was lowered at 2.5 cm intervals down a vertical access tube sunk at the crest of the dike to acquire information of soil water content. The experiments comprised 6 phases of flooding between 0 and 1.25 m from the dike's base. Results of the flooding experiments revealed that the boundary between two soil layers at a depth of about 0.6 m recorded an anomalously high soil water content of 0.32 $\mathrm{m}^3\mathrm{m}^{-3}$. This occurrence was likely due to the poor cohesion within the soil particles at this zone thereby creating a preferential infiltration path here. A breach of this nature is common with dike structures constructed with sand and when not detected early and checked could lead to the eventual collapse of the structure. A solution to a breach of this nature might be to construct the dike body with a more cohesive material e.g. clay. However, this measure would limit the application of GPR due to the strong attenuation of GPR waves in clay.

Parallel reference measurements were also performed with common midpoint (CMP) method, a non-invasive application of GPR with 900 MHz and 500 MHz monostatic antennas, along the $\sim$ 2 m crest length of the dike model. GWS-derived soil water data were in addition compared with co-located measurements with the time domain reflectometry with intelligible microelements

(TRIME-TDR). The CMP method showed a poorer depth resolution than GWS and comparison of soil water data derived by the two methods yielded a root mean square deviation (RMSD) of 0.06 m^3m^{-3}. The CMP survey procedure and data processing are labour and time intensive. This makes the method less interesting especially for field scale measurements. However, the method is necessary because it provides a depth-velocity model of the subsurface from which the soil water content could be inferred.

Further infiltration investigations were performed with GWS on a full-scale sand dike model at Federal Institute of Water and Research (BAW), Karlsruhe using water sprinklers to simulate controlled precipitation events. The experiments were conducted on the wet plane of the dike model. Two soil water distribution phases, before and after 72 h of precipitation, were investigated. Results of the experiments revealed that this dike comprised of ~0.3 m thick inhomogeneous organic overburden with a relatively higher water storage capacity than the homogeneous sand layers below. Generally, the soil water content decreased with depth from the surface to a depth of about 0.3 m which represented the organic overburden. This was followed by a gradual increase to the final depth of about 1.6 m. The increase in soil water content in the sand layers below was due to accumulated infiltration from the upper layers.

An experiment with a suspended metal rod of about 25 cm length and diameter 4.5 cm unfortunately did not yield the expected results. This was designed to measure soil water. The suspended metal rod was lowered through an access tube at intervals of 5 cm while the GPR was operated in the common offset (CO) mode. The experiment failed to produce the expected results for at certain depths of the metal rod the radargram showed no reflections at all from the metal. This might be due to the following reason: The wavelength of the electromagnetic signal transmitted with the 500 MHz antenna was of about the same order as the depth of the upper surface of the metal rod. Destructive interference between the incident and reflected waves from the upper surface of the rod is likely to be the cause of zero reflections registered on the radargram.

Infiltration experiments with GWS and TRIME-TDR on dike models invite the following conclusions:

- GWS- and TRIME-TDR-derived soil water content distribution showed comparable trends with a root mean square deviation (RMSD) of about 0.11 m^3m^{-3}. Thus, the GWS method can be appropriately used to assess soil water content information. GWS had in addition the advantage of a much higher depth resolution. Furthermore, modal guided wave modelling analysis of the GWS methods revealed that the investigator has a further advantage of evaluating the level of attenuation and damping of the phase velocity of the electromagnetic wave through the soil under investigation.
- GWS can be used alongside commonly used methods like local temperature measurements, piezometry, conventional TDR and the electrical resistivity tomography (ERT) to monitor leakage in embankment dikes to ensure their safety.

A third experiment was performed in West Africa in the neighbourhood of the Bontioli Faunal Reserve (11 ° 10′ N, 03 ° 05′ W) near Dano, Burkina Faso (from August 1-19, 2006) using the combined application of the wide angle reflection and refraction (WARR) and the CO methods of GPR with 300 MHz monostatic antennas. I acquired soil water information in the near ∼ 0.1 m at distance intervals of 10 cm along a 1 km long transect. As reference measurements, the time domain reflectometry (TDR) and frequency domain reflectometry (FDR) probes were buried at 200 m intervals along the transect to sample soil water content data at 10 cm and 20 cm depths respectively. These 3 ground experiments, i.e. the GPR, TDR and FDR, were designed to map the spatial heterogeneity of soil water content along the 1 km long transect and to serve as reference experiments for a satellite equipment with a horizontal resolution of 25 km.

Experimental results and geostatistical analyses of the spatial soil water distribution pattern are summarised as follows:

- The apparent ground wave is more strongly radiated in a wet soil than in a dry one. This might be due to the better capacitive coupling between the antennas and the ground when the soil surface is wet than when dry.

- The GPR-derived soil water data revealed strong heterogeneities in both spatial and temporal soil water distribution, an information which is not adequately covered by the discrete point measurements offered by TDR and FDR. Temporal variation of soil water content was dominated by rainfall. The effect of evaporation on soil water content was insignificant in the raining season in which the measurements were taken. A contribution to the spatial soil water variability has always been the effect of topography. For the investigated region of Dano, however, the region was on the average a flat land, hence, topography played no significant role in the temporal and spatial distributions.

- Modelling exercises of the frequency dependence of the apparent ground wave propagation in soil through simulated radargrams with the Reflexw modelling tool Sandmeier (2007) revealed that it is strongly radiated and more easily registered by high frequency antennas than low ones. For a layered medium and at moderately low frequencies the apparent ground wave registered by the receiver is usually a composite of apparent ground wave phases propagating along the interfaces of the layered media.

- No concrete relationship could be established between the mean soil water content and the coefficient of variation (CV), which represents the ratio of the standard deviation to the mean soil water. A regression equation fitted to the CV-mean soil water data yielded an *R-squared* value of $R^2 = 0.306$. The F-test on the significance of the regression equation for $N = 8$ and $k = 2$ produced $F_{1,6} = 2.64$ which is less than the critical value of 5.99 at 95 % significance. Hence, there is a poor correlation between the mean soil water content and CV. It is thus difficult to predict the CV-mean soil water behaviour. Literature does not present conclusive results on the CV-mean soil water relationship.

- Geostatistical modelling of soil water data show consistency in the shape of the models and they display a kind of periodicity termed hole effect. This periodicity is likely caused by heterogeneities in the soil which influence the development of preferential water infiltration paths resulting in an oscillatory representation of the models about the sill.

- Measurement errors and small-scale variability of soil water distribution indicated by the nugget effect showed a strong tendency to increase during wetter conditions (R^2 = 0.88, $F_{1,6} = 44 > 5.99$ at 95 % significance).

- The mean water content seems not to be related to the correlation length (R^2 = 0.071, $F_{1,6} = 0.46 < 5.99$ at 95 % significance). The property is perhaps controlled by many composite processes operating on a single scale. The correlation lengths were found to be between 54 - 102 m. From the results of this analysis (for soil water content in the near-surface for depths 0-0.1 m), this means that the soil water content data as measured by the reference methods with TDR and SISOMOP which were placed at 200 m apart along the 1 km long transect were uncorrelated. Optimal positions for the TDR and SISOMOP points would have been say every 50 m. This could be determined first after a reconnaissance campaign with GPR.

- Comparison of GPR-derived dielectric coefficient with that of TDR and SISOMOP showed RMSD of 0.86 and 2.10 respectively. The relatively large deviation between GPR and SISOMOP might be due to the relatively deeper depth at which the latter retrieves soil water information. The exploration depths of GPR and TDR were ~ 10 cm as compared to ~20 cm of SISOMOP. Fluctuations in precipitation controlled soil water content were thus most predominant in the upper layer (~0.1 m) of the soil than the deeper layers. It is worth mentioning that the difference in soil water values between GPR and TDR on one hand and GPR and SISOMOP on the other hand can be partly attributed to the different frequencies at which these equipment operate. The soil dielectric coefficient is frequency dependent, hence, the various instruments measured different dielectric coefficients.

  GPR-derived soil water information show strong heterogeneity in the spatial soil water distribution pattern in Dano with a relatively larger number of data ($N > 9000$). Discrete point measurements from TDR and FDR fail to explain the spatial variation of soil water content (due to the poor data volume of 6) and are thus prone to show aliasing effects. The invasive character of point measurements add to additional errors. Hence, GPR-derived soil water data serve as appropriate ground truth data set for comparison with satellite measurements.

9.1 Difficulties and Open Questions

- The GPR technique is based on dielectric coefficient measurements. One problem with soil water content determinations based on dielectric measurements is that the relationships of soil water content with soil composition and also soil texture is a complex one which is not yet completely understood. A lot of mixing models have been suggested over the course of time which describe the dielectric behaviour of soil and its interaction with water but non of these most satisfactorily describe the complex soil-water system.

- Calibration is another problem with methods involving dielectric measurements. Ideally volumetric water content should be related specifically to the type of soil in which the observation is taken. The only *universal* calibration equation due Topp et al. (1980) (which is independent of soil texture, soil structure, salinity and temperature) is generally accepted in soil science applications. However, this calibration equation shows deviations e.g. for organic soils [e.g. Roth et al. (1992)]; volcanic and mineral soils of low bulk density [e.g. Miyamoto et al. (2001), Regalado et al. (2003)]. Is there an in-situ GPR method by which soil water information could be retrieved by just a single measurement? Will such a method produce auxiliary information on soil conductivity, porosity, salinity and texture?

- Up to date, as far as I know there is no generally accepted formula that gives the exact calculation of the exploration depth. The relation developed by Sperl (1999) from modelling exercises which I find most reasonable and hence adapted in this work still gives an approximate depth value. Exploration depth estimations are usually discussed only in relation to the wavelength of the transmitted electromagnetic wave. However, this depth is also dependent on the soil water content. As the soil water content increases the exploration depth decreases. In what way will additional factors like surface roughness, vegetation cover and wave polarization affect the exploration depth? Will numerical modelling answer these questions?

- *R-squared*- and F-tests performed to establish a correlation between the mean soil water content and the coefficient of variation failed to predict a relationship between the two ($R^2 = 0.31 F_{1,6} = 2.64 < 5.99$ at 95 % significance). There are mixed findings in the literature. While authors like Hubbard et al. (2002) reported of an increase in variation with high soil water content, others like Miyamoto et al. (2003) reported rather of a decrease in variation with soil water. Still authors like Western et al. (2004) reported of an increase as well as a decrease in variation with increasing soil water content. What factors actually control the variation of soil water content?

9.2 Outlook

The exploration depth of the ground wave needs to be investigated further. Experiment with the ground wave in the Dano region of Burkina Faso revealed that the apparent ground wave is better radiated in a wet soil that dry one. There is hence, the possibility of acquiring soil water information from ground wave amplitude data.

In Dano only the 300 MHz antennas were employed resulting in a single exploration depth of ~ 0.1 m. Higher and lower frequency antennas would give lower and higher exploration depths respectively. Soil water variability changes with depth. Environmental factors like precipitation and evaporation may cause higher variability at the surface than the subsurface. Investigation of depth dependent spatial soil water variability can be done with GPR by using different frequency antennas.

Although the GPR technique has often been used non-invasively as reference measurements of soil water content in various environments only a few applications exist on investigation of infiltration and leakages through levee structures. This will be an area of much interest for further investigation with GPR. Future flood experiments on dike models would be focused on the investigation of the temporal movement of the flood control wetting front.

Appendix A

GWS Application to Soil Water Content Determination on Dike Model A

A.1 Comparison of GWS and TRIME-TDR with 900 MHz Antenna

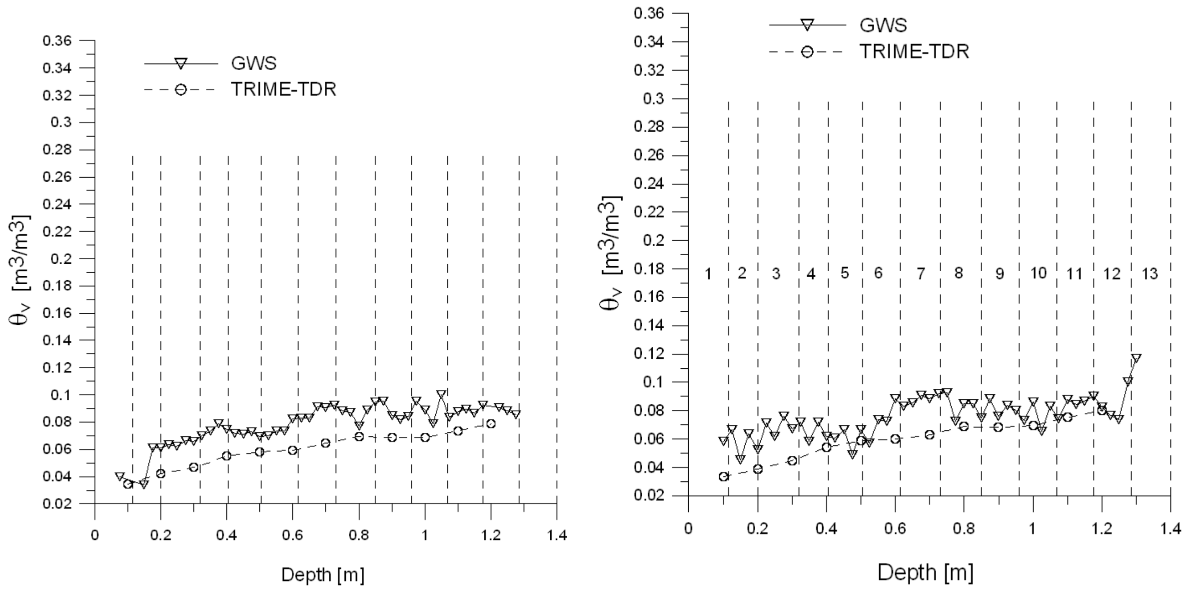

(a) Before flooding

(b) After flood level 0.3 m

Figure A.1: VWC distribution in dike model before and after flooding to 0.3 m level with the 900 MHz antenna.

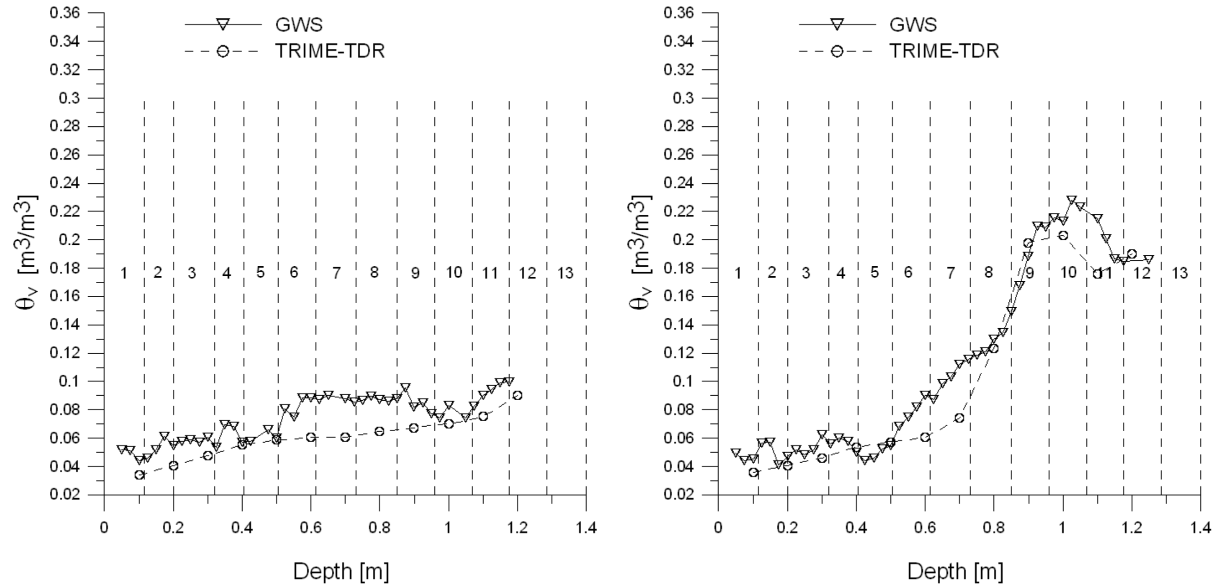

(a) After flood level 0.6 m

(b) After flood level 0.8 m

Figure A.2: VWC distribution in dike model after 0.6 m and 0.8 m flood levels with the 900 MHz antenna.

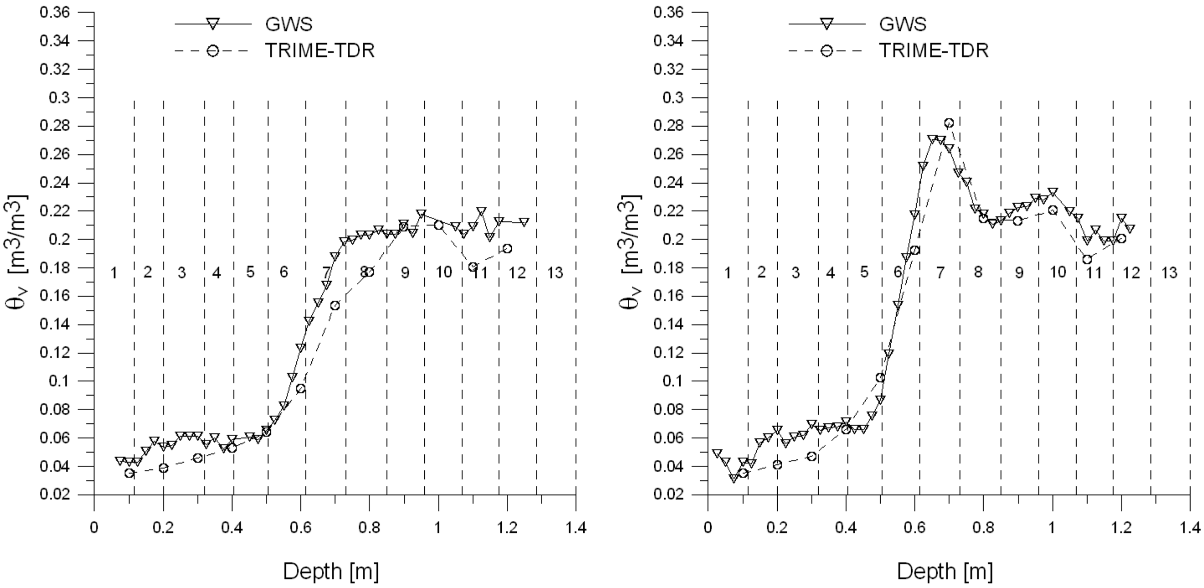

(a) After flood level 1.0 m

(b) After flood level 1.2 m

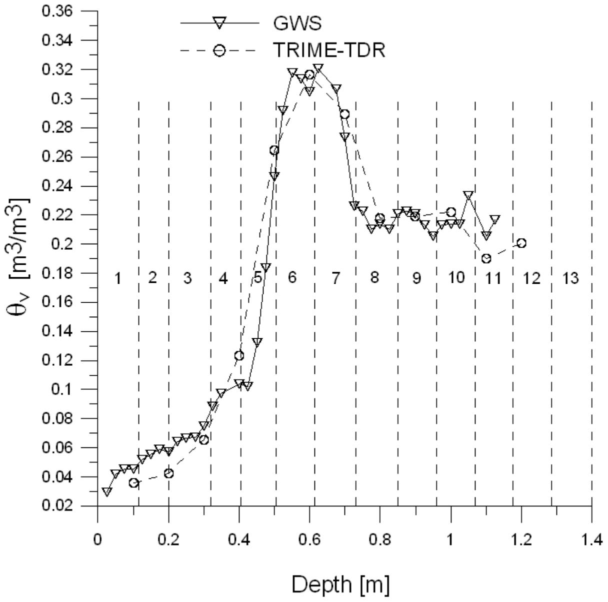

(c) After flood level 1.25 m

Figure A.3: VWC distribution in dike model after 1.0 m, 1.2 m and 1.25 m flood levels with the 900 MHz antenna.

Appendix B

Modal Analysis of GPR Guided Wave Propagation along a Metal Rod

In TDR and GPR applications it is generally assumed that the guided waves propagate with the velocity of the medium surrounding the wave guide. In order to explore the validity of this assumption the propagation velocity is analysed using a cylindrical soil model with a metal rod of radius a in its centre (Fig. B.1).

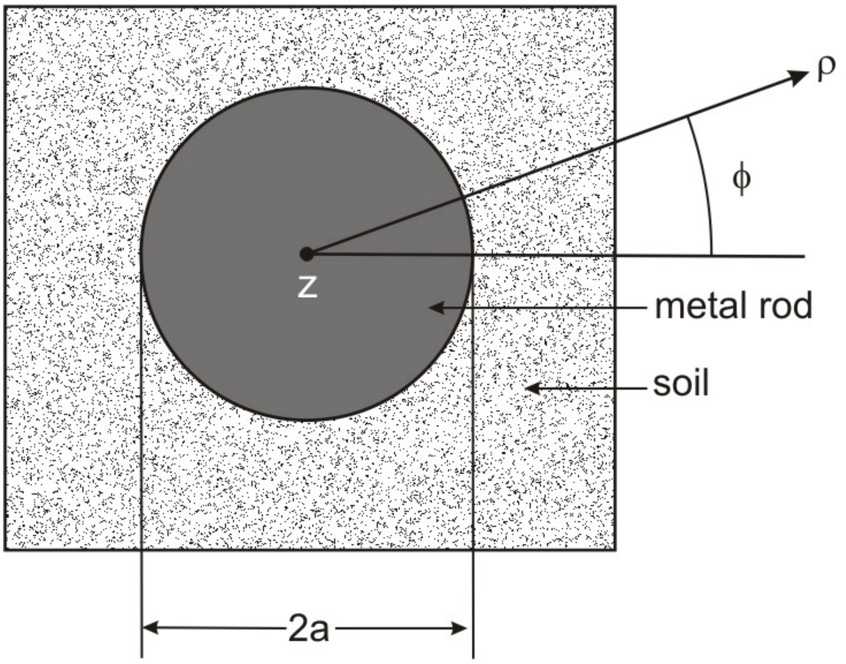

Figure B.1: Cylindrical soil model with metal rod at the centre

Writing Maxwell's equations for the main transverse magnetic (TM) mode in cylindrical coordinates ρ, ϕ, z with $\frac{\partial}{\partial \phi} = 0$, gives

$$\begin{aligned} -\frac{\partial H_\phi}{\partial z} &= (\sigma - i\omega\varepsilon\varepsilon_0)E_\rho && \text{(B.1)} \\ \frac{1}{\rho}\frac{\partial}{\partial \rho}(\rho H_\phi) &= (\sigma - i\omega\varepsilon\varepsilon_0)E_z && \text{(B.2)} \\ \frac{\partial E_\rho}{\partial z} - \frac{\partial E_z}{\partial \rho} &= i\omega\mu_0 H_\phi && \text{(B.3)} \end{aligned}$$

Eqs. (B.1)-(B.3) are three equations in the three variables E_ρ, E_z and H_ϕ

$\frac{\partial}{\partial z}\cdot$ Eq.(B.1) gives

$$-\frac{\partial^2 H_\phi}{\partial z^2} = (\sigma - i\omega\varepsilon\varepsilon_0)\frac{\partial E_\rho}{\partial z} \tag{B.4}$$

$\frac{\partial}{\partial \rho}\cdot$ Eq. (B.2) gives

$$\frac{\partial}{\partial \rho}\left(\frac{1}{\rho}\frac{\partial}{\partial \rho}(\rho H_\phi)\right) = (\sigma - i\omega\varepsilon\varepsilon_0)\frac{\partial E_z}{\partial \rho} \tag{B.5}$$

$$\begin{aligned} (\sigma - i\omega\varepsilon\varepsilon_0)\left(\frac{\partial E_\rho}{\partial z} - \frac{\partial E_z}{\partial \rho}\right) &= -\frac{\partial^2 H_{phi}}{\partial z^2} - \frac{\partial}{\partial \rho}\left(\frac{1}{\rho}\frac{\partial}{\partial \rho}(\rho H_{phi})\right) && \text{(B.6)} \\ &= -\frac{\partial^2 H_\phi}{\partial z^2} - \frac{\partial}{\partial \rho}\left(\frac{1}{\rho}H_\phi + \frac{\partial H_\phi}{\partial \rho}\right) && \text{(B.7)} \\ &= -\frac{\partial^2 H_\phi}{\partial z^2} + \frac{1}{\phi^2}H_\phi - \frac{1}{\rho}\frac{\partial H_\phi}{\partial \rho} - \frac{\partial^2 H_\phi}{\partial \rho^2} && \text{(B.8)} \end{aligned}$$

and using Eq. (B.3):

$$i\omega\mu_0(\sigma - i\omega\varepsilon\varepsilon_0)H_{phi} = k^2 H_\phi \tag{B.9}$$

This leads to the solution for H_ϕ with $k^2 = \omega^2\varepsilon\varepsilon_0\mu_0 + i\omega\mu_0\sigma$ i.e.

$$\sigma - i\omega\varepsilon\varepsilon_0 = \frac{k^2}{i\omega\mu_0} \tag{B.10}$$

$$\frac{\partial^2 H_\rho}{\partial \rho^2} + \frac{1}{\rho}\frac{\partial H_\phi}{\partial \rho} + \frac{partial^2 H_\phi}{\partial z^2} + \left(k^2 - \frac{1}{\rho^2}\right)H_{phi} = 0 \tag{B.11}$$

With the ansatz $H_{phi} \sim e^{ihz}$,

$$\rho^2\frac{\partial^2 H_{phi}}{\partial \rho^2} + \rho\frac{\partial H_\phi}{\partial \rho} + [(k^2 - h^2)\rho^2 - 1]H_\phi = 0 \tag{B.12}$$

Substituting $\gamma^2 = k^2 - h^2$ into Eq. (B.12) results in a Bessel differential equation of the form

$$x^2 y + y + (x^2 - \upsilon^2) = 0 \tag{B.13}$$

with solutions $J_1(x)$ and $Y_1(x)$ where $x = \gamma\rho$ and $\upsilon = 1$. Writing

$$h = \sqrt{k^2 - \gamma^2} = \alpha + i\beta \Rightarrow e^{ihz} = e^{i\alpha z} e^{-\beta z} \tag{B.14}$$

with $v_{\mathrm{ph}} = \frac{\omega}{\alpha}$ and $\beta > 0$

$$H_\phi(\rho, z, t) = \left\{ \begin{array}{c} J_1(\gamma\rho) \\ Y_1(\gamma\rho) \end{array} \right\} e^{i(hz-\omega t)} \tag{B.15}$$

From Eq. B.1,

$$E_\rho = \frac{1}{i\omega\varepsilon\varepsilon_0 - \sigma} \frac{\partial H_\phi}{\partial z} = \frac{ih}{i\omega\varepsilon\varepsilon_0 - \sigma} H_\phi(\rho,\ z,\ t) \tag{B.16}$$

Thus,

$$E_\rho = \frac{ih}{i\omega\varepsilon\varepsilon_0 - \sigma} \left\{ \begin{array}{c} J_1(\gamma\rho) \\ Y_1(\gamma\rho) \end{array} \right\} e^{i(hz-\omega t)} = \frac{h\omega\mu_0}{k^2} \left\{ \begin{array}{c} J_1(\gamma\rho) \\ Y_1(\gamma\rho) \end{array} \right\} e^{i(hz-\omega t)} \tag{B.17}$$

From Eq. B.2,

$$\begin{aligned} (\sigma - i\omega\varepsilon\varepsilon_0)E_z &= \frac{1}{\rho} \frac{\partial}{\partial(\gamma\rho)} (\gamma\rho H_\phi) \\ &= \frac{1}{\rho} H_\phi + \gamma \frac{\partial}{\partial(\gamma\rho)} \Big(H_\phi(\gamma, z, t) \Big) \end{aligned} \tag{B.18}$$

with

$$\frac{d}{dx} \left\{ \begin{array}{c} J_1(x) \\ Y_1(x) \end{array} \right\} = \left\{ \begin{array}{c} J_0(x) \\ Y_0(x) \end{array} \right\} - \frac{1}{x} \left\{ \begin{array}{c} dJ_1(x)/dx \\ dY_1(x)/dx \end{array} \right\} \tag{B.19}$$

Eq. B.18 reads

$$(\sigma - i\omega\varepsilon\varepsilon_0)E_z = \gamma \left\{ \begin{array}{c} J_0(\gamma\rho) \\ Y_0(\gamma\rho) \end{array} \right\} e^{i(hz-\omega t)} \tag{B.20}$$

Thus, with Eq. B.9,

$$\begin{aligned} E_z &= \frac{\gamma}{\sigma - i\omega\varepsilon\varepsilon_0} \left\{ \begin{array}{c} J_0(\gamma\rho) \\ Y_0(\gamma\rho) \end{array} \right\} e^{i(hz-\omega t)} \\ &= \frac{i\omega\mu_0\gamma}{k^2} \left\{ \begin{array}{c} J_0(\gamma\rho) \\ Y_0(\gamma\rho) \end{array} \right\} e^{i(hz-\omega t)} \end{aligned} \tag{B.21}$$

For the two regions of interest, i.e. the inner region ($0 < \rho < a$) and the outer region $0 < \rho < \infty$ of the model, we obtain solutions by using $J_0(\gamma\rho)$ and $J_1(\gamma\rho)$ for $\rho < a$ with $\gamma_i^2 = k_i^2 - h_i^2$ where $k_i^2 = i\omega\mu_0(\sigma_i - i\omega\varepsilon_i\varepsilon_0)$ and $Y_0(\gamma\rho)$ and $Y_1(\gamma\rho)$ for $\rho > a$ with $\gamma_a^2 = k_a^2 - h_i^2$ where $k_a^2 = i\omega\mu_0(\sigma_a - i\omega\varepsilon_a\varepsilon_0)$ respectively.

The complete set of solutions for $\rho < a$ is

$$\begin{aligned} H_\phi &= CJ_1(\gamma_i\rho)e^{i(hz-\omega t)} && \text{(B.22)}\\ H_\rho &= +\frac{h\omega\mu_0}{k_i^2}CJ_1(\gamma_i\rho)e^{i(hz-\omega t)} && \text{(B.23)}\\ E_z &= +\frac{i\omega\mu_0\gamma_i}{k_i^2}CJ_0(\gamma_i\rho)e^{i(hz-\omega t)} && \text{(B.24)} \end{aligned}$$

with $\gamma_i = \sqrt{k_i^2 - h^2}$ and the arbitrary constant C. Similarly, for $\rho > a$, the set of solutions is

$$\begin{aligned} H_\phi &= AY_1(\gamma_a\rho)e^{i(hz-\omega t)} && \text{(B.25)}\\ H_\rho &= +\frac{h\omega\mu_0}{k_a^2}AY_a(\gamma_i\rho)e^{i(hz-\omega t)} && \text{(B.26)}\\ E_z &= +\frac{i\omega\mu_0\gamma_a}{k_a^2}AY_0(\gamma_a\rho)e^{i(hz-\omega t)} && \text{(B.27)} \end{aligned}$$

with $\gamma_a = \sqrt{k_i^2 - h^2}$ and constant A.

For $\rho = a$, the tangential components E_z and H_ϕ must be continuous. Thus,

$$\begin{aligned} AY_1(\gamma_a a) &= CJ_1(\gamma_i a) && \text{(B.28)}\\ \frac{\gamma_a}{k_a^2}AY_0(\gamma_a a) &= \frac{\gamma_i}{k_i^2}CJ_0(\gamma_i a) && \text{(B.29)} \end{aligned}$$

Dividng Eq. (B.28) by Eq. (B.29) gives

$$\frac{k_a^2}{\gamma_a}\frac{Y_1(\gamma_a a)}{Y_0(\gamma_a a)} = \frac{k_i^2}{\gamma_i}\frac{J_1(\gamma_i a)}{J_0(\gamma_i a)} \tag{B.30}$$

i.e.

$$\frac{k_a^2}{\sqrt{k_a^2 - h^2}}\frac{Y_1\left(\sqrt{k_a^2 - h^2}a\right)}{Y_0\left(\sqrt{k_a^2 - h^2}a\right)} - \frac{k_i^2}{\sqrt{k_i^2 - h^2}}\frac{J_1\left(\sqrt{k_i^2 - h^2}a\right)}{J_0\left(\sqrt{k_i^2 - h^2}a\right)} = 0 \tag{B.31}$$

Eq. B.31 must be solved for h. The solution is obtained with MATLAB software using the Bessel function representations *besselj (v,x)* and *bessely (v,x)*, with $v = 0, 1$ and searching for it minimum of the absolute value with *fminsearch*.

A corresponding equation for the propagation conditions of the TM surface wave along a cylindrical conductor embedded in a homogeneous lossless dielectric was published by Sommerfeld (1899) and Goubau (1950).

Table B.1 shows the values $\frac{\alpha}{k_a} - 1$ [%], $\frac{1}{\beta}$ [m] and $\frac{c}{v_{\mathrm{ph}}\sqrt{\varepsilon_a}-1}$ [%] for different conductivities σ_a [S/m] of the embedded dielectric with the assumption that $\sigma_i = 10^7$ S/m for the iron cylindrical conductor, $a = 0.02$ m for the radius of the conductor , $v = 5 \cdot 10^8\ s^{-1}$ for the radar frequency, $\varepsilon_a = 9$, $\varepsilon_i = 1$, ${k_i}^2 = \frac{\varepsilon_i \omega^2}{c^2 + i\omega\mu_0\sigma_i}$ and ${k_a}^2 = \frac{\varepsilon_a \omega^2}{c^2 + i\omega\mu_0\sigma_a}$

σ_a [S/m]	$\alpha/k_a - 1$ [%]	$1/\beta$ [m]	$c/V_{ph}\sqrt{\varepsilon_a} - 1$ [%]
10^{-3}	5.4	15.1	-5.1
$3 \cdot 10^{-2}$	5.8	0.502	-5.5
1	3.4	0.025	-3.4

Table B.1: Attenuation effects of the electromagnetic wave propagation for different conductivities of the embedding dielectric

Obviously, there is a strong dependence of the propagation length $1/\beta$ on the conductivity of the embedding medium, whereas its influence on the wave velocity is only minor.

Appendix C

Soil Water Content Determination with the Ground Wave Method in Dano, Burkina Faso (West Africa)

C.1 Histograms of Soil Water Content Distribution

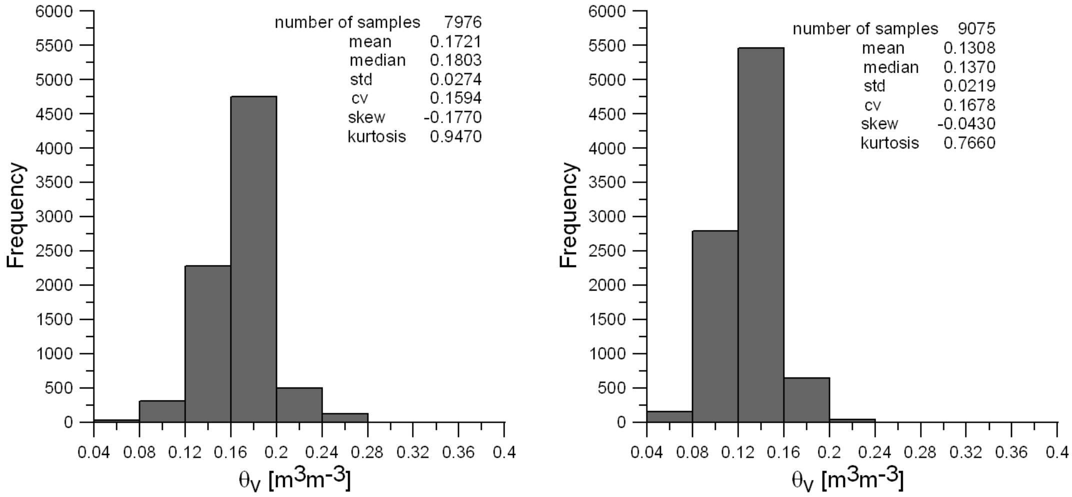

(a) 7th August 2006

(b) 9th August 2006

Figure C.1: Histograms of soil water content (August 7-19, 2006.

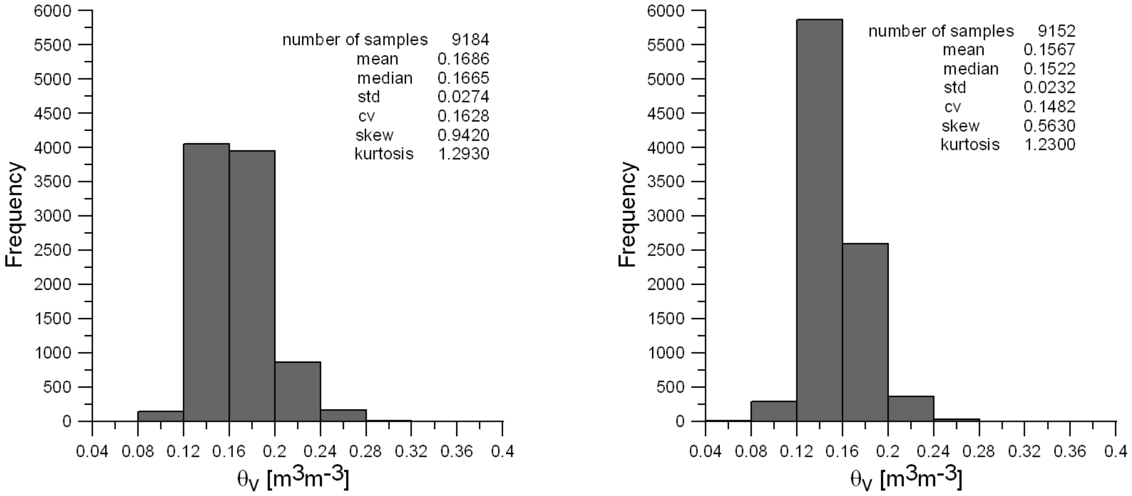

(a) 17th August 2006 (b) 18th August 2006

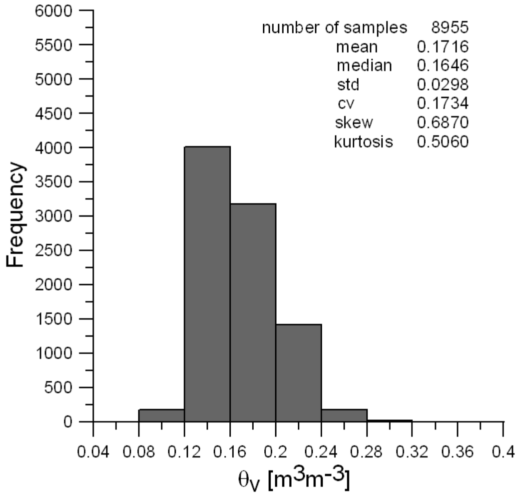

(c) 19th August 2006

Figure C.2: Histograms of soil water content (August 7-19, 2006.

C.2 Comparison of GPR-derived Dielctric Coefficient with SISOMOP and TDR

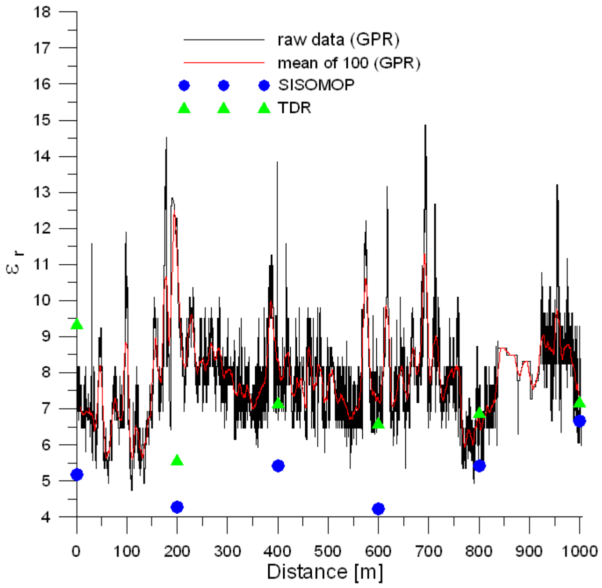

Figure C.3: Comparison of GPR-derived soil dielectric coefficient with that of TDR and SISOMOP (August 3, 2006).

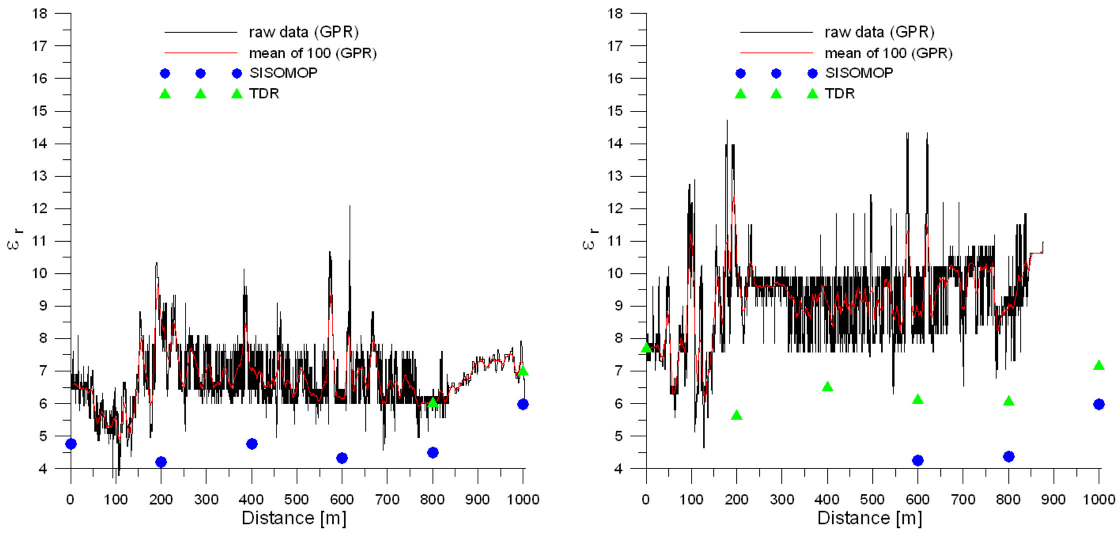

(a) 5th August 2006

(b) 7th August 2006

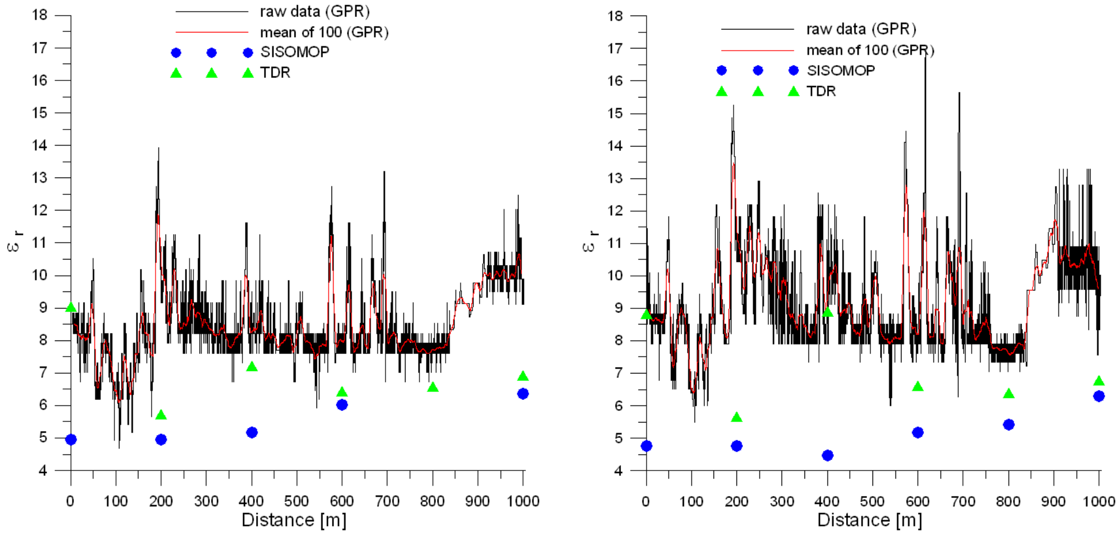

(c) 18th August 2006

(d) 19th August 2006

Figure C.4: Comparison of GPR-derived soil dielectric coefficient with that of TDR and SISOMOP (August 5-19, 2006).

C.3 Rainfall, Evaporation and GPR-derived Mean Soil Water Content

Date	Antecedent Rainfall [mm/day]	Evaporation [mm/day]	GPR-derived Mean Soil Water Content [m^3m^{-3}]
30 Jul 06	26.1	3.26	N/A
31 Jul 06	22.8	3.95	N/A
1 Aug 06	0	1.73	0.2032
2 Aug 06	0	0.60	N/A
3 Aug 06	0	3.19	0.1443
4 Aug 06	0	2.42	0.1297
5 Aug 06	1.1	1.53	0.1197
6 Aug 06	3.1	3.00	N/A
7 Aug 06	0	2.98	0.1721
8 Aug 06	0.4	2.62	N/A
9 Aug 06	0	2.17	0.1308
10 Aug 06	0	2.66	N/A
11 Aug 06	45.8	1.73	N/A
12 Aug 06	5.3	3.39	N/A
13 Aug 06	0.6	3.71	N/A
14 Aug 06	17.0	4.08	N/A
15 Aug 06	0.1	3.59	N/A
16 Aug 06	1.7	1.39	N/A
17 Aug 06	0	2.90	0.1686
18 Aug 06	0.6	2.17	0.1567
19 Aug 06	0.4	2.72	0.1716

Table C.1: Rainfall rates, evaporation rates and GPR-derived soil water content listed with dates of measurement (July 30 - August 19, 2006).

C.4 Geostatistical Modelling of Soil Water Content

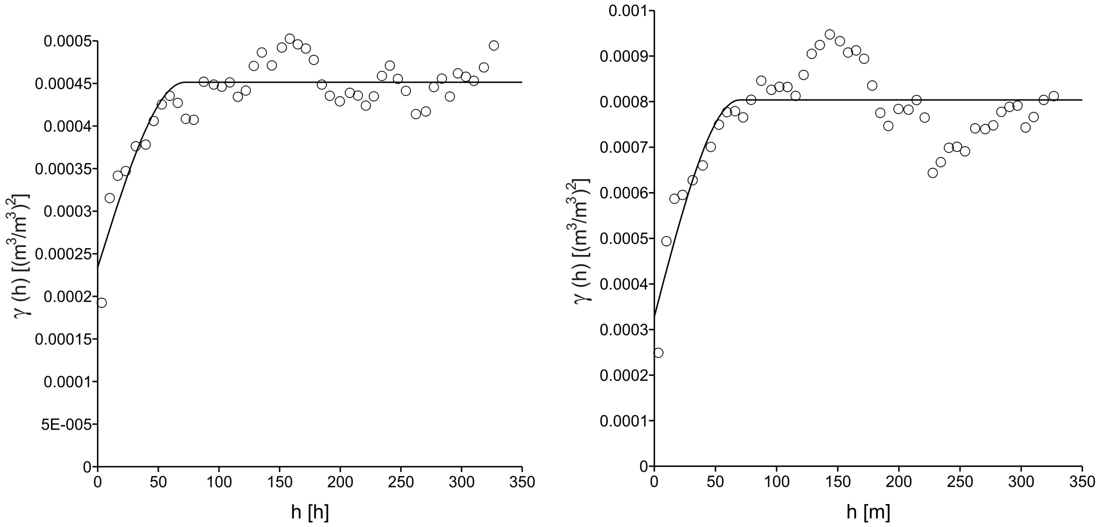

(a) 9th August 2006
(b) 17th August 2006

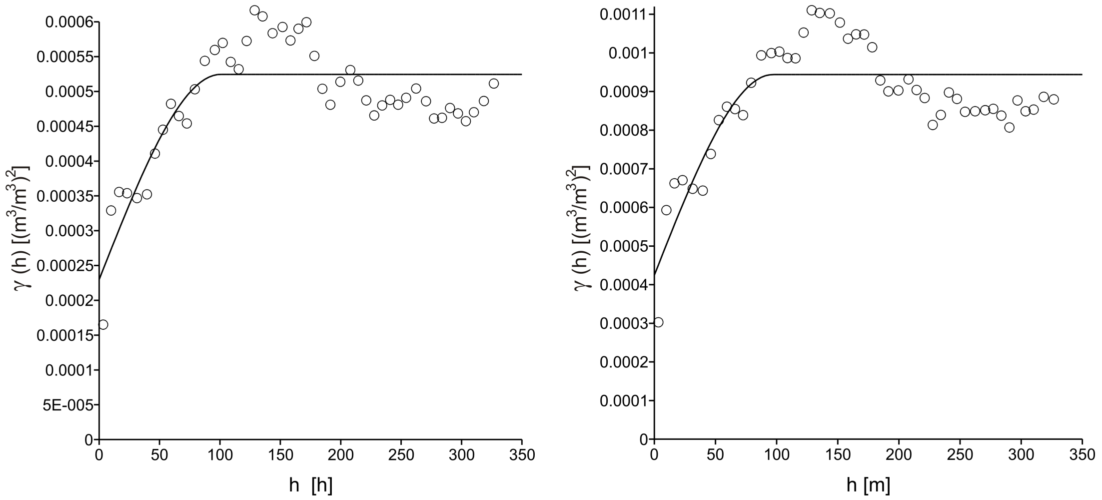

(c) 18th August 2006
(d) 19th August 2006

Figure C.5: Semi-variograms for volumetric water content. Solid lines represent spherical models fitted to experimental values (August 9-19, 2006).

Appendix D

Description and Principle of Operation of SIR-3 Equipment

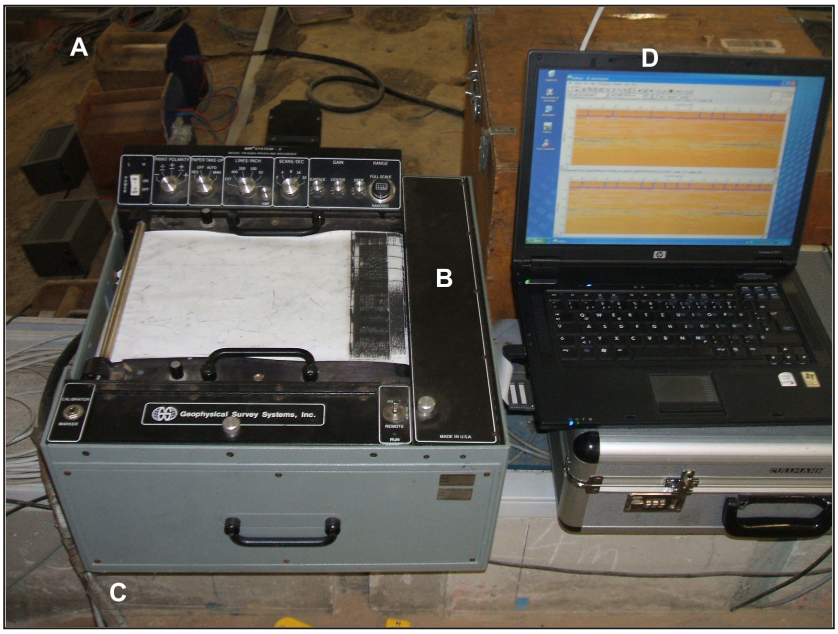

Figure D.1: Photograph of the SIR-3 system: 12 V DC battery source (A); SIR-3 control unit (B); cable to antenna (C) and laptop (D).

D.1 General Description of SIR-3

The Subsurface Interface Radar (SIR$^{©}$) System-3 (from the Geophysical Survey Systems Inc.) is a portable broadband pulse radar system capable of detecting the position and depth of objects buried in dielectric materials.

The Subsurface Interface Radar Control Unit supplies power and synchronizing signals to a transducer which outputs a pulse of electromagnetic energy into the ground, air, or other dielectric material. The pulse, travelling near the speed of light, is reflected by interfaces of objects under the surface, and the reflected energy is detected by the receiver antenna. The receiver converts the pulse, several nanoseconds in duration, to an analogue signal tens of milliseconds in duration and returns this signal to the radar unit.

The control unit sends the signal to a laptop where it is A-D converted and stored in Reflexw format.

Power for the system is derived from a 12 V DC source.

D.2 Pre-Data Run Settings

After all the cables have been properly connected at both ends and the unit switched on the system has to be well tuned before it becomes ready to record data meaningfully. Basically, two main pre-data run operations are performed.

- The first set of calibrations comprise of setting the *scan rate*, the *trace length*, *sample number*. By activating a *calibrator/marker* button the recorded signals in the *auto* and *manual* modes are synchronised with the help of a *signal postion* button, which can be rotated through an angle of 180 ° both in the clockwise and anticlockwise directions.
- For recording data the *calibrator/marker* button is moved to the *marker* position. This is the data recording mode and once again the radar signals in the *auto* and *manual* modes are synchronised with the help of the *signal position* button. The signal intesity is carefully adjusted with the help of *surface*, *center* and *deep* buttons to avoid signal clipping. The system is finally put switched to the *manual* mode for data run. The SIR system produces a pulse to indicate the start of scan.

List of Figures

List of Tables

Used Software

- Adobe Photoshop 7: graphics.
- CorelDraw Graphics 12 : graphics.
- Golden Software Grapher 4 : statistical analysis, scripts and plots.
- Golden Software Surfer 8 : variogram calculation, kriging.
- LaTeX: typesetting and layout.
- Matlab 7 : statistical analysis, scripts and plots.
- Microsoft Excel : data processing.
- Microsoft Word : typesetting.
- Reflexw 4.5 (Sandmeier, 2007): GPR data processing and FD simulation.
- xmgrace : statistical and regression analyses, plots.

List of Used Symbols and Acronyms

$\mathbf{A}$	Magnetic vector potential	[Vsm^{-1}]
α	Attenuation constant	[m^{-1}]
$\mathbf{B}$	Magnetic flux density	[T]
β	Phase constant	[m^{-1}]
c	Electromagnetic wave velocity in vacuum (3×10^8)	[ms^{-1}]
C_i	Ionic concentration	[mole l^{-1}]
C	Capacitance	[CV^{-1}]
$\mathbf{D}$	Electric flux density	[Cm^{-2}]
δ	Dirac's delta function ($\delta(x) = \infty$ for $x = 0$; $\delta(x) = 0$ for $x \neq 0$)	
$\mathbf{E}$	Electric field strength	[Vm^{-1}]
f	frequency	[s^{-1}]
f_0	Relaxation frequency	[s^{-1}]
h	Distance	[m]
$\mathbf{H}$	Magnetic field strength	[Am^{-1}]
i	$\sqrt{-1}$	
I	Current	
$\mathbf{j}$	Free current density	[Am^{-2}]
$\mathbf{k}$	Wave number vector	[m^{-1}]
l	Length	[m]
n	Refractive Index	[]
N	Natural number	
$\mathbf{r}$	Position vector	[m]
v	Velocity	[m^{-1}]
v_{ph}	Phase velocity of electromagnetic wave in soil	[m^{-1}]
V	Volume	[m^3]
V'	Volumetric fraction	[m^{3}m^{-3}]
ω	Angular frequency ($2\pi f$)	[s^{-1}]
ϕ	Phase angle	[°]
φ	Angle	[°]
Φ	Effective porosity	[m^{3}m^{-3}]
$\mathbf{P}$	Polarisation density	[Cm^{-2}]
γ	Semivariance	

τ	Relaxation time	[s]
κ	Constant in mixing model (0.5)	[]
λ	Wavelength	[m]
Λ	Skin depth	[m]
σ	Electrical conductivity	[S/m]
σ_{eff}	Effective electrical conductivity	[S/m]
σ_{dc}	Bulk electrical conductivity	[S/m]
ε_0	Dielectric coefficient of free space	[Fm^{-1}]
ε	Dielectric coefficient	[]
ε_r	Relative dielectric coefficient	[]
ε_{eff}	Effective dielectric coefficient	[]
ρ	Electric charge density	[Cm^{-3}]
R	Receiver	
R	Reflection coefficient	[]
t	Time	[s]
T	Transmitter	
T	Transmission coefficient	[]
μ	Magnetic permeability	[Hm^{-1}]
μ_0	Magnetic permeability of free space ($4\pi \times 10^7$)	[Hm^{-1}]
μ_r	Relative magnetic permeability	[]
∇	Nabla operator ($\partial/\partial x, \partial/\partial y, \partial/\partial z$)	
χ	polarizability	[$\mathrm{Cm}^2\mathrm{V}^{-1}$]
χ_e	Electric susceptibilty	[]
ϑ	Loss angle	[°]
$\tan\vartheta$	Loss tangent	[]
θ_g	Gravimetric water content	[kgkg^{-1}]
θ_v	Volumetric water content	[$\mathrm{m}^3\mathrm{m}^{-3}$]
Θ	Scalar potential	[V]
z	Depth	[m]
Z	Electromagnetic wave impedance	[Ω]

ASCII	American Standard Code for Information Interchange
AC	Alternating Current
AMMA	African Monsoon Multidisciplinary Analyses
AMSR-E	Advanced Microwave Scanning Radiometer-Earth Observing System
CO	Common Offset
CMP	Common Midpoint
DC	Direct Current
ERT	Electrical Resistivity Tomography
FDR	Frequency Domain Reflectometry
FZK	Forschungszentrum Karlsruhe (Karlsruhe Research Centre)
DWD	German Weather Service

GETFUND	Ghana Educational Trust Fund
GPI	Geophysical Institute
GPR	Ground Penetrating Radar
GWS	Guided Wave Sounding
GSSI	Geophysical Survey Systems Inc.
IMK	Institute for Meteorology and Climate Research
LM	Local Model
N/A	Not Available
NMM	Neutron Moderation Measurements
NMR	Neutron Magnetic Resonance
RADAR	Radio Detection and Ranging
RC	Reflection Coefficient
RMSD	Root Mean Square Deviation
SIR	Surface Interface Radar
SISOMOP	Soil Moisture Group
SMG	Simple Soil Moisture Probe
SOP	Special Observation Period
TDR	Time Domain Reflectometry
TRIME-TDR	Time Domain Reflectometry with Intelligent Micro-Elements
VWC	Volumetric Water Content
WAM	West African Monsoon
WARR	Wide Angle Reflection and Refraction

References

al Hagrey, S. A. and Michaelson, J. (2002). Resistivity and percolation study of preferential flow in vadose zone at Brockhorst, Germany. *Geophysics*, 64 (3):746–753.

Altese, E., Bolognani, O., Mancini, M., and Troch, P. A. (1996). Retrieving soil moisture over bare soil from ERS-1synthetic aperture radar data: sensitivity analysis based on theoretical surface scattering model and field data. *Water Resources Research*, 32 (3):653–661.

Alumbaugh, D., Chang, P. Y., Paprocki, L., Brainard, J. R., Glass, R. J., , and Rautman, C. A. (2002). Estimating moisture contents in the vadose zone using cross-borehole ground penetrating radar: a study of accuracy and repeatability. *Water Resources Research*, 38:1309.

Anderson, M. G. and Burt, T. P. (1978). The role of topography in controlling through flow generation. *Earth Surface Processes*, 3:331–344.

Annan, A. P. (1973). Radio interferometry depth sounding. part 1 - theoretical discussion. *Geophysics*, 38(3):557–580.

Annan, A. P. (1996). Transmission, dispersion and GPR. *Journal of Engineering and Environmental Geophysics*, pages 125–136.

Annan, A. P. and Davis, J. L. (1976). Impulse radar sounding in permafrost. *Radio Science*, 11:383–394.

Arcone, S. A., Lawson, D. E., Delaney, A. J., Strasser, J. C., and Strasser, J. D. (1998). Ground-penetrating radar reflection profiling of ground water and bedrock in an area of discontinuous permafrost. *Geophysics*, 63:558–669.

Arcone, S. A., Peapples, P. R., and Liu, L. (2003). Propagation of ground penetrating radar (GPR) pulse in a thin waveguide. *Geophysics*, 68:1922–1933.

Asmussen, L. E., Perkins, H. F., and Allison, H. D. (1986). Subsurface descriptions by ground penetrating radar for watershed delineations. *Research Bulletin, University of Georgia, College of Agriculture Experiment Stations*, 340.

Bailey, J. T., Evans, S., and Robin, d. Q. G. (1964). Radio echo soundings of polar ice sheets. *Nature*, 204:420–421.

Balanis, C. A. (1997). *Antenna Theory, Analysis and Design*. John Wiley and Sons, New York, NY. 2nd Edition.

Barling, R. D., Moore, I. D., and Grayson, R. B. (1994). A quasi-dynamic wetness index for characterizing the spatial distribution of zones of surface saturation and soil water content. *Water Resources Research*, 30:1029–1044.

Baver, L. D., Gardner, W. H., and Gardner, W. R. (1997). *Soil Physics*. Wiley, New York.

Becker, R., Brandelik, A., Hübner, C., Schädel, W., Scheuermann, A., and Schlaeger, S. (2002). Soil and snow moisture measurement system with subsurface transmission lines for remote sensing and environmental applications. In *Results of the Soil Moisture Group of the University of Karlsruhe, in Proceedings of the Open Symposiumon Propagation and Remote Sensing*, Garmisch-Partenkirchen, Germany. URSI Commission-F.

Becker, R., Brandelik, A., Hübner, C., Schädel, W., Scheuermann, A., and Schlaeger, S. (2005). Spatial time domain reflectometry with rod probes. In *Proceedings of the 6th Conference on Electromagnetic Wave Interaction with Water and Moist Substances*, Weimar, Germany. ISEMA.

Behrendt, J. C., Drewry, D., Jankowski, E., and England, A. W. (1979). Aeromagnetic and radar ice sounding indicate substantially greater area for dufek intrusion in Antarctica. *American Geophysical Union Transactions*, 60:245.

Beldring, S., Gottschalk, L., Seibert, J., and Tallaksen, L. M. (1999). Distribution of soil moisture and groundwater levels at patch and catchment scales. *Agricultural and Forest Meteorology*, 98:305–324.

Bell, F. G. (2000). *Engineering Properties of Soil and Rocks*. Blackwell Publishers, Berlin.

Beres, M. J. and Haeni, F. P. (1991). Application of ground-penetrating-radar methods in hydrogeologic studies. *Ground Water*, 29:375–386.

Berktold, A., Wollny, K. G., and Alstetter, H. (1998). Subsurface moisture determination with the ground wave of GPR. In *Proceedings, 7th International Conference on Ground Penetrating Radar*, pages 675–680, Lawrence, KS.

Binley, A., Winship, P., West, J. L., Pokar, M., and Middleton, R. (2001). High-resolution characterization of vadose zone dynamics using cross-borehole radar. *Water Resource Research*, 37:2639–2652.

Binley, A., Winship, P., West, L. J., Pokar, M., and Middleton, R. (2002). Seasonal variation of moisture content in unsaturated sandstone inferred from borehole radar and resistivity profiles. *Journal of Hydrology*, 267:160–172.

Birchak, J. R., Gardner, C. G., Hipp, v., and Victor, J. M. (1974). High dielectric constant microwave probes for sensing soil moisture. In *Proceedings of IEEE*, volume 62 (1), pages 93–98.

Bogorodsky, V. V., Bentley, C. R., and Gudmandsen, P. E. (1985). *Radio glaciology*. D. Reidel Publishing Company, Tokyo.

Boll, J., van Rijn, R. P. G., Weiler, K. W., and Ewen, J. A. (1996). Using ground-penetrating radar to detect layers in a sandy field soil. *Geoderma*, 70 (2-4):117–132.

Brekhovskikh, L. M. (1960). *Waves in Layered Media*. Academic Press, London.

Brekhovskikh, L. M. (1980). *Waves in Layered Media*. Academic Press, London.

Brewster, M. and Annan, A. P. (1994). Ground penetrating radar monitoring of a controlled DNAPL release: 200 MHz radar. *Geophysics*, 59:1211–1221.

Brown Jr, W. E. (1972). Moon. *Earth, Moon and Planets*, 4:133.

Bryan, M. L. (1974). Ice thickness variability on Silver Lake, Genesee County, Michigan-a radar approach. In *Advanced Concepts in the Study of Snow and Ice Resources.*, pages 213–223.

Bárdossy, A. and Lehmann, W. (1998). Spatial distribution of soil moisture in a small catchment-part 1: geostatistical analysis. *Journal of Hydrology*, 206:1–15.

Caldecott, R., Irons Jr, D. A., Moffatt, D. L., Peters Jr, L., Puskar, R. J., Toth, J. F., and Young, J. D. (1972). *Electromagnetic pulse sounding for surveying underground water: Electro Science Laboratory Report 401X-1*. Ohio State University.

Campbell, D. J. and Henshell, J. K. (2001). Soil water content. In *Soil and Environmental Analysis*, pages 315–348. Marcel Dekker, New York.

Cape, J. (1997). *Development of Value Selection Method for Choosing between Alternative Soil Moisture Sensors*, volume AIT2. Land and Water Resources Research and Development Corporation Project, Canberra, ACT.

Carr, J. R. (1995). *Numerical analysis for geological sciences*. Prentice Hall, Engelwood Cliffs, NJ.

Chanzy, A. (2003). *Evaporation from soils: In Encyclopaedia of Water Science (Stewar, B. A. and Howell, T. A. eds.)*. Marcel Dekker, USA.

Chanzy, A., Tarussov, A., Judge, A., and Bonn, F. (1996). Soil water content determination using a digital ground-penetrating radar. *Soil Science Society of America Journal*, 60:1318–1326.

Charlesworth, P. (2005). Soil water monitoring. national program for sustainable irrigation. *Land and Water*, page 38.

Clarke, G. K. C. (1987). Fast glacier flow: ice streams, surging, and tidewater glaciers. *Journal of Geophysical Research*, 92:8835–8841.

Clement, W. P. and Ward, A. L. (2003). *Using ground penetrating radar to measure soil moisture:Handbook of Agricultural Geophysics*. American Society of Agricultural Engineers, Las Vegas, NV.

Cook, J. C. (1960). Proposed monocycle-pulse, VHF radar for airborne ice and snow measurements. *AIEE Transactions on Communication and Electronics.*, 79(2):588–594.

Cressie, N. C. (1993). *Statistics for Spatial Data*. John Wiley and Sons Inc., USA.

Daily, W., Ramirez, A., la Brecque, D., and Nitao, J. (1992). Electrical resistivity tomography of vadose water movement. *Water Resources Research*, 28:1429–1442.

Dalton, F. N. (1992). Development of the time domain reflectometry for measuring soil water content and bulk soil electrical conductivity. In *Measurement of Soil Physical Properties: Bridging Theory and Practice*, volume 30, pages 143–167, Madison.

Daniels, D. J. (1996). *Surface-Penetrating Radar*, volume 6. IEE Radar, Sonar, Navigation and Avionics, London.

Davidson, M. W. J., Le Toan, T., Mattia, F., Satalino, G., Manninen, T., and Borgeaud, M. (2000). On the characterisation of agricultural soil roughness for radar remote sensing studies. *IEEE Transactions on Geoscience and Remote Sensing*, 38 (2):630–640.

Davis, J. L. and Annan, A. P. (2002). Ground penetrating radar to measure soil water content. In *J.H. Dane and G.C. Topp (eds) Methods of Soil Analysis, Part 4: Physical Methods.*, pages 446–463, Madison, WI. Soil Science Society of America, Inc.

Davis, J. L. and Annan, S. P. (1989). Ground penetrating radar for high resolution mapping of soil and rock stratigraphy. *Journal of Geophysical Prospecting*, 37 (5):531–551.

de Loor, S. G. P. (1968). Dielectric properties of heterogeneous mixtures containing water. *Journal Microwave Power*, 3 (2):67–73.

de Loor, S. G. P. (1983). The dielectric properties of wet materials. *IEEE Transactions of Geoscience and Remote Sensing*, GE-21:364–369.

Debruyckere, L. F. A., Franks, S. W., Beven, K. J., and de Troch, F. P. (1996). Towards the upscaling of local surface flux models. *Phyics and Chemistry of the Earth*, 21 (3):183–188.

Debye, P. J. W. (1945). *Polar Molecules*. Dover Press.

Deryck, L. (1978). Natural propagation of electromagnetic waves in tunnels. *IEEE Transactions on Vehicular Technology*, Vt-27 (3):145–151.

DIN18121 (1988). Site investigation of soil samples. determination through oven drying. *German Standard Part 1. Water Content.*

Dirksen, C. and Dirksen, C. (1999). *Soil Physics Measurements.* Catena Verlag, Reiskirchen.

Dobson, M. C., Ulaby, F. T., El-Rayes, M., and Hallikainen, M. (1984). Microwave dielectric behaviour of wet soil, Part ii: Four component dielectric mixing model. *RSL Technical Report, Remote Sensing Laboratory, University of Kansas Center for Research, Inc*, pages 545–552.

D'Odorico, P., Ridolfi, L., Porporato, A., and Rodriguez-Iturbe, I. (2000). Preferential states of seasonal soil moisture: The impact of climate fluctuations. *Water Resources Research*, 36:2209–2219.

Du, S. (1996). *Determination of water content in the subsurface with the ground wave of ground penetrating radar.* PhD thesis, University of Munich.

Du, S. and Rummel, P. (1996). Reconnaissance studies of moisture in the subsurface with GPR. In *Proceedings of the Fifth International Conference on Ground Penetrating Radar*, pages 1241–1248, Kitchener, Ontario, Canada.

Dubois, J.-C. (1995). Borehole radar experiment in limestone: Analysis and data processing. *First Break*, 13:57–67.

D'Urso, G. and Minacapilli, M. (2006). A semi-empirical approach for surface soil water content estimation from radar without apriori information on surface roughness. *Journal of Hydrology*, 321:297–310.

Ellis, R. G. and Oldenburg, S. W. (1994). The pole-pole 3d dc resistivity inverse problem: A conjugate gradient approach. *Geophysics Journal International*, 119:187–194.

Endres, A. L., Clement, W. P., and Rudolph, D. L. (2000). Ground penetrating radar imaging of an aquifer during a pumping test. *Ground Water*, 38:566–576.

Entin, J. K., Robock, A., Vinnikov, K. Y., Hollinger, S. E., Liu, S. X., and Namkhai, A. (2000). Temporal and spatial scales of observed soil moisture variations in the extratropics. *Journal of Geophysical Research-Atmospheres*, 105 (D9):11865–11877.

Eppstein, M. J. and Dougherty, D. E. (1998). Efficient three-dimensional data inversion: soil characterization and moisture monitoring from cross-well ground-penetrating radar at the Vermont test site. *Water Resources Research*, 34 (8):1889–1900.

Evans, D. L., Farr, T. G., van Zyl, J. J., and Zebker, H. A. (1988). Radar Polarimetry: Analysis, Tools and Applications. *IEEE Transactions on Geoscience and Remote Sensing*, 26 (6):774–789.

Evans, S. (1963). Radio techniques for the measurement of ice thickness. *Applied Geophysics*, 11:406–410.

Evett, S., Laurent, J.-P., Cepuder, P., and Hignett, C. (2002). Neutron scattering, capacitance, and TDR soil water content measurements compared on four continents. In *17th World Congress of Soil Science*, volume 5, pages 1021–1–1021–10, Bangkok, Thailand.

Famiglietti, J. S., Deveraux, J. A., Laymon, C. A., Tsegaye, T., Houser, P. R., Jackson, T. J., Graham, S. T., Rodell, M., and van Oevelen, P. J. (1999). Ground-based investigation of soil moisture variability within remote sensing footprints during the Southern Great Plains 1997 (SGP97) hydrology experiment. *Water Resources Research*, 35:1839–1851.

Fischer, E., McMechan, G. A., and Annan, A. P. (1992). Acquisition and processing of wide aperture ground penetrating radar data. *Journal of Geophysics*, 57 (3):495–503.

Fisher, E., McMechan, G. A., and Annan, A. P. (1992). Acquisition and processing of wide-aperture ground-penetrating radar data. *Geophysics*, 57 (3):495–504.

Forster, K. R. and Schwan, H. P. (1989). Dielectric properties of tissues and biological materials: a critical review. *Critical Review in Biomed Engineering*, 17 (1):25–104.

Galagedara, L. W., Parkin, G. W., and D., R. J. (2004). Measuring and modelling of GPR ground wave depth penetration under transient soil moisture conditions. In *10th International Conference on Ground Penetrating Radar*, Delft, Netherlands.

Galagedara, L. W., Parkin, G. W., and Redman, J. D. (2003). An analysis of the ground-penetrating radar direct ground wave method for soil water content measurement. *Hydrological Processes*, 17 (18):3615–3628.

Galagedara, L. W., Parkin, G. W., and Redman, J. D. (2005a). Measuring and modelling of direct ground wave depth penetration under transient soil moisture conditions. *Subsurface Sensing Technologies and Applications*, 6 (2):193–205.

Galagedara, L. W., Parkin, G. W., Redman, J. D., von Bertoldi, P., and Endres, A. L. (2005b). Field studies of the gpr ground wave method for estimating soil water content during irrigation and drainage. *Journal of Hydrology*, 301 (1-4):182–197.

Galagedara, L. W., Parkin, G. W., Redman, J. D., von Bertoldi, P., and Endres, A. L. (2005c). Numerical modelling of GPR to determine the direct ground wave sampling depth. *Vadose Zone Journal*, 4:1096–1106.

Gardner, M. K. C., Robinson, D., Blyth, K., and Cooper, J. D. (2001). Soil water content. In *Soil and Environmental Analysis*, pages 1–64. Marcel Dekker, New York.

Ghose, R. and Slob, E. C. (2006). Quantitative integration of seismic and gpr reflections to derive unique estimates for water saturation and porosity in subsoil. *Geophysical Research Letters*, 33:540–544.

Gilson, E. W., Redman, J. D., Pilon, J., and Annan, A. P. (1996). Near surface applications of borehole radar. In *Symposium on the Application of Geophysics to Engineering and Environmental Problems*, pages 545–553, Colorado.

Gish, T. J., Dulaneya, W. P., Kung, K. J. S., Daughtrya, C. S. T., Doolittle, J. A., and Miller, P. T. (2002). Evaluating use of ground-penetrating radar for identifying subsurface flow pathways. *Soil Science Society of America Journal*, 66:1620–1629.

Gogineni, S., Chuah, T., Allen, C., Jezek, K., and Moore, R. K. (1998). An improved coherent radar depth sounder. *Journal of Glaciology*, 44 (148):659–669.

Goovaerts, P. and Chiang, C. N. (1993). Temporal persistence of spatial patterns for mineralizable nitrogen and selected soil properties. *Soil Science Society of America Journal*, 57:372–381.

Goubau, G. (1950). Surface waves and their application to transmission lines. *Journal of Applied Physics*, 21:1119–1128.

Grayson, R. B., Western, A. W., Chiew, F. H. S., and Blöschl, G. (1997). Preferred states in spatial soil moisture patterns: Local and non-local controls. *Water Resources Research*, 33:2897–2908.

Greaves, R. J., Lesmes, D. P., Lee, J. M., and Toksoz, M. N. (1996). Velocity variations and water content estimated from multi-offset, ground-penetrating radar. *Journal of Geophysics*, 61 (3):683–695.

Griffiths, D. J. (1999). *Introduction to Electrodynamics*. Prentice Hall, New Jersey.

Grote, K., Hubbard, S., and Rubin, Y. (2003). Field-scale estimation of volumetric water content using GPR ground wave techniques. *Water Resources Research*, 39 (11):SBH5–1 – SBH5–11.

Grote, K., Hubbard, S. S., Harvey, J., and Rubin, Y. (2004). Evaluation of infiltration in layered pavements using surface GPR reflection techniques. *Journal of Applied Geophysics*, 57:129–153.

Grote, K., Hubbard, S. S., and Rubin, Y. (2002). GPR monitoring of volumetric water content in soils applied to highway construction and maintenance. *The Leading Edge*, 21:482–485.

Hagrey, S. A. and Müller, C. (2000). Gpr study of pore water content and salinity in sand. *Geophysical Prospecting*, 48 (1):63–85.

Hagrey, S. A. and Müller, C. (2002). GPR- history, trends, and future developments. *Subsurface Sensing Technologies and Applications*, 3 (4):253–270.

Hallikainen, M. (1984). Retrieval of snow water equivalent from Nimbus-7 SMMR data: Effect of land-cover categories and weather conditions. *IEEE Journal of Oceanic Engineering*, OE-9 (5):372–376.

Hallikainen, M. T., Ulaby, F. T., Dobson, M. C., El-Rayes, M. A., and Wu, L. (1984). Microwave dielectric behaviour of wet soil Part i: Empirical models and experimental observations from 1.4 to 18 GHz. *IEEE Transactions on Geoscience and Remote Sensing*, pages 25–34.

Harms, F. (1907). Electromagnetic waves on a wire with insulated cylindrical coating. *Annalen der Physik*, 23:44–60. (published in german).

Hasted, J. B. (1973). *Aqueous Dielectrics*. Chapman and Hall, London.

Hauck, C. (2002). Frozen ground monitoring using dc resistivity tomography. *Geophysical Research Letters*, 29 (21):2016.

Hayashi, T. (2005). Defect imaging with guided waves in a pipe. *The Journal of the Acoustical Society of America*, 117 (4 Pt 1):2134–2140.

Heimovaara, T. J. (1994). Frequency domain analysis of time domain reflectometry waveforms: 1. Measurement of the complex dielectric permittivity of soils. *Water Resources Research*, 30:189–199.

Herkelrath, W. N., Hamburg, S. P., and Murphy, F. (1991). Automatic, real-time monitoring of soil moisture in a remote field area with time domain reflectometry. *Water Resource Research*, 26:2311–2316.

Hilhorst, M. A. (1998). *Dielectric characteristics of soil*. PhD thesis, Wageningen Agricultural University, Wageningen, The Netherlands.

Hillel, D. (1973). *Soil and Water: Physical Principles and Processes*. Academic Press, New York.

Hoekstra, P. and Delaney, A. (1974). Dielectric properties of soils at UHF and microwave frequencies. *Journal of Geophysical Research*, 79:1699–1708.

Hondros, D. (1909). On electromagnetic wire waves. *Annalen der Physik*, 30:905–950. (published in german).

Hubbard, S., Grote, K., and Rubin, Y. (2002). Mapping the volumetric soil water content of a california vineyard using high-frequency GPR ground wave data. *The Leading Edge*, 21:552–559.

Hubbard, S., Peterson Jr, J. E., Majer, E. L., Zawislanski, P. T., Williams, K. H., Roberts, J., and Wobber, F. (1997). Estimation of permeable pathways and water content using tomographic radar data. *The Leading Edge*, 16:1623–1630.

Huisman, J. A., S., H. S., Redman, J. D., and P, A. A. (2003a). Measuring soil water content with ground penetrating radar: A review. *Vadose Zone Journal*, 2:476–491.

Huisman, J. A., Snepvangers, J. J. J. C., Bouten, W., and Heuvelink, G. B. M. (2002). Mapping spatial variation in surface soil water content: comparison of ground-penetrating radar and time domain reflectometry. *Vadose Zone Journal*, 269:194–207.

Huisman, J. A., Snepvangers, J. J. J. C., Bouten, W., and Heuvelink, G. B. M. (2003b). Monitoring temporal development of spatial soil water content variation: comparison of ground-penetrating-radar and time domain reflectometry. *Vadose Zone Journal*, 2:519–529.

Huisman, J. A., Sperl, C., Bouten, W., and Verstraten, J. M. (2001). Soil water content measurements at different scales: accuracy of time domain reflectometry and ground-penetrating radar. *Journal of Hydrology*, 245:48–58.

Hull, R., Osgood Jnr, R. M., and Parisi, J. (2003). *Dielectric Properties of a porous medium*. Springer Verlag, Heidelberg.

Hupet, F. and Vanclooster, M. (2002). Intraseasonal dynamics of soil moisture variability within a small agricultural maize cropped field. *Journal of Hydrology*, 261:86–101.

Hülsmeyer, C. (1904). Method of detecting remote metallic objects through electric waves. *German Patent*, 165546. published in german.

Igel, J. (2007). *On the Small-Scale Variability of Electrical Soil Properties and its Influence on Geophysical Measurements*. PhD thesis, Faculty of Geosciences, Johann Wolfgang Goethe University of Frankfurt on the Main, Germany.

Igel, J., Preetz, H., Noell, U., and Schmalholz, J. (2006). Determination of small scale soil water content variability in the near-surface using geophysical methods. *Feuchtemessung in Forschung und Praxis*, 2:169–175. published in german.

Igel, J. S., Anschütz, H. R., Schmalholz, J., Wilhelm, H., Breh, W., Hötzel, H., and Hübner, C. (2001). Methods for determining soil moisture with the ground penetrating radar. In *Proceedings of the Fourth International Conference on Electromagnetic Wave Interaction with Water and Moist Substances*, pages 484–491, Weimar.

IMKO, G. (2000). *Theoretical aspects on measuring soil moisture using TRIME*. IMKO GmbH, Ettlingen, Germany. http://www.imko.de/Peter/THEORY.pdf.

IMKO, G. (2001). *TRIME-FM User Manual*. IMKO GmbH, Ettlingen, Germany. http://www.imko.de/Peter/FM-manual-e.pdf.

Jackson, T. J. (1990). Laboratory evaluation of a field-portable dielectric soil moisture probe. *IEEE Transactions on Geoscience and Remote Sensing*, 28:241–245.

Jackson, T. J. and Le Vine, D. E. (1996). Mapping surface soil moisture using an aircraft-based passive microwave instrument: Algorithm and example. *Journal of Hydrology*, 184:85–99.

Jackson, T. J., Le Vine, D. M., Hsu, A. Y., Oldak, A., Starks, P. J., and Swift, C. T. (1999). Soil moisture mapping at regional scales using microwave radiometry: the southern great plains hydrology experiment. *IEEE Transactions on Geoscience and Remote Sensing*, 37 (5):2136–2151.

Jackson, T. J., Le Vine, D. M., Swift, C. T., J., S. T., and Schiebe, F. R. (1995). Large area mapping of soil moisture using the estar passive microwave radiometer in washita'92. *Remote Sensing of Environment*, 53:27–37.

Jaynes, D. B. and Hunsaker, D. J. (1989). Spatial and temporal variability of water content and infiltration on a flood irrigated field. *Transactions ASAE*, 32:1229–1238.

Johansen, S. E., Amundsen, H. E. F., Røsten, T., Ellingsrud, S., Eidesmo, T., and Bhuyian, A. H. (2005). Subsurface hydrocarbons detected by electromagnetic sounding. *First break*, 23:31–36.

Johansson, S. and Dahlin, T. (1996). Seepage monitoring in an earth embankment dam by repeated resistivity measurements. *European Journal of Engineering and Environmental Geophysics*, 1:229–247.

Journel, A. G. and Huijbregts, C. J. (1978). *Mining Geostatistics*. Academic Press, London.

Junior, V. V., Carvalho, M. P., Dafonte, J., and Freddi, O. S. (2005). Spatial variability of soil water content and mechanical resistance of brazilian ferralsol. *http://www.elsevier.com/locate/still*. (assessed on September 20, 2007).

Kachanoski, R. G. and de Jong, E. (1988). Scale dependence and the temporal persistence of spatial patterns of soil water storage. *Water Resources Research*, 24:85–91.

Kachanoski, R. G., Rolston, D. E., and De Jong, E. (1985). Spatial variability of a cultivated soil as affected by past and present microtopography. *Soil Science Society of America*, 49:1082–1087.

Keary, P. and Brooks, M. (1991). *An Introduction to Geophysical Exploration*. Blackwell Scientific Publications, Bosten, Massachusetts.

King, R. W. P., Owens, M., and Wu, T. T. (1992). *Lateral Electromagnetic Waves: Theory and Applications to Communications, Geophysical Exploration and Remote Sensing*. Springer Verlag, Heidelberg.

King, R. W. P., Smith, G. S., Owens, M., and Wu, T. T. (1981). *Antennas in Matter: Fundamentals, Theory, and Applications*. MIT, Cambridge.

Kirby, M. J. (2001). Modelling the interactions between soil surface properties and soil erosion. *Catena*, 46:89–102.

Krige, D. (1951). A statistical approach to some basic mine valuation problems on the witwatersrand. *Journal of Chem. Metall. Min. Soc. South Africa*, 52:119–139.

Königer, F., Nüesch, R., Rabl-Lasar, W., Roth, J., Ruppert, P., and Schuhmann, R. (2005). Alternative surface covering of landfill using the taupe sealing monitoring system. In *Proceedings of the 6th Conference on Electromagnetic Wave Interaction with Water and Moisture Substances*, Weimar. ISEMA.

Laurent, J. P., Delage, L., Breda, L., Chanzy, A., and Chevallier, C. (2001). On the use of TDR TRIME-tube system for profiling water-content in soils. In *TDR 2001:Second International Symposium and Workshop on the Time Domain Reflectometry for Innovative Geotechnical Applications, Evanston, IL.*, pages 82–94.

Laurent, J. P., Delage, L., Zairi, A., Nouna, B. B., and Adjmi, T. (2005). Monitoring soil water profiles with a commercial TDR system: Comparative field tests and laboratory calibration. *Vadose Zone Jounral*, 4:1030–1036.

Ledieu, J., De Ridder, P., De Clerck, P., and Dautrebande, S. (1986). A method of measuring soil moisture by time domain reflectometry. *Journal of Hydrology*, 88:319–328.

Leonard, J. P., Roland, L. J., Jerry, S. Z., Gary, F. A., Roger, J. P., Walter Jnr, E. B., Stanley, H. W., and Philip, L. J. (1974). The apollo lunar sounder radar system. In *Proceedings of the IEEE*, volume 62 (6), pages 769–788.

Lerner, R. M., Enticknap, R. G., Guillette, R. A., Nackoney, O. G., and Chick, R. W. (1967). *Geodar Report EPS-I, MIT Lincoln Lab, Lexington, MA*. MIT.

Lesmes, D. P., Herbstzuber, R., and Wertz, D. (1999). Terrain permittivity mapping:GPR measurements of near-surface soil moisture. In *Proceedings SAGEEP'99*, pages 575–582, Oakland, CA.

Li, Y. G., Oldenburg, D. W., Dahlin, T., and Zhou, B. (1992). Approximate inverse mapping in dc resistivity problems. *Geophysical Journal International*, 109:343–362.

Lichtenecker, K. and Rother, K. (1931). Derivation of logarithmic mixng rule from the general principles of stationary flow. *Physikalische Zeitschrift*, 32:255–260.

Lin, H. (2006). Temporal stability of soil moisture spatial pattern and subsurface preferential flow pathways in the shale hills catchment. *Vadose Zone Journal*, 5(1):317 – 340.

Liu, S. (2001). Spatial variation of soil moisture in china: geostatistical characterization. *Annual Review of Earth and Planetary Sciences*, 205:20–37.

Logsdon, S. (2000). Effect of cable length on time domain reflectometry calibration for high surface area soils. *Soil Science Society of America*, 64:54–61.

Loke, M. H. and Barker, R. D. (1995). Least-squares deconvolution of apparent resistivity pseudosections. *Geophysics*, 60:1682–1690.

Lunt, A., Hubbard, S. S., and Rubin, Y. (2005). Soil moisture content estimation using ground-penetrating radar reflection data. *Journal of Hydrology*, 307:254–269.

Lutz, P., Garambois, S., and Perroud, H. (2003). Influence of antenna configurations for gpr survey: Information from polarization and amplitude versus offset measurements. In *Bristow, C. S. and Jol, H. M. (eds) Ground Penetrating Radar in Sediments*, volume 211, pages 299–313.

Marquart, N. P. (2000). *Comparison of the Finite Difference Methode with the Split Step Methode in the creation of synthetic radargrams with consideration of the frequency-dependent effective soil permittivity: Diploma thesis submitted to the Geophysical Institute*. University of Karlsruhe, Germany. (published in german).

Martinez, A. and Byrnes, A. P. (2001). Modelling dielectric-constant values of geologic materials: An aid to ground-penetrating radar data collection and interpretation. In *Current Research in Earth Sciences, Kansas Geological Survey*, volume 247 (1), page 16.

Martinez-Fernandez, J. and Ceballos, A. (2003). Temporal stability of soil moisture in a large-field experiment in spain. *Soil Science Society of America Journal*, 67(6):1647 – 1656.

Matheron, G. (1970). The theory of regionalised variables and its applications. *Les cahiers du Centre de Morphologie Mathematique, Ecoles des Mines*, 5:212 p.

Mayer, V. (1994). *Problems with the Interpretation of Radar Data - Diploma thesis submitted to the Geophysical Institute*. University of Karlsruhe, Karlsruhe, Germany. (published in german).

Mayer, V. (2005). *Modelling of electromagnetic wave propagation in relation to measured laboratory material properties*. PhD thesis, Geophysical Institute, University of Karlsruhe, Germany. (published in german).

Mayer, V., Sperl, C., and Seher, W. (1998). Comparison of GPR measurements of the ground wave with FDTD modelling. In *Proceedings of the 4th meeting of the Environmental and Engineering Geophysical Society, European Section, September 14-17*, Barcelona, Spain.

McCann, D. M., Jackson, P. D., and Fenning, P. J. (1988). Mcomparison of the seismic and ground probing radar methods in geological surveying. *IEE Proceedings*, 135:380–390.

McClave, J. and Sincich, T. (2006). *Statistics*. Prentice Hall, New York.

Merkler, G., Blinde, A., Armbruster, A., and Döscher, H. D. (1985). Field investigations for the assessment of permeability and identification of leakage in dams and dam foundations. In *Proceedings ICOLD 15th Congress, Q58, R7*, Lausanne, Switzerland.

Merkler, G. P., Militzer, H., Hötzl, H., Armbruster, H., and Brauns, J. (1989). Detection of subsurface flow phenomena. In *Lecture Notes in Earth Sciences*, volume 27. Springer Verlag, Heidelberg.

Merz, B. and Plate, E. (1997). An analysis of the effects of spatial variability of soil and soil moisture on runoff. *Water Resources Research (AGU)*, 33 (12):2909–2922.

Miyamoto, T. and Chikushi, J. (2006). Time domain reflectometry calibration for typical upland soils in kyushu, japan. *Jarq-Japan Agricultural Research Quarterly*, 40 (3):225–231.

Miyamoto, T., Kobayashi, R., Annaka, T., and Chikushi, J. (2001). Applicability of multiple length tdr probes to measure water distributions in an andisol under different tillage systems in japan. *Soil Tillage Research*, 60:91–99.

Miyamoto, T., Putiso, M., Shiono, T., Taruya, H., and Chikushi, J. (2003). Spatial and temporal distribution of soil water content in fields under different vegetation conditions based on tdr measurements. *Japan Agricultural Research Quarterly*, 37 (4):243–248.

Moore, I. D., Burch, G. J., and Mackenzie, D. H. (1988). Topographic effects on the distribution of surface soil water and the location of ephemeral gullies. *Transactions American Society of Agricultural Engineering*, 31:1098–1107.

Morey, R. M. (1974). Continuous subsurface profiling by impulse radar. In *Proceedings of the Engineering Foundation Conference on Subsurface Exploration for Underground Excavation and Heavy Construction*, pages 213–232.

Nakashima, Y., Zhou, H., and Sato, M. (2001). Estimation of ground water level by GPR in an area with multiple ambiguous reflections. *Journal of Applied Geophysics*, 47:241–249.

Navarkhele, V. V. and Nakade, S. T. and. Shaikh, A. A. (2006). A dielectric approach to determine water content in soil using microwave transmission technique at j-band. *Indian Institute of Science*, 86:723–729.

Newton, R. W. (1977). *Microwave remote sensing and its applcation to soil moisture detection*. PhD thesis, Texas A and M University.

Nickel, H., Sender, F., Thierbach, R., and Weichart, H. (1983). Exploring the interior of salt domes from boreholes. *Geophysical Prospecting*, 31:131–148.

Nielsen, D. R., Biggar, J. W., and Erh, K. T. (1973). Spatial variability of field measured soil water properties. *Hilgardia*, 42:215–259.

Olhoeft, G. R. (1984). Applications and limitations of ground penetrating radar. In *Proceedings of the 54th Annual International Meeting and Exposition*, pages 147–148, Atlanta, GA. (Expanded Abstracts).

Olhoeft, G. R. (1987). Electrical properties from 10-3 to 10 9 hz – physics and chemistry. In *Proceedings of the 54th Physics and Chemistry Conference of Porous Media II*, pages 281–298, Ridgefield.

Olhoeft, G. R. (1993). Velocity, attenuation, dispersion, and diffraction hole-to-hole radar processing. In *Proceedings of the Fourth Tunnel Detection Symposium on Subsurface Exploration Technology*, pages 309–322, Golden, Colorado. Colorado School of Mines.

Olhoeft, G. R. (1994). Geophysical observations of geological, hydrological and geochemical heterogeneity. In *Proceedings of the Application of Geophysics to Engineering and Environmental Problems*, pages 129–141, Bosten.

Olhoeft, G. R. (1998). Electrical, magnetic, and geometric properties that determine ground penetrating radar performance. In *Proceedings of GPR-7th International Conference on Ground Penetrating Radar*, pages 177–182, Lawrence, KS.

Olsson, O., Falk, L., Forslund, O., Lundmark, L., and Sandberg, E. (1992). Borehole radar applied to the characterization of hydraulically conductive fracture zones, in crystalline rock. *Geophysical Prospecting*, 40:109–142.

Owe, M., de Jeu, R. A. M., and Walker, J. (2001). A methodology for surface moisture and vegetation opitcal depth retreival using microwave polarization difference index. *IEEE Transaction on Geoscience and Remote Sensing*, 39 (8):1643–1664.

Pansu, M. and Gautheyrou, J. (2006). *Handbook of soil analysis*. Springer Verlag, Heidelberg.

Parkhomenko, E. I. (1967). *Electrical Properties of Rocks*. Plenum Press, New York.

Parkin, G., Redman, D., von Bertoldi, P., and Zhang, Z. (2000). Measurement of soil water content below a wastewater trench using ground penetrating radar. *Water Resources Research*, 36(8):2147–2154.

Parsiani, H., Torres, M., and Rodriguez, P. (2004). Material characteristics in fourier domain (mcfd) formulation, a signature to determine soil type, moisture, and vegetation health, based on multilayer ground penetrating radar reflection. In *Proceedings on Signal and Image Processing*, pages 602–607, Hawaii.

Peterson, J. E. J. (2001). Pre-inversion corrections and analysis of radar tomographic data. *Journal of Environmental and Engineering Geophysics*, 6:1–18.

Pettinelli, E. A., Matteo, D., Paolucci, F., Bella, F., Vannaroni, G., Cereti, A., Del Vento, D., Mattei, E., Riccioni, S., De Santis, A., and Annan, A. P. (2005). Early-time GPR signal analysis: Implications for water content measurement. advanced ground penetrating radar. In *Proceedings of the 3rd International Workshop*, pages 51–54.

Piefke, G. (1959). The transmission characteristics of a corrugated guide. *IRE Transactions on Antenna and Propagation*, pages S183–S190.

Pindyck, R. S. and Rubinfeld, D. L. (1991). *Economic Models and Economic Forecasts*. McGRAW-Hill INC., Singapore.

Powers, M. H. (1997). Modelling frequency-dependent GPR. *The Leading Edge*, 16:1657–1662.

Preko, K. and Rings, J. (2007). Volumetric water content measurements of a dike model using electrical and electromagnetic techniques. *Innovative Feuchtemessung in Forschung und Praxis*, 3:75–82.

Preko, K. and Wilhelm, H. (2006). Volumetric soil water content monitoring of a dike model using GPR techniques. *Innovative Feuchtemessung in Forschung und Praxis*, 2:65–71.

Qiu, Y., Fu, B., Wang, J., and Chen, L. (2001). Spatial variability of soil moisture content and its relation to environmental indices in a semi-arid gully catchment. *Journal of Arid Environments*, 49 (4):723–750.

Ramos, M. C. and Mulligan, M. (2005). Spatial modelling of the impact of climate variability on the annual soil moisture regime in a mechanized mediterranean vineyard. *Journal of Hydrology*, 1-4:287–301.

Regalado, C. M., Muñoz Carpena, R., Socorro, A. R., and Hernández Moreno, J. M. (2003). Time domain reflectometry models as a tool to understand the dielectric response of volcanic soils. *Geoderma*, 117:313–330.

Reynolds, J. M. (1997). *An Introduction to Applied and Environmental Geophysics*. John Wiley and Sons, New York, NY.

Reynolds, S. G. (1970). The gravimetric method of soil water determination part iii: an examination of factors influencing soil moisture variability. *Journal of Hydrology*, 11:288–300.

Rings, J., Hauck, C., Scheuermann, A., and Preko, K. (2006). Geophysical monitoring of dike water content. In *EGU General Assembly*, Vienna.

Rinker, J. N., Evans, S., and Robin, G. d. Q. (1966). Radio ice sounding techniques. In *Proceedings of 4th Symposium on Remote Sensing of Environment (University of Michigan)*, pages 793–800.

Ritsema, C. J. and Dekker, L. W. (1998). Three-dimensional patterns of moisture, water repellency, bromide and ph in a sandy soil. *Journal of Contaminant Hydrology*, 31:295–313.

Robin, G. d. Q. (1930). Principles, methods and results of electrodynamic thickness measurement of glacier ice. *Zeitschrift fur Gletscherkunde*, 18:24.

Roth, C. H., Malicki, M. A., and Plagge, R. (1992). Empirical evaluation of the relationship between soil dielectric constant and volumetric water content as the basis for calibrating soil moisture measurements by TDR. *Journal of Soil Science*, 43:1–13.

Roth, K., Schulin, R., Flühler, H., and Attinger, W. (1990). Calibration of time domain reflectometry for water content measurement using a composite dielectric approach. *Water Resources Research*, 26:2267–2273.

Rucker, D. F. and Ferré, T. P. A. (2005). Automated water content reconstruction of zero-offset borehole ground penetrating radar data using simulated annealing. *Journal of Hydrology*, 309 (1-4):1–16.

Rumsey, D. (2003). *Statistics for Dummies*. Wiley Publishing Inc., Indianapolis, Indiana.

Saint-Amant, M. and Strangway, D. W. (1970). Dielectric properties of dry geologic materials. *Geophysics*, 35 (4):624–645.

Salvatore, D. and Reagle, D. (2001). *Schaum's Outline of Statistics and Econometrics*. McGraw-Hill, New York. 2nd Edition.

Sandmeier, K.-J. (2007). *REFLEXW - Processing and interpretation software for GPR, seismic and borehole data*. Sandmeier Scientific Software, http://www.sandmeier-geo.de. Version 4.5.

Sato, M. and Miwa, T. (2000). Polarimetric borehole radar system for fracture measurement. *Subsurface Sensing Technologies and Applications*, 1:161–175.

Scheuermann, A. (2005). *Non steady state moisture penetration through quasi-homogeneous soil dikes*. PhD thesis, Institute for Soil Mechanics and Rock Mechanics, University of Karlsruhe, Germany. (published in german).

Scheuermann, A. and Bieberstein, A. (2006). Evaluation of infiltration processes in dams and dikes through moisture measurements with TDR. *Wasserwirtschaft*, 96 (1/2):37–41. (published in german).

Scheuermann, A., Brauns, J., Schlaeger, S., Becker, R., and Hübner, C. (2002). Monitoring of dams and dike with TDR. In *11. Feuchtetag*, Weimar. (published in german).

Scheuermann, A., Schlaeger, S., Hübner, C., Brandelik, A., and Brauns, J. (2001). Monitoring of the spatial soil water distribution on a full-scale dike model. In *Proceedings of the Fourth International Conference on Electromagnetic Wave Interaction with Water and Moist Substances*, pages 343–350, Weimar. MEPA.

Schlaeger, S., Hübner, C., and Becker, R. (2005). Simple soil moisture probe for low-cost measurement applications. In *Proceedings of the 6th Conference on Electromagnetic Wave Interaction with Water and Moisture Substances*, Weimar. ISEMA.

Schlesinger, W. H. (1997). *Biogeochemistry: an Analysis of Global Change*, volume 2. Academic Press, San Diego, CA. Chapter 10: The Water Cycle.

Schmalholz, J. (2007). *Georadar for small-scale high-resolution dielectric property and water content determination of soils*. PhD thesis, Faculty VI, Belin University of Technology, Germany.

Schmalholz, J., Stoffregen, H., Kemna, A., and Yaramanci, U. (2004). Imaging of water content distributions inside a lysimeter using GPR tomography. *Vadose Zone Journal*, 3:1106–1115.

Schröder, G. and Treiber, H. (2002). *Engineering Optics*. Vogel Verlag. (published in german).

Schubert, E. (1999). *Radiation characteristics of ground penetating radar antennas: Preparatory Outline for Physics Practical 3*. Geophysical Institute, University of Karlsruhe, Karlsruhe, Germany. (published in german).

Schön, J. H. (1996). *Physical Properties of Rocks: Fundamentals and Principles of Petrophysics; Handbook of Geophysical Exploration, section 1, Seismic Exploration*, volume 18. Elsevier, Oxford.

Seher, W. (1998). *The use electromagnetic methods in the determination of soil moisture through dielectric coefficient measurements: Diploma thesis submitted to the Geophysical Institute*. University of Karlsruhe, Karlsruhe, Germany. (published in german).

Serbin, G. and Or, D. (2003). Near-surface soil water content measurements using horn antenna radar. *Vadose Zone Journal*, 2:500–510.

Serbin, G. and Or, D. (2004). Ground-penetrating radar measurement of soil water content dynamics using a suspended horn antenna. *IEEE Transactions on Geoscience and Remote Sensing*, 42 (8):1695–1705.

Shih, S. F., Doolittle, J. A., Myhre, D. L., and Schellentrager, G. W. (1986). Using radar for groundwater investigation. *Journal of Irrigation and Drainage Engineering*, 112 (2):110–118.

Simmons, G., Strangway, D. W., Bannister, L., Baker, R., Cubley, D., LaTorraca, G., and Watts, R. (1972). lunar planetary sounding. In *Lunar Geophysics*, pages 258–271.

Singh, V. P. (1997). *Kinematic Wave Modeling in Water Resources, Environmental Hydrology*. Wiley-Interscience.

Smoltczyk, U. (2001). *Soil Engineering 1-3: Geotechnical Principles*. Ernst, Wilhelm und Sohn, Berlin. (published in german).

Soil Survey Staff, U. S. D. A. (1975). *Soil Taxonomy: a basic system of soil classification for making and interpreting soil surveys. Agricultural Handbook*, volume 436. U.S. Government Printing Office, Washington, D.C.

Sommerfeld, A. (1899). The propagation of electromagnetic waves along a wire. *Annalen der Physik*, 67:233–299. (published in german).

Sommerfeld, A. (1948). *Lectures on theoretical Physics*. Dietericher Verlag. (published in german).

Sperl, C. (1999). *Determination of soil water content in an agro-ecosystem using the ground wave of ground penetrating radar*. PhD thesis, University of Munich. published in german.

Spiegel, M. and Stephens, L. (2007). *Schaum's Outline of Statistics*. McGraw-Hill, New York. 4th Edition.

Stacheder, M. (1996). Die time domain reflectometry in der geotechnik. *Applied Geology, University of Karlsruhe, Karlsruhe*, 40:170.

Stacheder, M., Fundinger, R., and Koehler, K. (1994). A new time domain reflectometry system (TRIME) to measure soil moisture and electrical conductivity. In *Symposium and workshop on time domain reflectometry in environmental, infrastructure, and mining applications. Special publication*, pages 55–65, Weimar. United States. Bureau of Mines.

Stacheder, M., Köhler, K., Fundinger, R., and Blume, P. (1997). Measuring moisture with the time domain reflectometry. In *Conference Report 9*, pages 39–50, Weimar. (published in german).

Stoffregen, H., Yaramanci, U., Zenker, T., and Wessolek, G. (2002). Accuracy of soil water content measurements using ground penetrating radar: Comparison of ground penetrating radar and lysimeter data. *Journal Hydrology*, 267:201–206.

Strobbia, C. and G., C. (2005). Multilayer ground penetrating radar guided waves in shallow soil layers for estimating soil water content. *Geophysics*, 72 (4):J17–J29.

Terzaghi, K., Peck, R. B., and Mesri, G. (1996). *Soil Mechanics in Engineering Practice*. Wiley-Interscience.

Theimer, B. D., Nobes, D. C., and Warner, B. G. (1994). A study of the geoelectrical properties of peatlands and their influence on ground-penetrating radar surveying. *Geophysics Prospecting*, 42:179–209.

Theune, U. (1999). *Detection of leakages in water structures fibre optical temperature techniques*. PhD thesis, Geophysical Institute, University of Karlsruhe, Germany. (published in german).

Thierbach, R. (1974). Electromagnetic reflections in salt deposits. *Journal of Geophysics*, 40:633–637.

Thompson, L. G., Mosley-Thompson, E., and Petit, J. R. (1979). Glaciological interpretation of microparticle concentrations from the French 905-m Dome c, Antarctica core. *Sea Level, Ice and Climatic Change, IAHS-AISH*, 131:227–234.

Tillard, S. and Dubois, J. C. (1994). Analysis of GPR data:wave velocity determination. *Journal of Applied Geophysics*, 33 (1-3):77–91.

Topp, G. C. and Davis, J. L. (2005). Measurement of soil water content using time-domain reflectometry (TDR): A field evaluation. *Soil Science Society of America Journal*, 49:19–24.

Topp, G. C., Davis, J. L., and Annan, A. P. (1980). Electromagnetic determination of soil water content. measurements in coaxial transmission lines. *Water Resources Research*, 16:574–582.

Topp, G. C.and Davis, J. L. and Annan, A. P. (1982). Electromagnetic determination of soil water content using TDR: In applications to wetting fronts and steep gradients. *Soil Science Society of America Journal*, 46:672–678.

Trangmar, B. B., Yost, R. S., and Uehara, G. (1985). Application of geostatistics to spatial studies of soil properties. *Advances in Agronomy*, 38:45–94.

Trangmar, B. B., Yost, R. S., Wade, M. K., Uehara, G., and Sudjadi, M. (1987). Spatial variation of soil properties and rice yield on recently cleared land. *Soil Science Society of America Journal*, 51:668–674.

Tsang, T., Kong, J. A., and Simmons, G. (1973). Interference patterns of a horizontal electric dipole over layered dielectric media. *Journal of Geophysics Research*, 78:3287–3300.

Täumer, K., Stoffregen, H., and Wessolek, G. (2006). Seasonal dynamics of preferential flow in a water repellent soil. *Vadose Zone Journal*, 5 (1):405–411.

Ulaby, F. T., Bengal, T. H., Dobson, M. C., East, J. R., Garvin, J. B., and Evans, D. L. (1990). Microwave dielectric properties of dry rocks. *Institute of Electrical and Electronics Engineers, Transactions on Geoscience and Remote Sensing*, 28 (3):325–336.

Ulaby, T., Moore, R. K., and Fung, A. K. (1982). *Microwave Remote Sensing: Active and passive: Radar Remote Sensing and Surface Scattering Emission Theory*, volume 2. Addison-Wesley, Reading, Massachusetts.

Unterberger, R. R. (1978). Radar propagation in rock salt. *Geophysical Prospecting*, 26 (2):312–328.

van Dam, R. L., Schlager, M. J., and Huisman, J. A. (2002). Iron oxides as cause of GPR reflections. *Geophysics*, 67:536–545.

van der Kruk, J., R., S., and G., G. A. (2006). Properties of surface waveguides derived from separate and joint inversion of dispersive TE and TM GPR data. *Geophysics*, 71 (1):K19–K29.

van Overmeeren, R. A., Sariowan, S. V., and Gehrels, J. C. (1997). Ground penetrating radar for determining volumetric water content: results of comparative measurements at two sites. *Journal of Hydrology*, 197:316–338.

van Pelt, R. S. and Wierenga, P. J. (2001). Temporal stability of spatially measured soil matric potential probability density function. *Soil Science Society of America Journal*, 65:668–677.

Vanclooster, M., Mallants, D., Diels, J., and Feyen, J. (1993). Determining local scale transport parameters using the time domain reflectometry (TDR). *Journal of Hydrology*, 148:93–107.

Vanclooster, M., Mallants, D., Diels, J., and J., F. (1952). Determination of soil moisture by neutron scattering. *Soil Science*, 73:391–401.

Vellidis, G., Smith, M. C., Thomas, D. L., and Asmussen, L. E. (1990). Detecting wetting front movement in a sandy soil with ground-penetrating radar. *Transactions of the American Society of Agricultural Engineers*, 33 (6):1867–1874.

Voss, T. (2006). *Exploration depth experiments over the direct ground wave of radar: Student research project submitted to the Institute of Applied Geosciences*. Technical University of Berlin. (published in german).

Waite, A. H. (1966). International experiments in glacier sounding. *Canadian Journal of Earth Sciences*, 3:887.

Waite, A. H. and Schmidt, S. J. (1962). Gross errors in height indication from pulsed radio altimeters operating over thick ice and snow. In *Proceedings - Institute of Radio Engineers*, volume 50, pages 1516–1520.

Walford, M. (1985). Exploration of temperate glaciers. *Physics Bulletin*, 36:108–109.

Wang, J. R. and Schmugge, T. J. (1980). An emprical model for complex dielectric permittivity of soils as a function of water content. *IEEE Transactions on Geoscience*, pages 288–295.

Weihermüller, L., Huisman, J. A., Lambot, S., Herbst, M., and Vereecken, H. (2007). Mapping the spatial variation of soil water content at the field scale with different ground penetrating radar techniques. *Journal of Hydrology*, 340:205–216.

Weiler, K. W., Steenhuis, T. S., Boll, J., and Kung, K. J. S. (1998). Comparison of ground penetrating radar and time domain reflectometry as soil water sensors. *Soil Science Society of America Journal*, 62:1237–1239.

Wensink, W. A. (1993). Dielectric properties of wet soils in the frequency range 1-3000 MHz. *Geophysical Prospecting*, 41:671–696.

Western, A. W. and Blöschl, G. (1999). On the spatial scaling of soil moisture. *Journal of Hydrology*, 217:203–224.

Western, A. W., Blöschl, G., and Grayson, R. B. (1998). Geostatistical characterization of soil moisture patterns in the tarrawarra catchment. *Journal of Hydrology*, 205:20–37.

Western, A. W., Grayson, R. B., and Blöschl, G. (2002). Scaling of soil moisture: a hydrologic perspective. *Annual Review of Earth and Planetary Sciences*, 205:20–37.

Western, A. W., Zhoua, S.-L., Grayson, R. B., McMahon, T. A., Blöschl, G., and Wilson, D. J. (2004). Spatial correlation of soil moisture in small catchments and its relationship to dominant spatial hydrological processes. *Journal of Hydrology*, 286 (1-4):113–134.

Wetzel, P. J. and Chang, J. T. (1987). Concerning the relationship between evapotranspiration and soil moisture. *Journal of Climate and Applied Meteorology*, 26:18–27.

Wilhelm, H. and Brandelik, A. (1998). Soil moisture determination with electromagnetic methods. *Project Proposal C12B*. (published in german).

Wollny, K. G. (1999). *The nature of the ground wave and its application for soil moisture determination*. PhD thesis, Faculty of Geosciences, University of Munich, Germany. (published in german).

Wood, E. F. (1997). Effects of soil water aggregation on surface evaporative fluxes. *Journal of Hydrology*, 190:397–412.

Wraith, J. M., Robinson, D. A., Jones, S. B., and Long, D. S. (2006). Spatially characterizing apparent electrical conductivity and water content of surface soils with time domain reflectometry. *Computers and Electronics in Agriculture*, 46:239–261.

Wörsching, H., Becker, R., Schlaeger, S., and Bieberstein, A. (2006). Moisture determination with Spatial TDR on large clay dike models. *Innovative Feuchtemessung in Forschung und Praxis*, 2:215–221. (published in german).

Xu, X., Wu, J., and He, Z. (2006). Application of GPR to detection of hidden dangers to underwater hydraulic structures. *Journal of Hydrology*, 132 (1):12–20.

Ya, A., Pachepsky, A., Guber, K., and Jacques, D. (2005). Temporal persistence in vertical distributions of soil moisture contents. *Soil Science Society of America Journal*, 69(2):347 – 352.

Yee, K. S. (1996). Numerical solutions of initial boundary value problems involving maxwell's equations in isotropic media. *IEEE Transactions on Antennas and Propagation*, AP-14:302–307.

Yeh, C. and Zoughi, R. (1994). Microwave detection of finite surface cracks in metals using rectangular waveguides. *Research in Nondestructive Evaluation*, 6 (1):35–55.

Yilmaz, Ö. (1987). *Seismic Data Processing*. Society of Exploration Geophysicists, Oklahoma. 3rd Edition.

Zeng, X. and McMechan, G. (1997). GPR characterisation of buried tanks and pipes. *Geophysics*, 62 (3):797–806.

Acknowledgements

This work was carried out at the Geophysical Institute, University of Karlsruhe, Germany with support from the Ghana Educational Trust Fund (GETFUND). Experiments on the dike model at the Institute for Water and River Basin Management (University of Karlsruhe) were conducted with the kind permission of Dr. Boris Lehrmann. The work in Burkina Faso was jointly funded by AMMA, IMK and FZK. I am very grateful to Prof. Dr. Christoph Kottmeier for the opportunity to be part of the AMMA project in Dano, Burkina Faso, West Africa.

I wish to express my sincere gratitude to my supervisor Prof. Dr. Friedemann Wenzel (Head of the Geophysical Institute, Karlsruhe) for excellent working conditions and the many invaluable suggestions.

I am highly indebted to Prof. Dr. Helmut Wilhelm for the opportunity to carry out this research at the University of Karlsruhe. I also acknowledge his continued support during very difficult times and for creating a very pleasant working environment without which this work could not have been brought this far.

Dr. Karl-Josef Sandmeier *Jupp* (Sandmeier Scientific Software) readily provided me with all the needed tools of his software package Reflexw and also gave me several tutorial lessons on data processing, logical editing and modelling. All my data were processed with Reflexw. Dr. Volker Mayer deserves my deepest gratitude. He has been a great help in my field work. Despite his busy schedule he always found time to help me on data acquisition strategies with the SIR-3 GPR equipment. This equipment could not have been properly operated without his help. Mr. Martin Flinspach was kind enough to introduce me to the application of the GPR technique.

I wish to express my profound to thanks to Mr. Werner Scherer and Mr. Thomas Hartmut (Electronic Laboratory, Geophysical Institute, Karlsruhe) for containing so many complaints of a defect equipment and for constructing a very reliable GPR support system that enabled me feasibly conduct my experiments in Burkina Faso, West Africa.

Finally, I acknowledge the friendliness and pleasant working atmosphere created by the entire staff of the Geophysical Institute, Karlsruhe.